12-17-2010

Development of a Simulation Model for Fluidized Bed Mild Gasifier

AKM Monayem Hossain Mazumder
University of New Orleans

Development of a Simulation Model for Fluidized Bed Mild Gasifier

A Thesis

Submitted to the Graduate Faculty of the
University of New Orleans
in partial fulfillment of the
requirements for the degree of

Master of Science
in
Engineering
Mechanical

By

A.K.M. Monayem Hossain Mazumder

B.S. Bangladesh University of Engineering and Technology, 2006

December, 2010

ACKNOWLEDGEMENT

I would like to take this opportunity to thank my advisor, Dr. Ting Wang, for his guidance and support while working under him as a graduate student. None of this would be made possible without Dr. Ting Wang's hard work and dedication to his students and the University of New Orleans. I would also like to thank Drs. Paul J. Schilling, Melody A. Verges, and Carsie A. Hall, III for being a part of my thesis committee.

I would like to acknowledge the support from the Louisiana Governor's Energy Initiative, administered by the Louisiana Board of Regents via the Clean Power and Energy Research Consortium (CPERC) and the Grant from the Department of Energy.

Furthermore, I would also like to thank my fellow colleague students and researches, Dr. Jobaidur Rahman Khan, Dr. T. S. Dhanasekaran, Dr. Armin Silaen, Jason Kent, and other from the Energy Conversion and Conservation Center (ECCC) for their help, support and valuable suggestions.

Finally, I would like to thank all my family and friends for their support throughout the years while I pursed both, my Bachelors of Science and Masters of Science degree in Mechanical Engineering. They have always been there for me with constant support in dealing with difficult times and made the good times even more enjoyable, and for that I am very grateful.

TABLE OF CONTENTS

LIST OF FIGURES

LIST OF TABLES

NOMENCLATURE

a	local speed of sound (m/s)
c	concentration (mass/volume, moles/volume)
c_p	heat capacity at constant pressure (J/kg-K)
c_v	heat capacity at constant volume (J/kg-K)
D	mass diffusion coefficient (m^2/s)
D_H	hydraulic diameter (m)
D_{ij}	mass diffusion coefficient (m^2/s)
D_t	turbulent diffusivity (m^2/s)
E	total energy (J)
g	gravitational acceleration (m/s^2)
G	incident radiation
Gr	Grashof number ($L^3.\rho^2.g.\beta.\Delta T/ \mu^2$)
H	total enthalpy (W/m^2-K)
h	species enthalpy (W/kg-m^2-K)
J	mass flux; diffusion flux (kg/m^2-s)
k	turbulence kinetic energy (m^2/s^2)
k	thermal conductivity (W/m-K)
m	mass (kg)
M_W	molecular weight (kg/kgmol)
M	Mach number
p	pressure (atm)
Pr	Prandtl number (ν/α)
q	heat flux
q_r	radiation heat flux
R	universal gas constant (8314.34 J/Kmol-K)
S	source term
Sc	Schmidt number (ν/D)
t	time (s)

T	temperature (K)
U	mean velocity (m/s)
X	mole fraction (dimensionless)
Y	mass fraction (dimensionless)
x, y, z	coordinates

Greek letter

β	coefficient of thermal expansion (K^{-1})
ε	turbulence dissipation (m^2/s^3)
ε_w	wall emissivity
κ	von Karman constant
μ	dynamics viscosity (kg/m-s)
μ_k	turbulent viscosity (kg/m-s)
v	kinematic viscosity (m^2/s)
v'	stoichiometric coefficient of reactant
v''	stoichiometric coefficient of product
ρ	density (kg/m^3)
ρ_w	wall reflectivity
σ	Stefan-Boltzmann constant
σ_s	scattering coefficient
τ	stress tensor ($kg/m\text{-}s^2$)

Subscript

i	reactant i
j	product j
r	reaction r

ABSTRACT

A mild gasification method has been developed to provide an innovative clean coal technology. The objective of this study is to developed a numerical model to investigate the thermal-flow and gasification process inside a specially designed fluidized-bed mild gasifier using the commercial CFD solver ANSYS/FLUENT. Eulerain-Eulerian method is employed to calculate both the primary phase (air) and secondary phase (coal particles). The Navier-Stokes equations and seven species transport equations are solved with three heterogeneous (gas-solid), two homogeneous (gas-gas) global gasification reactions. Development of the model starts from simulating single-phase turbulent flow and heat transfer to understand the thermal-flow behavior followed by five global gasification reactions, progressively with adding one equation at a time. Finally, the particles are introduced with heterogeneous reactions. The simulation model has been successfully developed. The results are reasonable but require future experimental data for verification.

Keywords: Clean coal technology, coal gasification, fluidized-bed, mild gasifier, CFD, heterogeneous and homogeneous reaction, finite rate model, multi-phase flow.

CHAPTER ONE
INTRODUCTION

1.1 Background

1.1.1 Brief History of Coal Use

Coal is the most abundant fuel in the fossil family, and it has the longest and most varied history. Archeologists have found evidence that the Romans in England used coal in the second and third centuries (100-200 AD).

The English found in the 1700's that coal could produce a fuel that burned cleaner and hotter than wood charcoal. However, it was the overwhelming need for energy to run the new machinery invented during the Industrial Revolution in 1700's that provided the real opportunity for coal to become a dominant worldwide energy source.

During the 1300's the Hopi Indians in North American, what is now the U.S. Southwest, used coal for cooking, heating, and baking the pottery. Coal was re-discovered in the United States by explorers in 1673. However, commercial coal mines did not start operation until the 1740's in Virginia.

A major event that played a role in expanding the use of coal was the Industrial Revolution. James Watt invented the steam engine, which made it possible for machines to do work previously done by humans and animals. Mr. Watt used coal to make the steam to run his engine.

The Industrial Revolution spread to the United States in the first half of 1800's. Steamships and steam-powered railroads, which used coal to fuel their boilers, were becoming the leading modes of transportation. More uses for coal were found in the second half of the 1800's.

During the Civil War, weapon factories began to use coal. By 1875, coke (which is made from coal) replaced charcoal as the primary fuel for iron blast furnaces to make steel. In 1880, coal was first used to generate electricity for homes and factories.

1.1.2 United States Coal Reserves

One quarter of the world's coal reserves are found in the United States. The energy content of United States' coal reserves exceeds the world's known oil reserves. Coal is the USA's largest domestic energy resource, and more than 50 percents of the United States electricity supply comes from coal. At the current rates of use, United States' coal reserves are enough to last for 250 years. There is still enough coal underground in this country to provide energy for the next 200 to 300 years. The dependence of the U.S. on coal as source of energy will continue as the Energy Information Administration projects a 26 percent increase in the United States electricity demand from 2007 to 2030, with coal remaining the main fuel source.

1.1.3 Impurities inside Coal

Unfortunately, coal is not a perfect fuel. Trapped inside coal are trace impurities such as nitrogen and sulfur. When coal burns, these impurities (NO_x and SO_x) are released into the air, which can react with water vapor in the air and form droplets that fall to earth as weak forms of sulfuric and nitric acid which are known as "acid rain." Similar with any other carbon-based fuel, burning coal produces carbon dioxide. Carbon dioxide is a colorless, odorless gas, but in the atmosphere, it is one of several gases that can trap the earth's heat, causing the "greenhouse effect" which changes the earth's climate. In addition, burning coal also releases flying ashes that add to the problem of air pollution.

1.1.4 Method of using Coal

The method of using coal can be divided into (a) combustion, (b) pyrolysis, (c) liquefaction, and (d) gasification. In combustion, coal is directly burned to produce heat. In pyrolysis, coal is decomposed through heating in the absence of oxygen. Volatile matters inside the coal will be released when coal is heated, leaving only carbon (char) and tar. In liquefaction, coal is converted into liquid fuel. In gasification, coal is converted into synthetic gas (syngas).

Gasification is a process that converts any carbon-based materials, such as coal, pet-coke, biomass, or various wastes, into a synthetic gas (syngas) through an oxygen-limited reaction. The clean syngas can be used as a fuel to produce electricity or valuable products such as chemicals, fertilizers, and transportation fuels. In contrast to a combustion process that takes place in excess oxidant conditions, gasification process takes place in sub-stoichiometric

conditions. Generally, the amount of O_2 used is only 35% or less of the amount required for complete combustion. The main differences between combustion and gasification are listed in Table 1.1.

Table 1.1 Comparisons between Combustion and Gasification

Combustion	Gasification
✓ Occurs in excess-oxidant conditions ✓ Releases heat (exothermic) ✓ Produces heat	✓ Occurs in oxidant-lean conditions ✓ Less production of air pollutants gas ✓ Absorbs heat (endothermic) ✓ Produces syngas

Gasification has a lower environmental impact compared to traditional combustion technologies because of the following reasons:

(a) Gasification can recover available energy from low-value materials, such as municipal solid waste and pet-coke.
(b) Syngas is cleaned before combustion, thus reducing air pollutants such as NO_x and SO_x.
(c) By-products of gasification (sulfur and slag) are nonhazardous and marketable.
(d) High efficiency
(e) Low CO_2 production per kW output due to higher efficiency.
(f) Carbon dioxide (CO_2) can be captured prior to syngas combustion. It gives the least cost and most efficient way of capturing CO_2 from a fossil-fuel based power plant.

1.1.5 Brief Description of IGCC System

A very efficient way to use the syngas as fuel in electricity generation is by employing the Integrated Gasification Combined Cycle (IGCC). Schematic of an IGCC system is presented in Fig. 1.1. IGCC combines the gasification system with the gas clean-up system and the combined power system. The syngas produced by the gasifier is cleaned and used as a fuel for the gas turbines. The high pressure and hot gases produced in the combustor then expand through the gas turbines to drive the air compressor and an electric generator. The hot exhaust gases from the gas turbines are sent to HRSG (Heat Recovery Steam Generator), producing steam that expands through a steam turbine to drive another electric generator.

Integrated Gasification Combined Cycle (IGCC) also provides a more efficient method of capturing carbon dioxide (CO_2) than in the conventional pulverized coal burning power plants. IGCC demonstration plants have been operating since the early 1970's and some of the plants constructed in the 1990's are now entering successful commercial services.

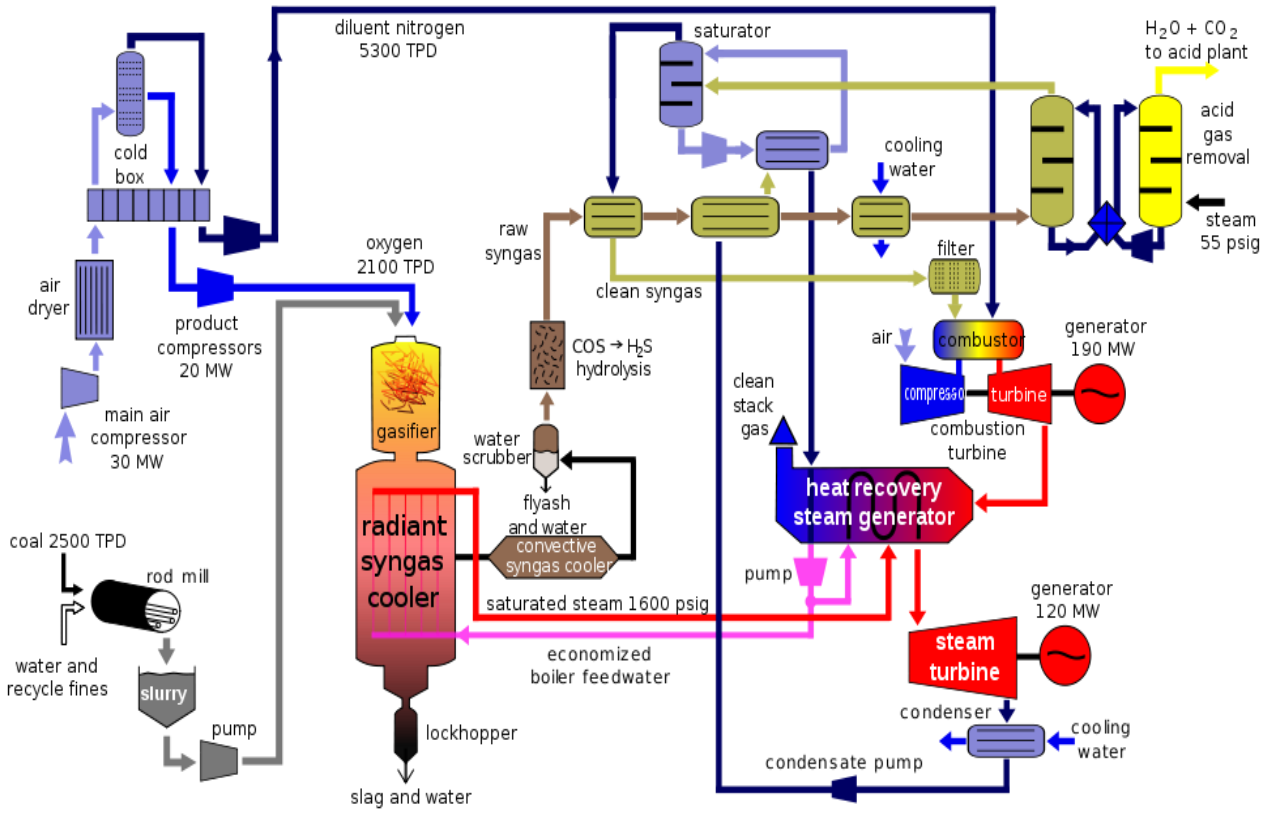

Figure 1.1 Schematic of an IGCC system (Source: Wikipedia, 2006).

1.2 Literature Review

1.2.1 Clean Coal Technology

Many years ago, people do not like to use coal as a fuel because it is dirty and produces heavy pollutants during combustion. But things have changed in the last 20 years; ways have been developed to capture the pollutants trapped in coal before the impurities can escape into the atmosphere. Today, new technologies have been developed that can filter out 99 percent of the tiny particles and remove more than 95 percent of the acid rain pollutants in coal. New technologies also have been developed that can cut back on the release of carbon dioxide by burning coal more efficiently. Many of these technologies belong to a family of energy systems called "clean coal technologies."

The Clean Coal Technology Program began in 1985 when the United States and Canada decided to do something about the "acid rain" because acid rain is responsible for damaging rivers, lakes, forests, and buildings in both countries. Since many of the pollutants that formed "acid rain" were coming from big coal-burning power plants in the United States, the U.S. Government took the lead in finding a solution. One of the steps taken by the U.S. Department of Energy (DOE) was to create a partnership program between the government, several states, and private companies to test new methods to make coal burning much cleaner. This became the "Clean Coal Technology Program." There are several ways to make coal cleaner by removing "acid rain" pollutants such as sulfuric acid and nitric acid (SO_x and NO_x) and "greenhouse gas" such as carbon dioxide (CO_2) gas.

1.2.1.1 Knocking of SO_x out of coal

Sulfur is a yellowish substance that exists in tiny amounts in coal. In some coals found in Ohio, Pennsylvania, West Virginia and other eastern states in the USA, sulfur makes up from 3 to 10 percent of the weight of coal. For some coals found in Wyoming, Montana and other western states in the USA, the sulfur can be only 1 percent or less than 1 percent of the weight of the coal. But still, it is important that most of this sulfur be removed before it goes up a power plant's smokestack.

One way is to clean the coal from sulfur before it arrives at the power plant by simply crushing the coal into "small chunks" and "washing" it. Some of the sulfur that exists in tiny speck in coal called "pyritic sulfur" (because it is combined with iron to form iron pyrite) can be washed out of the coal in this manner. Typically, in one washing process, the coal chunks are fed into a large water-filled tank. The coal floats to the surface while the sulfur impurities sink.

Note that, not all of coal's sulfur can be removed by washing because some of the sulfur in coal is actually chemically connected to coal's carbon molecules instead of existing as separate particles. This type of sulfur is called "organic sulfur". Several processes have been tested to mix the coal with chemicals that break the sulfur away from the coal molecules, but most of these processes have proven too expensive. That's why most of modern power plants and all plants built after 1978 are required to have special devices installed that clean the sulfur from the coal's combustion gases before the gases get into the atmosphere. The technical name for these devices

is "flue gas desulfurization units". Another name is "scrubbers" because they "scrub" the sulfur out of the smoke released by coal-burning boilers.

Most scrubbers rely on a very common substance found in nature called "limestone." Limestone can be made into a white powder by crushing and processing. Such as a sponge absorbs water, limestone can be made to absorb sulfur gases under the right conditions.

In most scrubbers, limestone is mixed with water and sprayed into the coal combustion gases (called "flue gases"). The limestone captures the sulfur and "pulls" it out of the gases. The limestone and sulfur combine with each other to form either a wet paste (like toothpaste), or a dry powder. In either case, the sulfur is trapped and prevented from escaping into the air. The Clean Coal Technology Program tested several new types of scrubbers that proved to be more effective, lower cost, and more reliable than older scrubbers.

1.2.1.2 Knocking of NO_x out of coal

About 79% by volume of the air is nitrogen and 21% is oxygen. Normally, nitrogen atoms float around joining each other like chemical couples. But when air is heated, for example in a coal boiler's flame, these nitrogen atoms break apart and join with oxygen. This forms "nitrogen oxides" or "NO_x" . NO_x can also be formed from the atoms of nitrogen that are trapped inside coal. In the air, NO_x is a pollutant. It is also one of the pollutants that forms "acid rain," and it can help form "ground level ozone," another type of pollutant that can make the air dingy. NO_x can be produced by any fuel that burns hot enough. For example, automobiles produce NO_x when they burn gasoline. But a lot of NO_x comes from coal-burning power plants, so the Clean Coal Technology Program developed new ways to reduce this pollutant.

One of the best ways to reduce NO_x is to prevent it from forming in the first place. Scientists have found ways to burn coal in burners where there is more fuel than air in the hottest combustion chambers. Under these conditions, most of the oxygen in air combines with the fuel, rather than with the nitrogen. The burning mixture is then sent into a second combustion chamber where a similar process is repeated until all the fuel is burned. This concept is called "staged combustion" because coal is burned in stages. A new family of coal burners called "low-NO_x burners" has been developed using this way of burning coal. These burners can reduce the amount of NO_x released into the air by more than half.

There is also a family of new technologies that work like "scrubbers" by cleaning NO_x from the flue gases (the smoke) of coal burners. Some of these devices use special chemicals called "catalysts" that break apart the NO_x into non-polluting gases. Although these devices are more expensive than "low-NO_x burners," they can remove up to 90 percent of NO_x pollutants.

In the future, there may be an even cleaner way to burn coal in a power plant, or maybe, there be a way that doesn't burn the coal at all.

1.2.2 History of Gasification

Gasification process has been used for hundreds of years, with the earliest practical gasification process being reported to have taken place in 1792. Murdoch, a Scottish engineer, pyrolyzed coal to produce gas which he then used to light his home. In 1812, the first gas company was established in London to produce gas from coal to light the Westminster Bridge. The first gas plant to manufacture syngas from coal was built in the United States in 1816 to light the streets of Baltimore. Soon, more gas plants followed in Boston and New York. By 1875, manufactured gas was being widely used for home lighting. More than 1200 gas plants were in operation in the United States by the late 1920s as manufactured gas was used in domestic and industrial applications. During the World War II, over 1 million air-blown gasifiers were in operation to generate synthetic gas from wood and charcoal to power vehicles and generate steam and electricity. Note that no gas clean up system was used in the above applications, so the combusted gases are dirty under the standard of present day. However, the discovery of large quantities of low-cost natural gas after World War II put an end to the synthetic gas manufacturing industry. It wasn't until the 1960’s and 1970’s that the interest in gasification technologies was renewed.

1.2.3 Coal Gasification

Figure 1.2 presents the typical processes undergoing by coal particles in gasification. The gasification of coal particles involves two major steps: (a) thermal decomposition (pyrolysis and devolatilization) and (b) combustion of solid residue from the first step. Coal particles undergo pyrolysis when they enter the hot combustion environment. Moisture contained in the particles boils and leaves the particles when the particle temperature reaches the boiling temperature.

The volatiles are then released as particle temperature continues to increase. This volatile release process is called devolatilization. The volatiles are then thermally cracked into lighter gases, such as H_2, CO, C_2H_2, CH_4, etc. These lighter gases can react with O_2, releasing some of the heat needed for the pyrolysis.

With only char and ash left, the particles undergo combustion to produce CO and CO_2, leaving only ash. The thermal decomposition occurs relatively slowly, while the combustion of carbon is faster so the combustion heat can continuously support devolatilization and gasification process.

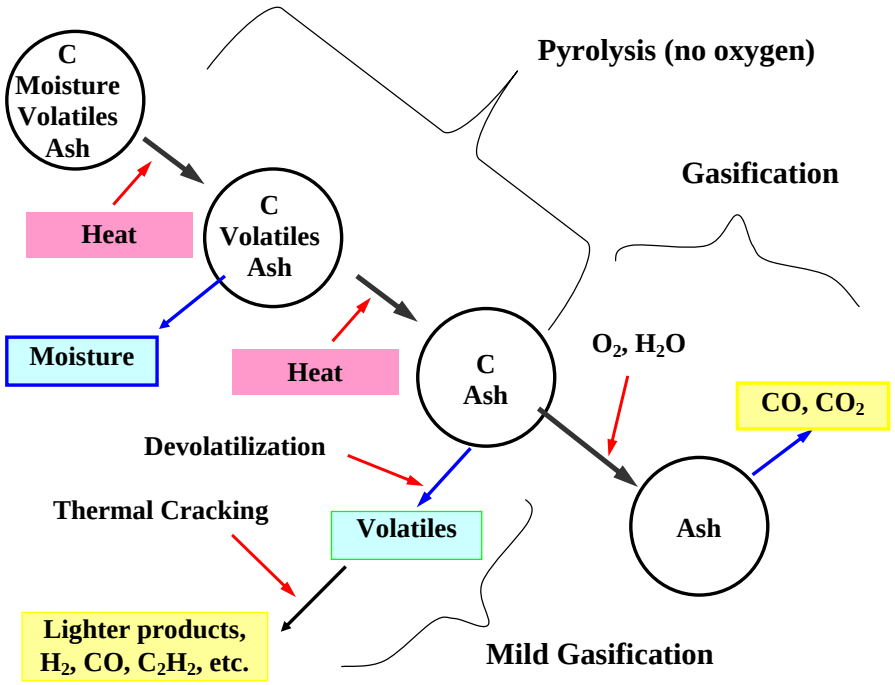

Figure 1.2 Simplified global gasification processes of coal particles (sulfur and other minerals are not included in this figure). Heat can be provided externally or internally through combustion of char, volatiles, and CO.

1.2.3.1 Devolatilization

Devolatilization is a decomposition process of hydrocarbon material when they are heated. Devolatilization rates are influenced by temperature, residence time, particle size, and coal type. The heating causes bonds to rupture and both of coal's organic and mineral parts to decompose. The process starts at temperature around 100 °C (212 °F) with desorption of gases, such as water steam, CO_2, CH_4, and N_2, which are stored in the coal pores. When the

temperature reaches above 300 °C (572 °F), the released liquid hydrocarbon called tar becomes important. Gaseous hydrocarbons such as CO, CO_2, and water steam are also releazed. Coal particle is in a plastic state, where it undergoes drastic change in size and shape, when the temperature is above 500 °C (932 °F). The coal particle then becomes hard again, and is called char, when temperature reaches around 550 °C (1022 °F). As heating continues, H_2 and CO are releazed.

Coal particles undergo swelling as they are heated. Small particles behave differently than larger particles. Smaller particles expand at lower temperature than larger particles. Aside from expanding, particles also change shape during swelling. Usually, the sharp edges of the particles become rounded off. The structure of the coal particles at the end of de-volatilization is influenced by the amount of volatiles contained in the coal. Intensive volatiles release in high volatile coal results in larger particle porosity, while low volatile particles have smaller porosity and burn on the surface.

The pyrolysis conditions affect the physical properties of coal chars. Experiment by Gale et al. (1995), which was conducted at maximum particle temperatures between 570 °C (1058 °F) and 1355 °C (2471 °F) and heating rates between 10^4 and 2 x 10^5 K/s, showed that micro-pore (CO_2) surface area generally increases with increasing residence time and mass releases for lignite and bituminous coals. It also showed that the micro-pore surface area of char increases with increasing maximum particle temperature and heating rate.

The volatile matters generated during heating can significantly influence the temperature distribution in the particle. The volatiles generated near the center of the particle travel to the particle surface and escape. The flow of these volatiles from the particle center to the particle surface can reduce the convective heat transfer from surroundings to the particles surface. It is reported that the heat transfer coefficient decreases 10 times during fast heating of coal particles mixed with hot solid heat carrier. This reduced heat transfer rate to the particle surface results in a temperature plateau of the particle surface on the level of about 400 °C (752 °F) and lasts during the whole time of volatiles release. Another explanation for this temperature plateau given by Davies and Brown (1969) is that this is due to a strong effect of de-volatilization.

In general, the larger the particle size, the smaller amount the volatile yields. This is because in larger particles, more volatiles may crack, condense, or polymerize, with some carbon deposition occurring during their migration from inside the particle to the particle surface. High

pressure has similar effect on the de-volatilization rates. Anthony et al. (1975) reported that devolatilization rates are higher at lower pressures. An increase in pressure increases the transit time of volatiles to reach the particle surface.

Seebauer et al. (1997) investigated the effects of pressure, particle size and heating rate on coal pyrolysis using thermogravimeteric analysis. The pressure used in the study ranged from 1 to 40 atm and heating rate from 0.03 to 0.1 K/s. Seebauer et al. found that the total volatiles yield decreased with increasing pressure. Sun et al. (1997) studied the pyrolysis of two Chinese coals under pressure ranging from 1 to 13 atm with a heating rate as low as 0.33 K/s. It was reported that, at high pressure, the total volatiles yield decreases with increasing pressure. The total weight loss is almost independent of pressure at low temperatures (about less than 837 K).

Fatemi et al. (1987) studied the pressure effects on de-volatilization of pulverized coal up to temperature 1373 K and pressure 68 atm in an entrained-flow reactor. They indicated that the tar yield decreases significantly with increasing pressure up to 13.8 atm. Weight loss and gas yield decreases with increasing pressure up to 13.8 atm, and there is no significant effect above this pressure.

Wall et al. (2002) reviewed the pressure effect on variety aspects of coal reactions reported in open literature. In general, the total volatile and tar yields decrease with increasing pressure. This effect is more pronounced at higher temperatures and is less pronounced at high pressures. Increasing pressure improves fluidity of the coal melt and reduces char reactivity.

1.2.3.2 Carbon Particle Combustion/Gasification

The steps involved in a reaction between gas and a solid particle are as follow:

1. Transport of reactants to solid surface by convection and/or diffusion.
2. Adsorption of reactant molecule on the surface.
3. Reaction steps involving various combinations of adsorbed molecules, the surface, and the gas-phase molecules.
4. Desorption of product molecules from the surface.
5. Transport of product molecules away from solid surface by convection and/or diffusion.

Due to the porous structure of char particles, chemical reactions between gases and the solid occur both on the outer and the inner surfaces of the particles. Reacting gases diffuse from the free space to the particle outer surface and then diffuse into the particle through the porous

structure. As the reaction proceeds, the size of the available pores increases, which increases the inner particle surface. The particle active surface reaches a maximum at burnout of about 40%. The total active surface area is then decrease as a result of connection of enlarging neighboring pores.

1.2.3.3 Modeling Particle Combustion

(a) Kinetics/Diffusion Fixed-Core Model

The kinetics/diffusion fixed-core model takes into account the diffusion and kinetic rates of the combustion. The size of the particle during the combustion is assumed to be constant. The particle consumption rate is defined as follow,

$$\frac{dm_p}{dt} = \frac{P_g}{\frac{1}{k_d} + \frac{1}{k_s}} A_0 \tag{1.1}$$

Where m_p is the particle mass, P_g is the partial pressure of the gas phase species, A_0 is the original particle surface area, k_d is the diffusion rate constant and k_s is the kinetics rate constant.

(b) Shrinking Core Model

The shrinking core model accounts for the reduction in the particle radius as the combustion occurs. The effect of diffusion through the ash layer surrounding the particle is also taken into account. The particle consumption rate is defined as follow,

$$\frac{dm_p}{dt} = \frac{P_g A_0}{\frac{1}{k_d} + \frac{1}{k_s}\left(r_p / R_p\right)^2 + \frac{1}{k_{dash}}\left(\frac{R_p}{r_p} - 1\right)} \tag{1.2}$$

Where m_p is the particle mass, P_g is the partial pressure of the gas phase species, A_0 is the initial particle surface area, k_d is the diffusion rate constant, k_s is the kinetics rate constant, and $k_{d,ash}$ is the ash diffusion constant, r_p is the instantaneous radius of the particle, and R_p is initial radius of the particle.

(c) Random Pore Model

The random pore model (Bhatia and Perlmutter, 1980) accounts for the evolution of the particle reactive surface during the combustion. The rate of mass change of the particle is defined as follow,

$$\frac{dm_p}{dt} = R_k m_{po}(S + A_o) \tag{1.3}$$

Where m_p is the particle mass, m_{po} is the initial particle mass, R_k is the kinetic rate, and A_0 is the initial particle surface area. S is the instantaneous internal reactive surface area, which is defined as follow,

$$\frac{S}{S_o} = 1 - x\sqrt{1 - \psi \ln(1-x)} \tag{1.4}$$

Where S_o is the initial reactive area, x is the conversion factor, and ψ is the structure parameter for the particular char/coal type.

1.2.4 Gasification Global Reactions

Coal gasification occurs when the coal is heated in limited oxygen and steam in a gasification reaction chamber. The gasification process is very complicated, A simplified main global reactions involved in gasification process can be modeled as follows:

Heterogeneous reactions:

$C(s) + ½\ O_2 \rightarrow CO$	$\Delta H°_R$ = -110.5 MJ/kmol	(R1.1)
$C(s) + CO_2 \rightarrow 2CO$	$\Delta H°_R$ = +172.0 MJ/kmol (Gasification, Boudouard reaction)	(R1.2)
$C(s) + H_2O\ (g) \rightarrow CO + H_2$	$\Delta H°_R$ = +131.4 MJ/kmol (Gasification)	(R1.3)

Homogeneous reactions:

$CO + ½\ O_2 \rightarrow CO_2$	$\Delta H°_R$ = -283.1 MJ/kmol	(R1.4)
$CO + H_2O\ (g) \rightarrow CO_2 + H_2$	$\Delta H°_R$ = -41.0 MJ/kmol (Water-shift)	(R1.5)

The gasification of char by CO_2 and H_2O, reactions (R1.2) and (R.1.3), respectively, are endothermic reactions. The exothermic two-step char combustion, reactions (R1.1) and (R1.4) are needed to supply the energy needed in the gasification reactions. The synthetic gas produced mainly consists of CO and H_2 with minor CH_4.

1.2.5 Types of Gasifiers

There are four main gasifier types: (a) entrained-flow gasifier, (b) transport gasifier, (c) moving-bed gasifier, and (d) fluidized-bed gasifier. Explanations of each type and its examples are presented below. The comparisons of these gasifiers are summarized in Table 1.2.

1.2.5.1 Entrained-Flow Gasifier

Figure 1.3 presents a simplified schematic the entrained-flow gasifier. In an entrained-flow gasifier, very fine fuel particles (< 100 μm) are suspended in a stream of oxygen/air and steam. Coal particles mix thoroughly with steam and oxygen, and the syngas produced exits through the outlet. Entrained-flow gasifiers operate at very high temperature 1370-1650 °C (2500-3000 °F). Ash in the coal melts and is discharged as molten slag from the bottom of the gasifier. Entrained-flow gasifiers are available in larger capacities compared to other types. The flow moves fast in the gasifier with a residence time typically about 3~5 seconds. The fast flow rate and better mixing of fuel and oxidant in the entrained-flow gasifier when compared to moving-bed and fluidized-bed gasifiers results in a higher carbon conversion efficiency and a higher yield. However, an entrained-flow gasifier does have disadvantages as it requires the highest amount of oxygen and produces the lowest heating value gas.

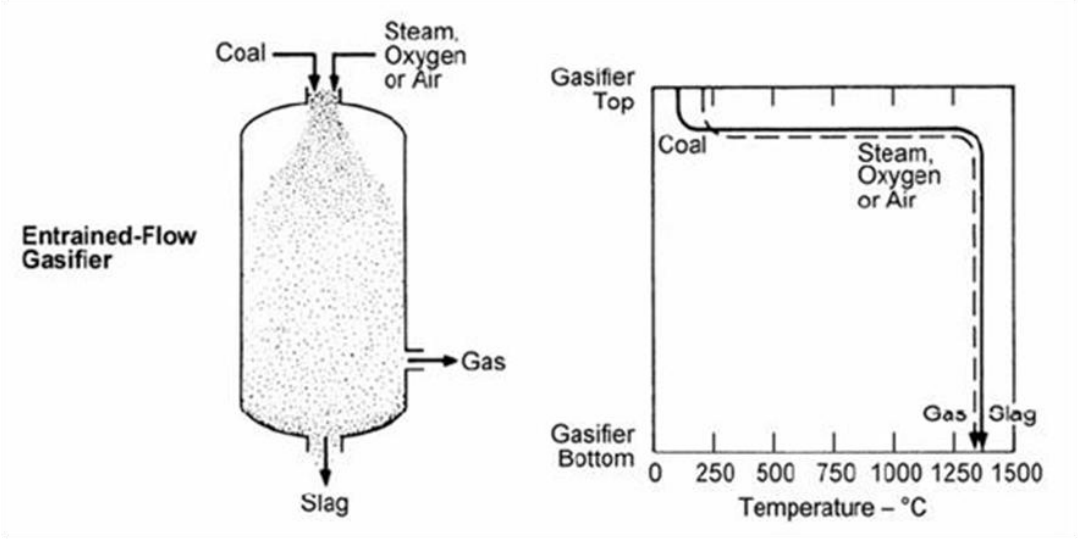

Figure 1.3 Schematic of a downdraft an entrained-flow gasifier [Holt (2004)]

Examples of commercial entrained-flow gasifiers are given below:

(i) Shell Coal Gasification Process (SCGP)

The Shell gasifier is a high-pressure, dry-fed, oxygen-blown, entrained-flow gasifier. Dry pulverized coal is fed into the high-pressure vessel with transport gas, which is usually nitrogen, through a lock hopper system. Shell gasifier does not use refractory bricks for its wall, but instead uses membrane walls. Steam and oxygen enter into the gasifier together with dry coal particles. The gas temperature can reach 1370 °C (2500 °F). Because of the high temperature, no hydrocarbon volatiles and moisture will be left. At the high operating temperature, ash in the coal melts and flows down the membrane wall. When the raw syngas at the temperature of 1370-1650 °C (2500-3000 °F) leaves the vessel, it contains a small amount of unburned carbon as well as about half of the molten ash. To prevent the molten ash from sticking to the wall, the raw syngas is partially cooled down to around 870 °C (1600 °F) by quenching it with cooled recycle product gas. The raw syngas goes through a further cooling process in the syngas cooler unit for further clean up. The first commercial IGCC plant using the Shell gasifier is Buggenum, Netherlands, which was built in 1993. The plant is able to achieve an overall efficiency of 43%. It can process up to 2000 tons per day of coal.

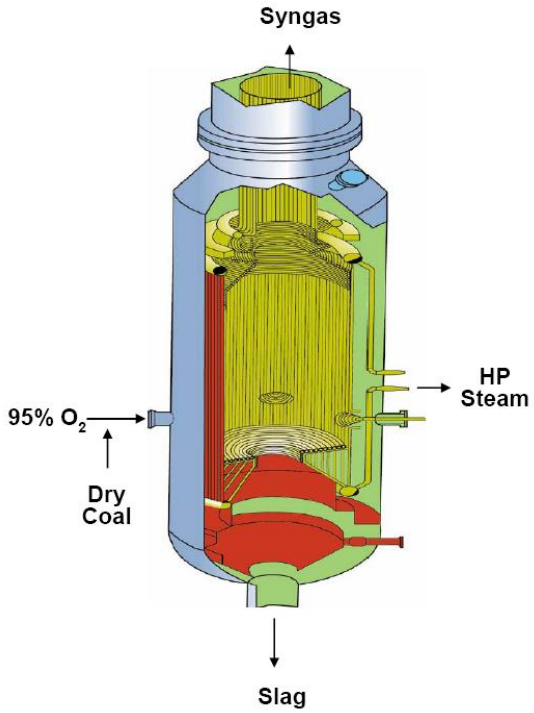

Figure 1.4 Schematic of the Shell gasifier

(ii) General Electric Gasifier (Previously Texaco gasifier)

The General Electric (GE) gasifier (Fig. 1.5) operates in the temperature range of 1250-1450 °C (2280-2650 °F) and pressure of 3 MPa for power generation and 6-8 MPa for H_2 and chemical synthesis. Coal slurry and oxidant are introduced from the top of the gasifier. The water in the slurry mixture replaces the steam which is normally injected into the system. The hot raw gas produced during the gasification process flow toward the bottom of the gasifier. The molten ash flows down the refractory-lined walls. The hot raw gas temperature is around 1400 °C (2550 °F). Two ways of raw syngas cooling are available: (a) cooling by water quenching, or (b) cooling in a radiant cooler. When water quench is used, the raw syngas is also cleaned from molten ash.

The first true IGCC demonstration technology was at the Southern California Edison Cool Water Station in 1984 and used a GE (Texaco) gasifier. The Cool Water gasifier was moved to a commercial installation at the Coffeyville refinery in Kansas after the completion of the demonstration program in 1989. The gasifier is still in operation at the refinery, converting petroleum coke into ammonia. There are currently 64 plants with GE gasifiers operating worldwide with 10 more plants are in the planning.

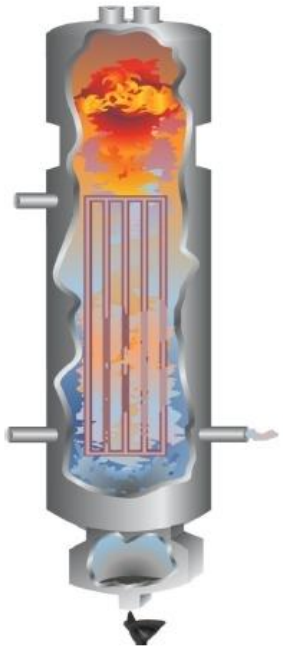

Figure 1.5 Schematic of the General Electric gasifier

(iii) Conoco-Phillips (E-Gas) Gasifier

The E-Gas gasifier is a two-stage, high-pressure, oxygen-blown, slurry-fed, slagging gasifier. Coal is mixed with water to make coal-slurry. About 80% of the coal slurry and 100% of the oxidant are injected into the first stage, while the remaining coal slurry is injected into the second stage. The first stage is located at the bottom part of the gasifier, a horizontal cylinder with one burner at each end. One is used for fresh coal slurry, and the other is for recycled unburned char. Oxidation is dominant in the first stage, increasing the temperature to about 1316-1427 °C (2400-2600 °F). The ash melts and forms molten slag, which flows down and out of the vessel through a tap hole. The molten ash is quenched in a water bath and is removed.

The hot gas from the first stage flows up to the second stage where the remaining 20% coal slurry is injected. The slow endothermic gasification reactions are dominant in the second stage. Gas temperature reduces to around 1035 °C (1900 °F). The syngas and the unburned char leave the gasifier from the top. The unburned char is removed from the syngas in the gas clean-up system and is recycled back into the gasifier's first stage.

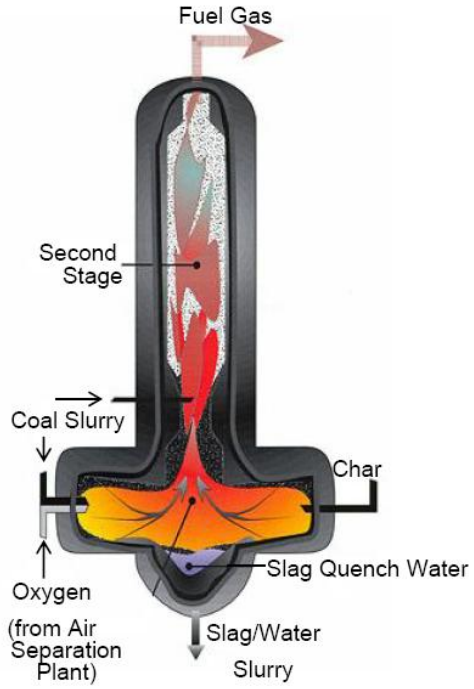

Figure 1.6 Schematic of the Conoco-Phillips (E-Gas) gasifier

(iv) PRENFLO (PREssurized ENtrained-FLOw) Gasifier

PRENFLO is a further development of Kopper-Totzek process developed in 1940s, which operates at atmospheric pressure. PRENFLO was developed by Uhde, which later merged with Krupp Koppers. PRENFLO is a one-stage, high pressure, dry-fed, oxygen-blown, slagging gasifier. The gas temperature inside a PRENFLO gasifier can exceed 2000 °C (3630 °F) and uses membrane wall. PRENFLO gasifiers are used in the world's largest solid-feedstock-based IGCC power plant in Puertolanno, Spain.

Figure 1.7a shows an illustration of a PSG (PRENFLO with Steam Generation) gasifier. Coal is injected together with oxygen and steam through several injectors in the lower part of the gasifier. Raw syngas is then sent through the waste heat boiler to cool down and produce steam. The exit gas temperature is 1350-1600 °C (2460-3910 °F). In a PDQ (PRENFLOW with Direct Quench), illustrated in Fig. 1.7b, coal and oxygen/steam are injected in the upper part of the gasifier. Raw syngas is directly quenched by water in the lower part of the gasifier. The syngas is cooled down to 200-250 °C (390-480 °F).

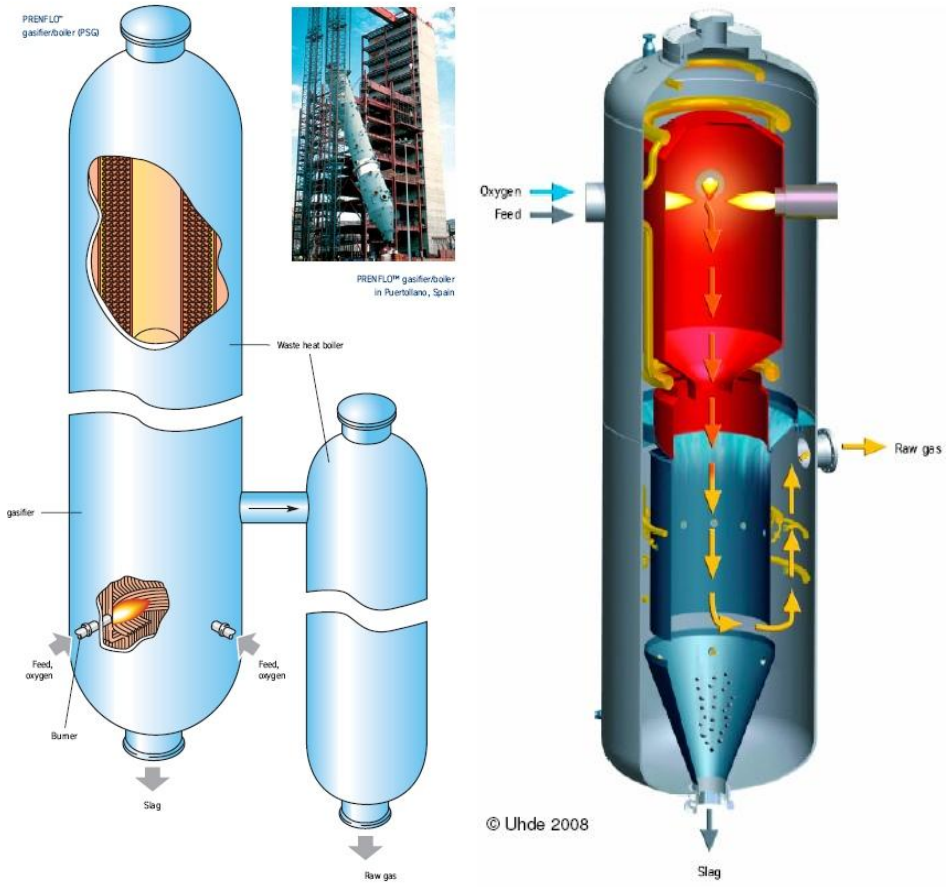

(a) PSG (b) PDQ

Figure 1.7 (a) PRENFLO with Steam Generation (PSG) and (b) PRENFLO with Direct Quench (PDQ)

1. 2.5.2 Transport Gasifier

The Kellogg Brown & Root (KBR) transport gasifier, whose schematic is shown in Fig. 1.8, is a circulating-bed reactor that uses fine pulverized coal and limestone. The reactor consists of a mixing zone, a riser, cyclones, and a standpipe. Oxidant and steam are fed at the bottom of the gasifier in the mixing zone. The amount of oxidant fed is carefully controlled to limit char combustion inside the gasifier. The steam added to the gasifier functions as a reactant and a moderator to control the gas temperature. Oxidant reacts with the recycled unburned char. To avoid premature combustion with oxygen, coal (and lime) is injected in the upper section of the mixing zone. The endothermic char gasification primarily occurs in the riser. The gas and particles flow up through the riser and into the cyclones, where the syngas and solids are separated by gravity and/or centrifugal forces. The syngas exits the reactor and passed through the gas cooler, while the solids are discharged back into the mixing zone through the standpipe. The entrained-solids circulate the reactor through the riser, the cyclone, and the standpipe. The KBR transport gasifier is a non-slagging gasifier. The moderate operating temperature (but sufficiently high to thermally crack heavy volatiles and tar) and the use of dry coal means that the syngas has low tar and oil contents. The exit syngas temperature is around 1000 °C (1830 °F). One of the advantages of the transport gasifier is that coal is injected in the relatively low-temperature region (gasification region), so a typical problem related to fuel-injector's reliability does not present.

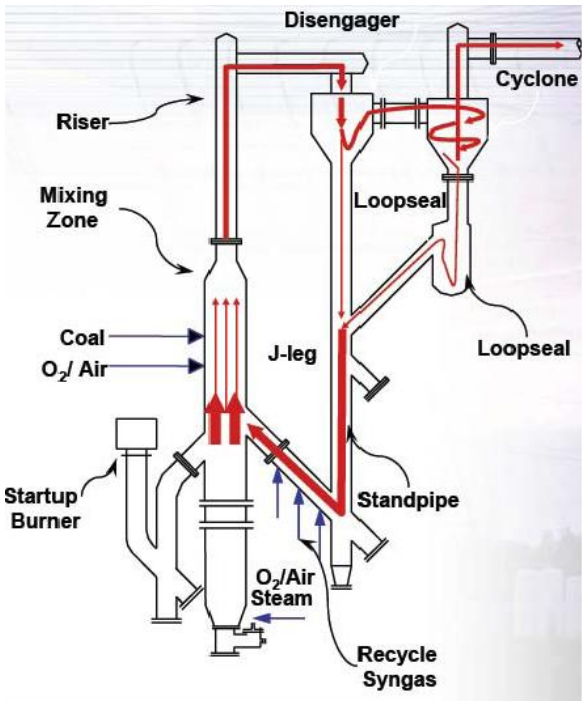

Figure 1.8 Kellog Brown & Root (KBR) transport gasifier

1. 2.5.3 Moving-Bed Gasifier

In a moving-bed gasifier, steam and air/oxygen flows through a fixed bed of solid fuel particles as shown in Fig. 1.9. Fresh coal is fed from the top, while air or oxygen is injected from the bottom. This configuration, the steam and oxygen/air feed is counter-current to the coal feed, is referred to as **"updraft"** or counter-current moving-bed gasifier. Coal moves downward slowly. Its residence time can reach 1 hour. The syngas exits from the upper part of the gasifier. Ash and unreacted char are removed from the bottom. The depth of coal bed is kept constant by adding fresh coal from the top. Another configuration is the **"downdraft"** or co-current moving-bed gasifier, where steam and air/oxygen are fed from the top, co-current to the coal feed.

A counter-current moving-bed gasifier can be divided into four zones (from top to bottom): (i) the drying/preheating zone, (ii) the de-volatilization zone, (iii) the gasification zone, and (iv) the combustion zone. The coal in the top zone is dried/preheated by hot gas that is flowing from the bottom. The coals then moves down to the de-volatilization zone, where heat from the hot gas drives volatiles out of coal particles. Gasification occurs in the next zone, and any remaining char is then reacted in the gasification zone. Syngas produced by an updraft

moving-bed gasifier has high tar content because the tar released during the de-volatilization process is carried away by the hot gas which is flowing up from gasification zone.

Ash can be removed from the bottom in the form of dry ash or slag. If dry ash is desired, the gasifier temperature is usually kept below ash fusion temperature (1300 °C or 2370 °F). Moving-bed gasifiers have advantage of high char conversion, high thermal efficiency, and low exit gas temperature (450-600 °C or 840-1110 °F). However, they have a disadvantage of low throughput (or yield).

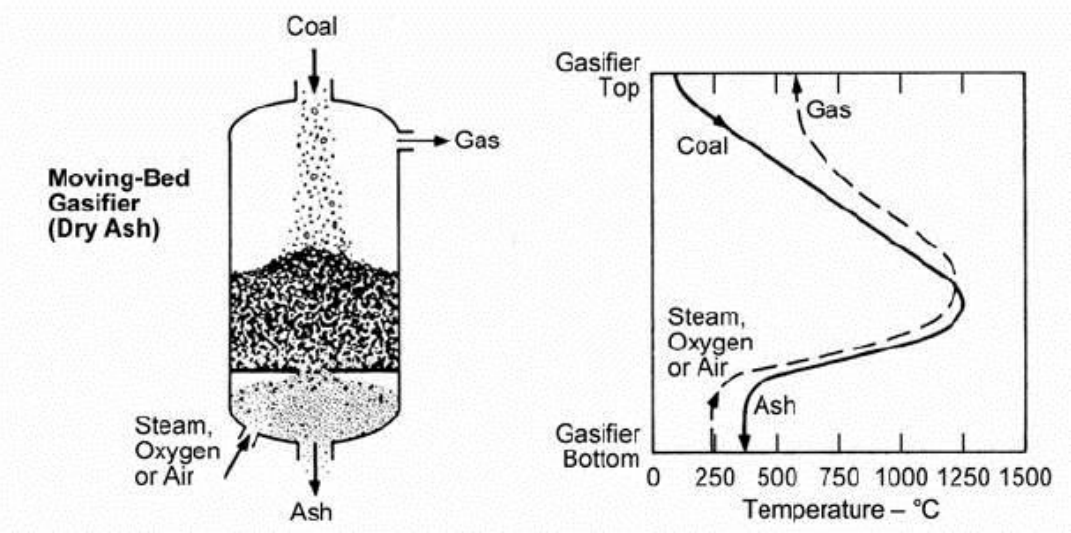

Figure 1.9 Schematic of a counter-current moving-bed gasifier [Holt (2004)]

Examples of commercial moving-bed gasifier are:

(i) British Gas/Lurgi (BGL)

The British Gas/Lurgi (BGL) coal gasifier (Fig. 1.10) is a dry-fed, pressurized, fixed-bed, and slagging gasifier. The reactor wall is water cooled and refractory lined. The coal mixture enters from the top of the gasifier via a lock hopper system. Oxygen and steam enter through injector on the sidewall. A motor-driven coal distributor/mixer stirs and evenly distributes the incoming coal mixture inside the gasifier. The coal mixture descends gradually through several process zones. The top layer of the bed is the pyrolysis and de-volatilization layer. The coal is transformed into char and moves down the next zone, which is the gasification zone. Below the gasification zone, any remaining carbon is oxidized, and the ash content melts and becomes slag. The slag flows down through the opening on the bottom of the gasifier into a quench chamber. The syngas leaves the reactor through the exit at the top of the gasifier at temperature approximately 550 °C (1020 °F).

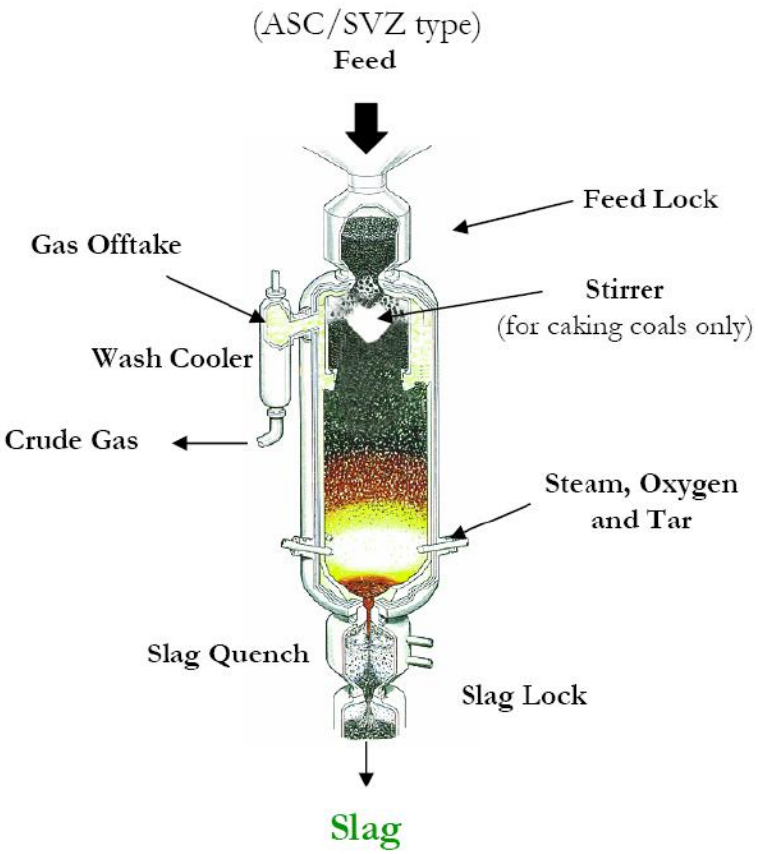

Figure 1.10 Schematic of the Britigh Gas Lurgi moving-bed gasifier

1. 2.5.4 Fluidized-Bed Gasifier

In a fluidized-bed gasifier, air or oxygen is injected upward at the bottom of solid fuel bed, suspending the fuel particles. Schematic of a fluidized-bed gasifier is presented in Fig. 1.11. The size (5-10mm) and weight of the particles prevent them from blowing out. The fuel feed rate and the gasifier temperature are lower compared to those of entrained-flow gasifiers. The operating temperature of a fluidized-bed gasifier is around 1000 °C (1830 °F), which is roughly only half of the operating temperature of a coal burner. This lower temperature has several advantages:

- ✓ Lower NO_x emission. The temperature is not hot enough to break apart the nitrogen molecules and cause the nitrogen atoms to join with oxygen atoms to form NO_x.
- ✓ No slag formation. The temperature is not hot enough to melt ash. It is suitable for coals of any rank (high or low ash content)

- ✓ Lower syngas temperature, which means cheaper syngas cooling system prior to gas clean up.

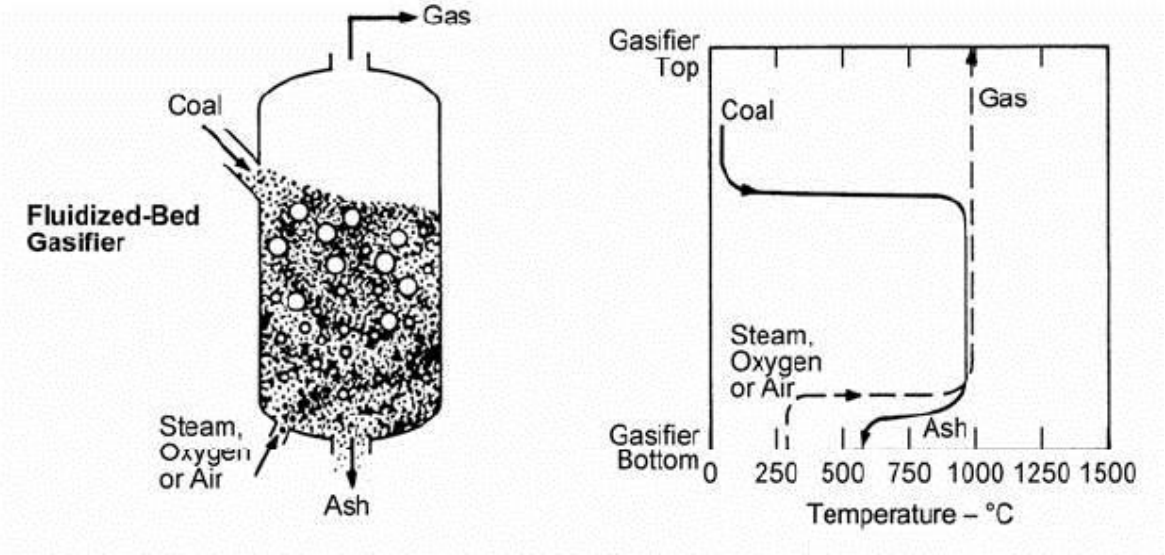

Figure 1.11 Schematic of fluidized-bed gasifier [Holt (2004)]

Fluidized-bed gasifiers require moderate supply of oxygen and steam. Examples of commercial fluidized-bed gasifier are:

(i) High Temperature Wrinkler (HTW)

High Temperature Wrinkler (HTW) was developed by Rheinbraun in Germany to gasify lignite's for the production of a reducing gas for iron ore. A schematic of an HTW gasifier is presented in Fig. 1.12. The gasifier is of refractory-lined vessel equipped with water jacket. Coal is dropped into the fluidized bed which consists of particles, semi-coke, and coal. The gasifier is fluidized by the injection of air or oxygen/steam from the bottom. The temperature of the bed is kept at around 800 °C (1470 °F), which is below the ash fusion temperature. An additional gasification gas is added at the freeboard to decompose undesirable byproducts formed during gasification. The operating pressure can vary from 1 to 3 MPa. The raw syngas exiting the top of gasifier is then passed through a cyclone to remove particulates and then cooled. Particulates recovered in the cyclone are recycled back into the gasifier.

The HTW technology was successfully applied to produce methanol from lignite's at Berrenrath, Germany, between 1986 and 1997. The plant was shut down at the end of 1997 because the process was no longer considered economically viable. In 1989, a 140 ton/day plant was commissioned in Wesseling, Germany, to supplement research and development of the HTW technology, including the study to future applications for power generation through and

Integrated Gasification Combined Cycle system (IGCC). There is presently a project to build a 400 MW IGCC plant in Czech Republic using the HTW technology developed at the Wesseling plant.

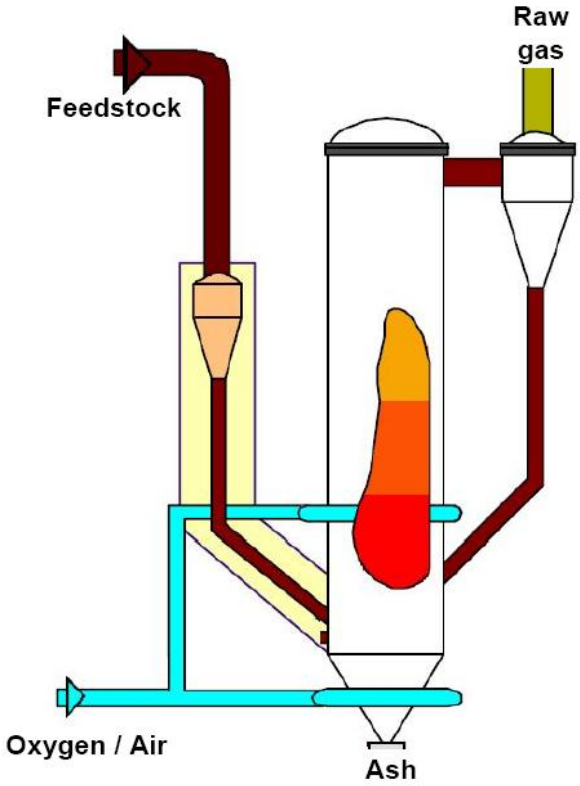

Figure 1.12 Schematic of the High Temperature Wrinkler (HTW) Gasifier

(ii) Kellogg-Rust-Westinghouse (KRW)

A schematic of a Kellogg-Rust-Westinghouse (KRW) gasifier is shown in Fig. 1.13. The fuel and oxidant enter the bottom of the gasifier through concentric high-velocity jets, ensuring thorough mixing of the fuel and oxidant and of the bed of char and limestone that collects in the gasifier. Upon entering the gasifier, the coal releases its volatiles which then immediately burns, releasing heat needed for the gasification. The combusted volatiles form large bubbles that rise up to the center of the gasifier. This causes the char and the sorbent in the bed to move down the sides of the gasifier and back into the central jet. The char in the bed reacts with the steam, which is injected together with the oxidant and also through multiple other injections on the bottom of the gasifier, to form syngas. The ash particles formed are denser than the coal, thus they settle down to the bottom of the gasifier and are then removed. Any particles that escaped

the gasifier through the exit at the top is recaptured in the cyclone gas clean-up system and is then injected back into the gasifier.

In 1997 through 2000, a 965MW Integrated Gasification Combined Cycle (IGCC) demonstration plant using the KRW technology was carried out in Pinon Pine, Nevada, by Sierra Pacific Resources and was sponsored by the US Department of Energy (DOE) as part of its Clean Coal Technology Program. It was the only large-scale coal-base IGCC plant using the KRW technology. Unfortunately, the plant faced numerous problems. It had 18 gasifier start-ups and all of them failed due to equipment design.

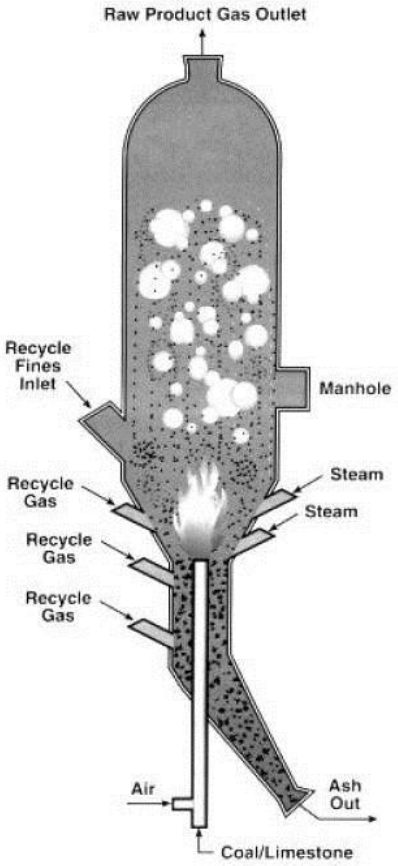

Figure 1.13 Schematic of a Kellogg-Rust-Westinghouse (KRW) gasifier.

Table 1.2 Summary of coal gasifier comparisons

Gasifier Type	Entrained-flow	Transport	Moving-bed	Fluidized-bed
Process Description	Solid particles are mixed thoroughly with air and steam and are entrained by the flow.	Circulating-bed reactor consist of mixing zone, riser, cyclones, and stand pipe	Coal is fed from top and moves down by gravity. Air and steam are injected from bottom.	Solid particle bed is fluidized by air and steam.
Technology Providers	Shell,GE,Conoco-Phillips (E-Gas), Future Energy, sSiemens	Kellogg-Brown Root (KBR)	BGL, Lurgi	HTW, KRW
Fuel feed:				
Size	<100mm	< 400mm	5-50mm	5-10mm
Caking coal	No	Yes	Yes	Yes
Coal rank	Dry feed -- any Slurry feed -- high rank	Any	Any	Any
Operating issues:				
Syngas temperature	High (1300-1600 ºC)	Moderate (1000 ºC)	Low (around 600 ºC)	Moderate (1000 ºC)
Oxidant demand	High	Moderate	Low	Moderate
Steam demand	Low	Moderate	High	Moderate
Throughput	High (residence time is 3-5 seconds)	High	Low (residence time is 30 minutes to 1 hour)	Low

1.2.6 Mild Gasification Method

The method for obtaining gasification, partial gasification, and mild gasification are different. One can distinguish them by knowing the definition of them. The definition of gasification, partial gasification, and mild gasification are as follows:

Gasification or full gasification is the method in which the feedstock's goes through complete de-volatilization, gasification, and the thermal cracking process into light composition of CO, H_2 and CH_4 as the major combustible components of so called synthetic gas (or syngas).

Partial gasification only gasifies a portion of char.

Mild gasification emphasizes preserving the heavy volatiles without further gasifying fixed carbon or thermally cracking the volatiles into lighter components.

To be specific, "Mild gasification" refers to the level of thermal cracking of volatiles by controlling the temperature and residence time; while "Partial gasification" refers to the fraction of char that is gasified by controlling the contact surface and time between CO_2/H_2O with the char after de-volatilization.

There are two different conceptual designs of Mild gasifier are available: (a) Wormser Mild gasifier, (b) ECCC Mild gasifier. Explanations of each type are presented below.

1.2.6.1 Wormser Mild Gasifier

Figure 1.14 illustrates the Wormser mild gasifier that was designed by Alex Wormser (2008), Wormser Energy Solutions, Marblehead, MA, USA. Different from the full gasification process, mild gasification is a process of devolatilizing a heavy carbonaceous fuel (biomass, coal, petroleum bottoms, etc.) in an oxygen deficient environment to create a fuel gas out of the volatile hydrocarbon components of the feedstock without thermally cracking further. The exit gas can be cleaned and used in a gas turbine to generate electricity, while the char is combusted in a conventional boiler to provide steam for power generation as well. The volatiles have energy density about six times denser than fully-gasified syngas, so the flow volume is much less resulting in smaller piping and clean up system. Since no additional energy is needed to fully gasify the volatiles, the mild-gasification process requires less energy and thus less air for combustion than the full char gasification of conventional gasify. This renders the Wormser mild gasifier to be about $1/3^{rd}$ the size of a full gasifier with the corresponding decrease in capital cost. By retaining the largest hydrocarbon molecules possible without risking condensation of the tars on the clean-up equipment, the heating value of the syngas is higher than an air blown full gasification cycle. Along with allowing the size of all the clean-up equipment to be smaller, the higher heating value also makes it easier for the plant operator to select a gas turbine capable of using this fuel.

By no means, the only option, Fig. 1.14 is one conceptual design of a mild gasifier that contains the following: an inlet tube, burners, draft tube, deflector, distributor, char exit, syngas cooler, syngas exit, and fluidized bed. Feedstock, such as coal, is injected from the bottom of the draft tube via the inlet tube. As soon as the coal is introduced into the draft tube, it will be instantly heated and pyrolyzed by the char circulating in the draft tube. The char leaving the draft tube is diverted into the fluidized bed by the deflector. In this particular design, steam and air are introduced into the bed to fluidize it and to provide reactants for some limited gasification reactions. While the feedstock is not fully gasified, some of the carbon is converted to CO and CO_2 to provide the heat necessary for de-volatilization. There are burners, (in this case fueled by recycle gas) for introducing more heat into the draft tube. The syngas exits from the top of the gasifier, while the excess char is removed from the bottom to maintain a controlled bed level of char. While this example uses gasification reactions to generate some of the heat necessary, it is

important to remember no chemical reactions need to take place to achieve mild gasification. As long as a heat source is present, the coal volatiles will boil off and generate the syngas.

The concept of mild gasification can enable existing coal power plants nearing the end of their service life to be retrofitted with a mild gasifier and gas turbine to increase their efficiency by up to 18 percentage points (50% more) while decreasing emissions. By retrofitting old plants we can increase power on the grid and decrease harmful emissions [Wormser, 2008].

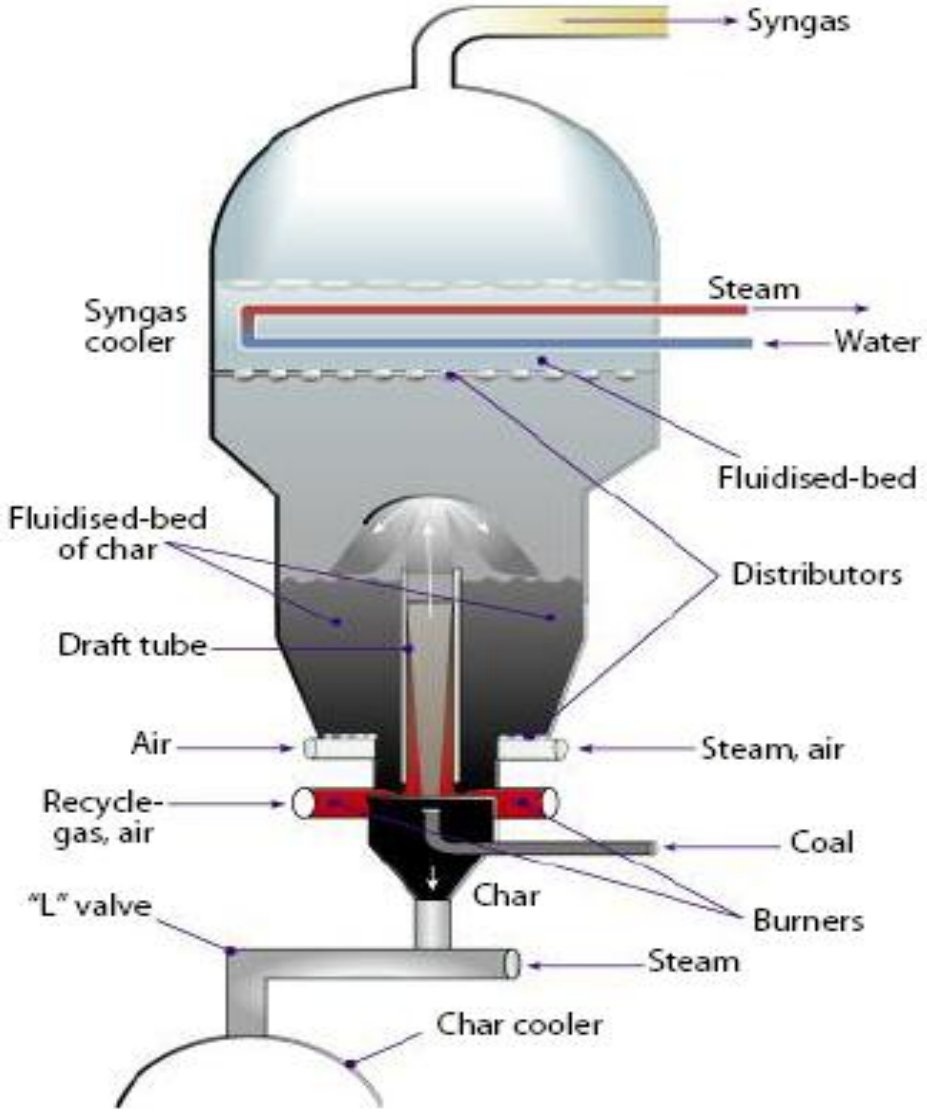

Figure 1.14 Schematic diagram of a Mild Gasifier [Wormser (2008)]

1.2.6.2 ECCC Mild Gasifier

Figure 1.15 presents an illustration of an Energy Conversion and Conversion Center (ECCC) mild gasifier, designed by the ECCC team (2009), University of New Orleans, LA, USA. ECCC's mild gasifier is also a conceptual design of mild gasifier based on the principle of Wormser mild gasifier (2008).

The conceptual design of the ECCC mild-gasifier contains the following components: a coal inlet tube, fluidization air inlet, combustion inlet, draft tube, deflector, char outlet, heat exchanger, recycled syngas exit, syngas exit, fluidized bed of char, and T-handle. Coal is introduced into the base of the draft tube via the coal inlet hose that is threaded into the coal inlet tube. Here it mixes with the combustion byproducts and is de-volatilized. Once it leaves the draft tube the flow rides along the deflector depositing the char into the fluidized bed. Fluidization gasses are blown into a plenum via two rectangular flanged ducts. The top of the plenum is screened allowing the fluidization air to enter the bed. Note that the grate has two distinct geometries. The planar region closest to the outer wall of the gasifier fluidizes the outer portion of the bed and the conical region resembling a sump that will fluidize the innermost part of the bed. Once in the bed, char will be agitated with fluidization action until it is conducted out of the bed by one of the char outlet ducts on either side of the gasifier outer wall.

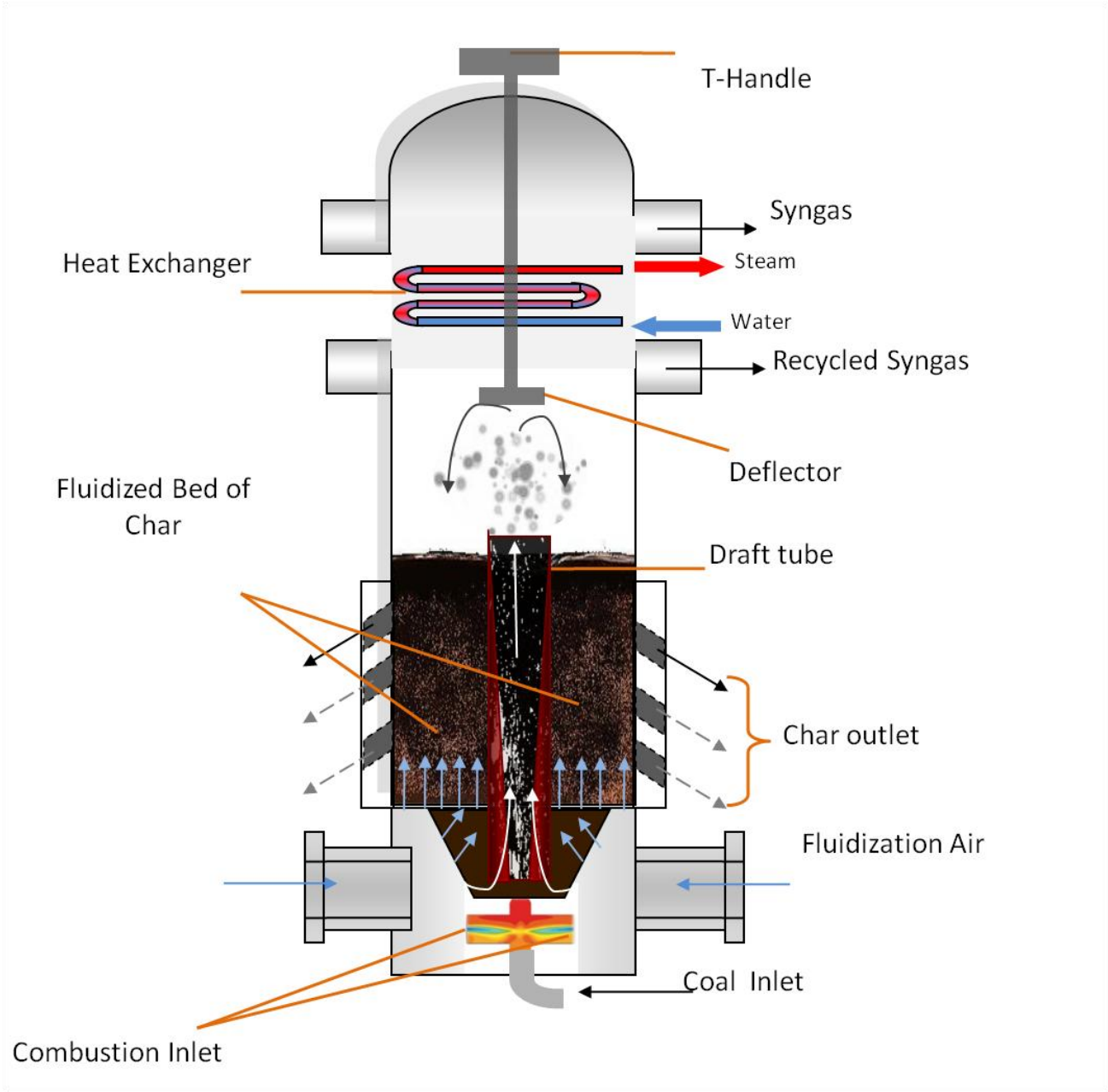

Figure 1.15 Schematic diagram of the cold-flow model of the ECCC Mild Gasifier

1.3 Motivation and Objectives

From the literature review, it is clear that there are many factors that affect the performance, efficiency, and reliability of the exiting coal-fired power plants. The Mild air-blown Gasification Integrated Combined cycle (MaGIC) technology seems technically, financially, and politically attractive to retrofitting old, inefficient, and dirty Pulverised Coal (PC) plants with less issue than building a full-blown IGCC plant. Since the MaGIC technology is still at conceptual level, both the Wormser's and ECCC's mild gasifiers have not been proven. The ECCC team is currently using both experimentation and computer modeling to optimize its mild gasifier design. The ECCC team has designed a cold flow apparatus for observing flow behavior under different conditions to validate CFD results. This study is part of the computational simulation effort of the overall project in designing, manufacturing, and testing the ECCC's mild gasifer. The specific objective of this study is to perform a comprehensive numerical investigation of Fluidized Bed Mild Gasifiers with the specific goals of establishing a robust and reliable gasification computational model and gaining understanding of thermal-flow and gasification process to help improve ongoing design of the ECCC mild gasifier with the following tasks:

- ✓ Establishing a computational model using commercial code ANSYS/Fluent for mild gasification in the ECCC's fluidized-bed mild gasifier
- ✓ Investigating the thermo-flow behavior inside the gasifier with or without particles
- ✓ Examining and selecting appropriate correlation of minimum fluidization velocity
- ✓ Incorporating gasification/thermo-flow interactions into a commercial CFD code
- ✓ Selecting appropriate global gasification reaction equations
- ✓ Examining and selecting appropriate reaction rate
- ✓ Incorporating solid-gas heterogeneous reaction model
- ✓ Investigating the effect of various inlet conditions
- ✓ Investigating the effect of various multiphase models

CHAPTER TWO
FLUIDIZED BED GASIFICATION

Since the ECCC mild gasifer is based on fluidized bed design, this chapter is dedicated to review the past and existing fluidized bed theory and technology and apply them to simulate and modify the existing ECCC mild gasifer design.

2.1 Pyrolysis of Coal

The word pyrolysis is created from the Greek word "pyro" means "fire" and "lysys" means "decomposition". It is the chemical decomposition of condensed substances by heating that occurs spontaneously at high temperatures. Pyrolysis differs from other high temperature processes such as combustion and hydrolysis in that it does not involve reactions with oxygen, water or any other reagents. It's a special case of thermolysis which is most commonly used for organic materials. In general, pyrolysis of organic substances produces gas and liquid products and leaves a solid residue richer in carbon content. The word carbonization is known as extreme pyrolysis, which leaves mostly carbon as the residue. In the chemical industry, this chemical process is heavily used, for example, to produce charcoal, to produce coke from coal, to convert biomass into syngas, to produce methanol from wood, to turn waste into safely disposable substances, and for transforming medium-weight hydrocarbons from oil into lighter ones like gasoline. The specialized uses of pyrolysis are known as different names, such as dry distillation, destructive distillation, or cracking. It also plays an important role in several cooking procedures, such as baking, frying, grilling, and caramelizing.

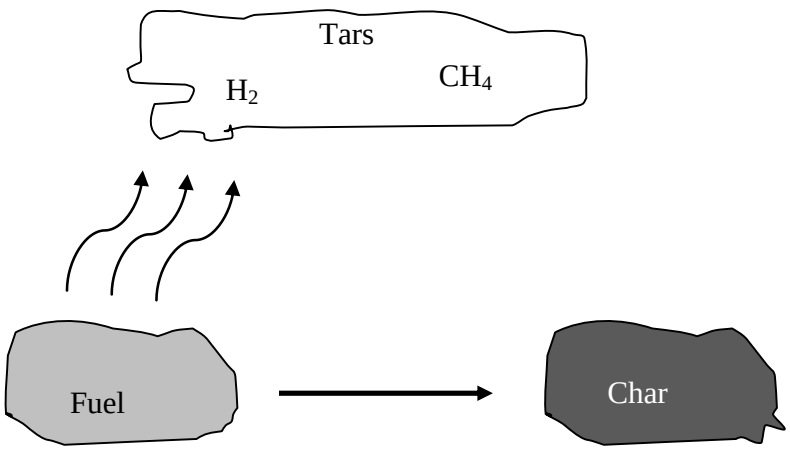

Figure 2.1 Schematic drawing of Pyrolysis of Carbonaceous Fuels

2.2 Liquefaction of Coal

The word "liquefy" means to turn anything into liquid state. Therefore, "liquefaction" is the process of change from a gas to a liquid through condensation, usually by cooling, or a change from a solid to a liquid through melting, usually by heating or by grinding and blending with another liquid to induce dissolution. In the energy industry, coal "liquefaction" is the process of producing synthetic liquid fuels from coal that is economical to transport and use as fuel. The coal liquefaction processes are classified as (a) direct conversion to liquids processes and (b) indirect conversion to liquids processes. Direct processes are also divided into (i) carbonization and (ii) hydrogenation.

Carbonization processes

The carbonization conversion occurs through destructive distillation and it produces condensable coal tar, oil and water vapor, non-condensable synthetic gas, and a solid residue-char. The condensed coal tar and oil are then further processed by hydrogenation to remove sulfur and nitrogen species, after which they are processed into fuels.

The typical example of carbonization is the Karrick process. The process was invented by Lewis Cass Karrick in the 1920s. The Karrick process is a low-temperature carbonization process, where coal is heated at 360 °C (680 °F) to 750 °C (1380 °F) in the absence of air. These temperatures optimize the production of coal tars richer in lighter hydrocarbons than normal coal tar. However, the produced liquids are mostly a by-product and the main product is semi-coke, a solid and smokeless fuel.

Hydrogenation processes

One of the main methods of direct conversion of coal to liquids by hydrogenation process is the Bergius process developed by Friedrich Bergius in 1913. In this process, dry coal is mixed with heavy oil recycled from the process. The reaction occurs at between 400 °C (750 °F) to 5000 °C (9030 °F) and 20 to 70 MPa hydrogen pressure. The reaction is as follows:

$$n\,C + (n + 1)\,H_2 \rightarrow C_nH_{2\,n+2}$$

H-Coal process, developed by Hydrocarbon Research, Inc., in 1963, mixes pulverized coal with recycled liquids, hydrogen and catalyst in the ebullated bed reactor. Advantages of this process are that dissolution and oil upgrading are taking place in the single reactor; products have high H/C ration, and a fast reaction time, while the main disadvantages are high gas yield, high hydrogen consumption, and limitation of oil usage only as boiler oil because of impurities.

The SRC-I and SRC-II (Solvent Refined Coal) processes developed by Gulf Oil and implemented as pilot plants in the United States in the 1960s and 1970s. The Nuclear Utility Services Corporation developed hydrogenation process which was patented by Wilburn C. Schroeder in 1976. The process involved dried, pulverized coal mixed with roughly 1wt% molybdenum catalysts. Hydrogenation occurred by use of high temperature and pressure synthesis gas produced in a separate gasifier. The process ultimately yielded a synthetic crude product, Naphtha, a limited amount of C_3/C_4 gas, light-medium weight liquids (C_5-C_{10}) suitable for use as fuels, small amounts of NH_3 and significant amounts of CO_2. Other single-stage hydrogenation processes are the Exxon Donor Solvent Process, the Imhausen High-pressure Process, and the Conoco Zinc Chloride Process.

Chevron Corporation developed a process invented by Joel W. Rosenthal called the Chevron Coal Liquefaction Process (CCLP). It is unique due to the close-coupling of the non-catalytic dissolver and the catalytic hydro-processing unit. The oil produced had properties that were unique when compared to other coal oils; it was lighter and had far fewer heteroatom impurities. The process was scaled-up to the 6 ton per day level, but not proven commercially.

Indirect conversion processes

The main indirect process is the Fischer-Tropsch process. In this process, coal is first gasified to make syngas (mixture of CO and H_2 gas). Then, Fischer-Tropsch catalysts are used to convert the syngas into light hydrocarbons (such as ethane) which are further processed into gasoline and diesel. This method was used on a large technical scale in Germany between 1934

and 1945 and is currently being used by Sasol in South Africa. In addition to creating gasoline, syngas can also be converted into methanol, which can be used as a fuel, or into a fuel additive.

2.3 Gasification

Gasification is a process that converts carbonaceous materials such as coal, petroleum into carbon monoxide (CO) and hydrogen (H_2) by reacting with raw material at high temperatures with a controlled amount of oxygen (O_2) and steam (H_2O). The resulting gas mixture ($CO+H_2$) is called synthesis gas or syngas. Gasification is a method for extracting energy from almost any type of organic materials such as wood, biomass, or even plastic waste. The advantage of gasification is that using the syngas is potentially more efficient than direct combustion of the original fuel because it can be combusted at higher temperatures or even in fuel cells. Gasification can also begin with materials that are not otherwise useful fuels such as bio-fuel, organic waste, house waste, or compost. Gasification of fossil fuels is currently widely used on industrial scales to generate electricity.

Chemical Reaction inside a Gasifier

The carbonaceous material undergoes several different processes inside a gasifier,

1. The pyrolysis or de-volatilization process occurs as the carbonaceous particle heats up. Volatiles are released and char is produced, resulting in up to 70% weight loss for coal. The process is dependent on the structure and composition of the char and the properties of the carbonaceous material, which will then undergo gasification reactions.
2. The combustion process occurs as the volatile products and some of the char reacts with oxygen (O_2) to form carbon monoxide (CO) and carbon dioxide (CO_2), which provides heat for the subsequent gasification reactions. The basic reaction is following,

   $C(s) + ½\ O_2 \rightarrow CO$

   $CO + ½\ O_2 \rightarrow CO_2$

   Where, "C" represents a carbon containing organic compound.
3. The gasification process occurs as the char reacts with carbon dioxide (CO_2) and steam (H_2O) to produce carbon monoxide (CO), and hydrogen (H_2), via the following reaction

   $C(s) + CO_2 \rightarrow 2CO$

   $C(s) + H_2O\ (g) \rightarrow CO + H_2$

4. In addition, the reversible gas phase water gas shift reaction reaches equilibrium very fast at the temperatures in a gasifier. This balances the concentrations of carbon monoxide (CO), steam (H_2O), carbon dioxide (CO_2) and hydrogen (H_2).

   $CO + H_2O\ (g) \leftrightarrow CO_2 + H_2$

In essence, a limited amount of oxygen (O_2) or air (O_2+3.76N_2) is introduced into the reactor to allow some of the organic material to be "burned" to produce carbon monoxide (CO) and energy, which derives a second reaction that converts further organic material to hydrogen (H_2) and additional carbon dioxide (CO_2).

Gasification processes can be used in small business and building applications, where the wood source is sustainable. A new zero carbon biomass gasification plants have been installed in Europe that produce tar free syngas from the wood and burn it in a reciprocating engines connected to a generator with heat recovery. A gasification technology using plastic-rich waste as a feed has been developed in recent years.

Commercially use Gasifier

Four types of gasifier are currently available for commercial use. They are,

a. Entrained flow gasifier

b. Transport gasifier

c. Moving bed gasifier

d. Fluidized bed gasifier

A description of the above four gasifier has been given in chapter one. Since the studied ECCC mild gasifer is based on fluidized bed technology, only fluidized bed technology is discussed in more details below.

2.4 Fluidization

Fluidization is a process similar to liquefaction whereby a granular material is converted from a static solid-like state to a dynamic fluid-like state. This process occurs when a fluid (liquid or gas) is passed up through the granular (solid) material.

When a gas flow is introduced through the bottom of a bed of solid particles, it will move upwards through the bed via the empty spaces between the particles. At low gas velocities, aerodynamic drag force (F_d) on each particle is also low, and thus the bed remains in a fixed state. Increasing the velocity, the aerodynamic drag forces (F_d) will begin to counteract the

gravitational forces (F_g), causing the bed to expand in volume as the particles move away from each other. Further increasing the velocity, it will reach a critical value at which the upward drag forces will exactly equal the downward gravitational forces ($F_d = F_g$), causing the particles to become suspended within the fluid. At this critical value, the bed is to be fluidized and will exhibit fluidic behavior and the velocity at this critical stage is known as minimum fluidization velocity. By further increasing gas velocity, the bulk density of the bed will continue to decrease, and its fluidization becomes more violent, until the particles no longer form a bed and are "conveyed" upwards by the gas flow. When fluidized, a bed of solid particles will behave as a fluid, like a liquid or gas.

Fluidization can be broadly classified into particulate fluidization or bubbling fluidization. Particulate fluidization occurs in liquids. As the velocity of the liquid is increased past the minimum fluidization velocity, the bed expands uniformly, and uniform conditions prevail in the liquid-solid mixture. In contrast, bubbling fluidization occurs in gas-solid fluidized beds. Here, when the bed is fluidized, large pockets of gas, free of particles, are seen to rise through the bed.

2.5 Fluidized Bed

A fluidized bed is formed when a quantity of a solid particulate substance usually present in a holding vessel is placed under appropriate conditions to cause the solid/fluid mixture to behave as a fluid. This is usually achieved by the introduction of pressurized fluid through the particulate medium. Fluidized beds are used as a technical process which has the ability to promote high levels of contact between gases and solids.

The properties of fluidized bed is such, the upper surface of the bed is relatively horizontal, which is analogous to hydrostatic behavior. The bed can be considered to be an inhomogeneous mixture of fluid and solid that can be represented by a single bulk density. Furthermore, an object with a lower density than the bed will float, whereas an object with a higher density than the bed will sink. Thus the bed can be considered to exhibit the fluid behavior expected of Archimedes' principle. As the "density", actually the solid volume fraction of the suspension, of the bed can be altered by changing the fluid fraction, objects with different densities comparative to the bed can, by altering either the fluid or solid fraction, be caused to float or sink.

In a fluidized bed a characteristic set of basic properties can be utilized, indispensable to modern process and chemical engineering; these properties include the following,

- ✓ Extremely high surface area contact between fluid and solid per unit bed volume
- ✓ Frequent particle- particle and particle-wall collisions
- ✓ High relative velocities between the fluid and the dispersed solid phase

-High levels of intermixing of the particulate phase

Brief History of Fluidized Bed Use

In 1920s, the Winkler process was developed to gasify coal in a fluidized bed, using oxygen. It was not commercially successful.

The first large scale commercial implementation, in the early 1940s, was the fluid catalytic cracking (FCC) process, which converted heavier petroleum cuts into gasoline. Carbon-rich "coke" deposits on the catalyst particles and deactivates the catalyst in less than one second.

By the 1950s, fluidized bed technology was being applied to mineral and metallurgical processes such as drying, calcining, and sulfide roasting.

In the 1960s, several fluidized bed processes dramatically reduced the cost of some important monomers. For example, the Sohio process for acrylonitrile and the oxy-chlorination process for vinyl chloride.

In the late 1970s, several fluidized bed process for the synthesis of polyethylene dramatically reduced the cost of this important polymer, making its use economical in many new applications. The polymerization reaction generates heat and the intense mixing associated with fluidization prevents hot spots where the polyethylene particles would melt.

Currently, most of the processes that are being developed for the industrial production of carbon nano-tubes use a fluidized bed.

Fluidized beds are used for several purposes, such as fluidized bed reactor (types of chemical reactor), fluidized bed boiler, fluidized bed gasifier, and fluidized bed combustor etc. The detailed descriptions are given below.

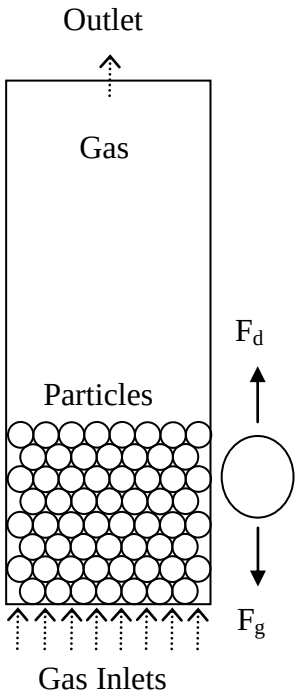

Figure 2.2 Schematic drawing of a Fluidized Bed

2.5.1 Fluidized Bed Reactor (FBR)

A Fluidized Bed Reactor (FBR) is a type of reactor device that can be used to carry out a variety of multiphase chemical reactions. In this type of reactor, a fluid (gas or liquid) is passed through a granular solid material at high enough velocities to suspend the solid and cause it to behave as though it were a fluid. This process is called fluidization. Because of many important advantages of FBR, it is now used in many industrial applications.

2.5.1.1 Advantages of FBR

The increase in Fluidized Bed Reactor (FBR) use in today's industrial world is largely due to the inherent advantages of the technology.

- ✓ **Uniform Particle Mixing:** As in packed beds, the fluidized beds do not experience poor mixing due to the intrinsic fluid-like behavior of the solid material. This complete mixing allows for a uniform product that can often be hard to achieve in other reactor designs.
- ✓ **Uniform Temperature Gradients:** The problem of local hot or cold spots within reaction bed often happen in packed beds is avoided in FBR. In other reactor types, these

local temperature differences, especially hot spots, can result in product degradation. That's way FBRs are well suited to exothermic reactions.

- ✓ **Ability to Operate Reactor in Continuous State:** The fluidized bed nature of these reactors allows for the ability to continuously withdraw product and introduce new reactants into the reaction vessel.

2.5.1.2 Disadvantages of FBR

As in any design, the fluidized bed reactor (FBR) does have it draw-backs, which any reactor designer must take into consideration.

- ✓ **Erosion of Internal Components:** The fluid-like behavior of the fine solid particles within eventually results in the wear of the reactor vessel. This can require expensive maintenance and upkeep for the reaction vessel and pipes.
- ✓ **Pumping Requirements and Pressure Drop:** The requirement for the fluid to suspend the solid material necessitates that a higher fluid velocity is attained in the reactor. In order to achieve this, more pumping (or blowing) power and thus higher energy costs are needed. In addition, the pressure drop associated with deep beds also requires additional pumping power.
- ✓ **Lack of Current Understanding:** Current understanding of the actual behavior of the materials in a fluidized bed is rather limited. It is very difficult to predict and calculate the complex mass and heat flows within the bed. Due to this lake of understanding, a pilot plant for new processes is required.

2.5.1.3 Current Research on FBR

Due to the advantages of fluidized bed reactor (FBR), a large amount of research is dedicated to this technology. Most current research aims to quantify and explain the behavior of the phase interactions in the bed. Specific research topics include the following,

- ✓ Particle size distributions
- ✓ Phase interactions
- ✓ Various transfer coefficients
- ✓ Velocity and pressure effects
- ✓ Computational modeling

The aim of this research is to produce more accurate models of the inner movements and phenomena of the bed. This will enable scientists and engineers to design better, more efficient reactors that may effectively deal with the current disadvantages of the technology and expand the range of fluidized bed reactor (FBR) for mild gasification application.

2.5.2 Fluidized Bed Boiler (FBB)

In a typical coal boiler, coal would be crushed into very fine particles, blown into the boiler, and ignited to form a long, lazy flame or in other types of boilers, the burning coal would rest on grates. But in a "fluidized bed boiler," crushed coal particles float inside the boiler, suspended on upward-blowing jets of air. The floating coal, called the "bed" would bubble and tumble around like boiling lava inside a volcano. This bubble and tumble phenomena are known as "fluidized." That's how the name "fluidized bed boiler" came about. The first "fluidized bed boiler" was built in Washington DC in 1979. It was small by today's standards, but large enough to provide heat and steam for much of the university campus. There are two major reasons fluidized bed boiler can burn coal cleaner.

First reason: the tumbling action allows limestone to be mixed in with the coal. Limestone is a sulfur sponge which absorbs sulfur pollutants. As coal burns in a fluidized bed boiler, it releases sulfur. But just as rapidly, the limestone tumbling around beside the coal captures the sulfur. A chemical reaction occurs, and the sulfur gases are changed into a dry powder that can be removed from the boiler. This dry powder is called *calcium sulfate* that can be processed into the wallboard for building walls.

Second reason: a fluidized bed boiler burns coal cleaner in that it burns "cooler." Now, cooler in this sense is still pretty hot about 760 °C (1400 °F). But older coal boilers operate at temperatures nearly twice that almost 1650 °C (3000 °F). An air pollutant, NO_x forms when a fuel burns hot enough around 1650 °C (3000 °F) to break apart nitrogen molecules in the air and join with oxygen atoms. But 760 °C (1400 °F) isn't hot enough for that to happen, so very little NO_x forms in a fluidized bed boiler.

That's why a fluidized bed boiler can burn very dirty coal and remove 90% or more of the sulfur and nitrogen pollutants. Fluidized bed boilers can also burn wood, ground-up railroad ties, even soggy coffee grounds.

A new type of fluidized bed boiler encases inside a large pressure vessel known as "pressurized fluidized bed boiler." Burning coal in a pressurized fluidized bed boiler produces a high-pressure stream of combustion gases that can spin a gas turbine to make electricity, then boil water for a steam turbine — two sources of electricity from the same fuel. The future boilers using this system will be able to generate 50% more electricity than a regular power plant. Because it uses less fuel to produce the same amount of power, a more efficient "pressurized fluidized bed boiler" will reduce the amount of carbon dioxide (CO_2) which is known a greenhouse gas released from coal-burning power plants.

2.5.3 Fluidized Bed Gasifier (FBG)

A fluidized bed gasifier employs a similar principle of a conventional combustion fluidized bed but with only partial oxidant to convert carbonaceous feedstock to produce steam, process heat, chemicals, electric power etc. The functional requirements of the fluidized bed gasifier (FBG) are to convert efficiently and reliably the carbonaceous fuel into raw reducing gas, ash, char, and possibly raw liquid products by combining carbonaceous fuel with oxidant, steam, and/or an external heat source. For solids transport, aeration and the inert gases, such as nitrogen and recycled product gas also fed to the gasifier.

2.5.3.1 Fluidized Bed Gasifier Design Consideration

The design of fluidized bed gasifiers requires developing the transport models of conservation of mass, momentum, and energy. The mass and energy balances are closely coupled and their solutions provide estimates of solids and gas composition, temperature profiles, and input and output stream conditions by applying empirical reaction kinetic and multiple phase mixing models. The momentum balances provide the gasifier pressure profile and total pressure drop by applying appropriate fluidized bed phase density models. The design of fluidized bed gasifiers involves the selection of several interrelating design, operating, and performance parameters and requires the consideration of performance and cost trade-offs for any specific application. The fluidized bed gasifier is designed to promote a reaction environment having good gas-particle contacting, good particle-particle mixing, and relatively uniform temperature conditions, and to avoid operational difficulties resulting from the agglomeration, deposition, erosion, and corrosion of carbonaceous fuels.

2.5.3.1.1 Pressurized Bubbling Bed Coal Partial Oxidizer

Figure 2.3 represents a pressurized coal fueled bubbling bed partial oxidizer showing their major components and features. Partial oxidation is a type of chemical reaction which occurs when a sub-stoichiometric fuel-air mixture is partially combusted in a reformer, creating a hydrogen-rich synthetic gas or syngas (mixture of CO and H_2) which can then be put to further use, for example in a fuel cell. Generally, the amount of O_2 used is only 35% or less of the amount required for complete combustion.

The vessels are un-cooled refractory lined pressure vessels having appropriately located nozzles for gas and solids inlet and outlet flows and man-ways for inspection and maintenance. The bubbling bed partial oxidizer is divided axially into several perceived functional zones: the ash/char separation zone at the bottom, followed by the combustion zone, then the gasification zone, and the freeboard zone at the top. Each of these zones is provided with a diameter (or width) resulting in acceptable fluidization and mixing at the local flow conditions and a height sufficient to perform the zone functions effectively.

When gasifying caking coals, the coal is introduced into the **combustion zone** via a vertical jet that intensely mix the feed streams of oxidant, coal, recycled fuel gas, and steam with internally circulating char, ash, and sorbent particles entrained into the jet. This results in the complete and rapid consumption of oxygen, the pyrolysis and partial combustion of char and volatiles, and the generation of a hot zone in the jet that allows ash agglomeration. Non-caking coals fed more simply by mechanical or pneumatic means at the vessel wall, since coal agglomeration is not a concern in this case, but high reactivity coals might still be fed through a central jet to avoid non-uniform volatiles release in the bed.

In the **ash/char separation zone**, controlled fluidization results in efficient segregation of the larger ash agglomerates from the char particles, acting as a mechanism to maintain high char content in the bed but low carbon content in the drained ash. Bottom bed drainage is performed with countercurrent cooling of the draining ash and heating of injected gases. Bed drainage must be controlled to provide and maintain sufficient gasifier bed depth.

The **gasification zone** is an expanded lower velocity zone above the combustion zone where the slower char-steam/carbon dioxide reforming reactions occur that result in efficient utilization of the coal char. The reaction conversion of this zone is greatly influenced by the large bubbles issued from the combustion zone jet.

The **freeboard** is both a disengaging zone for the very large bubbles that break the bubbling bed surface and a zone for homogeneous fuel gas conversions to occur. Tar formation is relatively small, but various ash-related deposits can form within the gasifier vessel.

To reduce carbon losses the recycle cyclone must be placed at a sufficient elevation above the relatively dense fluidized bed to provide a sufficiently long stand leg to balance the circulation loop pressure profile. The bed elutriation will tend to result in recycled fine particles having low bulk density compared to the dense fluidized bed. Fine recycled particles must be injected into the combustion zone effectively to provide additional carbon conversion.

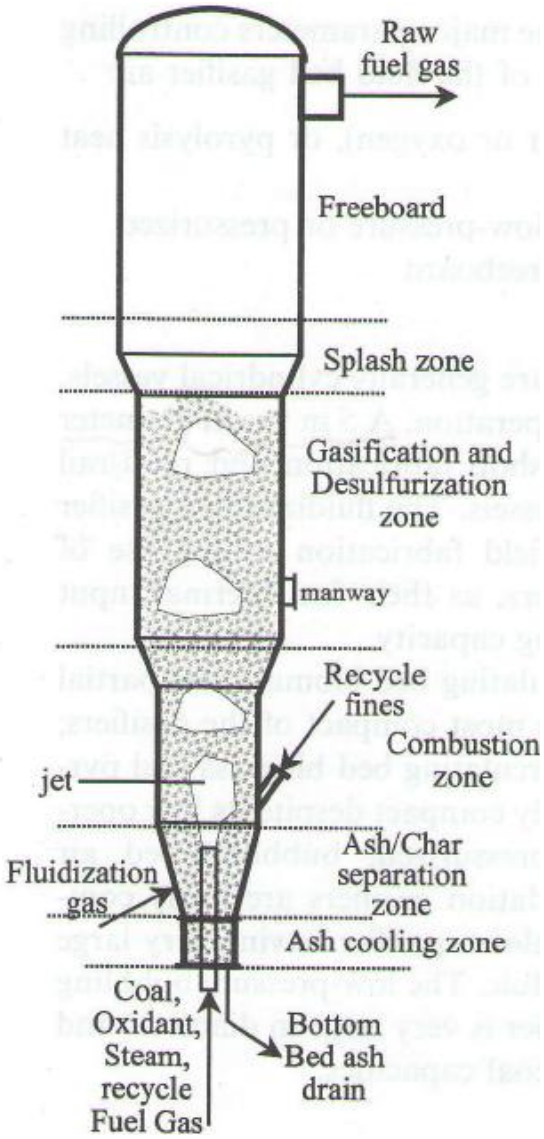

Figure 2.3 Schematic drawing of pressurized bubbling coal partial oxidizer [Wen-Ching Yang (2003)]

2.5.3.1.2 Pressurized Bubbling Bed Coal Carbonizer

Figure 2.4 represents a pressurized bubbling bed coal carbonizer showing their major components and features. This vessel is about half the total height of and smaller in diameter than the coal partial oxidizer vessel due to its primary objective of generating a char product rather than a low-carbon ash. Similar central jet feeding of coal may be used into a combustion zone, but segregated char-ash draining is not required. Simpler top bed overflow drainage can be used to control the bed height. Generally, there is also no need to recycle overhead fines back into the carbonizer vessel, this stream being primarily product char. The fluidized bed carbonizer may operate at a lower temperature than the fluidized bed partial oxidizer. Thus the bubbling bed coal carbonizer design is significantly simpler than the bubbling bed coal partial oxidizer design.

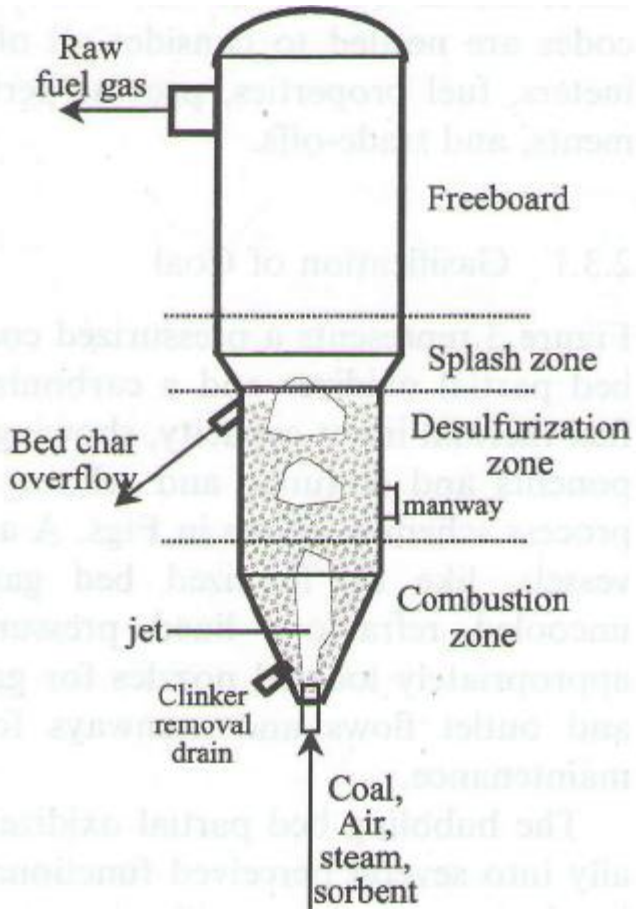

Figure 2.4 Schematic drawing of pressurized bubbling bed coal carbonizer [Wen-Ching Yang (2003)]

Several design decisions and estimates that must be addressed to generate a reliable and efficient pressurized bubbling bed coal partial oxidizer and carbonizer are given below:

- ✓ Fluidized bed temperature
- ✓ Coal and sorbent feed size distributions
- ✓ Oxidant/coal, steam/coal, recycle fuel gas/coal feed ratios
- ✓ Gasification and combustion zone fluidization velocity
- ✓ Freeboard zone velocity and height to minimize particle carryover
- ✓ Oxidant injection design
- ✓ Steam and recycle fuel gas distribution for fluidization to avoid dead zones in the bed
- ✓ Coal feed location(s) and transport method
- ✓ Recycled fine particles feed location and transport method
- ✓ Combustion zone height and gasification zone height required for effective partial oxidation, carbonization, and desulfurization
- ✓ Overall gasifier and recycle loop pressure drop profiles and heat losses
- ✓ Design to accommodate multiple fuel types

Since the fluidized bed gasifier designs have been typically evolved from conventional fluidized bed combustor, a review of fluidized bed combustors is provided below.

2.5.4 Fluidized Bed Combustor (FBC)

Fluidized bed combustors burn carbonaceous fuels to produce steam, process heat, and electric power. The major distinction of fluidized bed combustors compared to other combustor is that carbonaceous fuel combustion occurs at a relatively low temperature of 760–930 °C, within an almost uniform temperature reactor environment. The functional requirements for fluidized bed combustors (FBC) are generally more complex than those for fluidized bed gasifiers (FBG): they must efficiently and reliably combust the carbonaceous fuel, achieve specified sulfur removal performance with economic consumption of sorbent, generate a raw combustion gas meeting flow and temperature specifications, and generate steam meeting flow, pressure, temperature, and quality requirements.

Carbonaceous fuel is fed into a fluidized bed consisting primarily of sulfur-sorbent (limestone) particles, or inert particles, and containing smaller portions of fuel char and ash

particles. The bed is fluidized by air, fed in excess of that needed for complete fuel combustion, to perform combustion within the relatively well-mixed, relatively uniform temperature of the fluidized bed. The fluidized bed combustor operates at near-atmospheric pressure for steam generation, process heat production, or at elevated pressure for combined cycle power generation.

2.5.4.1 Fluidized Bed Combustor Design Consideration

The design of fluidized bed combustors (FBC) and the fluidized bed gasifiers (FBG) both require developing the conservation of mass, momentum, and energy. The FBC mass and energy balances are closely coupled and their solutions provide estimates of solids and gas composition, temperature profiles and input and output stream conditions by applying empirical reaction kinetic and multiple phase mixing models. The momentum balances provide the combustor pressure and velocity profiles by applying appropriate fluidized bed phase density models.

The design of fluidized bed combustors involves the selection of several interrelating design, operating, and performance parameters and requires the consideration of performance and cost trade-offs for any specific application. The fuel properties such as heating value, volatile/fixed carbon ratio, moisture, ash, sulfur, and nitrogen content etc represent the major parameters that the designer must apply for designing of FBC as these properties may limit the potential performance such as thermal efficiency, environmental, operating cost, availability that can be achieved by FBC. The design consideration of a FBC must also accounts the most significant operating problems that arise: tube failures, refractory damage, plugging and erosion of nozzles and drains, deposits and blockages of seal valve, wear and plugging of coal and limestone feed lines, coal feeding system, ash handling system.

2.5.4.1.1 Bubbling Bed Atmospheric Fluidized Bed Combustor

The features of bubbling bed Atmospheric Fluidized Bed Combustor (AFBC) are illustrated in Fig. 2.5. The configuration and operating conditions of bubbling bed AFBC are influenced by the coal properties, the steam conditions (superheated temperature and pressure), the unit capacity and turndown requirements. Compared to the circulating bed AFBC, bubbling bed AFBC with coals is more suitable for smaller capacity steam generators because of its low fluidization velocity (1.5–4 m/s) resulting in a large fluidized bed cross-sectional area.

Nonetheless, several large-capacity bubbling bed AFBC units have been constructed and are successfully operating.

The bubbling bed AFBC has two fluidized compartments on a single level. The air inlet plenum, or wind box, is compartmentalized so that individual bed sections can be de-fluidized for control, and these bed sections may have physical boundaries between them. The key features are the dense bubbling bed with its splash zone and freeboard zone, the air distributor, the coal and limestone feed arrangements, the heat transfer surface arrangements, and the fines recycling.

Typical bubbling bed temperatures are 815–870 °C (1500–1600 °F), and excess air levels range from 20 to 25%, with lower reactivity coals requiring higher excess air, higher temperatures, and less coal feed points than higher reactivity coals. Bubbling bed AFBC places horizontal heat transfer surface within the dense fluidized bed, achieving high heat transfer coefficients but also facing the possibility of steam tube erosion. Heat transfer surface is also placed above the dilute freeboard zone where convective steam generation occurs. Bubbling bed combustor dense beds are generally about 1–1.5 m deep, allowing them to achieve acceptable pressure drops (15–25 kPa), while the splash zone and freeboard height is about 10 m from the top of the dense bed.

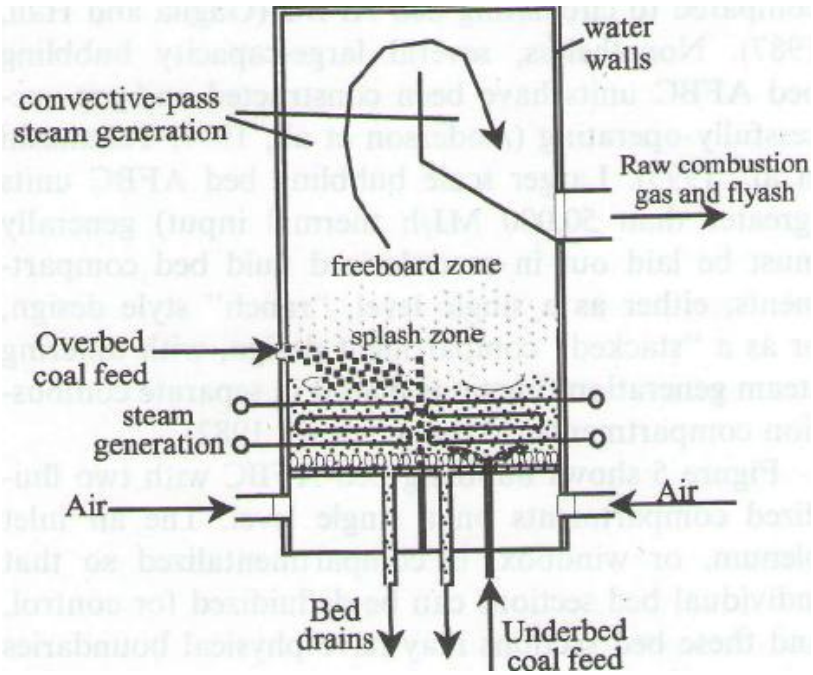

Figure 2.5 Schematic drawing of bubbling bed Atmospheric Fluidized Bed Combustor (AFBC) [Wen-Ching Yang (2003)]

2.5.4.1.2 Circulating Bed Atmospheric Fluidized Bed Combustor

The features of circulating bed Atmospheric Fluidized Bed Combustor (AFBC) are illustrated in Fig. 2.6. Circulating bed AFBC uses a more complex combustor design than bubbling bed AFBC. It uses no heat transfer in the dense, reducing, primary bubbling bed zone, and it places all heat transfer surfaces exposed to high bed velocity in a vertical orientation to minimize the possibility of erosion. Refractory covering is also used to protect the metal heat transfer surfaces. The dense, primary, bubbling bed zone is usually refractory lined to minimize heat transfer surface erosion. The dense bed is a turbulent bed fluidized by sub-stoichiometric primary air (about half of the total air) at a fluidization velocity of about 2–4 m/s. The dense bed is supported by an air distributor whose primary function is to distribute air uniformly to induce particle mixing between injected coals and recycle solids, and carry out partial coal oxidation. The distributor must operate within specified pressure drop limits, without plugging, erosion damage, or buckling.

Coal is fed to the dense bed by a small number of simple slide chutes fed by rotary valves. Alternatively, coal may be fed at a single point into the solids recirculation leg. Limestone (less than 6 mm in diameter) is normally fed separately above the bed. Re-circulating bed media are fed hot into the primary bed zone at a ratio of 50 to 100 times the coal feed rate. Various types of reinjection, non mechanical valves and seals are used, such as seal pots, L-valves, J-valves etc. These are simple refractory lined ducts having solids holding volumes that provide a loop seal, and appropriate aeration nozzles that induce and control solids flow. The bed-to-surface heat transfer coefficient by solids convection and radiation is lower in circulating bed AFBC than in bubbling bed AFBC due to the lower bed density and vertical heat transfer surface orientation. The dilute zone of the furnace is water-walled, with the heat transfer surfaces placed at the perimeter of the rectangular vessel enclosure. Additional vertical heat transfer surface walls or "wing walls" (Fig. 2.6) may be hung within the vessel to increase its heat removal capacity. Another means to increase the heat transfer surface is to place an "external heat exchanger" in the circulating solids loop.

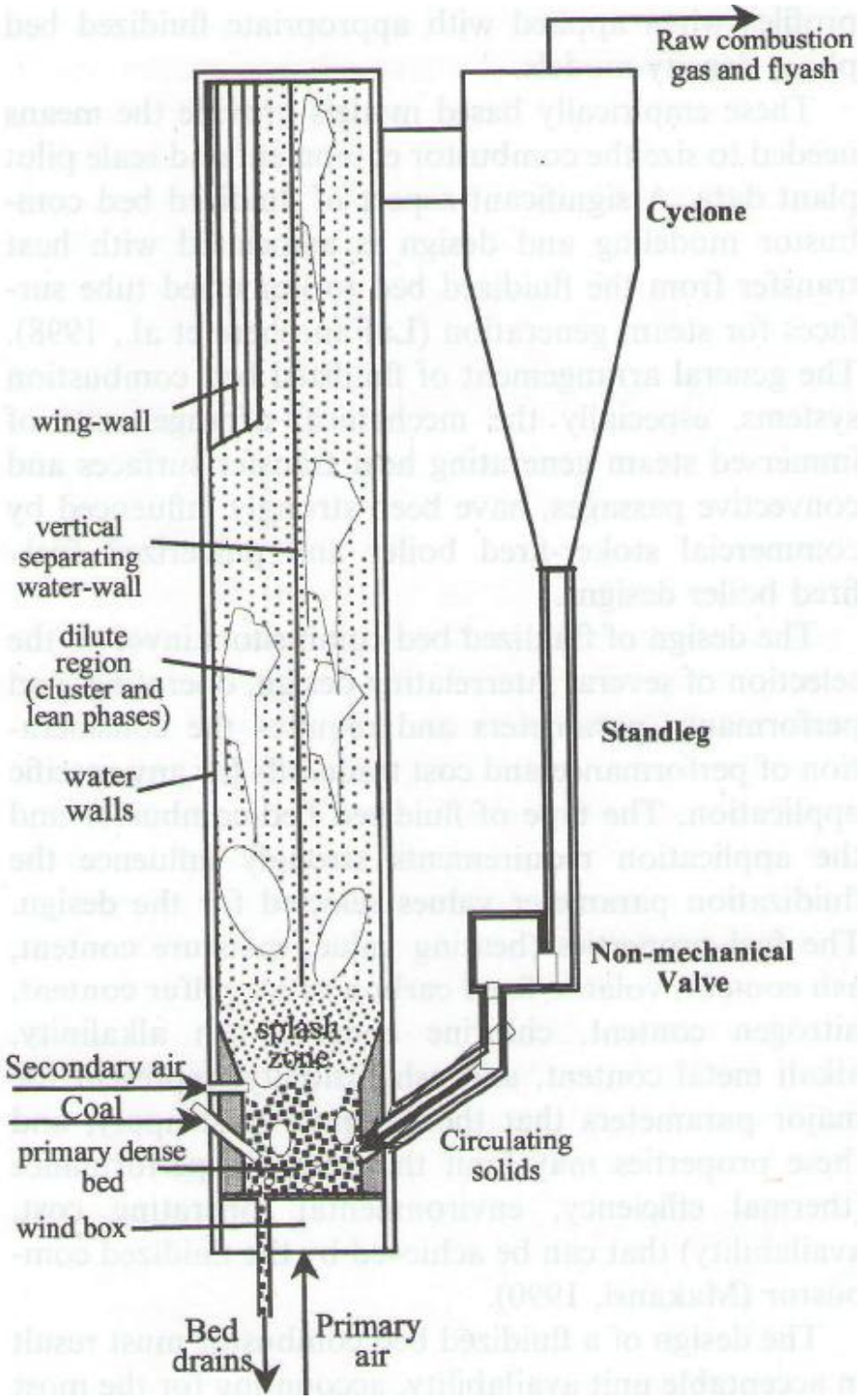

Figure 2.6 Schematic drawing of circulating bed Atmospheric Fluidized Bed Combustor (AFBC) [Wen-Ching Yang (2003)]

2.5.4.1.3 Bubbling Bed Pressurized Fluidized Bed Combustor

As with bubbling bed and circulating bed Atmospheric Fluidized Bed Combustor (AFBC) technology evolution, bubbling bed Pressurized Fluidized Bed Combustor (PFBC) has led the development over the still-to-be-demonstrated circulating bed PFBC. Bubbling bed and circulating bed PFBC both appear to be attractive options for advanced high-efficiency power generation systems for large electric generating applications.

Figure 2.7 illustrates the bubbling bed Pressurized Fluidized Bed Combustor (PFBC) power plant configuration, showing the main power plant components. The figure is representative of bubbling bed PFBC with the currently commercial process configuration: to remove particulate from the combustion gas multiple stages of cyclones are used and the combustion gas is expanded through a turbine expander designed to tolerate large particulate content in the gas. The stack gas must be further cleaned of particulates in commercial equipment to meet environmental standards. The PFBC unit and several other components are located in a large external pressure vessel that is pressurized and cooled by the warm compressor air. Bubbling PFBC uses dense bed depth adjustment as a means for load control, exposing normally immersed heat transfer surfaces to the freeboard zone; a vessel for storage and transfer of bed ash is used for this purpose and is housed in the external pressure vessel. An external heat exchanger is also housed in this pressure vessel.

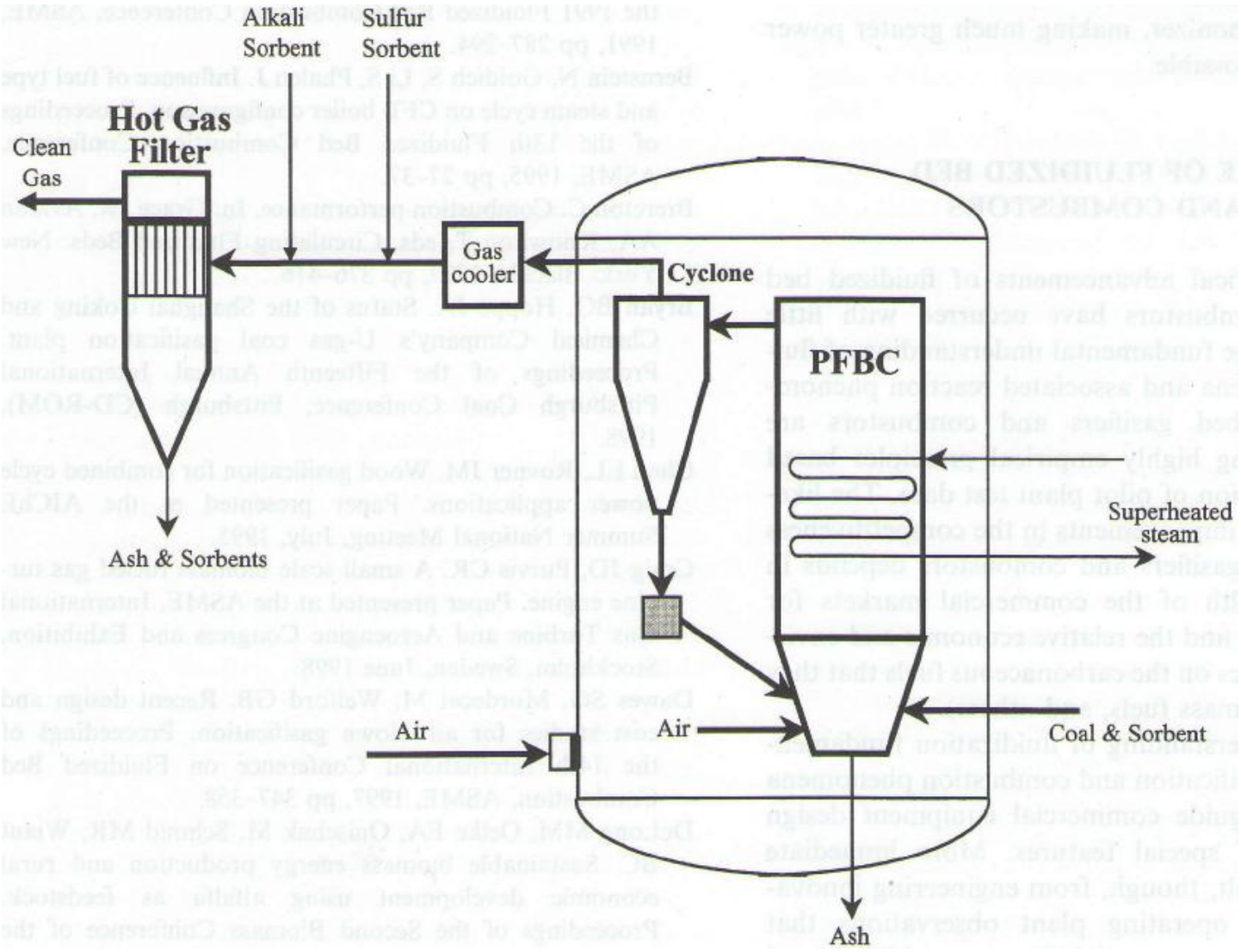

Figure 2.7 Schematic drawing of bubbling bed Pressurized Fluidized Bed Combustor (PFBC) [Wen-Ching Yang (2003)]

2.5.5 The Future of Fluidized Bed Gasifiers and Combustors

The recent practical advancements of fluidized bed gasifiers and combustors have occurred with little dependence on the fundamental understanding of fluidization phenomena and associated reaction phenomena. Fluidized bed gasifiers and combustors are designed following highly empirical principles based on the extrapolation of pilot plant test data. The likelihood of further improvements in the competitiveness of fluidized bed gasifiers and combustors depends in part on the health of the commercial markets for their applications and the relative economic and environmental pressures on the carbonaceous fuels that they utilize such as coals, biomass

fuels etc. Improved understanding of fluidization fundamentals related to gasification and combustion phenomena may eventually guide commercial equipment design and selection of special features. More immediate impacts may result, though, from engineering innovations based on operating plant observations that improve performance, reliability, operability, and cost. Experimentation such as laboratory scale conceptual testing, cold flow simulations, pilot plant parametric testing, and demonstration plant experience will continue to be an important avenue for such engineering innovations.

2.6 Theoretical and Empirical Prediction of Minimum Fluidization Velocity

A chemical engineering as well as mechanical engineering operation commonly involves the use of packed and fluidized beds. These are devices in which a large surface area for contact between a liquid and a gas (absorption, distillation) or a solid and a gas or liquid (adsorption, catalysis) is obtained for achieving rapid mass and heat transfer, and particularly in the case of fluidized beds, catalytic chemical reactions. The theory and empirical correlations associated with thermal-flow fundamentals in a packed bed are reviewed first, followed by in a fluidized bed.

2.6.1 Minimum Fluidization Velocity of Packed Beds

A typical packed bed is a cylindrical column that is filled with a suitable packing material. The liquid is distributed as uniformly as possible at the top of the column and flows downward, wetting the packing material. A gas is admitted at the bottom, and flows upward, contacting the liquid in a countercurrent fashion. An example of a packed bed is an absorber. Here, the gas contains some carrier species that is insoluble in the liquid (such as air) and a soluble species such as carbon dioxide or ammonia. The soluble species is absorbed in the liquid, and the lean gas leaves the column at the top. The liquid, rich in the soluble species, is taken out at the bottom.

From a fluid mechanical perspective, the most important issue is that of the pressure drop required for the liquid or the gas to flow through the column at a specified flow rate. To calculate this quantity we rely on a friction factor correlation attributed to Ergun. Other fluid mechanical issues involve the proper distribution of the liquid across the cross-section, and developing models of the velocity profile in the liquid film around a piece of packing material so that heat

and mass transfer calculations can be made. Design of packing materials to achieve uniform distribution of the fluid across the cross-section throughout the column is an important subject as well. Here, only the pressure drop issue is reviewed.

The **Ergun equation** that is commonly employed is given below,

$$f_p = \frac{150}{Re_p} + 1.75 \qquad (2.1)$$

Here, the friction factor f_p for the packed bed, and the particle Reynolds number Re_p, are defined as follows.

$$f_p = \left(\frac{\Delta p}{L}\right)\left(\frac{D_p}{\rho V_s^2}\right)\left(\frac{\varepsilon^3}{1-\varepsilon}\right) \qquad (2.2a)$$

$$\text{And } Re_p = \frac{D_p\, \rho\, V_s}{(1-\varepsilon)\,\mu} \qquad (2.2b)$$

Using the above friction factor f_p and the particle Reynolds number Re_p relations, the **Ergun equation** becomes,

$$\left(\frac{\Delta p}{L}\right)\left(\frac{D_p}{\rho_f\, V_s^2}\right)\left(\frac{\varepsilon^3}{1-\varepsilon}\right) = \frac{150\,(1-\varepsilon)\,\mu}{D_p\, \rho_f\, V_s} + 1.75 \qquad (2.3)$$

The various symbols appearing in the above equations are defined as follows.

Δp =Pressure Drop

L =Length of the Bed

ρ_p =Density of the particle

ρ_f =Density of the fluid

μ = Dynamic viscosity of the fluid

D_p = Equivalent spherical diameter of the particle defined by,

$$D_p = 6\frac{\text{volume of the particle}}{\text{surface area of the particle}} = \frac{6V_p}{A_p}$$

ε = Void fraction of the bed (ε is the ratio of the void volume to the total volume of the bed)

$$\varepsilon \equiv \frac{\text{volume voids}}{\text{volume of entire bed}}$$

$$\varepsilon \equiv \frac{\text{volume of entire bed} - \text{volume of particles}}{\text{volume of entire bed}}$$

$$\varepsilon \equiv \frac{\pi R^2 L - \dfrac{\text{weight of all particles}}{\text{particles density}}}{\pi R^2 L}$$

Where, R=inside radius of column

V_s= Superficial velocity ($V_s = \frac{Q}{A}$, where Q is the volumetric flow rate of the fluid and A is the cross-sectional area of the bed)

2.6.2 Minimum Fluidization Velocity of Fluidized Beds

A fluidized bed is a bed through which fluid flows at such a high velocity that the bed is loosened and the particle-fluid mixture behaves as though it is a fluid. Thus, when a bed of particles is fluidized, the entire bed can be transported like a fluid. Both gas and liquid flows can be used to fluidize a bed of particles. The most common reason for fluidizing a bed is to obtain vigorous agitation of the solids in contact with the fluid, leading to excellent contact between the solid and the fluid and between the solid and the wall. This means that nearly uniform temperatures can be maintained even in highly exothermic reaction situations where the particles are used to catalyze a reaction in the species contained in the fluid. In fact, fluidized beds were used in catalytic cracking in the petroleum industry in the past. The catalyst is suspended in the fluid by fluidizing a bed of catalytic particles so that intimate contact can be achieved between the particles and the fluid. Nowadays, fluidized beds used in catalyst regeneration, solid-gas reactors, combustion of coal, roasting of ores, drying, and gas adsorption operations.

First, consider the behavior of a bed of particles when the upward superficial fluid velocity is gradually increased from zero past the point of fluidization, and back down to zero then calculate the minimum fluidization velocity. The superficial velocity is the velocity of the fluid in the bed if no particles are present.

At first, when there is no flow, the pressure drop is zero, and the bed has a certain height as shown in Fig. 2.8. As the superficial velocity increases along the right arrow, tracing the path ABCD, at first, the pressure drop gradually increases while the bed height remains fixed. When

the point B is reached, the bed starts expanding in height while the pressure drop levels off and no longer increases as the superficial velocity is increased. This is happing when the upward force (or upward drag force, F_d) exerted by the fluid on the particles is sufficient to balance the net weight of the bed (or gravitational force, F_g) and the particles begin to separate from each other and float in the fluid. As the velocity is increased further, the bed continues to expand in height, but the pressure drop remains constant. It is possible to reach large superficial velocities without having the particles carried out with the fluid at the exit. This would occur if the superficial velocity is equal to the terminal settling velocity of the particles. The terminal settling velocity is explained later in 2.6.3.

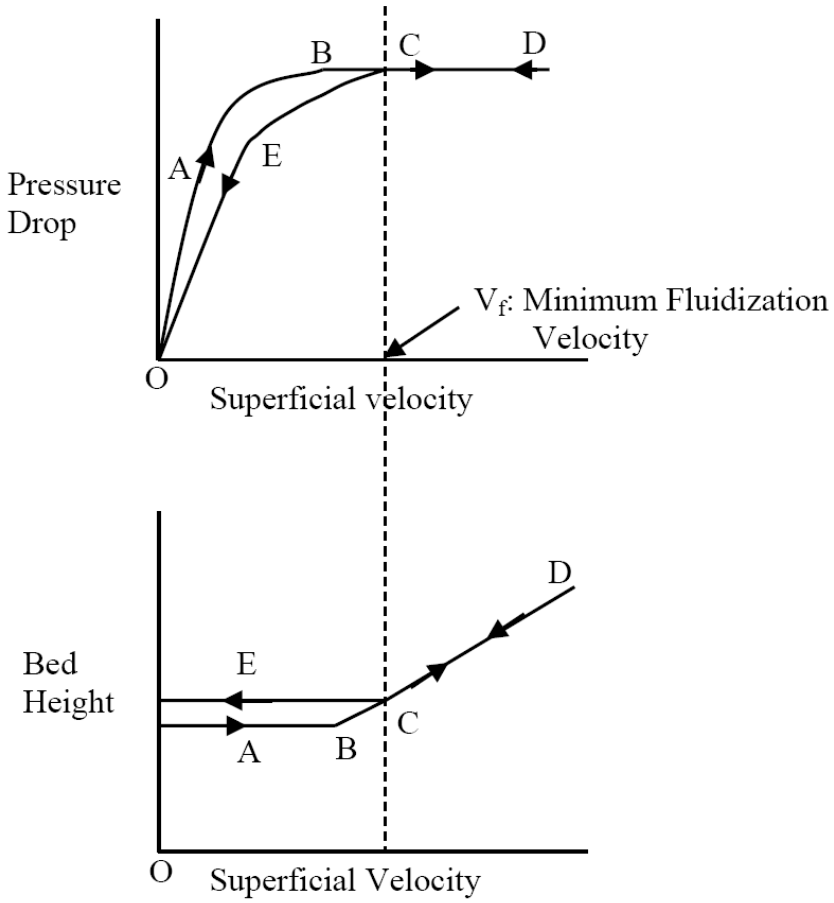

Figure 2.8 Schematic drawing of Minimum Fluidization Velocity

Now, if the path is traced backward by gradually decreasing the superficial velocity in the direction of the reverse arrows in the figure, it is found that the behavior of the bed follows the curves DCE. At first, the pressure drop stays fixed while the bed settles back down, and then begins to decrease when the point C is reached. The bed height no longer decreases while the

pressure drop follows the curve CEO. A bed of particles, left alone for a sufficient length of time, becomes consolidated, but it is loosened when it is fluidized. After fluidization, it settles back into a more loosely packed state; this is why the constant bed height on the return loop is larger than the bed height in the initial state. If the experiment is now repeated by increasing the superficial velocity from zero, the path will follow the set of curves ECD in both directions. Because of this reason, the velocity at the point C in the Fig. 2.8 is defined as the **minimum fluidization velocity** V_{mf}.

Calculation of V_{mf}

One can calculate minimum fluidization velocity, V_{mf} by balancing the net weight of the bed against the upward force exerted on the bed, namely the pressure drop across the bed "Δp" multiplied by the cross-sectional area of the bed "A". Ignoring the small frictional force exerted on the wall of the column by the flowing fluid, the force balance can be formulated as fallows

Upward force on the bed =Δp A (2.4)

If the height of the bed at this point is "L" and the void fraction is "ε", the volume of particles can be written as

Volume of particles = (1-ε) AL (2.5)

If the acceleration due to gravity is g, the net gravitational force on the particles (net weight) is

Net Weight of the particles, $W = (\rho_p - \rho_f)(1-\varepsilon) A L g$ (2.6)

Balancing the equation 2.4 and equation 2.6 yields the following relation,

$$(\Delta p) A = W = (1-\varepsilon)(\rho_p - \rho_f) A L g$$
$$\frac{\Delta p}{L} = (1-\varepsilon)(\rho_p - \rho_f) g \quad (2.7)$$

The various symbols appearing in the above equations are defined as follows.

Δp =Pressure Drop

L =Length of the Bed

A =cross-sectional area of column

ρ_p =Density of the particle

ρ_f =Density of the fluid

ε = Void fraction of the bed (ε is the ratio of the void volume to the total volume of the bed)

The point of maximum pressure drop shown in Fig. 2.4 is the point of minimum fluidization. The force balanced equations for the point of minimum are:

$$(\Delta p)\,A = W = (1-\varepsilon_{mf})(\rho_p - \rho_f)\,A\,L_{mf}\,g$$
$$\frac{\Delta p}{L_{mf}} = (1-\varepsilon_{mf})(\rho_p - \rho_f)\,g \qquad (2.8)$$

According to **Ergun equation** (Eq. 2.3), the pressure drop increases with the fluid velocity maintaining the following correlation. The first part of right hand side of Eq. 2.9 is the viscous effect and second part is the inertial effect of fluid.

$$\left(\frac{\Delta p}{L}\right)\left(\frac{D_p}{\rho_f V_s^2}\right)\left(\frac{\varepsilon^3}{1-\varepsilon}\right) = \frac{150\,(1-\varepsilon)}{N_{Re}} + 1.75 \qquad (2.9)$$

Where, $N_{Re} = \dfrac{D_p\,\rho_f\,V_s}{\mu_f}$ =average Reynolds number based upon superficial velocity

D_p = Equivalent spherical diameter of the particle

V_s= Superficial velocity

$$\left(\frac{\Delta p}{L}\right)\left(\frac{D_p}{\rho_f\,V_s^2}\right)\left(\frac{\varepsilon^3}{1-\varepsilon}\right) = \frac{150\,(1-\varepsilon)\,\mu_f}{D_p\,\rho_f\,V_s} + 1.75 \qquad (2.10)$$

At minimum fluidization, the superficial velocity V_s is equal to the minimum fluidization velocity V_{mf}. At this condition, the above Ergun equation (2.10) is rearranged with V_s being substituted by $V_{mf,}$ and L substituted by L_{mf}, and ε substituted by ε_{mf}

$$\left(\frac{\Delta p}{L_{mf}}\right)\left(\frac{D_p}{\rho_f\ V_{mf}^2}\right)\left(\frac{\varepsilon_{mf}^3}{1-\varepsilon_{mf}}\right)=\frac{150\,(1-\varepsilon_{mf})\,\mu_f}{D_p\ \rho_f\ V_{mf}}+1.75$$

$$\left(\frac{\Delta p}{L_{mf}}\right)=\frac{150\,\mu_f\ V_{mf}}{D_p^2}\frac{(1-\varepsilon_{mf})^2}{\varepsilon_{mf}^3}+\frac{1.75\,\rho_f\ V_{mf}^2}{D_p}\frac{(1-\varepsilon_{mf})}{\varepsilon_{mf}^3} \qquad (2.11)$$

The minimum fluidization velocity V_{mf} at which fluidization begins can be calculated by combining Eq. 2.8 and Eq. 2.11 to obtain the following quadratic equations

$$(1-\varepsilon_{mf})(\rho_p-\rho_f)g=\frac{150\,\mu_f\ V_{mf}}{D_p^2}\frac{(1-\varepsilon_{mf})^2}{\varepsilon_{mf}^3}+\frac{1.75\,\rho_f\ V_{mf}^2}{D_p}\frac{(1-\varepsilon_{mf})}{\varepsilon_{mf}^3}$$

$$(\rho_p-\rho_f)g=\frac{150\,\mu_f\ V_{mf}}{D_p^2}\frac{(1-\varepsilon_{mf})}{\varepsilon_{mf}^3}+\frac{1.75\,\rho_f\ V_{mf}^2}{D_p\ \varepsilon_{mf}^3} \qquad (2.12)$$

$$\frac{g\,\rho_f\,(\rho_p-\rho_f)D_p^3}{\mu_f^2}=\frac{150\,(1-\varepsilon_{mf})}{\varepsilon_{mf}^3}\left(\frac{D_p\ \rho_f\ V_{mf}}{\mu_f}\right)+\frac{1.75}{\varepsilon_{mf}^3}\left(\frac{D_p\ \rho_f\ V_{mf}}{\mu_f}\right)^2 \qquad (2.13)$$

Consider the Archimedes number, $Ar=\dfrac{g\,\rho_f\,(\rho_p-\rho_f)D_p^3}{\mu_f^2}$ (2.14)

and the Reynolds number at minimum fluidization, $Re_{mf}=\dfrac{D_p\ \rho_f\ V_{mf}}{\mu_f}$ (2.15)

Substituting the Eq. 2.14 and Eq. 2.15 to Eq. 2.13, "Ar" is obtained as,

$$Ar=\frac{150\,(1-\varepsilon_{mf})}{\varepsilon_{mf}^3}Re_{mf}+\frac{1.75}{\varepsilon_{mf}^3}Re_{mf}^2 \qquad (2.16)$$

By solving the above quadratic Eq. 2.16 the Reynolds number can be obtained and from Eq. 2.15, the minimum fluidization velocity, V_{mf}, can be obtained.

For large particles ($D_p \geq 1$ mm), inertial effects are important, and the full Ergun Eq. 2.16 must be used to determine V_{mf}. When in doubt, use the Ergun Eq. 2.16.

For a bed of small particles ($D_p \leq 0.1$ mm), the flow conditions at this stage are such that the Reynolds number is relatively small ($Re \leq 10$) so that the Kozeny-Carman Equation can be used to establish the point of onset of fluidization. Kozeny-Carman Equation is the simplified version of Ergun equation (Eq. 2.9), which is applicable to viscous flow dominant regime by removing the inertial part (second part of right hand side of Eq. 2.9). This yield,

$$V_{mf} = \frac{(\rho_p - \rho_f) g D_p^2}{150 \mu_f} \frac{\varepsilon_{mf}^3}{(1-\varepsilon_{mf})} \tag{2.17}$$

The state of the bed is as one of incipient fluidization, when the superficial velocity V_s is equal to V_{mf}. The void fraction "ε" at this state depends upon the material, shape, and size of the particles. For nearly spherical particles, McCabe, Smith, and Harriott (2001) suggested that ε lies in the range 0.40 to 0.45, increasing a bit with particle size.

2.6.3 Terminal Settling Velocity

Consider the upward flow of a gas through a bed of particles. At some superficial velocity, the upward drag force (F_d) exerted by the gas on the particles balances the downward body force of gravity (F_g). This is the condition of minimum fluidization (where, $F_d = F_g$). For particles with diameters in the range of 50 to 500 microns and densities in range of 0.2 to 5,000 kg/m^3, fluidization usually can be achieved smoothly with increasing gas velocity. As denoted by Geldart (1973), these characteristics embrace the majority of particles encountered in fluidized beds applications. For such particles, gas velocities above the minimum fluidization velocity result in the occurrence of gas bubbles in the bed, wherein some fraction of the gas flows through the suspension of particles as a continuum phase, while the remaining fraction flows as discrete bubbles rising through the suspension. This is the regime commonly called dense bubbling fluidization. The upper limit of gas velocity for this regime is related to terminal settling velocity of the particles, beyond which interfacial drag becomes sufficient to entrain the particles out of the bed. To establish the appropriate fluidization regime for any given application, one needs to

calculate the minimum fluidization velocity and the terminal settling velocity of the bed particles.

The superficial velocity of the gas for minimum fluidization (V_{mf}) can be calculated by solving the following quadratic equation for Re_{mf} :

$$Ar = \frac{150\left(1-\varepsilon_{mf}\right)}{\varepsilon_{mf}^3} Re_{mf} + \frac{1.75}{\varepsilon_{mf}^3} Re_{mf}^2$$

Where, the Archimedes number, $Ar = \dfrac{g\,\rho_f\left(\rho_p-\rho_f\right)D_p^3}{\mu_f^2}$

and the particle Reynolds number at minimum fluidization, $Re_{mf} = \dfrac{D_p\,\rho_f\,V_{mf}}{\mu_f}$

A free-falling object accelerates downwards due to gravity, the upward drag force acting on the object increases, causing the acceleration to decrease. At a particular speed, the downward gravitational force (F_g) equals the upward drag force (F_d). This causes the net force on the object to be zero, resulting in an acceleration of zero. This particular speed is known as terminal velocity (also called settling velocity).

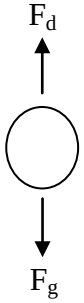

The terminal velocity (V_{ts}) is given by the expression:

$F_d = F_g$

$$\frac{1}{2}\rho_f\,V_{ts}^2\left(\frac{\pi}{4}D_p^2\right)C_D = \left(\rho_p-\rho_f\right)\left(\frac{\pi}{6}D_p^3\right)g$$

$$V_{ts} = \sqrt{\frac{4\,g\,D_p\left(\rho_p-\rho_f\right)}{3\,\rho_f\,C_D}} \qquad (2.18)$$

Where, C_D is the drag coefficient for a single particle.

The drag coefficient, C_D is equal to 0.44, in the case of spherical particles. But in the case of near-spherical particles, over the range $1 < Re_{ts} < 1{,}000$, C_D is given by the relationship

$$C_D = 18.5\, Re_{ts}^{-3/5} \tag{2.19}$$

Where the Reynolds number at terminal velocity (Re_t) is defined by the following equation

$$Re_{ts} = \frac{D_p\, \rho_f\, V_{ts}}{\mu_f} \tag{2.20}$$

Substituting Eq. 2.19 into Eq. 2.18, an explicit equation for the terminal settling velocity is

obtained, $V_{ts} = \left[0.072\, g\, \frac{D_p^{8/5} \left(\rho_p - \rho_f\right)}{\rho_f^{2/5}\, \mu_f^{3/5}} \right]^{5/7}$

Now, consider the condition one must impose on the superficial velocity so that particles are not carried out with the fluid at the exit. This would occur if the superficial velocity is equal to the terminal settling velocity of the particles.

Restricting attention to small particles ($D_p \leq 0.1$ mm), where Stokes Law can be used to calculate their terminal settling velocity as

$$V_{ts} = \frac{\left(\rho_p - \rho_f\right) g\, D_p^3}{18\, \mu_f} \tag{2.21}$$

By using the result for the minimum fluidization velocity for the case of small particles, given above Eq. 2.17, for finding the ratio of Eq. 2.21 and Eq. 2.17

$$\frac{V_{ts}}{V_{mf}} = \left(\frac{25}{3}\right) \frac{\left(1 - \varepsilon_{mf}\right)}{\varepsilon_{mf}^3}$$

For "ε" lying in the range 0.40 to 0.45, this yields a ratio ranging from 78 to 50.

2.7 Review of Fluidized Bed Research and Development (R&D)

Ergun (1952) critically reviewed and studied the exiting information on the flow of fluids through beds of granular solids. In this study, the author reported experimental results obtained for the purpose of testing the validity of the equation and numerous other data taken from the literature. He found that pressure losses are caused by simultaneous kinetic energy and viscous energy losses, and that the following comprehensive equation is applicable to all types of flow.

$$\left[\frac{\Delta p}{L}\right]=\left[150\,\frac{(1-\varepsilon)^2}{\varepsilon^3}\,\frac{\mu_f\ V_m}{D_p^2}\right]+\left[1.75\,\frac{(1-\varepsilon)}{\varepsilon^3}\,\frac{\rho_f\ V_m^2}{D_p}\right] \tag{2.22}$$

Viscous energy losses per unit length are expressed by the first term of right hand side of above equation $\left[150\,\frac{(1-\varepsilon)^2}{\varepsilon^3}\,\frac{\mu_f\ V_m}{D_p^2}\right]$ and the kinetic energy losses by the second term of right hand side $\left[1.75\,\frac{(1-\varepsilon)}{\varepsilon^3}\,\frac{\rho_f\ V_m^2}{D_p}\right]$. The author has been examined the above equation from the point of view of its dependence upon flow rate, properties of the fluids, and fractional void volume (ε), orientation, size, shape, and surface of the granular solids. Whenever possible, conditions were chosen so that the effect of one variable at a time could be considered. A transformation of the general equation indicates that the Blake-type friction factor has the following form:

$$f_v=1.75+150\,\frac{(1-\varepsilon)}{N_{Re}} \tag{2.23}$$

A new concept of friction factor, f_v, representing the ratio of pressure drop to the viscous energy term is discussed in Ergun's study.

Syamlal and Gidaspow (1985) developed a computer model for a hot fluidized bed for gasifying coal due to high rates of heat and mass transfer and solids mobility. Fluidized beds are also very useful for coal combustion to produce electric power. However, one of the main concerns using fluidized beds to commercialize is scale-up. This is due to the absence of an experimentally verified hydrodynamic theory that can describe the complicated transient gas and solid motion in a fluid bed. For fluidized bed combustion, the model by Adams and Welty (1979)

proved to be very useful for explaining heat transfer coefficients from a horizontal tube to a fluidized bed. Illinois Institute of Technology (IIT) developed a cold fluidized bed model for a two dimensional bed, which was able to predict void distribution, solids circulation, and bubbling behaviors. The IIT model was extended to a heated fluidized bed. Their results suggest that in a bubbling bed the large heat transfer coefficients can be computed from their hydrodynamic model without the use of any turbulence. The model itself computes a transient type behavior caused by the formation of bubbles, their propagation, and eruption at the top of the bed. All the computed variables including the void fraction, the gas and solid velocities, and the temperatures undergo a complex oscillatory behavior.

Syamlal (1987) developed a multi-particle model of fluidization. He simulates fluidization phenomena such as segregation, elutriation, and solids mixing. The constitutive relation known as particle-particle drag term requires for his model as accounting the momentum transfer between the particulate phases due to collisions. Earlier researchers developed empirical correlations and measured the particle-particle drag for dilute systems, such as pneumatic conveyors. But similar measurements are not possible in dense systems, such as fluidized bed. Therefore, based on the kinetic theory of dense gases, he derived an expression for the particle-particle drag term. He compared the predictions of the model with Yang and Keairns experimental data as to test the accuracy of that expression. Yang and Keairns (1982) fluidized uniform mixtures of dolomite and acrylic particles for various times and they also measured the rate of separation of the dolomite particles from the acrylic particles. They found that the dolomite particles settled rapidly because it was heavier and larger than the acrylic particles. Yang and Keairns' experimental data suggest that the rate of settling is strongly dependent upon the particle-particle drag. Therefore, for determining the accuracy of the particle-particle drag term, simulating of Yang and Keairns experiments is a useful tool. He found that the model predicts the initial rate of separation reasonably well. However, the predicted equilibrium concentrations of dolomite particles in the upper layer of acrylic particles do not agree with the experimental data. He thought this is because of the absence of granular stress from the model. Hence, further refinement of the particle-particle drag term can be sought only after including realistic granular stress in the multi-particle model.

Syamlal and O'Brien (1989) studied bubble behavior. They used a hydrodynamic model which treats a fluidized medium as a mixture of a gas and a granular (solid) phase. They

simulated the bubbles in fluidized beds of various particle sizes, with and without jets. They found that the predicted characteristics of bubble formation, bubble shape, bubble coalescence phenomena, bubble motion, bubble eruption at the surface, and the dynamics of the bed surface are in good qualitative agreement with experimental observations. They compared the bubble frequency, bubble volume, bubble rise velocities, wake angle, wake fraction, and pressure profile with experimental data and simpler theories. They examined the predicted gas and solids mixing by using a new graphical technique and found in good agreement with experimental observations.

Benyahia et al. (2004) investigated the ability of three gas-solids flow models such as standard granular kinetic theory and two gas-solids turbulence models to predict core-annular flow behavior commonly observed in dense gas/solids flows. Their study demonstrated that the granular kinetic theory, Balzer et al. 1996, and Cao and Ahmadi 1995 models give similar predictions for a dense fully developed flow in a vertical channel, and that the gas turbulence may not have a dominant effect in relatively dense gas/solids flows. Finally, the core-annular flow behavior with maximum solids concentration at the walls was not observed if the boundary condition causes production of granular energy at the wall. Boundary conditions that dissipate granular energy near the wall are needed to predict a core-annular flow structure.

Gunn (1978) measured experimentally heat transfer to particles in fixed beds and showed that either the Nusselt number maintains a constant value as the Reynolds number is reduced or the Nusselt number decreases to zero if axial dispersion has been neglected. A quantitative analysis of particle to fluid heat transfer on the basis of a stochastic model of the fixed bed leads to a constant value of the Nusselt group at low Reynolds number. When the analytical equation is included as an asymptotic condition, he derived an expression that describes the dependence of Nusselt group upon Reynolds number. He extended this expression to describe mass and heat transfer to fixed and fluidized beds of particles within the porosity range of 0.35 to 1.0. Both gas and liquid phase transfer groups are correlated up to a Reynolds number of 10^5.

Lun et al. (1984) studied the flow of an idealized granular material consisting of uniform smooth, but inelastic, spherical particles using statistical methods analogous to those used in the kinetic theory of gases. They developed two theories, one for the Couette flow of particles having arbitrary coefficients of restitution (inelastic particles) and a second for the general flow of particles with coefficients of restitution near one (slightly inelastic particles). The study of

inelastic particles in Couette flow follows the method of Savage & Jeffrey (1981). An ad hoc distribution function was used to describe the collisions between particles. They compared the results of this first analysis with other theories of granular flow, with the Chapman-Enskog dense-gas theory, and with experiments. Their theory agreed moderately well with experimental data and it is found that the asymptotic analysis of Jenkins & Savage (1983), which was developed for slightly inelastic particles, surprisingly gave results similar to the first theory even for highly inelastic particles. Therefore the "nearly elastic" approximation is pursued as a second theory using an approach that is closer to the established methods of Chapman-Enskog gas theory. Their new approach which determines the collisional distribution functions by a rational approximation scheme is applicable to general flow fields, not just simple shear. It incorporates kinetic as well as collisional contributions to the constitutive equations for stress and energy flux and is thus appropriate for dilute as well as dense concentrations of solids. When the collisional contributions are dominant, it predicts stresses similar to the first analysis for the simple shear case.

Ding and Gidaspow (1990) observed that for a better understanding of tube erosion in fluidized bed combustors, detailed knowledge of solids circulation, bubble motion, and frequencies of porosity oscillations is needed. They derived a predictive two-phase flow model starting with the Boltzmann equation for velocity distribution of particles. This model is a generalization of the Navier-Stokes equations of the type proposed by R. Jackson, except that the solids viscosities and stresses are computed by simultaneously solving a fluctuating energy equation for the particulate phase. The model predictions agree with time-averaged and instantaneous porosities measured in two-dimensional fluidized beds. They also predicted the observed flow patterns and bubbles.

Kuipers et al. (1992) developed a computational model for a hot gas-fluidized bed. They used the two-fluid model (TFM) approach. In that approach both phases are considered to be continuous and fully interpenetrating. They calculated local wall-to-bed heat transfer coefficients by simultaneously solving the two-fluid model (TFM) conservation of mass, momentum and energy equations. Their preliminary calculations suggest that the experimentally observed high wall-to-bed heat transfer coefficients of gas-fluidized beds can be predicated with the present hydrodynamic model without incorporation of turbulence terms in the transport equation. Their calculation clearly showed the enhancement of the wall-to-bed heat transfer process due to the

bubble-induced bed-material refreshment along the heated wall. The model proved its usefulness and distinguished itself advantageously from previous theoretical models by providing detailed information on the local behavior of the wall-to-bed heat transfer coefficients. The local wall-to-bed heat transfer coefficient is relatively large in the wake of the bubbles rising along a heated wall because of the vigorous solids circulation in the bubble wake.

Enwald et al. (1999) carried out a mesh refinement study and validation of two-fluid model closures for a bubbling fluidized bed application. The mesh refinement study indicates that a higher degree of mesh refinement is required for atmospheric than for pressurized fluidization. They evaluated statistical bubble parameters (bubble frequency, mean bubble rise velocity, mean pierced bubble length and mean bubble volume fraction). They computed the simulated statistical bubble quantities from voidage signals derived from the transient multidimensional solution of two-fluid models. The algorithm for computing these quantities was taken directly from the evaluation program treating the measurement signals. They developed a parallel version of the two-fluid model solver to remedy the long simulation times required to obtain acceptable statistical values, based on a domain decomposition method for distributed memory computers. They investigated a number of problems related to the parallelization. These are optimal treatment of velocity components on multi-block boundaries, frequency of data exchange at multi-block boundaries, local errors at multi-block boundaries and simulation time requirements.

Mathiesen et al. (2000) presented a computational study of the flow behavior in a cold-flow pilot-scale circulating fluidized bed. They developed a multi-fluid Computational Fluid Dynamics (CFD) model and verified against experimental data reported in the literature. The flow model is based on an Eulerian description of the phases where the kinetic theory of granular flow forms the basis for the turbulence modeling in the solid phases. The model is generalized for one gas phase and "N" number of solid phases to enable a realistic description of the particle size distributions in gas/solids flow systems. Each solid phase is characterized by a diameter, density and restitution coefficient. They performed the simulations with different superficial gas velocities, initial solids concentrations and standard deviations of the particle size distribution. They gave most emphasis to study the effects of different particle size distributions and the fluctuating behavior of the dilute gas/solids flow system. Altogether, the simulation results are in

very good agreement with the experimental data. They calculated mean diameters, axial and radial mean and turbulent velocities, and mass fluxes successfully.

Huilin et al. (2003) studied the dynamic behavior of gas-solids flow in a 6 m high riser using a transient two-dimensional (2D) hydrodynamic model based on the kinetic theory of granular flows. They obtained turbulent parameters, instantaneous and local gas-particle velocity, and void fraction. The classical core-annular flow structure was reflected by predicted time-averaged particle concentrations and velocities which were in agreement with experimental measurements, in particular, with those reported by Miller and Gidaspow [1992]. Predicted instantaneous solids concentration frequencies and total granular temperature compared well with the experimental data for various regions of the riser. They estimated high thermal conductivities of fluidized powders from the kinetic theory without adjusted parameters. They assessed the effects of initial conditions, riser diameter, inlet geometry and riser vertical inclination. They predicated the unexpected strong distortions of solids concentrations and vertical fluxes for small inclination angles of the order of 2^0. Therefore, analysis of experimental data should be carefully conducted to ensure that riser inclination is not too important over the length of the riser in order to eliminate potential artifacts due to this geometric parameter.

Jiradilok et al., (2006) studied the turbulent fluidization regime which is characterized by the co-existence of a dense, bottom region and a dilute, top bed. A kinetic theory based CFD code with a drag corrected for clusters captured the basic features of this flow regime: the dilute and dense regions, high dispersion coefficients and a strong anisotropy. The computed energy spectrum captures the observed gravity wave and the Kolmogorov -5/3 law at high frequencies. The computed turbulent kinetic energy is close to the measurements for Fluidized Catalytic Cracking (FCC) particles. The CFD simulations compared reasonably well with the measured core-annular flow experiments at very high solid fluxes. The computed solid pressures, granular temperatures, FCC viscosities and frequencies of oscillations were close to measurements reported in the literature. The computations suggested that unlike for the flow of group B particles, the oscillations for the FCC particles in the center of the riser are primarily due to the oscillations of clusters and not due to oscillations of individual particles. Therefore mixing is not on the level of individuals particles.

Panneerselvam, Savithri, and Surender (2007) carried out CFD simulations for the prediction of flow patterns in a liquid-solid fluidized bed using Eulerian- Eulerian framework.

They compared the CFD model predictions with the experimental findings reported by Limtrakul et al. (2005) and showed a good agreement. They further extended the CFD model to compute solid mass balance in the core and annular regions for verifying conservation of mass and energy flows due to various dissipation mechanisms. They also compared energy required for solid expansion in liquid fluidized bed with energy required for solid suspension in an equivalent stirred tank contactor at similar operating conditions. They investigated the influence of various inter-phase drag models proposed by Gidaspow (1994), Di Felice et al. (1994) and Syamlal and O'Brien (1988) on solid in liquid fluidized bed. Even though the models proposed by Di Felice et al. and Syamlal and O'Brien predicted the flow pattern of solid motion inside the fluidized bed only with reasonable accuracy, the model proposed by Gidaspow showed a better quantitative agreement with experimental data. They also carried out the effect of grid sensitivity, time step sensitivity and effect of inlet feed conditions for ensuring accuracy of numerical simulation prediction.

Reuge et al. (2008) validated a CFD models before they used for designing fluidized bed reactors. They collected the validation data from a fluidized bed of (Geldart's group B, 1973) alumina particles operated at different gas velocities involving two fluidization hydrodynamic regimes (bubbling and slugging). They measured the bed expansion, height of bed fluctuations, and frequency of fluctuations from videos of the fluidized bed. To simulate the experiments they used the Eulerian-Eulerian two fluid models MFIX (website: http://www.mfix.org). They evaluated two different models for the particle stresses Schaeffer model developed by Syamlal, Rogers and O'Brien (1993), and Schaeffer (1987) and Princeton model developed by Srivastava and Sundaresan (2003) including evaluations of different values of the restitution coefficient and internal angle of friction. 3D simulations are required for getting quantitative and qualitative agreement with experimental data. They observed that the results from the Princeton model are in better agreement with data than that from the Schaeffer model. They also observed both free slip and Johnson-Jackson boundary conditions gave nearly identical results. An increase in coefficient of restitution (e) from 0.8 to 1 leads to larger bed expansions and lower heights of fluctuations in the bubbling regime, whereas it leads to unchanged bed expansion and to a massive reduction in the height of fluctuations in the slugging regime. The angle of internal friction (Φ) in the range $10\text{-}40^0$ does not affect the bed expansion, but its reduction significantly reduces the height of fluctuations.

Wang et al. (2008) numerically analyzed hydrodynamics of three-dimensional gas-solid bubbling fluidized beds. They simulated the particle-particle interactions from the kinetic theory for flow of dense, slightly inelastic, slightly rough sphere proposed by Lun (1991) to account for rough sphere binary collisions and the frictional stress model proposed by Johnson et al. (1990) to consider the frictional contact forces between particles. Their model was evaluated by comparing with the measured particle distributions and velocities of Yuu et al. (2001) and experimental bed expansion of Taghipour et al. (2005). Their computed results indicated that their model gave better agreement with experimental data than the results from original kinetic theory for frictionless slightly inelastic sphere of Ding and Gidaspow (1990) with and without solid friction stress model.

Yan et al. (1999) improved a previous numerical model of fluidized-bed coal gasifiers to incorporate an overall energy balance. They used the improved model to simulate the performance of bubbling fluidized-bed coal gasifiers of different scales. Their simulations showed that the predicted overall carbon conversion, operating bed temperature and concentrations of individual gas species compared well with the experimental data from three pilot-scale and a full-scale fluidized-bed coal gasifiers. The water-gas shift reaction, either driven by kinetics or in equilibrium in the dilute phase has significant effects on the predictions for the pilot-scale air-blown gasifiers but has little effect on a commercial-scale oxygen-blown gasifier. This is attributed to the much faster oxidation rate of H_2 and CO near the distributor in the oxygen-blown commercialized gasifier than in the air-blown gasifiers. Their results also illustrated that about 26-41% of feed oxygen is consumed in the homogeneous combustion reactions in the simulation. The percentage of oxygen consumption in the homogeneous reaction increases with a decrease in coal rank and with an increase in operating pressure and temperature. Carbon conversions due to char gasification are significant when compared to those due to char combustion in the simulated gasifier.

Chejne and Hernandez (2002) developed a one-dimensional steady-state mathematical model and a numerical algorithm to simulate the coal gasification process in a fluidized-bed. The model incorporates two phases, the solid and the gas. The solid phase is composed of carbonaceous material, limestone and/or inert bed material. The gaseous phase participates in the emulsion with the solid phase and forms the bubble. Their model could predict temperature, converted fraction, and particle size distribution for the solid phase. For the gaseous phase, in

both emulsion and bubble, their model could predict profiles of temperature, gas composition, velocities, and other fluid-dynamic parameters. In the feed zone, they considered a Gaussian distribution for the solid particle size. This distribution changes due to elutriation, attrition, consumption and drag inside the reactor. They solved a system of 29 differential and 10 non-linear equations, derived from mass, momentum and energy balances for each phase, at any point along the bed height by the Gear and Adams Method (1971). They used experimental data from the Universidad de Antioquia and Universidad Nacional-Medellin to validate their model. Finally, the model were used to optimize the gasification process by varying several parameters, such as particle size distribution, excess of air, coal type, and geometry of the reactor.

Yu et al. (2007) developed a numerical model based on the two-fluid model (TFM) including the kinetic theory of granular flow (KTGF) and complicated reactions to simulate coal gasification in a bubbling fluidized bed gasifier (BFBG). They determined the coal gasification rates by combining Arrhenius rate and diffusion rate for heterogeneous reactions and using turbulent mixing rate for homogeneous reactions. They predicted the flow behaviors of gas and solid phases in the bed and freeboard which are not easy to be measured through the experiments. The calculated exit values of gas composition agreed well with the experimental data. They discussed the relationship between gas composition profiles with the height of gasifier and the distributions of temperature, gas and solid velocity and solid volume fraction.

Wang, Jin, and Zhong (2009) developed a comprehensive three-dimensional numerical model to simulate the coal gasification in a fluidized bed gasifier. They considered both gas-solid flow and chemical reactions. They modeled the gas phase with k-ε turbulent model and the particle phase with kinetic theory of granular flow. They also considered the coal pyrolysis, homogeneous reactions and heterogeneous reactions. They determined the reaction rates of homogeneous reaction and heterogeneous reaction by Arrhenius-Eddy dissipation reaction rate and Arrhenius-diffusion reaction rate, respectively. They carried out the simulations in a fluidized bed coal gasifier with a height of 2.0 m and a diameter of 0.22 m. They obtained the flow patterns, gas velocities, and particle velocities, composition profiles of gas product and distributions of reaction rates. They compared some calculated values with experimental data. The results showed that the predicted exit gas compositions were in a good agreement with the experiments. This indicated that their proposed three-dimensional models and simulations were successful, which provided a promising way to simulate the coal gasification in fluidized beds.

CHAPTER THREE
CFD FORMULATION AND THEORY

3.1 Problem Statement

Using Computational Fluid Dynamics (CFD) simulation is an economical and effective tool to study coal gasification. This study will investigate the thermal-flow and gasification process in a fluidized bed mild gasifier as shown in Fig. 3.2. Coal gasification is a multiphase reactive flow phenomenon. It is a multiphase problem between gases and coal particles and is also a reactive flow which involves homogeneous reactions among gases and heterogeneous reactions between coal particles and gases. The Eulerian-Eulerian method is adopted in this study because the concentrations of coal particles are dense in the fluidized bed and tracing each particle with the Lagrangian method is not realistic. Both gas phase (primary phase) and solid phase (secondary phase) is solved by using Eulerian method. All of solid particles are placed side by side inside the gasifier like a bed of granular material, and the gas mixture of gas phase is passed up through this bed and converts this granular material from a static solid-like state to a dynamic fluid-like state. This process is known as "fluidization". Both homogeneous (gas-gas) reaction and heterogeneous (gas-solid) reactions are simulated in this study. Detailed theory and formulation are discussed in this chapter.

Description of Preliminary Geometry

Due to the complexity of this simulation, this study is conducted following the approach below:

1. Single gas phase of thermal-flow behavior (no solids and no reactions.)
2. Single gas phase with chemical reaction assuming instantaneous gasification (no solids)
3. Multiphase of thermal-flow behavior (no reaction)
4. Multiphase of reactive thermal-flow (complete simulation)

Each step involves two geometries. Simplified 2-D preliminary geometry (Fig. 3.1) is used first to save computational time and followed by 2-D gasifier central-plane geometry once the computational setups and reaction models have been established and converged solutions in

the simplified 2-D geometry have been obtained. The height and width of the preliminary geometry is 1 m and 0.3 m, respectively. The preliminary geometry has seven perforated velocity inlets and one outlet. The width of each inlet is 0.02 m and width of outlet is 0.1 m.

Description of the Simulated Mild Gasifier Geometry

The central-plane geometry of the 2-D Mild Gasifier used in the simulation is shown in Figure 3.2. The height and width of the bench-top mild gasifier is 34.25 inch (87 cm) and 18 inch (45.75 cm), respectively. There are three velocity inlets, two for fluidized gas inlet and one for coal and transport gas inlet for the multi-phase case. The width of left and right horizontal gas inlet is 3 inch (7.65 cm) and vertical coal inlet is 2 inch (5 cm). There are four outlets, two for char and two for produced syngas. The width of the left and right horizontal syngas outlets are 5 inch (12.7 cm) and char outlet is 1.5 inch (3.8 cm) inclined 45 degrees. To create fluidization inside the gasifier, a total of 28 perforated interior surfaces of 0.15 inch (0.38 cm) width each are created side by side with equal distance apart A draft tube is designated inside the domain with 4 inch (10.15 cm) width to isolate fluidized bed from contacting oxygen in the air and to transfer heat to the fluidized bed through the draft tube wall. Above the draft tube, a deflector with 8 inch width is installed to block the particles from being entrained out of the fluidized bed with the gases. Coal and air enters the draft tube through the draft-tube's bottom inlet and react to produce heat which drives out the volatiles during the journey moving upward through the draft tube.

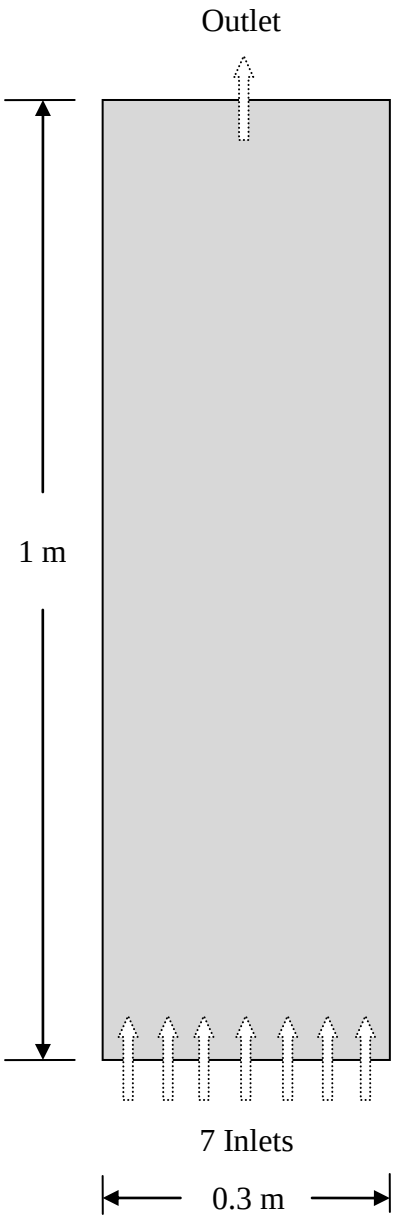

Figure 3.1 The simplified 2D preliminary geometry

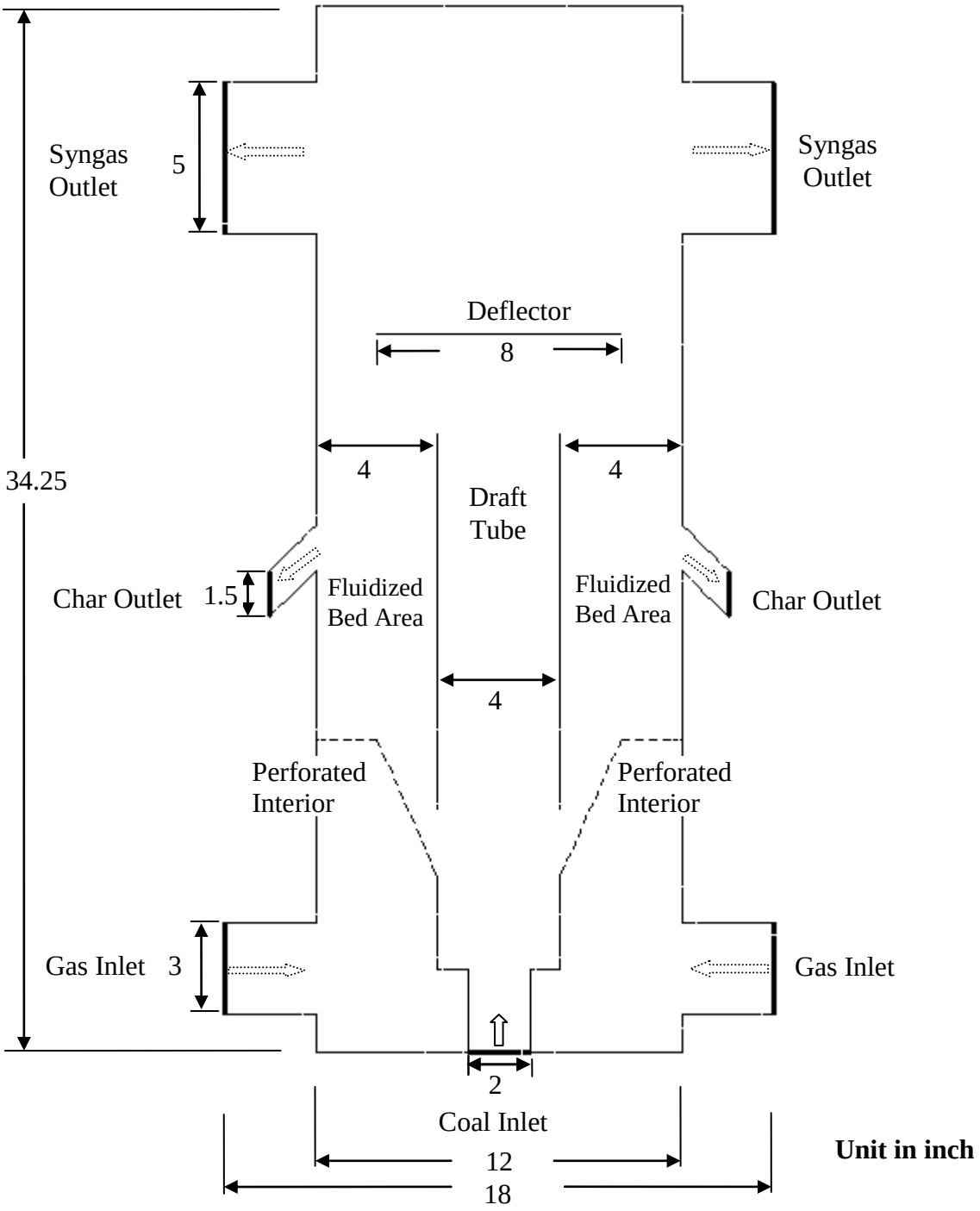

Figure 3.2 Schematic of the 2D simulated Fluidized Bed Mild Gasifier

3.2 Computational Model

3.2.1 Physical Characteristics of the Problem

The physical characteristics of the problem are modeled as follows,

1. The flow inside the domain is two dimensional, incompressible, and turbulent.
2. Gravitational force is considered.
3. Gas species involved in this study are Newtonian fluids with variable properties as functions of temperature. These variable properties are calculated by using piecewise-polynomial method.
4. Mass-weighted mixing-law for specific heat and incompressible-ideal gas for density is used for gas species mixture.
5. The walls are impermeable and adiabatic.
6. The flow is steady for single phase case and unsteady for multi- phase case.
7. No-slip condition (zero velocity) is imposed on wall surfaces.

3.2.2 General Governing Equations

As mentioned earlier, the Eulerian- Eulerian method is adopted for this study. In the Eulerian method for gas phase (primary phase), the 2-D Navier-Stokes equations as well as mass and energy conservation equations are solved. The governing equations for the conservations of mass, momentum, and energy are given as:

$$\frac{\partial \rho}{\partial t} + \nabla \bullet \left(\rho \, \vec{v} \right) = 0 \tag{3.1}$$

$$\frac{\partial}{\partial t}\left(\rho \vec{v}\right) + \nabla \bullet \left(\rho \vec{v} \vec{v}\right) = -\nabla p + \nabla \bullet \left(\bar{\bar{\tau}}\right) + \rho \vec{g} + \vec{F} \tag{3.2}$$

$$\frac{\partial}{\partial t}\left(\rho E\right) + \nabla \bullet \left(\vec{V}\left(\rho E + p\right)\right) = \nabla \bullet \left(k_{eff} \nabla T - \sum_{j} h_j \vec{J}_j + \left(\bar{\bar{\tau}}_{eff} \bullet \vec{v}\right)\right) + S_h \tag{3.3}$$

Where k_{eff} is the effective conductivity and $\vec{J}_j$ is the diffusion of species j.

As the momentum equations are solved with the complete two-dimensional Navier-Stokes equations, so, $\bar{\bar{\tau}}$, the stress tensor is given by,

$$\bar{\bar{\tau}} = \mu\left[\left(\nabla\vec{v} + \nabla\vec{v}^{T}\right) - \frac{2}{3}\nabla \bullet \vec{v} \bullet I\right] \tag{3.4}$$

Where μ is the molecular dynamic viscosity, I is the unit tensor, and the second term on the right-hand side is the effect of volume dilatation.

The first three terms on the right-hand side of equation (3.3) represent heat transfer due to conduction, species transport, and viscous dissipation. S_h is a source term including the enthalpy formation from the chemical reaction of the species. The energy E is defined as

$$E = h - \frac{p}{\rho} + \frac{v^2}{2} \tag{3.5}$$

Where h is the sensible enthalpy and for incompressible flow and is given as

$$h = \sum_j Y_j h_j + \frac{p}{\rho} \tag{3.6}$$

Y_j is the mass fraction of species j and

$$h_j = \int_{T_{ref}}^{T} c_{p,j} dT \tag{3.7}$$

T_{ref} is the reference temperature, taken as 298.15 K

3.2.3 Turbulence Model

The velocity field in turbulent flows always fluctuates. As a result, the transported quantities such as momentum, energy, and species concentration fluctuate as well. The fluctuations can be small scale and high frequency, which is computationally expensive to be

directly simulated. To overcome this, a modified set of equations that are computationally less expensive to solve can be obtained by replacing the instantaneous governing equations with their time-averaged, ensemble-averaged, or otherwise manipulated to remove the small time scales. However, the modifications of the instantaneous governing equations introduce new unknown variables. Many turbulence models have been developed to determine these new unknown variables (such as Reynolds stresses or higher order terms) in terms of known variables or low order terms. This is so called "closure" of the turbulence models.

General turbulence models widely available are:

a. Spalart-Allmaras (one equation)
b. k-ε models (two equation)
    i. Standard k-ε model
    ii. RNG k-ε model
    iii. Realizable k-ε model
c. k-ω models (two equation)
    i. Standard k-ω model
    ii. Shear-stress transport (SST) k-ω model
d. Reynolds Stress model (five equation)

3.2.3.1 Standard k-ε Model

The standard k-ε model is employed in this study to simulate the turbulent flow due to its suitability for a wide range of wall-bounded and free-shear flows. The standard k-ε model is the simplest of turbulence two-equation model in which the solution of two separate transport equation allows the turbulent velocity and length scales, which are to be independently determined. The k-ε model is a semi-empirical model with several constants, which were obtained from experiments.

All the three k - ε models have similar forms with major differences in the method of calculating the turbulent viscosity: the turbulent Prandtl numbers and the generation and destruction terms in the k-ε equations.

The standard k-ε model based on model transport equations for the turbulence kinetic energy (k) and its dissipation rate (ε). The model transport equation for (k) is derived from the

exact equation; while the model transport equation for (ε) is obtained using physical reasoning and bears little resemblance to its mathematically exact counterpart.

The turbulence kinetic energy (k), and its rate of dissipation (ε), are obtained from the following transport equations,

$$\frac{\partial}{\partial t}(\rho k)+\frac{\partial}{\partial x_i}(\rho k u_i)=\frac{\partial}{\partial x_j}\left[\left(\mu+\frac{\mu_t}{\sigma_k}\right)\frac{\partial k}{\partial x_j}\right]+G_k+G_b-\rho\varepsilon-Y_M+S_k \tag{3.8}$$

$$\frac{\partial}{\partial t}(\rho \varepsilon)+\frac{\partial}{\partial x_i}(\rho \varepsilon u_i)=\frac{\partial}{\partial x_j}\left[\left(\mu+\frac{\mu_t}{\sigma_\varepsilon}\right)\frac{\partial \varepsilon}{\partial x_j}\right]+C_{1\varepsilon}\frac{\varepsilon}{k}(G_k+C_{3\varepsilon}G_b)-C_{2\varepsilon}\rho\frac{\varepsilon^2}{k}+S_\varepsilon \tag{3.9}$$

In equations (3.8) and (3.9), G_k represents the generation of turbulence kinetic energy due to the mean velocity gradients and the Reynolds stress, calculated as

$$G_k=-\rho\overline{u_i' u_j'}\frac{\partial u_j}{\partial x_i} \tag{3.10}$$

G_b represents the generation of turbulence kinetic energy due to buoyancy, calculated as following,

$$G_b=\beta g_i\frac{\mu_t}{Pr_t}\frac{\partial T}{\partial x_i} \tag{3.11}$$

Pr_t is the turbulent Prandtl number and g_i is the component of the gravitational vector in the i-th direction. For standard k-ε model the value for Pr_t is set 0.85 in this study.

β is the coefficient of thermal expansion and is given as

$$\beta=-\frac{1}{\rho}\left(\frac{\partial \rho}{\partial T}\right)_p \tag{3.12}$$

Y_M represents the contribution of the fluctuating dilatation in compressible turbulence to the overall dissipation rate, and is defined as

$$Y_M = 2\rho\varepsilon M_t^2 \tag{3.13}$$

Where M_t is the turbulent Mach number which is defined as

$$M = \sqrt{\frac{k}{a^2}} \tag{3.14}$$

Where $a \left(\equiv \sqrt{\gamma RT}\right)$ is the speed of sound.

The turbulent (or eddy) viscosity, μ_t, is computed by combining k and ε as

$$\mu_t = \rho C_\mu \frac{k^2}{\varepsilon} \tag{3.15}$$

$C_{1\varepsilon}$, $C_{2\varepsilon}$, C_μ, σ_k and σ_ε are constants and have the following values

$C_{1\varepsilon} = 1.44$, $C_{2\varepsilon} = 1.92$, $C_\mu = 0.09$, $\sigma_k = 1.0$, and $\sigma_\varepsilon = 1.3$

These constant values have been determined from experiments using air and water for fundamental turbulent shear flows including homogeneous shear flows and decaying isotropic grid turbulence. They have been found to work fairly well for a wide range of wall- bounded and free-shear flows. The initial value for k and ε at the inlets and outlets are set as 1 m^2/s^2 and 1 m^2/s^3 respectively.

In general, turbulent flows are significantly affected by the presence of walls. Very close to the wall, viscous damping reduces the tangential velocity fluctuations. While kinematic blocking reduces the normal fluctuations, away from the wall, the turbulence is increased by the production of turbulence kinetic energy. In the near-wall region, the solution variables have large gradients, and the momentum and other scalar transports occur strongly. Therefore, accurate representation of the flow in the near-wall region is required for successful predictions of wall-bounded turbulent flows.

The k-ε turbulence model used in this study is primarily valid for turbulent core flows (i.e., the flow in the regions somewhat far from walls). Wall functions are used to make this turbulence model suitable for wall-bounded flows. Wall functions are a collection of semi-empirical formulas and functions that link the solution variables at the near-wall cells and the corresponding quantities on the wall. The wall functions consist of the following:

- ✓ Laws of the wall for mean velocity and temperature (or other scalars)
- ✓ Equations for near-wall turbulent quantities

Standard Wall Function

The law-of-the-wall for mean velocity gives

$$U^{+} = \frac{1}{\kappa}\ln\left(Ey^{+}\right) \tag{3.16}$$

Where,

$$U^{+} \equiv \frac{U_P C_\mu^{0.25} k_P^{0.5}}{\frac{\tau_w}{\rho}} \tag{3.17}$$

$$y^{+} \equiv \frac{\rho C_\mu^{0.25} k_P^{0.5} y_P}{\mu} \tag{3.18}$$

And

κ = von Karman constant (= 0.42)

E = empirical constant (= 9.793)

U_P = mean velocity of the fluid at point P

k_P = turbulence kinetic energy at point P

y_P = distance from point P to the wall

μ= dynamic viscosity of the fluid

The logarithmic law for mean velocity is valid for y^{+} > about 30 to 60

The wall function for the temperature is given as,

$$T^+ \equiv \frac{(T_w - T_P)\rho c_P C_\mu^{0.25} k_P^{0.5}}{q''} = Pry^+ + 0.5\rho.5\ \frac{C_\mu^{0.25} k_P^{0.5}}{q''} U_P^2 \qquad \left(y^+ < y_T^+\right) \tag{3.19}$$

Or,

$$T^+ = Pr_t\left[\frac{1}{\kappa}\ln\left(Ey^+\right) + P\right] + 0.5\rho\frac{C_\mu^{0.25} k_P^{0.5}}{q''}\left[Pr_t\ U_P^2 + (Pr - Pr_t)U_c^2\right] \qquad \left(y^+ > y_T^+\right) \tag{3.20}$$

Where, P is given as

$$P = 9.24\left[\left(\frac{Pr}{Pr_t}\right)^{3/4} - 1\right]\cdot\left[1 + 0.28e^{-0.007Pr/Pr_t}\right] \tag{3.21}$$

k_f = thermal conductivity of the fluid

ρ = density of fluid

c_P = specific heat of fluid

q" = wall heat flux

T_P = temperature at the cell adjacent to the wall

T_w = temperature at the wall

Pr = molecular Prandtl number ($\mu c_P / k_f$)

Pr_t = turbulent Prandtl number (= 0.85 at the wall)

A = 26 (van Driest constant)

κ = 0.4187 (von Karman constant)

E = 9.793 (wall function constant)

U_c = mean velocity magnitude at $y^+ = y^+_T$

y^+_T= non-dimensional thermal sublayer thickness.

The species transport is assumed to behave analogously to the heat transfer. The equation is expressed as

$$Y^+ \equiv \frac{(Y_{i,w} - Y_i)\rho c_p C_\mu^{0.25} k_P^{0.5}}{J_{i,w}} = \begin{cases} Scy^+, y^+ < y_c^+ \\ Sc_t\left[\frac{1}{\kappa}\ln\left(Ey^+\right) + P_c\right], y^+ > y_c^+ \end{cases} \tag{3.22}$$

Where Y_i is the local mass fraction of species i, Sc and Sc_t are the molecular and turbulence Schmidt numbers, and $J_{i,w}$ is the diffusion flux of species i at the wall. The molecular Schmidt number, Sc, is given as $\frac{\mu}{\rho D}$, where μ is the viscosity and D is the diffusivity. The P_c and y^+_c are calculated in a similar way as P and y^+_T, with the difference being that the Prandtl numbers are replaced by the corresponding Schmidt numbers.

For the k - ε turbulence model, the k-equation is solved in the whole domain, including the wall-adjacent cells. The boundary condition for k imposed at the wall is

$$\frac{\partial k}{\partial n} = 0 \tag{3.23}$$

Where n is the local coordinate normal to the wall. The production of kinetic energy, G_k, and its dissipation rate, ε, at the wall-adjacent cells, which are the source terms in k equation, are computed on the basis of equilibrium hypothesis with the assumption that the production of k and its dissipation rate assumed to be equal in the wall-adjacent control volume. The production of k and ε is computed as

$$G_k \approx \tau_w \frac{\partial U}{\partial y} = \tau_w \frac{\tau_w}{\kappa \rho C_\mu^{0.25} k_P^{0.5} y_P} \tag{3.24}$$

And

$$\varepsilon_P = \frac{C_\mu^{0.75} k_P^{1.5}}{\kappa y_P} \tag{3.25}$$

Enhanced Wall Function

The k-ε model is mainly valid for high Reynolds number fully turbulent flow. Special treatment is needed in the region close to the wall. The enhanced wall function is one of several methods that model the near-wall flow. In the enhanced wall treatment, the two-layer model is combined with the wall functions. The whole domain is separated into a viscosity-affected region and a fully turbulent region by defining a turbulent Reynolds number, Re_y,

$$Re_y = yk^{1/2} / \nu \tag{3.26}$$

Where k is the turbulence kinetic energy and y is the distance from the wall. The standard k-ε model is used in the fully turbulent region where Re_y > 200 and the one-equation model of Wolfstein (1969) are used in the viscosity-affected region with Re_y < 200. The turbulent viscosities calculated from these two regions are blended with a blending function (θ) to smoothen the transition.

$$\mu_{t,enhanced} = \theta\mu_t + (1-\theta)\mu_{t,l} \tag{3.27}$$

Where μ_t is the viscosity from the k-ε model of high Reynolds number, and $\mu_{t,l}$ is the viscosity from the near-wall one-equation model. The blending function is defined so it is equal to 0 at the wall and 1 in the fully turbulent region. The linear (laminar) and logarithmic (turbulent) laws of the wall are also blended to make the wall functions applicable throughout the entire near-wall region. A similar thermal wall function equation is employed for temperature calculation.

3.2.3.2 Other Models

Ignoring details here, the turbulent models available in this study are RNG k-ε model, standard k-ω model, the shear-stress transport (SST) k-ω model, and Reynolds stress model. RNG k-ε model was derived using renormalization group theory (Choudhury, 1993). It has an additional term in the ε-equation to improve the accuracy for rapidly strained flows. It uses the effective viscosity to account for low-Reynolds-number effects. Theoretically, this model is more accurate and reliable than the standard k-ε model. The standard k-ω model is an empirical model based on transport equations for the turbulence kinetic energy (k) and the specific dissipation rate (ω), which can also be considered as the ratio of ε to k (Wilcox, 1998). The low-Reynolds-number effect is accounted for in the k-ω model. The SST model is mixture of the k-ω model and the k-ε model: close to the wall it becomes the k-ω model while in the far field the k-ε model is applied (Menter, 1993).

3.2.4 Chemical Reaction Model

In this study, two different chemical reaction models are used in the CFD simulation: one for homogeneous gas-gas reactions and another for the heterogeneous (particle-gas) reactions. The key difference between these two models is related to how the carbon species is modeled. The homogeneous gas reaction assumes the carbon species gasified instantaneously, and the carbon is treated as a gas, while heterogeneous particle-gas reaction carbon as solid particles and they go through finite-rate reaction via a typical reaction at particle surface. These two models focus on different aspects of reaction processes and each has their own advantages. The assumptions, theory and limit of the instantaneous gasification are detailed below.

Instantaneous Gasification Model -- The interphase exchange rates of mass, momentum and energy are assumed to be infinitely fast. Carbon particles are made to gasify instantaneously, thus the solid-gas reaction process can be modeled as homogeneous combustion reactions. This approach is based on the locally-homogeneous flow (LHF) model proposed by Faeth (1987), implying infinitely-fast interphase transport rates. The instantaneous gasification model can effectively reveal the overall combustion process and results without dealing with the details of the otherwise complicated heterogeneous particle surface reactions, heat transfer, species transport, and particle tracking in turbulent reacting flow. The eddy-dissipation model is used to model the chemical reactions. The eddy-dissipation model assumes the chemical reactions are faster than the turbulence eddy transport, so the reaction rate is controlled by the flow motions.

The instantaneous gasification model can significantly reduce the computational time but can only provide a qualitative trend of gasification process. Although the instantaneous gasification model is crude, it catches the effect of thermal-fluid field (including turbulence structure) on chemical reactions, which are not readily available from the equilibrium method.

On the other hand, the particle combustion model provides a more accurate modeling of heterogeneous reaction by modeling the heat transfer and species transport. Due to its complex dealing of the heterogeneous combustion process intensive computational power is expected.

3.2.4.1 Instantaneous Gasification Model

The global instantaneous gasification mechanism is modeled to involve the following gaseous species: C, O_2, N_2, CO, CO_2, H_2O, C_6H_6, H_2 and volatiles ($CH_{2.121}O_{0.585}$) (Eq. 3.32 to Eq. 3.38). All of the species are assumed to mix in the molecular level. In this approach, carbon is modeled as a gas species based on the instantaneous gasification model describe above, and the complete combustion of carbon is modeled by a two-step reaction (Eq. 3.32 and Eq. 3.35). The mixing and transport of chemical species is modeled by solving the conservation equations describing convection, diffusion, and reaction sources for each component species. The species transport equations are solved by predicting the local mass fraction of each species, Yi, through the solution of a convection-diffusion equation for i-th species. The species transport equation in general form is given as:

$$\frac{\partial}{\partial t}(\rho Y_i) + \nabla \bullet (\rho \vec{v} Y_i) = -\nabla \bullet \vec{J}_i + R_i + S_i \tag{3.28}$$

Where R_i is the net rate of production of species i by chemical reaction. S_i is the rate of creation (a source term) from the dispersed phase. $\vec{J}_i$ is the diffusion flux of species i, which arises due to concentration gradients. Mass diffusion for laminar flows is given as

$$\vec{J}_i = -\rho D_{i,m} \nabla Y_i \tag{3.29}$$

For turbulent flows, mass diffusion flux is given as

$$\vec{J}_i = -\left(\rho D_{i,m} + \frac{\mu_t}{Sc_t}\right)\nabla Y_i \tag{3.30}$$

where Sc_t is the turbulent Schmidt number given as $\mu_t/\rho D_t$, where μ_t is the turbulent viscosity and D_t is the turbulent diffusivity.

The transport equations for each chemical species are

$$\frac{\partial}{\partial t}\left(\rho Y_C\right)+\nabla\cdot\left(\rho\vec{v}Y_C\right)=-\nabla\cdot\vec{J}_C+R_C \tag{3.31a}$$

$$\frac{\partial}{\partial t}\left(\rho Y_{O_2}\right)+\nabla\cdot\left(\rho\vec{v}Y_{O_2}\right)=-\nabla\cdot\vec{J}_{O_2}+R_{O_2} \tag{3.31b}$$

$$\frac{\partial}{\partial t}\left(\rho Y_{N_2}\right)+\nabla\cdot\left(\rho\vec{v}Y_{N_2}\right)=-\nabla\cdot\vec{J}_{N_2}+R_{N_2} \tag{3.31c}$$

$$\frac{\partial}{\partial t}\left(\rho Y_{CO}\right)+\nabla\cdot\left(\rho\vec{v}Y_{CO}\right)=-\nabla\cdot\vec{J}_{CO}+R_{CO} \tag{3.31d}$$

$$\frac{\partial}{\partial t}\left(\rho Y_{CO_2}\right)+\nabla\cdot\left(\rho\vec{v}Y_{CO_2}\right)=-\nabla\cdot\vec{J}_{CO_2}+R_{CO_2} \tag{3.31e}$$

$$\frac{\partial}{\partial t}\left(\rho Y_{H_2O}\right)+\nabla\cdot\left(\rho\vec{v}Y_{H_2O}\right)=-\nabla\cdot\vec{J}_{H_2O}+R_{H_2O} \tag{3.31f}$$

$$\frac{\partial}{\partial t}\left(\rho Y_{H_2}\right)+\nabla\cdot\left(\rho\vec{v}Y_{H_2}\right)=-\nabla\cdot\vec{J}_{H_2}+R_{H_2}. \tag{3.31g}$$

The reaction equations that need to be solved are given below.

$$C + ½\ O_2 \rightarrow CO \tag{3.32}$$

$$C + CO_2 \rightarrow 2CO \tag{3.33}$$

$$C + H_2O\ (g) \rightarrow CO + H_2 \tag{3.34}$$

$$CO + ½\ O_2 \rightarrow CO_2 \tag{3.35}$$

$$CO + H_2O\ (g) \rightarrow CO_2 + H_2 \tag{3.36}$$

$$CH_{2.121}O_{0.585} \rightarrow 0.585CO+0.853H_2+0.069C_6H_6 \tag{3.37}$$

(Volatile cracking)

$$C_6H_6+3O_2 \rightarrow 6CO+3H_2 \tag{3.38}$$

There are three approaches to solve these reactions.

(a) Eddy-dissipation model: The assumption in this model is that the chemical reaction is faster than the time scale of the turbulence eddies. Thus, the reaction rate is determined by the turbulence mixing of the species. The reaction is assumed to occur instantaneously when the reactants meet.

(b) Equilibrium model: The rate of chemical reaction is governed by the rate of mixing of gaseous oxidant and reactant. The reactions are fast compare to the time scale of turbulence. The gaseous properties become functions of the turbulent mixing rate and can be calculated using equilibrium considerations [Fletcher, 1983].

(c) Finite-rate reaction model: The rate of chemical reaction is computed using an expression that takes into account temperature and pressure and ignores the effects of the turbulent eddies.

In the homogeneous reaction simulation in this study, the reaction rate that appears as a source term, "R_i" in Eq. 3.28 is given by the eddy-dissipation model. The overall rate of reaction for the fastest burning fuels is controlled by turbulent mixing. The net rate of production of species i due to reaction r, $R_{i,r}$, is given by the smaller of the two given expressions below,

$$R_{i.r} = \nu'_{i,r} M_{w,i} A \rho \frac{\varepsilon}{\kappa} \min_R \left(\frac{Y_R}{\nu'_{R,r} M_{w,R}} \right) \tag{3.39}$$

$$R_{i.r} = \nu'_{i,r} M_{w,i} AB \rho \frac{\varepsilon}{\kappa} \frac{\sum_P Y_P}{\sum_j^N \nu''_{j,r} M_{w,j}} \tag{3.40}$$

Where,

Y_P is the mass fraction of any product species, P

Y_R is the mass fraction of a particular reactant, R

A is an empirical constant equal to 4.0

B is an empirical constant equal to 0.5

$\nu'_{i,r}$ is the stoichiometric coefficient for reactant i in reaction r

$\nu''_{j,r}$ is the stoichiometric coefficient for product j in reaction r

In the above Eqs. 3.39 and 3.40, the chemical reaction rate is governed by the large-eddy mixing time scale, κ/ε, and an ignition source is not required. This is based on the assumption that the chemical reaction is much faster than the turbulence mixing time scale, so the actual chemical reaction is not important.

The procedure to solve the reactions is as follows.

1. The net local production or destruction of species "i″ in each reaction is calculated by solving Eqs. 3.39 and 3.40.
2. The smaller of these values is substituted into the corresponding species transport Eq. 3.28 to calculate the local species mass fraction, Y_i.
3. Y_i is then used in Eq. 3.6 to calculate the net enthalpy production of each reaction equation.
4. The net enthalpy production becomes the source term in energy Eq. 3.3 that affects the temperature distribution. In an endothermic process, the net enthalpy production is negative, which becomes a sink term in the energy Eq. 3.3.

3.2.4.2 Finite Rate Model

In the finite-rate model, the reactions involve both homogeneous and heterogeneous reactions. The details of the two types of reactions are explained below.

Homogeneous Reaction

Finite-Rate/Eddy-Dissipation model is used to simulate the homogeneous reactions. Reaction rate based on the Laminar Finite-Rate Model and Eddy-Dissipation Model are calculated and compared. The minimum of the two results is used as the homogeneous reaction rate. The reason for taking the minimum reaction rate calculated from the eddy-dissipation model and finite rate model is, in practice, the Arrhenius rate acts as a kinetic "switch", preventing reaction before the flame holder; once the flame is ignited, the eddy-dissipation rate is generally smaller than the Arrhenius rate, and reactions are mixing-limited.

In this study, the homogeneous reactions are:

$$CO + 0.5O_2 \rightarrow CO_2 \quad (3.41)$$

$$CO + H_2O\ (g) \rightarrow CO_2 + H_2 \quad (3.42)$$

Where in equation (3.39) and (3.40), CO comes from the following carbon particle reactions:

$$C + 0.5O_2 \rightarrow CO \quad (3.43)$$

$$C + CO_2 \rightarrow 2CO \quad (3.44)$$

$$C + H_2O \rightarrow CO + H_2 \quad (3.45)$$

Which are modeled as the heterogeneous reactions described below.

Laminar Finite-Rate Model

The laminar finite-rate model computes the chemical source terms using Arrhenius expressions and ignores the effects of turbulent fluctuations. The net source of chemical species i due to reaction R_i (kg/m^3-s) is computed as the sum of the Arrhenius reaction sources over the N_R reactions that the species participate in, and is given as

$$R_i = M_{w,i} \sum_{r=1}^{N_R} \hat{R}_{i,r} \quad (3.46)$$

Where $M_{w,i}$ is the molecular weight of species i and $R_{i,r}$ is the Arrhenius molar rate of creation/destruction of species i in reaction r.

The r-th reaction can be written in a general form as

$$\sum_{i=1}^{N_R} \upsilon'_{i,r} M_i \underset{k_{b,r}}{\overset{k_{f,r}}{\Leftrightarrow}} \sum_{i=1}^{N} \upsilon''_{i,r} M_i \quad (3.47)$$

Where

N = number of chemical species in the system

$\upsilon'_{i,r}$ = stoichiometric coefficient for reactant i in reaction r

$\upsilon''_{i,r}$ = stoichiometric coefficient for product i in reaction r

M_i = symbol denoting species i

$k_{f,r}$ = forward rate constant for reaction r

$k_{b,r}$ = backward rate constant for reaction r.

The molar reaction of creation/destruction of species i in reaction r, which is $\hat{R}_{i,r}$ (kgmol/m^3-s) in equation (3.46), is given as

$$\hat{R}_{i,r} = \Gamma\left(\upsilon''_{i,r} - \upsilon'_{i,r}\right)\left(k_{f,r} \prod_{j=1}^{N_r} \left[C_{j,r}\right]^{\eta'_{j,r}} - k_{b,r} \prod_{j=1}^{N_r} \left[C_{j,r}\right]^{\eta''_{j,r}} \right) \tag{3.48}$$

Where,

N_r = number of chemical species in reaction r

$C_{j,r}$ = molar concentration of each reactant and product species j in reaction r (kgmol/m^3)

$\eta'_{j,r}$ = forward rate exponent for each reactant and product species j in reaction r

$\eta''_{j,r}$ = backward rate exponent for each reactant and product species j in reaction r.

Γ represents the net effect of third bodies on the reaction rate and is given by

$$\Gamma = \sum_{j}^{N_r} \gamma_{j,r} C_j \tag{3.49}$$

Where $\gamma_{j,r}$ is the third body efficiency of the j-th species in the r-th reaction.

The forward rate constant for reaction r, $k_{f,r}$, is computed using the Arrhenius expression

$$k_{f,r} = A_r T^{\beta} e^{-E_r/RT} \tag{3.50}$$

Where

A_r = pre-exponential factor (consistent unit)

β_r = temperature exponent (dimensionless)

E_r = activation energy for the reaction (J/kgmol)

R = universal gas constant (J/kgmol-K).

If the reaction is reversible, the backward rate constant, $k_{b,r}$, is computed from the forward rate constant using relation below

$$k_{b,r} = \frac{k_{f,r}}{K_r} \tag{3.51}$$

Where K_r is the equilibrium constant for the r-th computed from

$$K_r = \exp\left(\frac{\Delta S_r^0}{R} - \frac{\Delta H_r^0}{RT}\right)\left(\frac{p_{atm}}{RT}\right)^{\sum_{r=1}^{N_R}\left(\upsilon_{j,r}^{''} - \upsilon_{j,r}^{'}\right)} \tag{3.52}$$

Where, p_{atm} is the atmospheric pressure (101,325 Pa). The term within the exponential function represents the change in Gibbs free energy, and its components are computed as following,

$$\frac{\Delta S_r^0}{R} = \sum_{i=1}^{N}\left(\upsilon_{i,r}^{''} - \upsilon_{i,r}^{'}\right)\frac{S_i^0}{R} \tag{3.53}$$

$$\frac{\Delta H_r^0}{RT} = \sum_{i=1}^{N}\left(\upsilon_{i,r}^{''} - \upsilon_{i,r}^{'}\right)\frac{h_i^0}{R} \tag{3.54}$$

Where S_i^0 and h_i^0 are the standard-state entropy and standard-state enthalpy (heat of formation), respectively.

Heterogeneous Reaction

The particle reaction, R (kg/m^2-s), is expressed as

$$R = D_0 (C_g - C_s) = R_c(C_s)^N \tag{3.55}$$

Where

D_0 = bulk diffusion coefficient (m/s)

C_g = mean reacting gas species concentration in the bulk (kg/m^3)

C_s = mean reacting gas species concentration at the particle surface (kg/m^2)

R_c = chemical reaction rate coefficient (units vary)

N = apparent reaction order (dimensionless).

The concentration at the particle surface, C_s, is not known, so it is eliminated and the expression is recast as follows,

$$R = R_c\left[C_g - \frac{R}{D_0}\right]^N \tag{3.56}$$

This equation has to be solved by an iterative procedure, with the exception of the cases when N = 1 or N = 0. When N = 1, equation (3.56) can be written as

$$R = \frac{C_g R_c D_0}{D_0 + R_c} \tag{3.57}$$

In the cases of N = 0, if there is a finite concentration of reactant at the particle surface, the solid depletion rate is equal to the chemical reaction rate. If there is no reactant at the surface, the solid depletion rate changes abruptly to the diffusion-controlled rate.

The reaction stoichiometry of a particle undergoing an exothermic reaction in a gas phase is given as

particle species j (s) + gas phase species n $\rightarrow$ products.

Its reaction rate is given as

$$\overline{R}_{j,r} = A_p \eta_r Y_j R_{j,r} \tag{3.58}$$

$$R_{j,r} = R_{kin,r}\left(p_n - \frac{R_{j,r}}{D_{0,r}}\right)^{N_r} \tag{3.59}$$

where

$\overline{R}_{j,r}$ = rate of particle surface species depletion (kg/s)

A_p = particle surface area (m^2)

Y_j = mass fraction of surface species j in the particle

η_r = effectiveness factor (dimensionless)

$R_{j,r}$ = rate of particle surface species reaction per unit area (kg/m^2-s)

p_n = bulk partial pressure of the gas phase species (Pa)

$D_{0,r}$ = diffusion rate coefficient for reaction r

$R_{kin,r}$ = kinetic rate of reaction r (units vary)

N_r = apparent order of reaction r.

The effectiveness factor, r, is related to the surface area, and can be used in each reaction in the case of multiple reactions.

$D_{0,r}$ is given by

$$D_{0,r} = C_{1,r} \frac{\left[\left(T_p + T_\infty\right)/2\right]^{0.75}}{d_p} \tag{3.60}$$

Equation (3.60) is modification of relationship given by [Smith, 1982] by assuming negligible change in gas density.

The kinetic rate of reaction r is defined as

$$R_{kin,r} = A_p T^{\beta} e^{-(E_r/RT)} \tag{3.61}$$

The rate of particle surface species depletion for reaction order $N_r = 1$ is given by

$$\overline{R}_{j,r} = A_p \eta_r Y_j p_n \frac{R_{kin,r} D_{0,r}}{D_{0,r} + R_{kin,r}} \tag{3.62}$$

For reaction order $N_r = 0$,

$$\overline{R}_{j,r} = A_p \eta_r Y_j R_{kin,r} \tag{3.63}$$

3.2.4.3 Carbon Combustion Reaction Rates

Hurt and Mitchell (1992) investigated coal char combustion kinetics for ten US coals of various ranks. They observed that char reactivity decreased with increasing rank of the coal. Char reactivity decreases with increasing carbon content of the coal. The reactivity differences are more pronounced at low temperatures than at high temperatures. Hurt and Mitchell provided a char reactivity correlation, which is based on carbon content (coal rank) of the coal under conditions relevant to pulverized coal fired combustors.

Field (1968) conducted an experiment to measure rate of reaction $C(s) + \frac{1}{2} O_2 \rightarrow CO$. Gas temperature used by Field ranged from 1200 K to 1720 K at atmospheric pressure. Oxygen concentrations used ranged from 1% to 20%, and particle size ranged from 20 μm to 100 μm. The measured particle temperatures ranged from 1200 K to 2000 K.

It was assumed that the product formed inside char and on the surface of the char was carbon monoxide and that on average CO was transported to some distance from the particle before it could combine with oxygen to form carbon dioxide. The reaction rate was calculated from the weight loss of a char sample in a given transit time at a given oxygen concentration. An overall reaction rate coefficient is defined as the rate of removal of carbon per surface unit external surface area per unit atmosphere partial pressure of oxygen in the gas. Field found that the variation of the diffusional reaction rate coefficient was not strong. The experiment did not detect any effect of particle size on the reaction rate. The kinetic reaction rate was found to be $k = T (A+BT)$ where $A = -0.067$ m/(s-K) and $B = 5.26 \times 10^{-5}$ m/s-K^2.

Mayers (1934(a)) conducted an experiment to determine the rate of reaction $C(s) + CO_2 \rightarrow 2CO$, where graphite was used as the C. The experiment was conducted at atmospheric pressure. Mayers measured the reduction rate of CO_2. The effects of diffusion as the rate determining factor were eliminated by increasing the gas velocity across the particle surface, thus removing the concentration gradients.

The rate of reduction of CO_2 through the reaction appeared in two temperature ranges: (a) between 1125 K and 1225 K and (b) 1225 K and 1575 K. Mayers found that when CO_2 reacted with carbon at low temperatures ($T < 1250$ K), CO was formed at the same rate as that at which CO_2 disappeared. This is explained by the retention of half of the oxygen of the carbon dioxide by the graphite ($C + CO_2 \rightarrow CO + C\text{-}O_{solid}$). Mayers indicated that the CO_2 reduction rate at the high temperature range might be represented by two reactions: $C + CO_2 \rightarrow CO + C\text{-}O_{solid}$ and C-

$O_{solid} \rightarrow CO$, where the second reaction follows so rapidly on the first that there is no accumulation of C-O_{solid}. Thus the product of the CO_2 reduction is CO only. The CO_2 reduction rate is expressed in Arrhenius form $k = AT^n \exp(-E/RT)$ where n = 1.0, A = 4.4 m/s-K, and E = 1.62 x 10^{+8} J/kmol.

Mayers (1934(b)) conducted another experiment to measure the rate of $C(s) + H_2O(g) \rightarrow CO + H_2$, where graphite was used as the source of C, at atmospheric pressure in the temperature range of 1123-1433 K under conditions which eliminated the effects of diffusion as the rate determining process. Mayers found that the appearance CO and of CO_2 varied rather widely within the same temperature group, but their sum was found to be constant. The ratio CO/CO_2 of the products of reaction depends on the speed of the secondary reaction ($CO + H_2O \rightarrow CO_2 + H_2$) and on the time during which the mixture of gases remains in the heated zone. The rate of oxidation of carbon by steam appeared in temperature ranges 1133-1233 K and 1273-1433 K. Mayers reported that the rate of oxidation of C was of the same order of magnitude as the rate of appearance of C as CO when graphite was oxidized by CO_2. The kinetic reaction rate was found to be $k = AT^n \exp(-E/RT)$ where n = 1.0, A = 1.33 m/s-K, and E = 1.47 x 10^{+8} J/kmol.

In this study, three heterogeneous and two homogeneous reactions are modeled and their reaction rates are:

1. $C + 0.5O_2 \rightarrow CO$

   Rate coefficient: $R = A\,T^n \exp(-E/RT)$

   Where n = 0

   A = 92.32 kg/m^2-s

   E = 8.4x10^{+7} J/kmol.

The reaction rate is based on the work of Mann, A. P. and Kent, J. H. [1994]

2. $C + CO_2 \rightarrow 2CO$

   Rate coefficient: $R = A\,T^n \exp(-E/RT)$

   Where n = 0

   A = 23.3 kg/m^2-s

   E = 1.15x10^{+8} J/kmol.

The reaction rate is based on the work of Mann, A. P. and Kent, J. H. [1994]

3. $C + H_2O\,(g) \rightarrow CO + H_2$

   Rate coefficient: $R = A\,T^n \exp(-E/RT)$

Where n = 0

$A = 24.9\ kg/m^2\text{-}s$

$E = 1.125x10^{+8}$ J/kmol.

The reaction rate is based on the work of Mann, A. P. and Kent, J. H. [1994]

4. $CO + ½\ O_2 \rightarrow CO_2$

Rate coefficient: $R = A\ T^n \exp(-E/RT)$

Where n = 0

$A = 2.2x10^{+12}$

$E = 1.67x10^{+8}$ J/kmol.

The reaction rate is based on the work of Watanabe, H., and Otaka, M. [2006]

5. $CO + H_2O\ (g) \rightarrow CO_2 + H_2$

Rate coefficient: $R = A\ T^n \exp(-E/RT)$

Where n = 0

$A = 2.75x10^{+10}$

$E = 8.38x10^{+7}$ J/kmol.

The reaction rate is based on the work of Watanabe, H., and Otaka, M. [2006]

3.2.5 Boundary Conditions

Figure 3.3a and Fig. 3.3b shows the boundary conditions of the Preliminary Geometry (Case 3 in Ch. 5) and Fluidized Bed Mild Gasifier (Case 7 in Ch. 5) respectively. The detailed inlet conditions for heterogeneous (gas-solid) reaction with volatiles (Case 7 in Ch. 5) are given in Table 3.1.

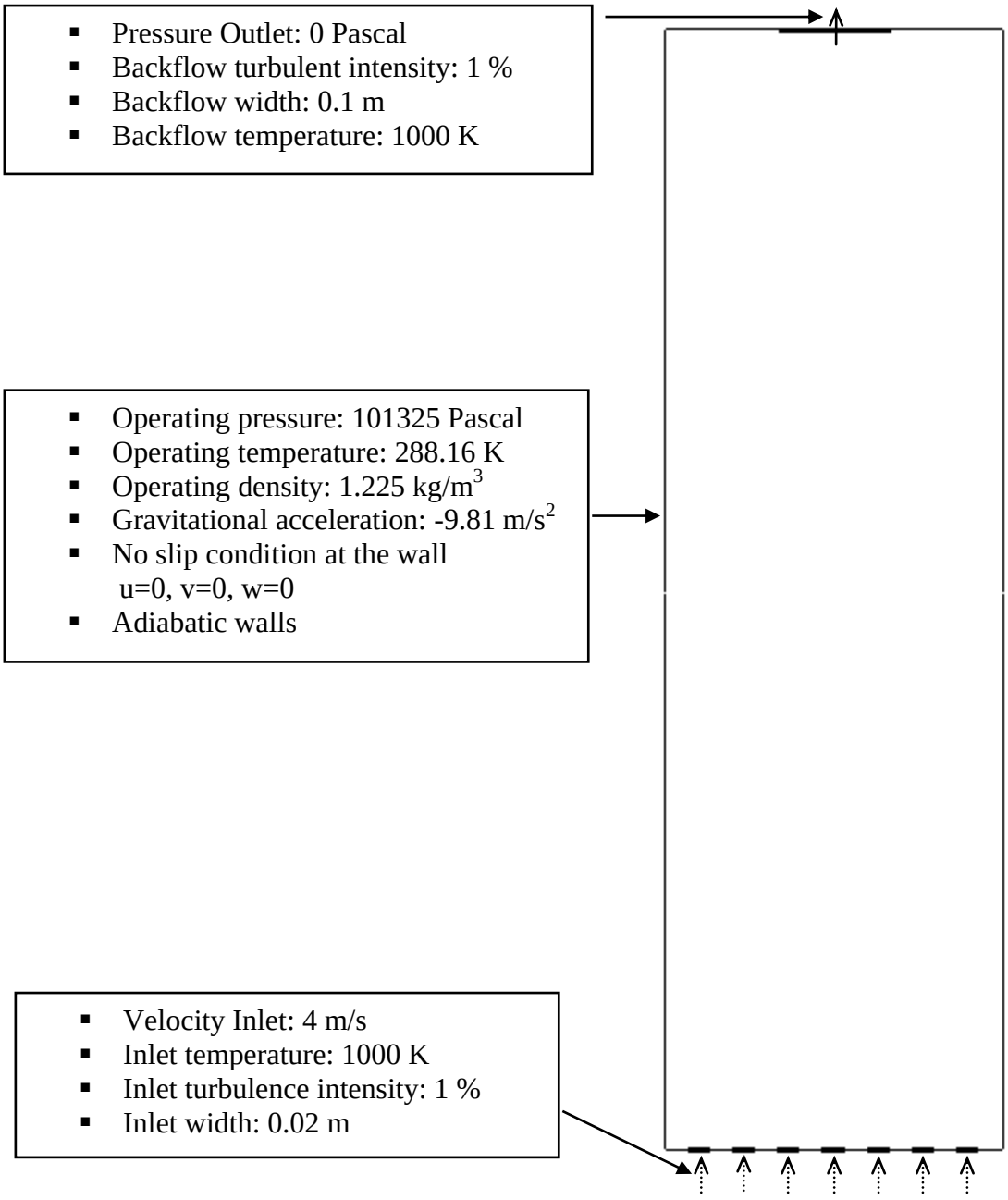

Figure 3.3a Boundary conditions of the Preliminary Geometry

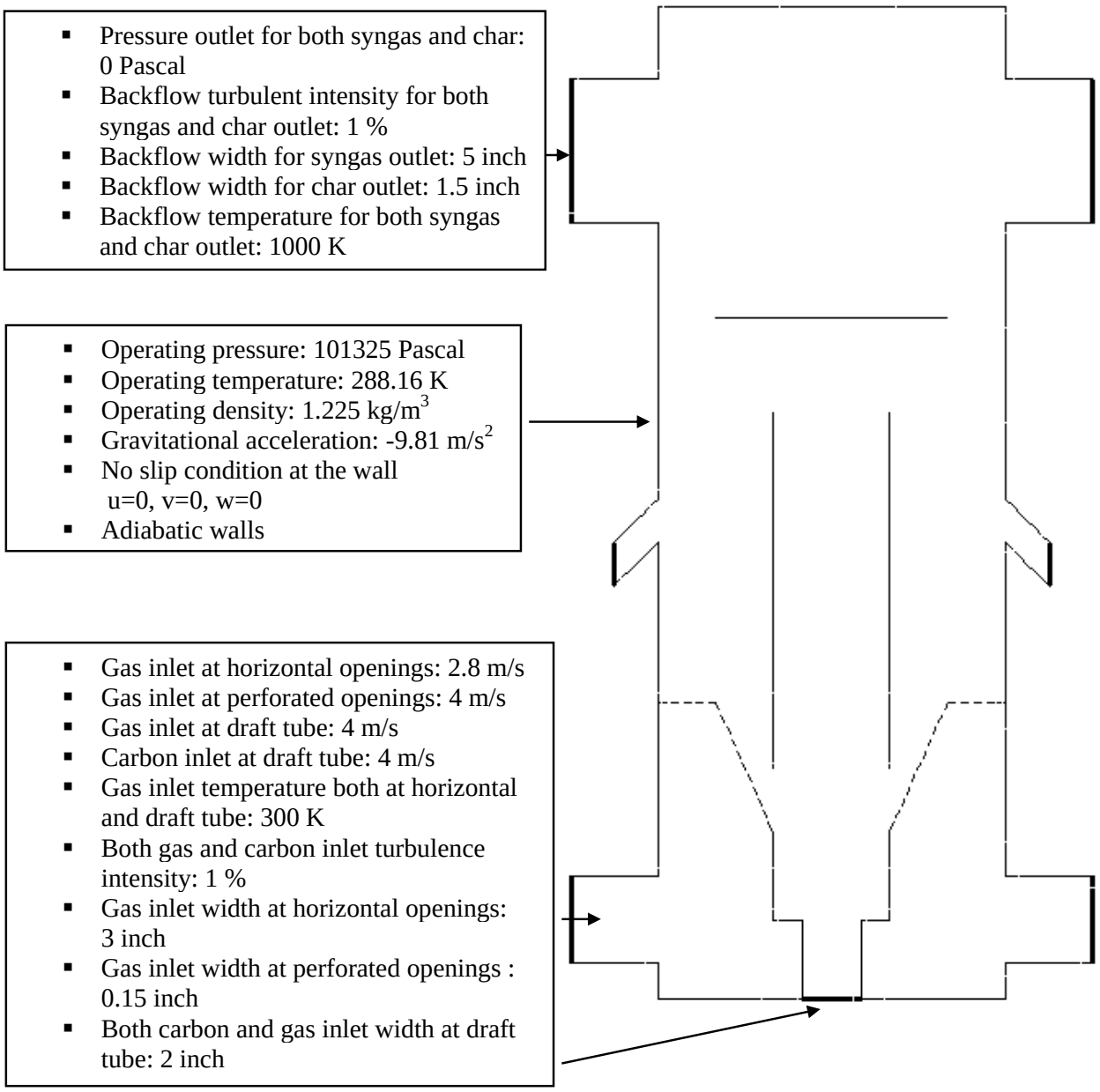

Figure 3.3b Boundary conditions of Fluidized Bed Mild Gasifier

Table 3.1 Parameters, inlet and operating conditions for heterogeneous (gas-solid) reaction with volatiles (Case 7 in Ch. 5)

Parameters	***Cases 7***	
Inlet position	Fluidized bed inlet	Draft tube inlet
Fuel	air	carbon solid, air, volatiles
Air inlet velocity at horizontal, m/s	2.8	
Air inlet velocity at perforated openings, m/s	4.0	
Air inlet velocity at draft tube, m/s		4.0
Carbon solid inlet velocity at draft tube, m/s		4.0
Inlet temperature, K	300	300
Mass fraction at inlet		
O_2	0.2331	0.12
N_2	0.7669	0.3946
$CH_{2.121}O_{0.585}$	0	0.4854
Operating pressure (pascal)	101325	101325
Operating temperature (K)	288.16	288.16
Operating density (kg/m^3)	1.225	1.225
Gravitational acceleration (m/s^2)	9.81	9.81
Wall temperature, K	Adiabatic	Adiabatic

It can be seen from Table 3.1 that carbon inlet velocity at draft tube is 4 m/s. The mass flow rate (kg/s) per unit depth of carbon is calculated below:

Mass flow rate of carbon of per unit depth = $\varepsilon_v \rho w V_{in}$ (w is the width of the inlet)

Where ε_v = volume fraction of carbon = 0.1

ρ = density of carbon = 2000 kg/m^3

w = 2 inch/unit depth = 0.0508 m^2/ m. The unit depth is chosen as 1 meter.

V_{in} = carbon inlet velocity = 4 m/s

Mass flow rate of carbon = 0.1 x 2000 x 0.0508 x 4 = 40.64 kg/s-m.

3.3 Computational Scheme

3.3.1 Solution Methodology

The major steps in the CFD simulation are divided into three: (a) preprocessing, (b) processing, and (c) post processing.

3.3.1.1 Preprocessing:

Preprocessing refers to the geometry generation, geometry mesh, model specifications and boundary specifications. Before any calculation can be done, computational domain has to be created. The commercial preprocessing software GAMBIT is used to generate and mesh geometries (computational domains). Quad meshes are used in the simplified 2-D domain. Once computational domain geometry has been meshed in GAMBIT, it is imported into the commercial CFD code ANSYS FLUENT R12.0 from ANSYS, Inc. Then, the appropriate models and boundary conditions are set.

3.3.1.2 Processing:

In the processing step, calculations are performed to obtain the solution for the governing equations. ANSYS FLUENT is a finite-volume based CFD solver written in language "C" and has the ability to solve fluid flow, heat transfer and chemical reactions in complex geometries and supports both structured and unstructured mesh. The solution is obtained through iteration until convergence criteria, which are set by the user, are satisfied. Residuals are used as means to determine the convergence. Residuals are the imbalanced errors in the governing equations over all the cells in the computational domain.

3.3.1.3 Post processing:

Post processing involves analyzing and interpreting solution obtained. Charts and various visualization schemes can be employed to aid in understanding the physics of the solution. The results are presented in the form of x-y plots, contour plots (e.g. temperature contour), velocity vector plots, streamline plots, and animations via the built-in plotting software in ANSYS/Fluent or the third part software, Tecplot.

3.3.2 Computational Grid

The geometry is generated and meshed in GAMBIT Version 2.4.6. 2-D structured mesh is used for meshing the simplified Preliminary Geometry as well as the 2-D Fluidized Bed Mild Gasifier (Fig. 3.4 and Fig. 3.5 respectively). In this study, a total of 18,750 cells are employed for simplified preliminary geometry and initially 6,960 cells for Fluidized Bed Mild Gasifier are employed, followed by denser grids of 30,876 (Fig. 3.5b) and 65,355 (Fig. 3.5c) meshes for the final case (Case 7). After the model has been meshed, it is exported to ANSYS FLUENT R12.0.

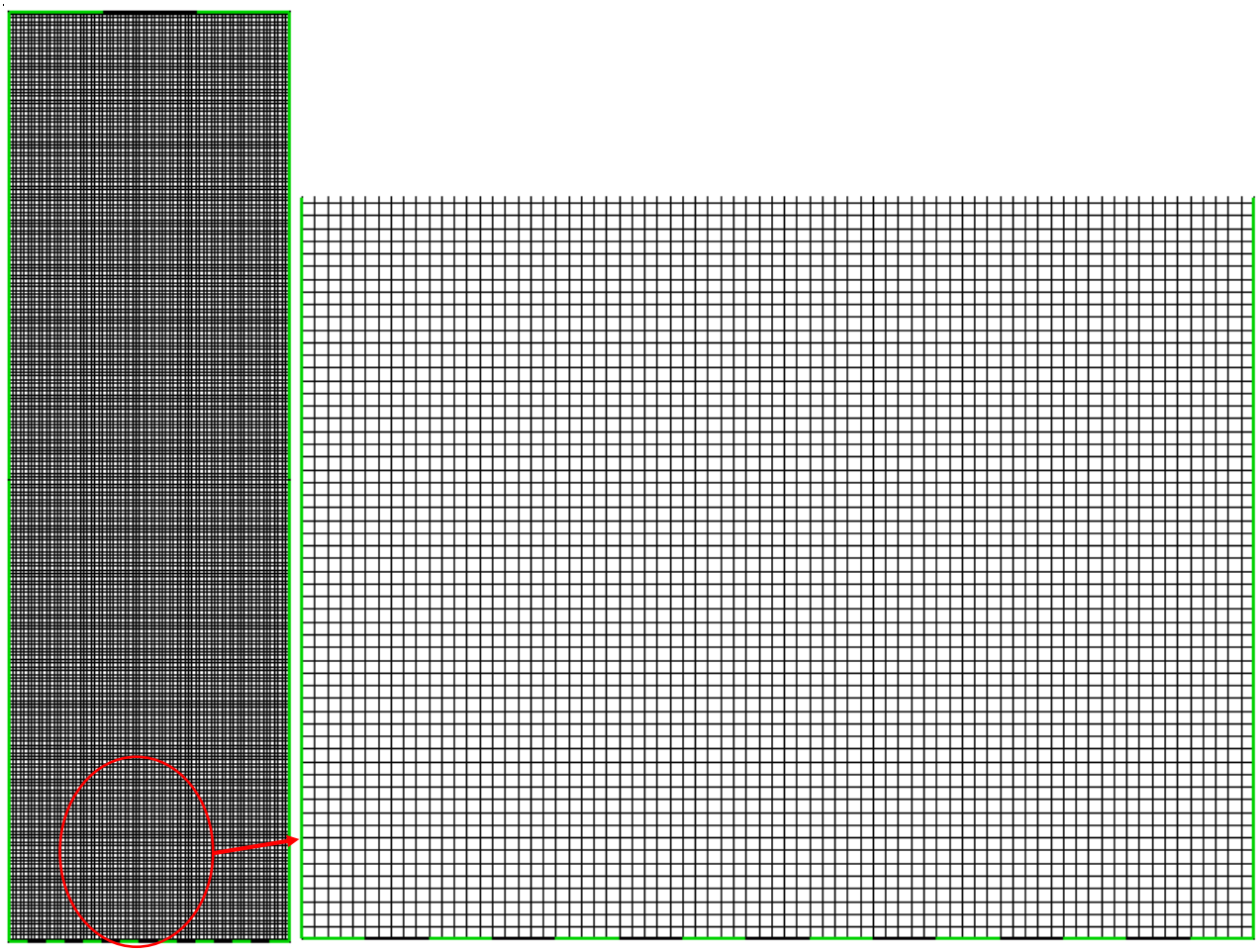

Figure 3.4 2D structured meshes (18,750 cells) of the simplified preliminary geometry

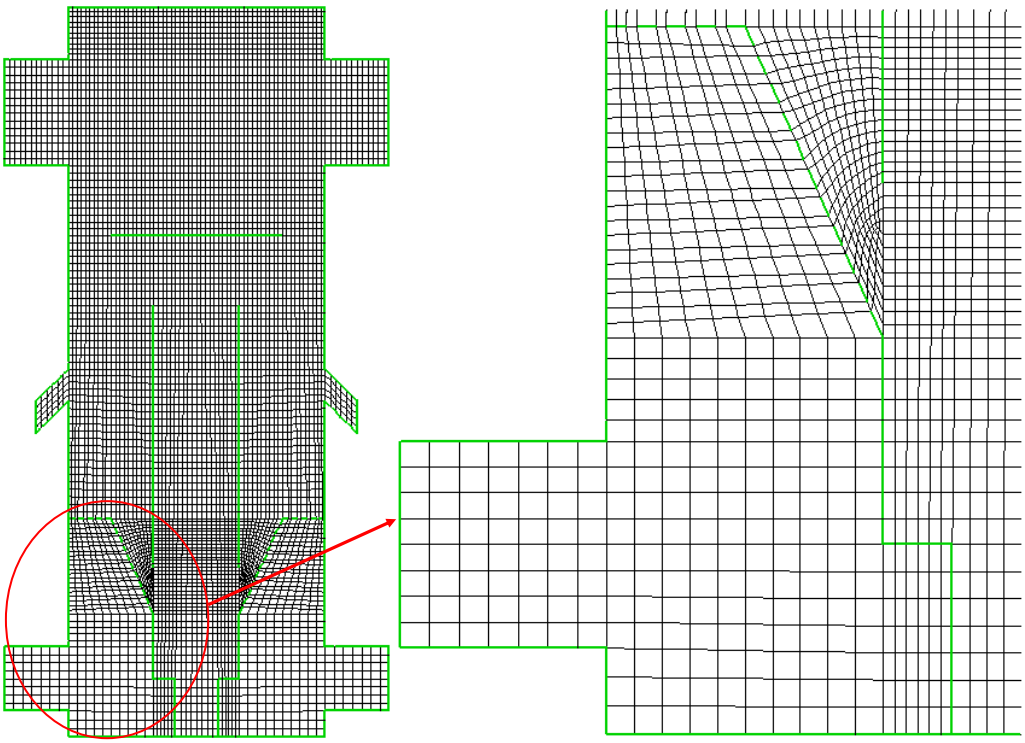

Figure 3.5a 2D structured meshes (6,960 cells) of Fluidized Bed Mild Gasifier

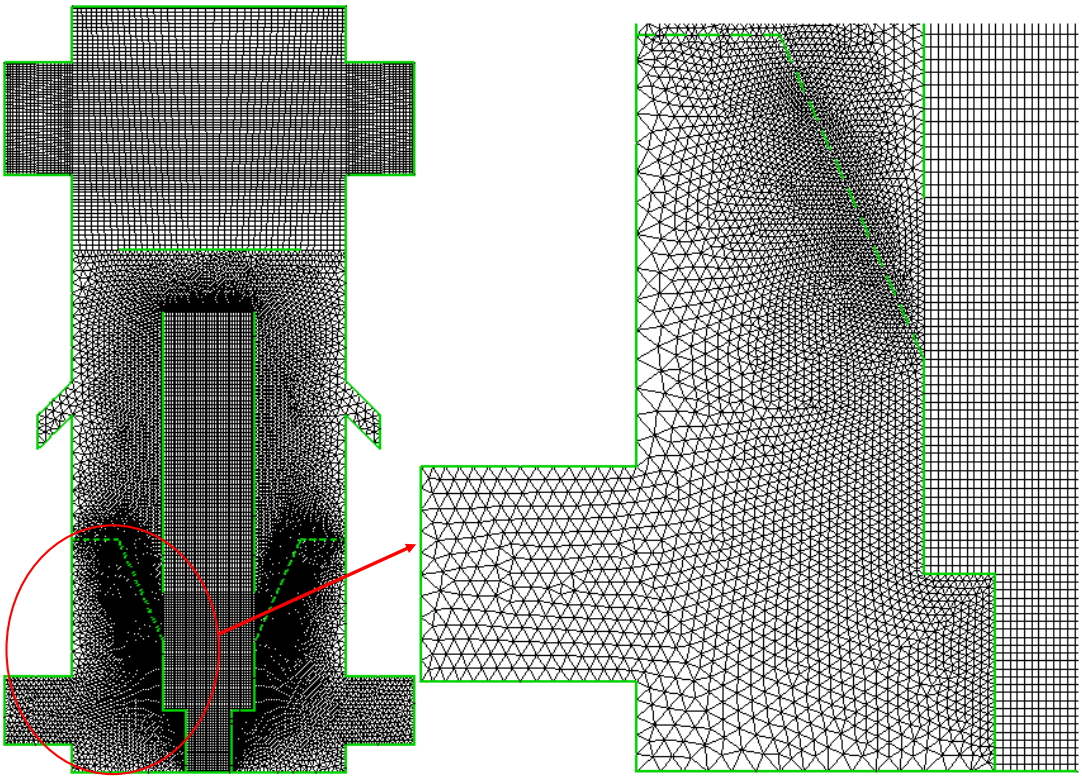

Figure 3.5b 2D both structured and unstructured meshes (30,876) of Fluidized Bed Mild Gasifier

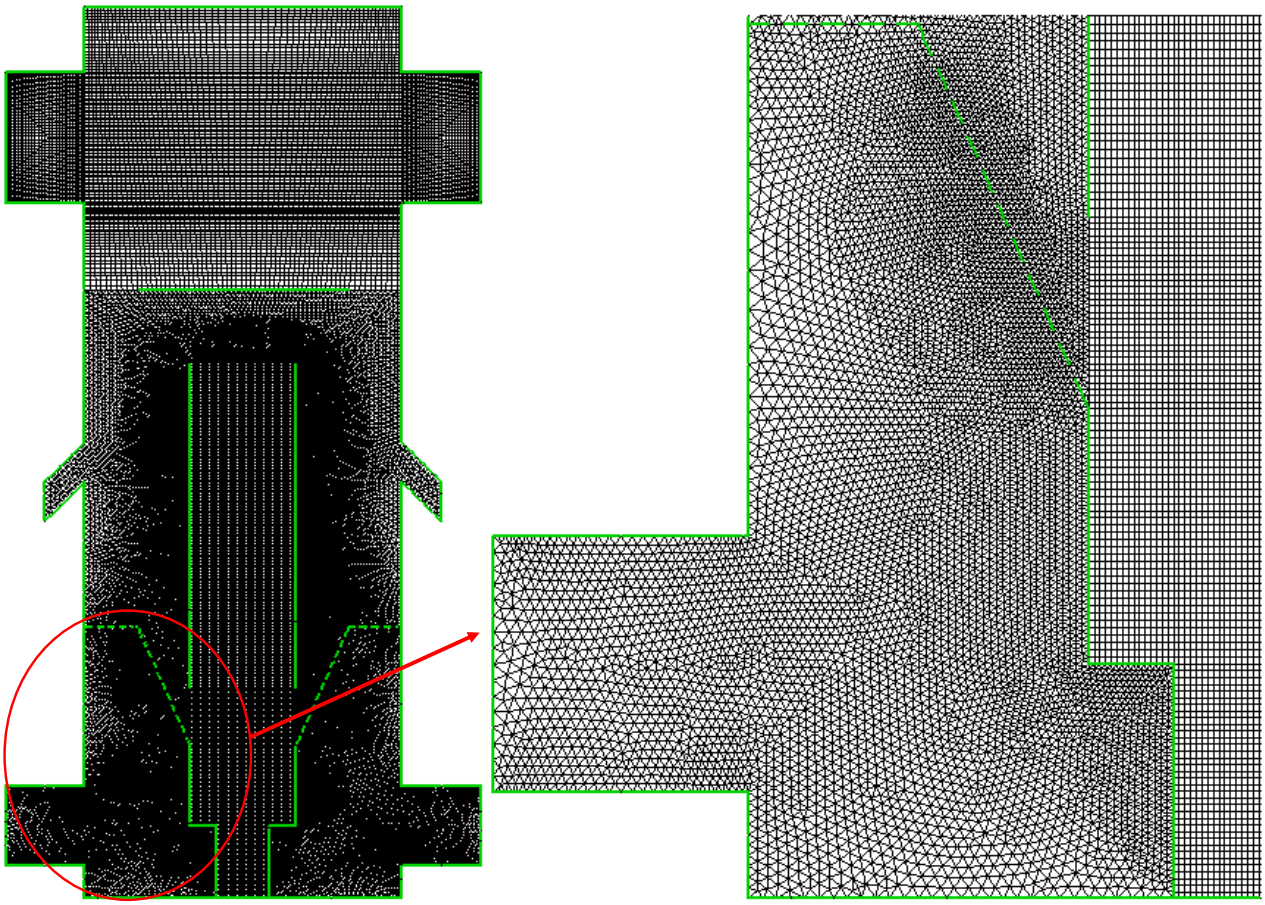

Figure 3.5c 2D both structured and unstructured (65,355 cells) of Fluidized Bed Mild Gasifier

3.3.3 Numerical Procedure

The procedure for performing the simulation in ANSYS FLUENT 12.0 is outlined below,

1. Create and mesh the geometry model using GAMBIT
2. Import geometry into ANSYS FLUENT 12.0
3. Define the solver model
4. Define the turbulence model
5. Define the species model
6. Define the materials and the chemical reactions
7. Define phases: primary and secondary phase
8. Define phase Interaction such as drag force, heterogeneous reaction etc.
9. Define the boundary conditions
10. Define region adaptation and patching

11. Initialize the calculations
12. Iterate/calculate until convergence is achieved
13. Post processes the results.

ANSYS FLUENT 12.0 offers two solution methods: (a) Pressure based solution method and (b) Density based solution method. Pressure based solution method solves the governing equations of continuity, momentum, energy, and species transport equations sequentially. In the Pressure based solution, the non-linear governing equations are **implicitly** linearized, which means that each unknown value is computed using a relation that includes both existing and unknown values from neighboring cells. As a result, each unknown will appear in more than one equation in the linear system produced. Thus, these equations must be solved simultaneously in order to obtain the unknown quantities.

The non-linear governing equations can also be linearized **explicitly** with respect to the dependent variables. If linearized explicitly, the unknown value in each cell is computed using a relation that includes only existing values.

The governing equations are discretized spatially to yield discrete algebraic equations for each control volume. There are several discretization schemes available in ANSYS FLUENT:

(a) First Order

(b) Second Order

(c) Power Law and

(d) QUICK

The second order scheme is used as the discretization scheme for momentum, turbulence kinetic energy "k" and dissipation rate "ε", energy, species equations. Volume fraction of solid phase uses the QUICK scheme. ANSYS FLUENT also provides three algorithms for pressure-velocity coupling in the Pressure Based solver:

(a) SIMPLE

(b) SIMPLEC and

(c) PISO

The SIMPLE algorithm (Patankar et. al, 1980) is used in this study to couple the pressure and velocity. The built-in standard k-ε turbulence model is used, and the model constants $C_{1\varepsilon}$, $C_{2\varepsilon}$, C_{μ}, σ_k and σ_t have the following values,

$C_{1\varepsilon} = 1.44$, $C_{2\varepsilon} = 1.92$, $C_{\mu} = 0.09$, $\sigma_k = 1.0$, and $\sigma\varepsilon = 1.3$.

The following boundary conditions on the surface geometry have been assigned in GAMBIT.

a. **Velocity inlet:** All the inlet surfaces are defined as velocity inlets. The velocity, temperature, and the mass fractions of all species of the gas mixture are specified.
b. **Pressure outlet:** The outlet surface is assigned as a pressure outlet boundary. Pressure, temperature, and species mass fractions of the gas mixture just downstream of the outlet (outside the domain) are specified. This information does not affect the calculations inside the computational domain but will be used if backflow occurs at the outlet.
c. **Walls**: The outside surfaces are defined as wall boundary. The walls are stationary with no-slip condition imposed (zero velocity) on the surface. For adiabatic case, the heat flux on the wall is set to "0" (zero). For constant wall temperature, the wall temperature of a certain constant value is specified.

The primary phase enters the computational domain through the inlets. The iterations are conducted alternatively between the primary and the secondary phases. The primary phase is updated in the next iteration based on the secondary phase calculation results, and the process is repeated.

The detailed steps of the calculation process are given below. Figure 3.6 depicts the flow chart of these steps.

(i) Fluid properties are updated based on the current solution or the initialized solution.
(ii) The momentum equations are solved using the current values of pressure and face mass fluxes to get the updated velocity field.
(iii) Equation for the pressure correction is calculated from the continuity equation, and the linearized momentum equations since the velocity field obtained in step (ii) may not satisfy the continuity equation.
(iv) The pressure correction equations obtained from step (iii) are solved to correct the pressure and velocity fields, and face mass such that the continuity equation is satisfied.
(v) The equations for turbulence are solved using the updated values of the other variables.

(vi) The homogeneous gas phase reactions are solved. Production and consumptions of each species are calculated.

(vii) Enthalpy changes due to reaction are calculated.

(viii) The species transport equations are solved. Changes in the species mass fraction due to reactions in steps (vi) and (xii) appear as source or sink terms in the species transport equation.

(ix) The energy equation is solved. This includes source or sink terms due to reactions in steps (vi) and (vii).

(x) Forces on the particles (secondary phase) such as drag force, lift force, virtual mass force are calculated.

(xi) Particles (secondary phase) heat transfer are calculated.

(xii) Heterogeneous reactions (gas-solid) are calculated. Production and consumptions of each species are calculated.

(xiii) Enthalpy changes due to reaction are calculated.

(xiv) The species transport equations are solved. Changes in the species mass fraction due to reactions in steps (xii) appear as source or sink terms in the species transport equation.

(xv) The energy equation is solved. This includes source or sink terms due to reactions in steps (xiii) and (xiv).

(xvi) Primary phase properties are updated based on the secondary phase.

(xvii) The equation is checked for convergence.

(xviii) If convergence criteria are met, the process is stopped. Otherwise, the process is repeated from step (i).

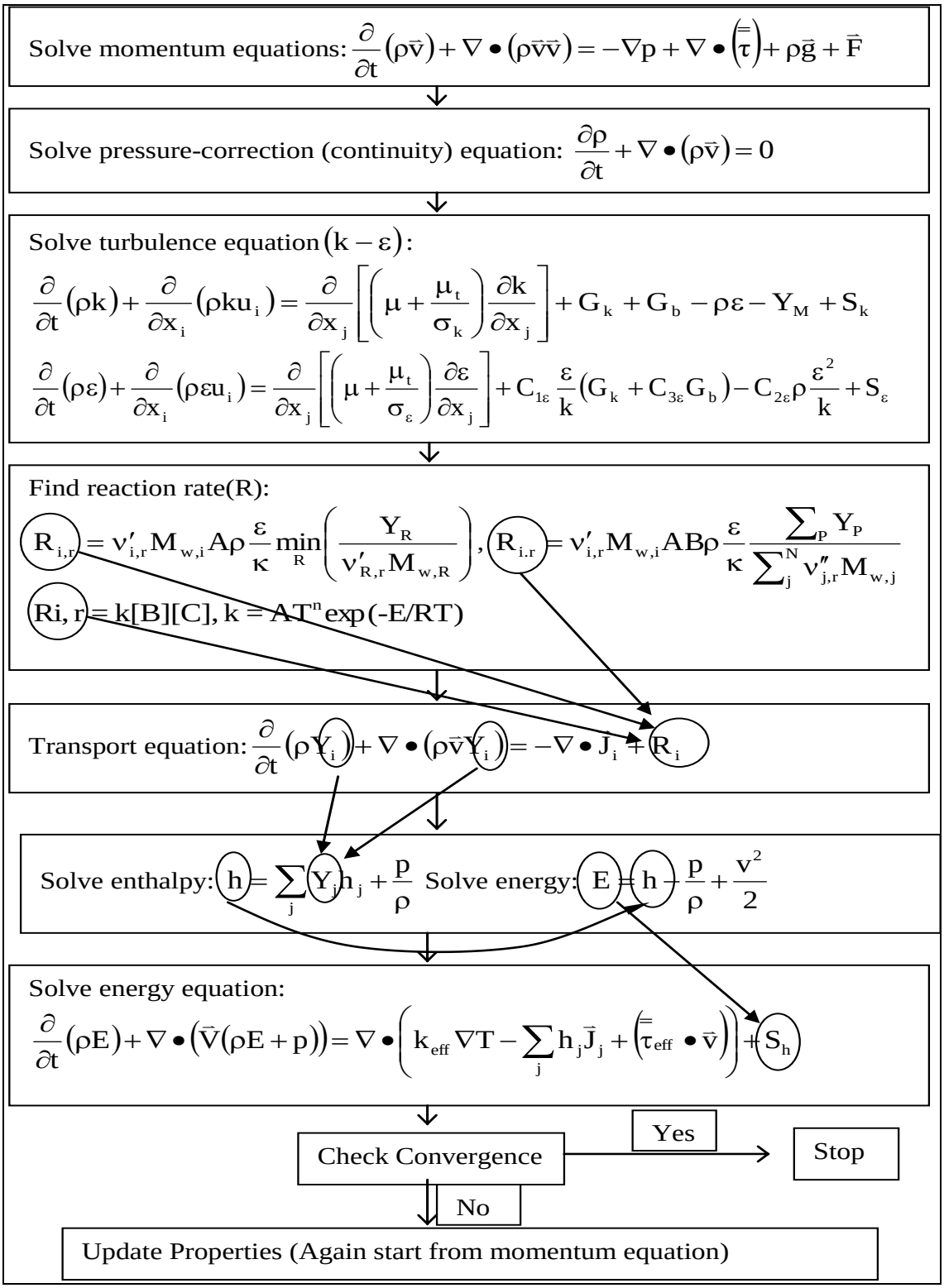

Figure 3.6 Outline of numerical procedures for the gaseous (primary) phase. The heterogeneous reaction (secondary) follows the similar process. Iterations proceed alternately between the primary and secondary phases.

3.3.4 Convergence Criterion

There are no universal metrics for judging convergence. Convergence can be hindered by a number of factors including the numbers of computational cells, under-relaxation factors, and complex flow physics. In this study, the convergence criterion of 10^{-3} for the residuals continuity, momentum, energy for gas and solid phase, turbulence kinetic energy "k" and dissipation rate "ε", species equations, and volume fraction of solid phase are chosen for the transient case.

For the ultimate case (Case 7: Heterogeneous reactions), the solution convergence is obtained by monitoring the residuals of the continuity, momentum, energy for gas and solid phase, turbulence, species equations, and volume fraction of solid phase separately:

- ✓ Continuity (mass conservation) < 8×10^{-1}
- ✓ X-velocity of gas phase < 6×10^{-3}
- ✓ X-velocity of solid phase < 3×10^{-6}
- ✓ Y-velocity of gas phase < 6×10^{-3}
- ✓ Y-velocity of solid phase < 2×10^{-6}
- ✓ Energy of gas phase < 5×10^{-4}
- ✓ Energy of solid phase < 5×10^{-7}
- ✓ k (turbulence energy) < 6×10^{-4}
- ✓ ε (turbulence dissipation) < 6×10^{-4}
- ✓ O_2 < 3×10^{-5}
- ✓ CO < 7×10^{-4}
- ✓ CO_2 < 7×10^{-4}
- ✓ H_2 < 7×10^{-4}
- ✓ H_2O < 5×10^{-5}
- ✓ Volume fraction of solid phase < 1×10^{-4}

Figure 3.7 shows the residuals for the transient ultimate case (Case 7: Heterogeneous reactions). The fluctuations in the residuals' history is not caused by instability of computation oscillations, rather it is a typical feature caused by alternating iterations between the solid and gas phases.

Physical iteration time step size is 1 x 10^{-4} seconds. Typically, 40,000 time steps is required to achieve convergence with 20 iteration in each time step. Somehow the computation does not work in the 32- node parallel processing cluster, but it only works on the following two systems:

- ✓ 2 x Pentium Core 2 Duo 2.53GHz with 4GB RAM computers parallel processing requires approximate 145 hours (6 days).
- ✓ 1 x Pentium Core 2 Quad 2.66GHz with 4GB RAM computer requires approximate 100 hours (4 days).

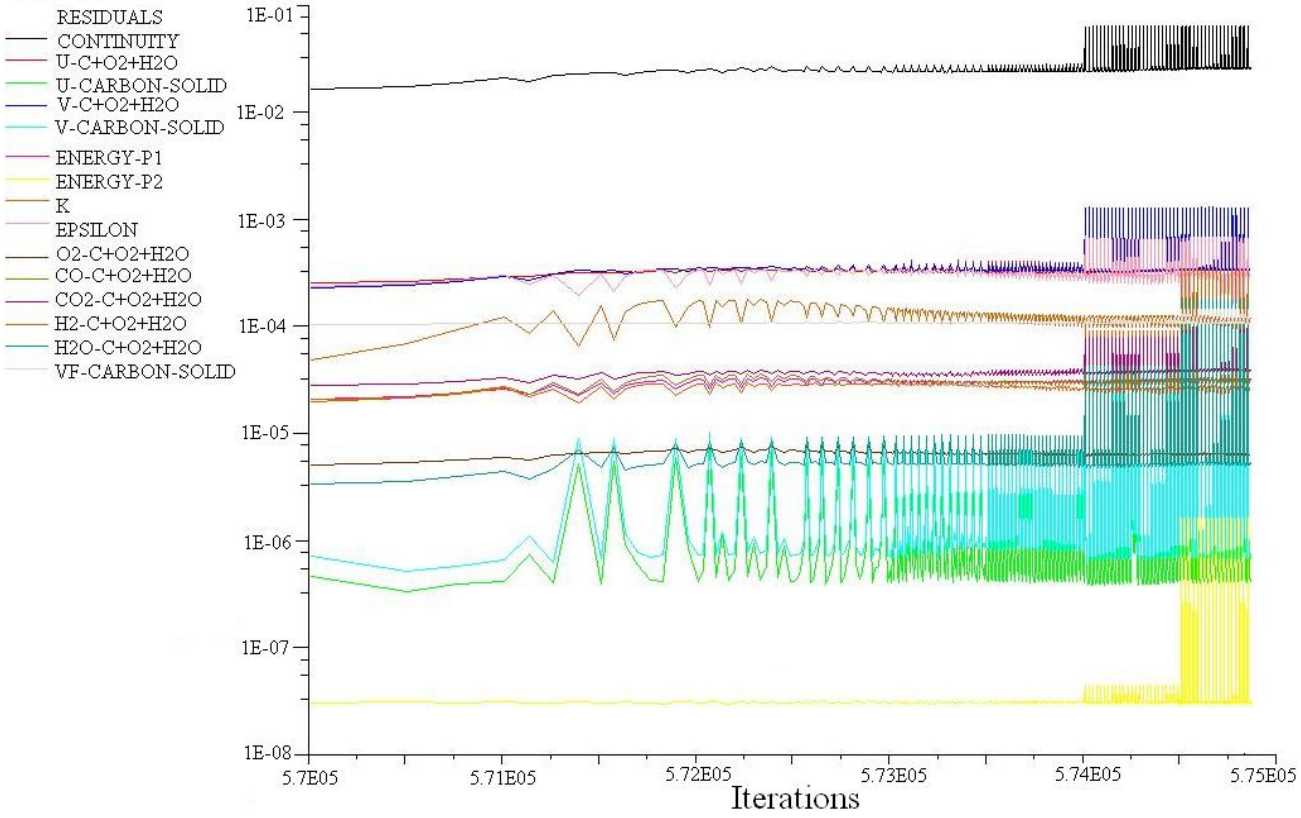

Figure 3.7 Residuals for the transient ultimate case (Case 7: Heterogeneous reactions). The fluctuations in the residuals' history is not caused by instability of computation oscillations, rather it is a typical feature caused by alternating iterations between the solid and gas phases.

Material properties:

Variable properties for enthalpy, specific heat and conductivity are used for each species. The specific heat is calculated using piecewise-polynomial relation as a function of temperature defined as,

$$\text{For } T_{min1} < T < T_{max1},\ F(T) = A_1T + A_2T^2 + A_3T^3 + \ldots$$
$$\text{For } T_{min2} < T < T_{max2},\ F(T) = B_1T + B_2T^2 + B_3T^3 + \ldots \quad (3.64)$$

The specific heat of the primary phase, which is a mixture of species, is also variable and is calculated as a mass fraction average of the individual species heat capacities, defined as

$$F = \sum_i Y_i F_i \quad (3.65)$$

Where F is the property (enthalpy, specific heat, or conductivity), Y_i is the mass fraction of species i and F_i is the property of species i.

Patching temperature:

The initial gas temperature in the gasifier is set the same as the gas temperature at inlets, which is 300 K in this study. Gasification will not occur at this temperature. The energy at this temperature is below the activation energy of the reactions; thus the reactions will not occur. High temperature is needed to start the reactions. Thus, the domain needs to be patched with high temperature. This process is akin to using a lighter to ignite combustion inside a combustor. This temperature patching is done by setting the temperature of the cells near the injections to 1000 K, which is high enough to start the reactions.

Under-relaxation factor:

The under-relaxation factor for variables can help convergence behavior of the variables. Equation 3.66 defines how the under-relaxation factor, α, affects the value of the variable.

$$\phi = \phi_{old} + \alpha\, \Delta\phi \quad (3.66)$$

ϕ is the variable and $\Delta\phi$ is the change in the variable. The value of under-relaxation factor, α, ranges from 0 to 1; therefore the smaller the under-relaxation factor -- the smaller the change in the variable during the iteration. It can help stabilize the convergence but requires more iteration steps to reach convergence. In this study, the under-relaxation factors are set to 0.3 for pressure, 0.7 for momentum, 0.2 for volume fraction of secondary phase, and 0.8 for species, k and ε.

CHAPTER FOUR
MODELING MULTIPHASE FLOWS

4.1 Introduction

In nature a large number of flows encounter mixtures of phases. The physical phases of matter are gas, liquid, and solid, but the concept of phase in a multiphase flow is different and it applied in a broader sense. In multiphase flows, a phase is defined as an identifiable class of material that has a particular inertial response and interaction with the flow in which it is immersed. For example, different-sized solid particles of the same material treated as different phases as each collection of particles with the same size will have a similar dynamical response to the flow field.

4.2 Multiphase Flow Regimes

Multiphase flow regimes can be grouped into four categories:

a. Gas-liquid or liquid-liquid flows
b. Gas-solid flows
c. Liquid-solid flows and
d. Three-phase flows

a. Gas-Liquid or Liquid-Liquid Flows

The following regimes are known as gas-liquid or liquid-liquid flows:

- ✓ Bubbly flows: This is the flow of fluid bubbles or discrete gaseous in a continuous fluid. Example: absorbers, aeration, air lift pumps, cavitations, evaporators, flotation, and scrubbers.
- ✓ Gas-droplet flows: This is the flow of discrete fluid droplets in a continuous gas. Example: atomizers, combustors, cryogenic pumping, dryers, evaporation, gas cooling, and scrubbers.
- ✓ Slug flows: This is the flow of large bubbles in a continuous fluid. Example: large bubble motion in pipes or tanks.
- ✓ Stratified/free-surface flow: This is the flow of immiscible fluids separated by an interface. Example: sloshing in offshore separator devices and boiling and condensation in nuclear reactors.

b. Gas-Solid Flows

The following regimes are known as gas-solid flows:

- ✓ Gas-particle flows: This is the flow of discrete particles in a continuous gas. Example: cyclone separators, air classifiers, dust collectors and dust-laden environmental flows.
- ✓ Pneumatic transport: This is the flow that depends on solid loading, Reynolds numbers, and particle properties. Example: transport of cement, grains, and metal powders.
- ✓ Fluidized bed: This consists of a vertical cylinder containing particles, into which a gas is introduced through a distributor and raising the bed of particles. Depending on the gas flow rate, bubbles appear and rise through the bed, intensifying the mixing within the bed. Example: fluidized bed reactors, fluidized bed boiler, fluidized beds gasifier and fluidized beds combustors.

c. Liquid-Solid Flows

The following regimes are known as liquid-solid flows:

- ✓ Slurry flows: This flow is the transport of particles in liquids. Example: slurry transport and mineral processing.
- ✓ Hydro-transport: This is the flow that describes densely-distributed solid particles in a continuous liquid. Example: mineral processing and biomedical and physiochemical fluid systems.
- ✓ Sediment transport: This is the flow that describes a tall column initially containing a uniform dispersed mixture of particles. At the bottom, the particles will slow down and form a sludge layer. Example: mineral processing.

d. Three-Phase Flows

Three-phase flows are combinations of the other flow regimes listed above.

- ✓ Bubbles in a slurry flow
- ✓ Droplets/particles in gaseous flows

4.3 Approaches of Multiphase Modeling

Two approaches are generally considered for simulating multiphase flows:

1. The Euler-Lagrange approach and
2. The Euler-Euler approach

4.3.1 Euler-Lagrange Approach

In the Euler-Lagrange approach, the fluid phase is treated as a continuum by solving the time-averaged Navier-Stokes equations, while the dispersed phase is solved by tracking a large number of particles, bubbles, or droplets through the calculated flow field. The dispersed phase exchange momentum, mass, and energy with the fluid phase. In this model, the fundamental assumption is that even though high mass loading is acceptable, the dispersed phase occupies a low volume fraction. During the fluid phase calculation, the particle or droplet trajectories are computed individually at particular intervals. This makes the model appropriate for the modeling of spray dryers, coal and liquid fuel combustion, and some gas-particle flows. This model is inappropriate for the modeling of fluidized beds, liquid-liquid mixtures, or any application where the volume fraction of the second phase is not negligible.

4.3.2 Euler-Euler Approach

In the Euler-Euler approach, the different phases are treated mathematically as interpenetrating continua. The concept of phasic volume fraction is introduced in this approach. These volume fractions are assumed to be continuous functions of space and time and their sum is equal to one. For each phase, conservation equations are derived to obtain a set of equations which have similar structure for all phases. These equations are closed by providing constitutive relations that are obtained from empirical information, or, in the case of granular (solid) flows, by application of kinetic theory. The three different Euler-Euler multiphase models are following

1. The volume of fluid (VOF) model
2. The mixture model
3. The Eulerian model

The Eulerian model of Euler-Euler approach is used in this study. The detailed description of this model is presented later section in this chapter.

4.3.2.1 The Volume of Fluid (VOF) Model

The volume of fluid (VOF) model is a surface-tracking technique applied to a fixed Eulerian mesh. It is designed for two or more immiscible fluids. In the VOF model, a single set of momentum equations is shared by the fluids, and the volume fraction of each of the fluids in each computational cell is tracked throughout the domain. The applications of the VOF model

are stratified flows, free-surface flows, the motion of large bubbles in a liquid, the prediction of jet breakup (surface tension), the steady or transient tracking of any liquid-gas interface etc.

4.3.2.2 The Mixture Model

The mixture model is designed for two or more phases (fluid or particulate). The mixture model solves for the mixture momentum equation and prescribes relative velocities to describe the dispersed phases. The applications of the mixture model are gas-particle flows with low loading, bubbly flows, sediment transport, cyclone separators etc. The mixture model is also used to model homogeneous multiphase flow with strong coupling without relative velocities for the dispersed phases. In addition, the mixture model can be used to calculate non-Newtonian viscosity. This model is suitable for flows in which the dispersed-phase volume fractions are less than or equal to 10%.

4.3.2.3 The Eulerian Model

The Eulerian model is the most complex multiphase models. This model allows for the modeling of multiple separate, yet interacting phases. The phases can be liquids, gases, or solids in nearly any combination. Any number of secondary phases can be modeled by this multiphase model, if sufficient memory is available. It solves a set of "n" momentum and continuity equations for each phase. There is a coupling between the pressure and inter-phase exchange coefficients in this model. The applications of the Eulerian multiphase model are bubble columns, risers, particle suspension, and **fluidized beds**.

In comparisons of above three model of Euler-Euler approach, the volume of fluid (VOF) model is suitable for stratified or free-surface flows, and the mixture and Eulerian models are appropriate for flows in which the phases mix or separate and/or dispersed-phase volume fractions exceed 10%.

Consider the following guidelines, to choose between the mixture model and the Eulerian model:

- ✓ If there is a wide distribution of the dispersed phases, the mixture model is more preferable than Eulerian model as it is less computationally expensive.

- ✓ If inter-phase drags laws that are applicable to the system, the Eulerian model give more accurate results than the mixture model. If the inter-phase drag laws are unknown or their applicability to the system is open to discussion, the mixture model is a better choice.
- ✓ To solve a simpler problem, the mixture model is a better choice, since it solves a smaller number of equations which requires less computational effort than the Eulerian model. If accuracy is more important than computational effort, the Eulerian model is a better choice.

4.4 Eulerian Multiphase Model Theory

The detailed descriptions of Eulerian multiphase model are presented here because this model is used in this study. A single set of conservation equations for momentum, continuity and energy is solved in a single-phase model. To change from a single-phase model to a multiphase model, additional sets of conservation equations have to be introduced. The modifications involve the introduction of the volume fractions "ε" for the multiple phases and the exchange mechanisms of momentum, heat, and mass between the phases.

4.4.1 Conservation Equations using Eulerian Multiphase Model

The equations for conservation of mass, momentum, and energy using in Eulerian multiphase model are presented below:

Conservation of Mass

The continuity equation for phase "q" is

$$\frac{\partial}{\partial t}\left(\varepsilon_q \rho_q\right)+\nabla \bullet \left(\varepsilon_q \rho_q \vec{v}_q\right)=\sum_{p=1}^{n}\left(\dot{m}_{pq}-\dot{m}_{qp}\right)+S_q \qquad (4.1)$$

Where, $\vec{v}_q$ = the velocity of phase "q"

$\dot{m}_{pq}$ = the mass transfer from phase "p" to "q"

$\dot{m}_{qp}$ = the mass transfer from phase "q" to "p"

ε_q =the volume fraction of phase "q"

S_q =the source term of phase "q"

Conservation of Momentum

The momentum balance for phase "q" is

$$\frac{\partial}{\partial t}\left(\varepsilon_q \rho_q \vec{v}_q\right)+\nabla\bullet\left(\varepsilon_q \rho_q \vec{v}_q \vec{v}_q\right)=-\varepsilon_q \nabla p+\nabla\bullet\left(\overline{\overline{\tau}}_q\right)+\varepsilon_q \rho_q \vec{g}+\sum_{p=1}^{n}\left(\vec{R}_{pq}+\dot{m}_{pq}\vec{v}_{pq}-\dot{m}_{qp}\vec{v}_{qp}\right)+\vec{F}_q+\vec{F}_{lift,q}+\vec{F}_{vm,q} \tag{4.2}$$

Where, $\overline{\overline{\tau}}_q$, is the stress-strain tensor of phase "q" given by

$$\overline{\overline{\tau}}_q=\varepsilon_q \mu_q\left(\nabla\vec{v}_q+\nabla\vec{v}_q^{T}\right)+\varepsilon_q\left(\lambda_q-\frac{2}{3}\mu_q\right)\nabla\bullet\vec{v}_q\bullet\overline{\overline{I}} \tag{4.3}$$

The inter-phase force, $\vec{R}_{pq}$ depends on the friction, pressure, cohesion, and other effects, and is subject to the conditions that $\vec{R}_{pq}=-\vec{R}_{qp}$ and $\vec{R}_{qq}=0$ is given by

$$\sum_{p=1}^{n}\vec{R}_{pq}=\sum_{p=1}^{n}K_{pq}\left(\vec{v}_p-\vec{v}_q\right) \tag{4.4}$$

μ_q = the shear viscosity of phase "q"

λ_q = the bulk viscosity of phase "q"

$\vec{F}_q$ = an external body force of phase "q"

$\vec{F}_{lift,q}$ = a lift force of phase "q"

$\vec{F}_{vm,q}$ = a virtual mass force of phase "q"

$\vec{R}_{pq}$ = an interaction force between phase "p" and "q"

∇p = the pressure gradient shared by all phases

$\vec{v}_{pq}$ = the inter-phase velocity

$\vec{g}$ =acceleration due to gravity

K_{pq} = the inter-phase momentum exchange coefficient

Conservation of Energy

To describe the conservation of energy in Eulerian multiphase model, a separate enthalpy equation is written for each phase:

$$\frac{\partial}{\partial t}\left(\varepsilon_q \rho_q h_q\right)+\nabla\bullet\left(\varepsilon_q \rho_q \vec{v}_q h_q\right)=-\varepsilon_q\frac{\partial p_q}{\partial t}+\overline{\overline{\tau}}_q:\nabla\vec{v}_q-\nabla\bullet\vec{q}_q+S_q+\sum_{p=1}^{n}\left(Q_{pq}+\dot{m}_{pq}h_{pq}-\dot{m}_{qp}h_{qp}\right) \quad (4.5)$$

Where, h_q= the specific enthalpy of the phase "q"

$\vec{q}_q$ =the heat flux of the phase "q"

S_q =a source term that includes sources of enthalpy

Q_{pq}=the intensity of heat exchange between the phase "p" and "q"

h_{pq}= the inter-phase enthalpy

4.4.2 Description of Momentum Equations

To describe the conservation of momentum equations in Eulerian model, several equations need to be written for each phase such as lift forces, virtual mass forces, inter-phase momentum exchange coefficients, solids pressure, solids shear stresses, and granular temperature.

4.4.2.1 Lift Forces

The effect of lift forces on the particles or droplets or bubbles are included in multiphase flows calculation. These lift forces act on a particle mainly due to velocity gradients in the primary-phase flow field. It is more significant for larger particles. If the particle diameter is much smaller than the inter-particle spacing and closely packed particles, the inclusion of lift forces is not appropriate.

The lift force acting on a secondary phase "p" in a primary phase "q" is computed from following equation,

$$\vec{F}_{lift} = -0.5\,\rho_q\,\varepsilon_p\left(\vec{v}_q - \vec{v}_p\right)\times\left(\nabla\times\vec{v}_q\right) \tag{4.6}$$

The lift force is insignificant in most cases compared to the drag force, so there is no reason to include this extra term. It is important to note that if the lift force is included in the calculation, this term needs not be included everywhere in the computational domain since it is computationally expensive to converge.

4.4.2.2 Virtual Mass Force

In multiphase flows, the effect of "virtual mass force" is when a secondary phase "p" accelerates relative to the primary phase "q". The inertia of the primary phase mass encountered by the accelerating particles or droplets or bubbles exerts a "virtual mass force" on the particles

$$\vec{F}_{vm} = 0.5\,\rho_q\,\varepsilon_p\left(\frac{d_q\,\vec{v}_q}{dt} - \frac{d_p\,\vec{v}_p}{dt}\right) \tag{4.7}$$

The term $\left(\frac{d_q}{dt}\right)$ denotes the phase material time derivative of the following form

$$\frac{d_q\,(\phi)}{dt} = \frac{\partial(\phi)}{\partial t} + \left(\vec{v}_q\cdot\nabla\right)\phi \tag{4.8}$$

The virtual mass effect is significant when the secondary phase density is much smaller than the primary phase density. The virtual mass force are neglected in this study as the secondary phase density (density of carbon solid is 2000 kg/m^3) is much bigger than the primary phase density (density of air is 1.225 kg/m^3).

4.4.2.3 Inter-phase Momentum Exchange Coefficient

One of the major differences between the single phase momentum equation and the Eulerian multiphase momentum equation is the inter-phase momentum exchange coefficient. This term is needed if the Eulerian multiphase momentum equation needs to be solved. Three

kinds of inter-phase momentum exchange coefficient are available: One for the fluid-fluid momentum equations known as fluid-fluid exchange coefficient, the second one for the fluid-solid momentum equation (granular flows) known as fluid-solid exchange coefficient, and the third one for the solid-solid exchange coefficient.

4.4.2.3.1 Fluid-Fluid Momentum Equations

For a fluid phase "q" the conservation of momentum equation is following

$$\frac{\partial}{\partial t}\left(\varepsilon_q \rho_q \vec{v}_q\right)+\nabla\bullet\left(\varepsilon_q \rho_q \vec{v}_q \vec{v}_q\right)=-\varepsilon_q \nabla p+\nabla\bullet\left(\overline{\overline{\tau}}_q\right)+\varepsilon_q \rho_q \vec{g}+\sum_{p=1}^{n}\left(K_{pq}\left(\vec{v}_p-\vec{v}_q\right)+\dot{m}_{pq}\vec{v}_{pq}-\dot{m}_{qp}\vec{v}_{qp}\right)+\vec{F}_q+\vec{F}_{lift,q} \tag{4.9}$$

The exchange coefficient for these types of liquid-liquid or gas-liquid mixtures is known as **fluid-fluid exchange coefficient,** K_{pq} which can be written as

$$K_{pq}=\frac{\varepsilon_q \varepsilon_p \rho_p f}{\tau_p} \tag{4.10}$$

Where, f = the drag function, is defined differently for the different exchange-coefficient models

τ_p = the "particulate relaxation time", is defined as

$$\tau_p=\frac{\rho_p d_p^2}{18\mu_q} \tag{4.11}$$

Where, d_p = the diameter of the droplets or bubbles of phase "p".

The definition of the drag function "f" includes a drag coefficient, C_D, that is based on the relative Reynolds number, Re. The drag function "f" is always multiplied by the volume fraction of the primary phase "q", as the fluid-fluid exchange coefficient K_{pq} should tend to zero whenever the primary phase is not present within the domain. The drag function "f" differs among the exchange coefficient models. From the model of Schiller and Naumann (1935)

$$f = \frac{C_D \, Re}{24} \tag{4.12}$$

Where,

$$C_D = \frac{24\left(1 + 0.15\,Re^{0.687}\right)}{Re} \qquad \text{when } Re \le 1000 \tag{4.13a}$$

$$C_D = 0.44 \qquad \text{when } Re > 1000 \tag{4.13b}$$

And Re is the relative Reynolds number. The relative Reynolds number for the primary phase "q" and secondary phase "p" is obtained based on the relative velocity between two phases as

$$Re = \frac{\rho_q \left| \vec{v}_p - \vec{v}_q \right| d_p}{\mu_q} \tag{4.14}$$

The Schiller and Naumann (1935) model is acceptable for all fluid-fluid pairs of phases.

4.4.2.3.2 Fluid-Solid Momentum Equations

For a solid phase "s" the conservation of momentum equation is

$$\frac{\partial}{\partial t}\left(\varepsilon_s \rho_s \vec{v}_s\right) + \nabla \bullet \left(\varepsilon_s \rho_s \vec{v}_s \vec{v}_s\right) = -\varepsilon_s \nabla p - \nabla p_s + \nabla \bullet \left(\overline{\overline{\tau}}_s\right) + \varepsilon_s \rho_s \vec{g} + \sum_{l=1}^{n}\left(K_{ls}\left(\vec{v}_l - \vec{v}_s\right) + \dot{m}_{ls}\vec{v}_{ls} - \dot{m}_{sl}\vec{v}_{sl}\right) + \vec{F}_s + \vec{F}_{lift,s} \tag{4.15}$$

Where, p_s = the solids pressure of the solid phase "s"

$K_{ls} = K_{sl}$ = the momentum exchange coefficient between fluid or solid phase "l" and solid phase "s".

The solid-phase stresses are derived by making an analogy between the random particle motion arising from particle-particle collisions and the thermal motion of molecules in a gas, taking into account the inelasticity of the granular phase. Similar to a gas, the intensity of the

particle velocity fluctuations determines the stresses, viscosity, and pressure of the solid phase. The kinetic energy associated with the particle velocity fluctuations is represented by a "pseudo-thermal" or granular temperature which is proportional to the mean square of the random motion of particles. The inter-phase momentum exchange coefficients in fluid-solid momentum equation are evaluated by a fluid-solid exchange coefficient and a solid-solid exchange coefficient.

(a) The fluid-solid exchange coefficient, K_{sl} can be written in the following general form,

$$K_{sl} = \frac{\varepsilon_s \rho_s f}{\tau_s} \tag{4.16}$$

Where, f = the drag function, is defined differently for the different exchange-coefficient models

τ_s = the "particulate relaxation time," is defined as

$$\tau_s = \frac{\rho_s d_s^2}{18 \mu_l} \tag{4.17}$$

Where, d_s = the diameter of particles of phase "s"

The definition of the drag function "f" includes a drag coefficient, C_D, that is based on the relative Reynolds number, Re_s. The drag function "f" differs among the exchange coefficient models. For the model of Syamlal and O'Brien (1989)

$$f = \frac{C_D \, Re_s \, \varepsilon_l}{24 \, v_{r,s}^2} \tag{4.18}$$

Where, $v_{r,s}$ =the terminal velocity for the solid phase "s"

And C_D = the drag coefficient with the following form derived by Valle (1948)

$$C_D = \left(0.63 + \frac{4.8}{\sqrt{Re_s / v_{r,s}}} \right)^2 \tag{4.19}$$

The Syamlal and O'Brien model is based on measurements of the terminal velocities of particles in fluidized or settling beds, with correlations that are a function of the volume fraction and relative Reynolds number

$$Re_s = \frac{\rho_l \left| \vec{v}_s - \vec{v}_l \right| d_s}{\mu_l} \tag{4.20}$$

Where the subscript "l" is for the fluid phase "l" and the subscript "s" is for the solid phase "s", and d_s is the diameter of the solid phase "s" particles.

The terminal velocity correlation for the solid phase "s" has the following form

$$v_{r,s} = 0.5 \left(A - 0.06\, Re_s + \sqrt{(0.06\, Re_s)^2 + 0.12\, Re_s \left(2B - A \right) + \left(A \right)^2} \right) \tag{4.21}$$

With $A = \varepsilon_l^{4.14}$

And $B = 0.8\, \varepsilon_l^{1.28}$ for $\varepsilon_l \le 0.85$

Or $B = \varepsilon_l^{2.65}$ for $\varepsilon_l > 0.85$

This model is appropriate when the solids shear stresses are defined according to M. Syamlal and T. J. O'Brien.

(b) The solid-solid exchange coefficient, K_{sl} can be written in the following general form,

$$K_{sl} = \frac{3\left(1 + e_{sl}\right)\left(\frac{\pi}{2} + C_{fr,sl} \frac{\pi^2}{8} \right) \varepsilon_s\, \rho_s\, \varepsilon_l\, \rho_l \left(d_l + d_s \right)^2 g_{o,sl} \left| \vec{v}_s - \vec{v}_l \right|}{2\,\pi \left(\rho_s\, d_s^3 + \rho_l\, d_l^3 \right)} \tag{4.22}$$

Where, e_{sl} = the coefficient of restitution

$C_{fr,sl}$ = the coefficient of friction between the solid phase "s" and "l" particles

d_l = the diameter of the particles of solid phase "l"

$g_{o,sl}$ = the radial distribution coefficient

The description of coefficient of restitution, the solid pressure, the radial distribution coefficient, the solid shear stresses, and the granular temperature are given below.

4.4.2.3.2.1 Solids Pressure

For granular (solid) flows in the compressible regime, i.e. where the solids volume fraction is less than its maximum allowed value, a solids pressure is calculated independently. This solids pressure is used for the pressure gradient term, ∇p_s in the granular-phase fluid-solid momentum equation. A granular temperature is introduced into the model and appears in the expression for the solids pressure because a Maxwellian velocity distribution is used for the particles. The solids pressure is composed of a kinetic term and a second term due to particle collisions:

$$p_s = \varepsilon_s \rho_s \theta_s + 2\rho_s (1+e_{ss}) \varepsilon_s^2 g_{o,ss} \theta_s \qquad (4.23)$$

Where e_{ss} = the coefficient of restitution for particle collisions

$g_{o,ss}$ = the radial distribution function

θ_s = the granular temperature

4.4.2.3.2.2 Radial Distribution Function

The radial distribution function, g_o, is a correction factor that modifies the probability of collisions between grains when the solid granular phase becomes dense. This is also a distribution function that governs the transition from the "compressible" condition where the spacing between the solid particles can continue to decrease, to the "incompressible" condition where no further decrease in the spacing can occur. This function may also be interpreted as the non-dimensional distance between spheres:

$$g_o = \frac{s + d_p}{s} \tag{4.24}$$

Where, s = the distance between grains and d_p = the diameter of particle.

The radial distribution function is closely connected to the factor "χ" of Chapman and Cowling's theory (1990) of non-uniform gases. "χ" is equal to 1 for a rare gas, and increases and tends to infinity when the molecules are so close together that motion is not possible.

There is no unique formulation for the radial distribution function in the literature but the following empirical functions can be used with discretion,

- ✓ For one solids phase,

$$g_o = \left[1 - \left(\frac{\varepsilon_s}{\varepsilon_{s,max}} \right)^{1/3} \right]^{-1} \tag{4.25}$$

- ✓ For "n" solids phases,

$$g_{o,kl} = \frac{1}{(1-\varepsilon_s)} + \frac{3\left(\sum_{k=1}^{n} \frac{\varepsilon_k}{d_k} \right) d_k \, d_l}{(1-\varepsilon_s)^2 (d_k + d_l)} \tag{4.26}$$

Syamlal (1993) used this formula that derived by Lebowitz (1964) for a mixture of hard spheres.

4.4.2.3.2.3 Solids Shear Stresses

Due to translation and collision, the solids stress tensor contains bulk and shear viscosities arising from particle momentum exchange.

Bulk Viscosity

The solids bulk viscosity accounts for the resistance of the granular particles to compression and expansion. It has the following form from Lun et al. (1984)

$$\lambda_s = \frac{4}{3}\varepsilon_s \rho_s d_s g_{o,ss}(1+e_{ss})\left(\frac{\theta_s}{\pi}\right)^{1/2} \quad (4.27)$$

Solids Shear Viscosity

The collisional and kinetic parts, and the optional frictional part, are added to give the solids shear viscosity:

$$\mu_s = \mu_{s,col} + \mu_{s,kin} + \mu_{s,fr} \quad (4.28)$$

- ✓ **Collisional Viscosity**

  The collisional part of the shear viscosity is modeled as from Gidaspow et al. (1992) and Syamlal et al. (1993)

$$\mu_{s,col} = \frac{4}{5}\varepsilon_s \rho_s d_s g_{o,ss}(1+e_{ss})\left(\frac{\theta_s}{\pi}\right)^{1/2} \quad (4.29)$$

- ✓ **Kinetic Viscosity**

  The kinetic part of the shear viscosity is modeled as from Syamlal et al. (1993)

$$\mu_{s,kin} = \frac{\varepsilon_s \rho_s d_s \sqrt{\theta_s \pi}}{6(3-e_{ss})}\left[1+\frac{2}{5}(1+e_{ss})(3e_{ss}-1)\varepsilon_s g_{o,ss}\right] \quad (4.30)$$

- ✓ **Frictional Viscosity**

  In dense flow at low shear, where the secondary volume fraction for a solid phase nears the packing limit, the generation of stress is mainly due to friction between particles. Schaeffer's expression can be used if the frictional viscosity is included in the calculation:

$$\mu_{s,fr} = \frac{p_s \sin\phi}{2\sqrt{I_{2D}}} \quad (4.31)$$

Where p_s = the solids pressure

ϕ = the angle of internal friction

I_{2D} = the second invariant of the deviatoric stress tensor.

The frictional stresses are usually written in Newtonian form:

$$\tau_{friction} = -P_{friction}\,\vec{\bar{I}} + \mu_{friction}\left(\nabla\vec{u}_s + \left(\nabla\vec{u}_s\right)^T\right) \tag{4.32}$$

The frictional stress is added to the stress predicted by the kinetic theory when the solids volume fraction exceeds a critical value. Then

$$P_s = P_{kinetic} + P_{friction} \tag{4.33}$$

$$\mu_s = \mu_{kinetic} + \mu_{friction} \tag{4.34}$$

The derivation of the frictional pressure is mainly semi-empirical, while the frictional viscosity can be derived from the first principles. The application of the modified Coulomb law leads to an expression of the form

$$\mu_{friction} = \frac{P_{friction}\sin\phi}{2\sqrt{I_{2D}}} \tag{4.35}$$

4.4.2.3.2.4 Granular Temperature

The granular temperature, θ_s, for the solids phase "s" is proportional to the kinetic energy of the fluctuating particles motion. The transport equation derived from kinetic theory takes the following form derived by J. Ding & D. Gidaspow (1990)

$$\frac{3}{2}\left[\frac{\partial}{\partial t}\left(\varepsilon_s\rho_s\theta_s\right) + \nabla\bullet\left(\varepsilon_s\rho_s\vec{v}_s\theta_s\right)\right] = \left(-p_s\,\bar{\bar{I}} + \bar{\bar{\tau}}_s\right):\nabla\vec{v}_s + \nabla\bullet\left(k_{\theta_s}\nabla\theta_s\right) - \gamma_{\theta_s} + \phi_{ls} \tag{4.36}$$

Where

$\left(-p_s \bar{\bar{I}} + \bar{\bar{\tau}}_s\right) : \nabla \vec{v}_s$ = the generation of energy by the solid stress tensor

$\left(k_{\theta_s} \nabla \theta_s\right)$= the diffusion of energy (k_{θ_s} is the diffusion coefficient)

γ_{θ_s} = the collisional dissipation of energy

ϕ_{ls} = the energy exchange between the fluid or solid phase "l" and the solid phase "s"

The above equation describing the diffusive flux of granular energy contains the term $\left(k_{\theta_s} \nabla \theta_s\right)$. The diffusion coefficient for granular energy k_{θ_s} is given by the model of Syamlal et al. (1993)

$$k_{\theta_s} = \frac{15\,\varepsilon_s\,\rho_s\,d_s\,\sqrt{\theta_s\,\pi}}{4\left(41-33\,\eta\right)}\left[1+\frac{12}{5}\,\eta^2\left(4\,\eta-3\right)\varepsilon_s\,g_{o,ss}+\frac{16}{15\,\pi}\left(41-33\,\eta\right)\eta\,\varepsilon_s\,g_{o,ss}\right] \qquad (4.37)$$

Where, $\eta = \frac{1}{2}\left(1+e_{ss}\right)$

The rate of energy dissipation within the solids phase "s" due to collisions between particles is represented by the collisional dissipation of energy γ_{θ_s}. This term is represented by the expression derived by Lun et al. (1984)

$$\gamma_{\theta_s} = \frac{12\left(1-e_{ss}^2\right)g_{o,ss}\,\rho_s\,\varepsilon_s^2\,\theta_s^{3/2}}{d_s\,\sqrt{\pi}} \qquad (4.38)$$

The transfer of the kinetic energy of random fluctuations in particle velocity from the fluid or solid phase "l" to solids phase "s" is represented by

$$\phi_{ls} = -3\,K_{ls}\,\theta_s \qquad (4.39)$$

4.4.3 Description of Energy Equations

To describe the conservation of energy in Eulerian multiphase model, a separate enthalpy equation is written for each phase:

$$\frac{\partial}{\partial t}\left(\varepsilon_q \rho_q h_q\right)+\nabla\bullet\left(\varepsilon_q \rho_q \vec{v}_q h_q\right)=-\varepsilon_q\frac{\partial p_q}{\partial t}+\overline{\overline{\tau}}_q:\nabla\vec{v}_q-\nabla\bullet\vec{q}_q+S_q+\sum_{p=1}^{n}\left(Q_{pq}+\dot{m}_{pq}h_{pq}-\dot{m}_{qp}h_{qp}\right) \quad (4.40)$$

Where, h_q= the specific enthalpy of the phase "q"

Q_{pq}=the rate of energy transfer between the phase "p" and "q"

h_{pq}= the inter-phase enthalpy

The rate of energy transfer between the phase "p" and "q" is to be a function of the temperature difference,

$$Q_{pq}=h_{pq}\left(T_p-T_q\right) \quad (4.41)$$

Where, $h_{pq}= h_{qp}$ = the heat transfer coefficient between the phase "p" and "q"

The heat transfer coefficient is related to the Nusselt number, Nu_p, of phase "p" is given by

$$h_{pq}=\frac{6\,k_q\,\varepsilon_q\,\varepsilon_p\,Nu_p}{d_p^2} \quad (4.42)$$

Here, k_q = the thermal conductivity of the phase "q".

The Nusselt number is determined from one of the many correlations reported in the literature. In the case of **fluid-fluid multiphase flows**, the correlation of Ranz and Marshall (1952) is given as

$$Nu_p=2.0+0.6\,Re_p^{1/2}\,Pr^{1/3} \quad (4.43)$$

Where, Re_p is the relative Reynolds number based on the diameter of the phase "p" and relative velocity. The relative Reynolds number for the primary phase "q" and secondary phase "p" is defined as

$$Re=\frac{\rho_q\left|\vec{v}_p-\vec{v}_q\right|d_p}{\mu_q} \quad (4.44)$$

And Pr is the Prandtl number of the phase "q"

$$\mathrm{Pr} = \frac{c_{p_q}\,\mu_q}{k_q} \tag{4.45}$$

In the **fluid-solid multiphase flows (or granular flows)**, the Nusselt number correlation given by Gunn (1978), applicable to a porosity range of 0.35 to 1.0 and a Reynolds number of up to 10^5, is given as

$$\mathrm{Nu_s} = \left(7 - 10\,\varepsilon_f + 5\,\varepsilon_f^2\right)\left(1 + 0.7\,\mathrm{Re_s^{0.2}}\,\mathrm{Pr}^{1/3}\right) + \left(1.33 - 2.4\,\varepsilon_f + 1.2\,\varepsilon_f^2\right)\mathrm{Re_s^{0.7}}\,\mathrm{Pr}^{1/3} \tag{4.46}$$

Where the subscript "f" is for the primary fluid phase "f" and the subscript "s" is for the secondary solid phase "s".
And Pr is the Prandtl number of the primary phase "f"

$$\mathrm{Pr} = \frac{c_{p_f}\,\mu_f}{k_f} \tag{4.47}$$

From Eqs.4.43and 4.46, the heat transfer coefficient in Eq. 4.42 can be calculated. The heat transfer coefficient is always multiplied by the volume fraction (ε) of the primary phase as it should tend to zero whenever one of the phases is not present within the domain.

4.5 Multiphase Turbulence Models

The velocity field in turbulent flows always fluctuates. The fluctuations can be small scale and high frequency, which is computationally expensive to be directly simulated. In a single phase, various types of closure models can be used to describe the effects of turbulent fluctuations of velocities. In comparison to single-phase flows, the modeling of turbulence in multiphase simulations is extremely complex as the number of terms to be modeled in the momentum equations in multiphase flows is large. General turbulence models in multiphase flows widely available are:

e. k-ε turbulence model options are
    i. Mixture turbulence model
    ii. Dispersed turbulence model
    iii. Turbulence model for each phase
f. Reynolds Stress turbulence model options are (RSM)
    i. Dispersed turbulence model
    ii. Mixture turbulence model

The standard k-ε mixture turbulence model is employed in this study to simulate the turbulent flow. The detailed descriptions of standard k-ε mixture turbulence model in multiphase flows are given below.

4.5.1 k-ε Mixture Turbulence Model

The standard k-ε model is the simplest and most robust of turbulence two-equation model in which the solution of two separate transport equation allows the turbulent velocity and length scales, to be independently determined. The k-ε model is a semi-empirical model with several constants, which were obtained from experiments. The mixture turbulence model is the default multiphase turbulence model. The k-ε mixture turbulence model in multiphase flows is applicable when phases separate and when the density ratio between phases is close to one. The turbulence kinetic energy (k), and its rate of dissipation (ε), are obtained from the following transport equations:

$$\frac{\partial}{\partial t}\left(\rho_m\, k\right)+\nabla\bullet\left(\rho_m\,\vec{v}_m\, k\right)=\nabla\bullet\left(\frac{\mu_{t,m}}{\sigma_k}\nabla k\right)+G_{k,m}-\rho_m\,\varepsilon \tag{4.48}$$

$$\frac{\partial}{\partial t}\left(\rho_m\,\varepsilon\right)+\nabla\bullet\left(\rho_m\,\vec{v}_m\,\varepsilon\right)=\nabla\bullet\left(\frac{\mu_{t,m}}{\sigma_\varepsilon}\nabla\varepsilon\right)+\frac{\varepsilon}{k}\left(C_{1\varepsilon}\,G_{k,m}-C_{2\varepsilon}\,\rho_m\,\varepsilon\right) \tag{4.49}$$

Where the mixture density ρ_m, mixture velocity $\vec{v}_m$, turbulent viscosity $\mu_{t,m}$, and production of turbulence kinetic energy, $G_{k,m}$ are computed from volume fraction and mass weighted equations as

$$\rho_m = \sum_{i=1}^{N} \rho_i \, \alpha_i \tag{4.50}$$

$$\vec{v}_m = \frac{\sum_{i=1}^{N} \rho_i \, \alpha_i \, \vec{v}_i}{\sum_{i=1}^{N} \rho_i \, \alpha_i} \tag{4.51}$$

Where α_i = the volume fraction of the phase "i"

$$\mu_{t,m} = \rho_m \, C_\mu \, \frac{k^2}{\varepsilon} \tag{4.52}$$

$$G_{k,m} = \mu_{t,m} \left(\nabla \vec{v}_m + \left(\nabla \vec{v}_m \right)^T \right) : \nabla \vec{v}_m \tag{4.53}$$

The constants in these equations are the same as those of standard k-ε model for the single phase. $C_{1\varepsilon}$, $C_{2\varepsilon}$, C_μ, σ_k and σ_t are constants and have the following values

$C_{1\varepsilon} = 1.44$, $C_{2\varepsilon} = 1.92$, $C_\mu = 0.09$, $\sigma_k = 1.0$, and $\sigma_t = 1.3$

4.6 Modeling Species Transport in Multiphase Flows

For each phase "q", the conservation equations for chemical species in multiphase flows can be solved through Eq. 4.54,

$$\frac{\partial}{\partial t}\left(\varepsilon^q \, \rho^q \, Y_i^q \right) + \nabla \bullet \left(\varepsilon^q \, \rho^q \, \vec{v}^q \, Y_i^q \right) = -\nabla \bullet \varepsilon^q \, \vec{J}_i^q + \varepsilon^q \, R_i^q + \varepsilon^q \, S_i^q + \sum_{p=1}^{n} \left(\dot{m}_{p^i q^j} - \dot{m}_{q^j p^i} \right) + R \tag{4.54}$$

Where, R_i^q = the net rate of production of homogeneous species "i" by chemical reaction for phase "q"

$\dot{m}_{q^j p^i}$ = the mass transfer source between species "i" and "j" from phase "q" to "p"

ε^q = the volume fraction for phase "q"

S_i^q = the rate of creation by addition from the dispersed phase plus any user-defined sources

R=the heterogeneous reaction rate

The species model panel for multiphase species transport simulations allows inclusion of volumetric, wall surface, and particle surface reactions. The homogeneous gas phase chemical reactions in multiphase are the same as a single-phase chemical reaction. The reactants and the products belong to the same mixture material and hence the same phase. The reaction rate is scaled by the volume fraction of the particular phase in the cell. There is no implicit relationship between the species of different phases. Explicit relationships between species of different phases can be specified through mass transfer and heterogeneous reactions.

Mass and Momentum Transfer with Multiphase Species Transport

The multiphase mass transfer model accommodates mass transfer between species of different phases. Each mass transfer mechanism defines the mass transfer phenomenon from one entity to another entity. An entity is either a particular species in a phase, or the bulk phase itself if the phase does not have a mixture material. The mass transfer mechanisms compute the net mass source/sink of each species in each phase. The net mass source/sink of a species is used to compute species and mass source terms.

Mass Transfer

Consider the following reactions:

$$a\,A + b\,B = c\,C + d\,D \qquad (4.55)$$

Assume that A and C belong to phase 1 and B and D to phase 2.

Mass source for the phase are given by following way,

$$S_1 = R\left(c\, M_c - a\, M_a \right) \tag{4.56}$$

$$S_2 = R\left(d\, M_d - b\, M_b \right) \tag{4.57}$$

Where, "S" is the mass source, "M" is the molecular weight, and "R" is the reaction rate.
The general expression for the mass source for the phase "i" is following,

$$S_{r_i} = -R \sum_{r_i} \gamma_j^r\, M_j^r \tag{4.58}$$

$$S_{p_i} = R \sum_{p_i} \gamma_j^p\, M_j^p \tag{4.59}$$

$$S_i = S_{p_i} + S_{r_i} \tag{4.60}$$

Where, "γ" is the stoichiometric coefficient, subscript "p" represents the product, and subscript "r" represents the reactant.

Momentum Transfer

Momentum transfer is more complicated than mass transfer. The net velocity, $\vec{u}_{net}$, of the reactants is given by,

$$\vec{u}_{net} = \frac{a\, M_a\, \vec{u}_1 + b\, M_b\, \vec{u}_2}{a\, M_a + b\, M_b} \tag{4.61}$$

The general expression for the net velocity of the reactants is given by,

$$\vec{u}_{net} = \frac{\sum_r \gamma_j^r\, M_j^r\, \vec{u}_{r_j}}{\sum_r \gamma_j^r\, M_j^r} \tag{4.62}$$

Where, subscript "j" represents the j^{th} item (either a reactant or a product).

Momentum transfer for the phases is given by,

$$S_1^{\vec{u}} = R\left(c\, M_c\, \vec{u}_{net} - a\, M_a\, \vec{u}_1 \right) \tag{4.63}$$

$$S_2^{\vec{u}} = R\left(d\, M_d\, \vec{u}_{net} - b\, M_b\, \vec{u}_2 \right) \tag{4.64}$$

The general expression is given by,

$$S_i^{\vec{u}} = S_{p_i}\, \vec{u}_{net} - R\sum_{r_i} \gamma_j^r M_j^r \vec{u}_i \tag{4.65}$$

If there is no momentum transfer, then the above term will be zero.

The superscript "u" is to differentiate between the mass source terms from the momentum source term.

Species Transfer

The general expression for source for species "k" in the phase "j" is given by,

$$S_{r_i^k} = -R \sum_{r_i^k} \gamma_j^{r^k}\ M_j^{r^k} \tag{4.66}$$

$$S_{p_i^k} = R \sum_{p_i^k} \gamma_j^{p^k}\ M_j^{p^k} \tag{4.67}$$

$$S_i^k = S_{p_i^k} + S_{r_i^k} \tag{4.68}$$

Heat Transfer

The net enthalpy of the reactants is given by,

$$H_{net} = \frac{a\, M_a \left(H_a + h_a^f \right) + b\, M_b \left(H_b + h_b^f \right)}{a\, M_a + b\, M_b} \tag{4.69}$$

Where, "h^f" represents the formation enthalpy, and "H" represents the enthalpy.
The general expression for "H_{net}" is given by,

$$H_{net} = \frac{\sum_r \gamma_j^r M_j^r \left(H_j^r + h^{f\,r}_j \right)}{\sum_r \gamma_j^r M_j^r} \tag{4.70}$$

If this enthalpy gets distributed to the products in the ratio of their mass production rates, heat transfer for the phases are given by,

$$S_1^H = R \left(c\, M_c\, H_{net} - a\, M_a\, H^a - c\, M_c\, h_f^c \right) \tag{4.71}$$

$$S_2^H = R \left(d\, M_d\, H_{net} - b\, M_b\, H^b - d\, M_d\, h_f^d \right) \tag{4.72}$$

The general expression for the heat source is given by,

$$S_i^H = S_{p_i}\, H_{net} - R \left(\sum_{r_i} \gamma_j^r M_j^r H_j^r + \sum_{p_i} \gamma_j^p M_j^p h^{f\,p}_j \right) \tag{4.73}$$

If there is no heat transfer then the different species only carry their formation enthalpies with them. Thus the expression for "H_{net}" will be,

$$H_{net} = \frac{\sum_r \gamma_j^r M_j^r h^{f\,r}_j}{\sum_r \gamma_j^r M_j^r} \tag{4.74}$$

The expression for S_i^H will be,

$$S_i^H = S_{p_i}\, H_{net} - R \left(\sum_{p_i} \gamma_j^p M_j^p h^{f\,p}_j \right) \tag{4.75}$$

CHAPTER FIVE
RESULTS AND DISCUSSIONS

The objective of this study is to establish a simulation model to investigate the thermal-flow and gasification process in a fluidized bed mild gasifier by using Eulerain multi-phase approach. Two different geometries are used in this study (a) a simplified preliminary geometry (b) a 2D fluidized bed mild gasifier (which reflects the mid-plane geometry of a 3D gasifier). The different cases simulated in this study are given below in Fig. 5.1. The first three cases are conducted in the preliminary geometry and the last four cases in the 2D fluidized bed mild gasifier.

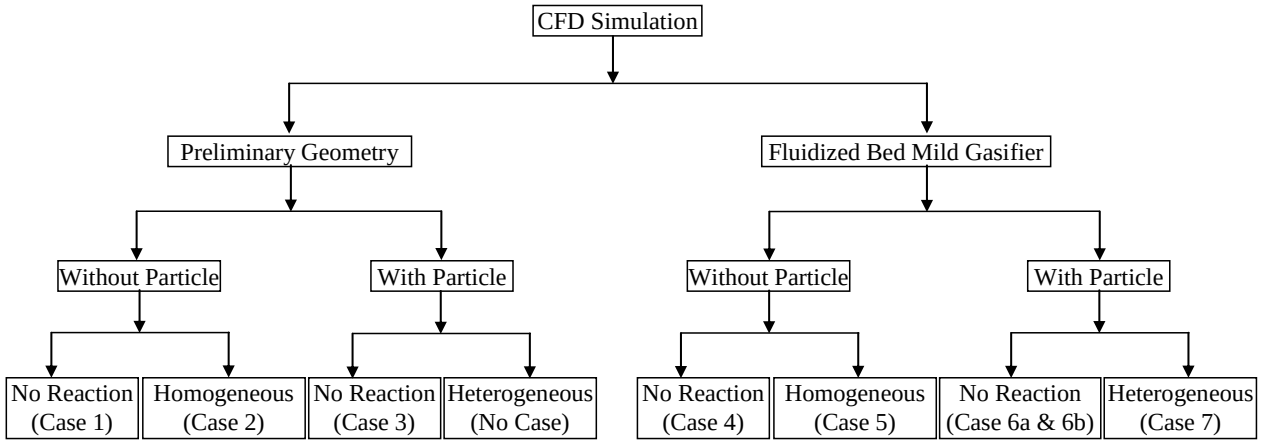

Parameters	***Case number***
Oxygen used at inlet	Case 2
Air used at inlet	Case 1, 3, 4, 5, 6, and 7

Figure 5.1 A Chart showing CFD simulation cases and inlet air or oxygen supply

Case 1: Thermo-flow behavior in the preliminary geometry (no solids and no reactions).

Case 2: Homogeneous reaction in the preliminary geometry (no solids).

Case 3: Thermo-flow behavior in the preliminary geometry with solid (no reactions).

Case 4: Thermo-flow behavior in the mild gasifier (no solids and no reactions).

Case 5: Homogeneous reaction with volatiles in the mild gasifier (no solids).

Case 6: Thermo-flow behavior in the mild gasifier with solid (no reactions).
Case 6a: 4 m/s solid inlet at draft tube and Case 6b: 5 m/s solid inlet at draft tube.

Case 7: Heterogeneous reaction (gas-solid) in the mild gasifier with volatiles (complete simulation).

Since there is no experimental result with which to be compared, this chart (Fig. 5.1) shows the process of building up the simulation model by going through simpler and more fundamental thermal-flow phenomena that can be reasonably judged by educated engineering intuition and experience. This is followed by progressively adding more complex features into the model and eventually achieves the objective of establishing the very complex multiphase reactive flow.

5.1 Studies on the Simple Preliminary Geometry (Cases 1, 2 and 3):

The study begins with an investigation of thermo-flow behavior without particles in a simplified 2D preliminary geometry. This simplified geometry (Fig. 5.2) is used first to save computational time. The height and width of the preliminary geometry is 1 m and 0.3 m, respectively. The preliminary geometry has seven perforated inlets at the bottom and one outlet at top of the domain. The width of each inlet is 0.02 m. The outlet is 0.1 m wide.

5.1.1 Case 1: Thermal-flow behavior (no solids and no reactions) in the simplified 2D preliminary geometry

Each of the seven perforated inlets has air passing through with a velocity 1 m/s at 1000 K. The inlet air temperature (1000 K) is higher than the room temperature (300 K) to simulate hot air entering the gasifier. Fig. 5.2 shows the flow field with two enlarged local flow patterns near inlet and outlet. The velocity pattern looks reasonable. The temperature is uniformly 1000 K since adiabatic wall condition is imposed. This reasonable thermal-flow result builds up the base for data input and the confidence of using the software.

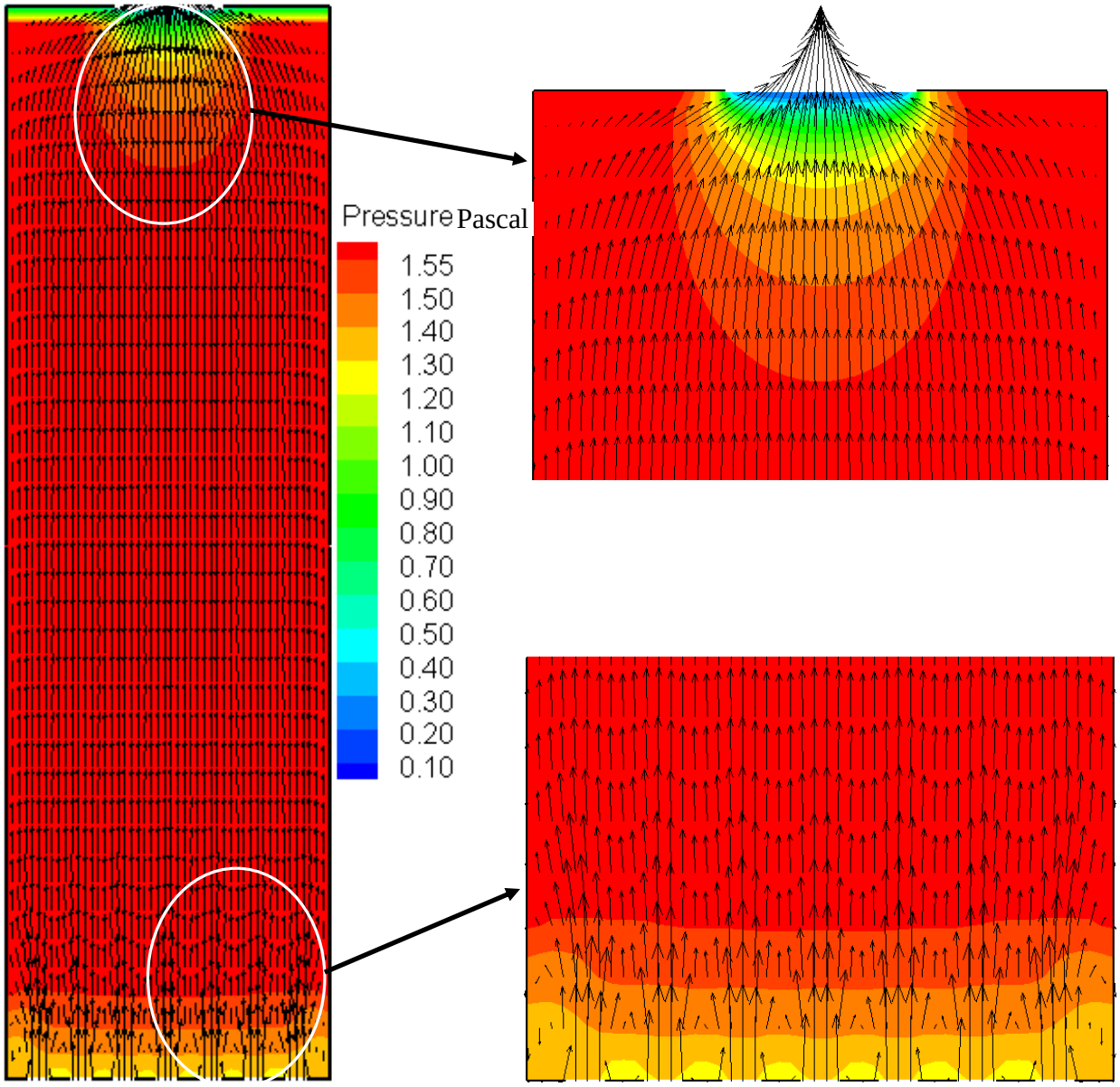

Figure 5.2 Air velocity vector plots in the simplified 2D preliminary geometry colored by static pressure (Pascal) distribution (Case 1)

5.1.2 Case 2: Homogeneous reactions (no solids) in the preliminary geometry

This case investigates the adiabatic flame temperature and distribution of gas mass fraction by introducing the following five global gasification reactions (R1.1 to R1.5) together in the simplified preliminary geometry. The mass weighted average of temperature and mass fraction of product gas are verified by the values calculated by hand under a thermal equilibrium condition.

The Global Gasification Reactions are modeled as:

$C(s) + ½ O_2 \rightarrow CO$	$\Delta H°_R$ = -110.5 MJ/kmol	(R1.1)
$C(s) + CO_2 \rightarrow 2CO$	$\Delta H°_R$ = +172.0 MJ/kmol (Gasification, Boudouard reaction)	(R1.2)
$C(s) + H_2O\ (g) \rightarrow CO + H_2$	$\Delta H°_R$ = +131.4 MJ/kmol (Gasification)	(R1.3)
$CO + ½ O_2 \rightarrow CO_2$	$\Delta H°_R$ = -283.1 MJ/kmol	(R1.4)
$CO + H_2O\ (g) \rightarrow CO_2 + H_2$	$\Delta H°_R$ = -41.0 MJ/kmol (Water-shift)	(R1.5)

["+" Endothermic (absorbing heat), ["-" Exothermic (releasing heat)]

The equilibrium result of the above five reactions can be obtained by combining them into one reacting equation: $3C(s) + 2H_2O\ (g) + O_2 \rightarrow 2CO + CO_2 + 2H_2$

According to hand calculations, the reactants gas mass fraction is: C(s) =0.35, O_2=0.30, H_2O=0.35, and the equilibriums gas mass fraction is: CO=0.54, CO_2=0.42, H_2=0.04.

This equilibrium result will be compared with the CFD results. If the gasifier is large enough and the residual time is sufficiently long, the CFD results should be identical with the equilibrium results.

Eqs.R1.1, R1.4 and R1.5 are combustion reactions releasing heat (exothermic), and Eqs.R1.2 and R1.3 are gasification reactions absorbing heat (endothermic). For the single phase simulation, all of the above reactions are treated as homogeneous reactions (i.e. Carbon, C(s) treated as "gas" for homogeneous reaction). This is a necessary stepping stone to gain confidence with the model before considering heterogeneous reaction calculation later.

The oxygen provided for all simulations is based on a theoretical amount (stochiometic) needed to produce all gasification produce for a complete carbon conversion. The theoretical energy needed to supply the gasification energy is calculated from the endothermic reactions R1.2 and R1.3.

The computed distributions of gas composition in the gasifier for Case 2 are illustrated in Fig. 5.3. The velocity vectors are colored by gas temperature in the simplified preliminary geometry and are illustrated in Fig. 5.4.

As the char (C) enters the gasifier as shown in Fig. 5.3,it burns to produce CO, according to reaction $C+0.5O_2 \rightarrow CO$ (R1.1).Due to a fast char reaction with oxygen, the mass fraction of

CO immediately increases from 0 to 0.54 as the gas enters the vessel. This reaction releases energy and raises the gas temperature. A large fraction of CO, produced from reaction (R1.1), reacts with some oxygen to yield CO_2 according to reaction $CO+0.5O_2 \rightarrow CO_2$ (R1.4). These two oxidation reactions release all the energy needed for all other endothermic reactions under a controlled condition with limited oxidation. The H_2O distribution shows that water vapor reacts with char as soon as it enters the gasifier and produces CO and H_2, as described by the steam-gasification reaction $C+H_2O \rightarrow CO+H_2$ (R1.3). The CO_2 produced in combustion as described by reaction (R1.4) reacts with the fresh char to produce more CO according to the Boudouard gasification reaction $C+CO_2 \rightarrow 2CO$ (R1.2). This is indicated by an increase in CO mass fraction and a decrease in CO_2 mass fraction in Fig. 5.3. Gasification of char with CO_2 (R1.2) is an efficient process to consume CO_2 to obtain CO. The water shift reaction $CO+H_2O \rightarrow CO_2+H_2$ (R1.5) plays a minor role in the gasifier because the mass fraction increase of H_2 is negligible compare to other product gas. As a result of these endothermic (absorbing heat) reactions R1.2 and R1.3, the gas temperature decreases to around 1070 K, which is nearly equal to the hand-calculated equilibrium temperature (1070 K or 1467 °F).

As shown in Fig. 5.3, 100% of the carbon has reacted once the gas exits the gasifier. This is due to the eddy-dissipation model used in this study. In the eddy-dissipation model, the chemical reactions are assumed to be faster than the turbulence time scale, so for the size of this simplified preliminary geometry, the residence time is sufficient for all the five global gasification reactions to be completed when the flow exits the gasifier.

The mass weighted averages of CO, CO_2, and H_2 at outlet of the domain are 0.54, 0.42, and 0.04, respectively, which are exactly equal to the hand calculated result of 0.54, 0.42, and 0.04 respectively. This case further builds up the confidence that five reactions in the single phase case can achieve converged and reasonable results.

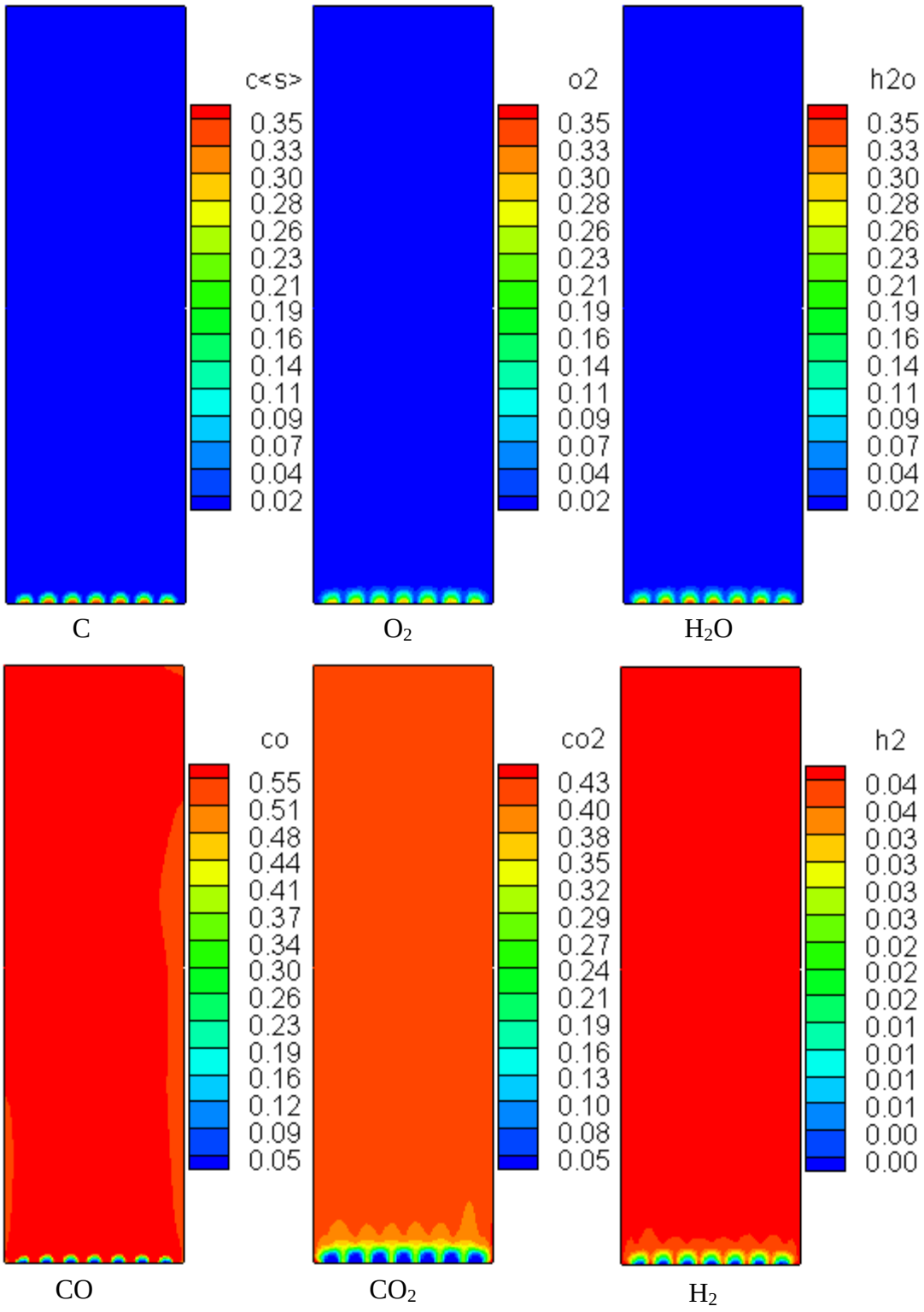

Figure 5.3 Distribution of gas mass fraction in the simplified 2D preliminary geometry (Case 2)

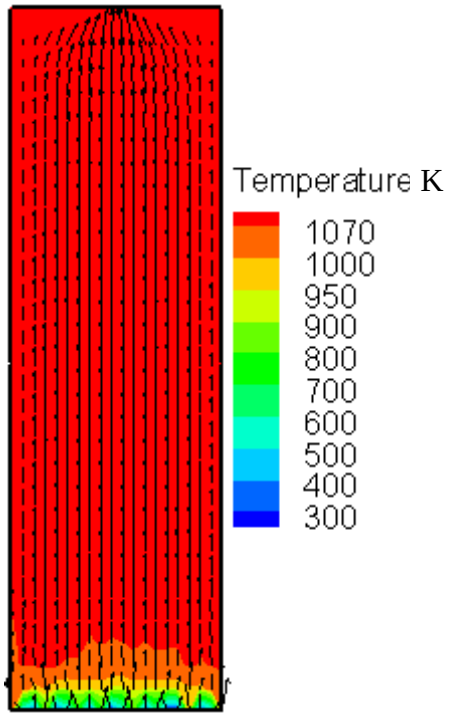

Figure 5.4 Gas velocity vector plots in the simplified 2D preliminary geometry colored by temperature (K) distribution with five single-phase reactions (Case 2)

5.1.3 Case 3: Thermal-flow behavior with solids (no reactions)

This case investigates the thermal-flow behavior with particles as well as the fluidization phenomena in the simplified preliminary geometry. The process of converting the granular (solid) material from a static solid-like state to a dynamic fluid-like state is known as "fluidization". For investigating the fluidization phenomena, all of the solid particles are placed side by side near the perforated inlets, like a bed of granular material, and the air passes up through the bottom of this bed.

Thirty percent of the whole domain is filled up with 5 mm diameter carbon particles. The air enters with velocity 4 m/s at 1000 K and passes up through the bed and changes the position of carbon particles. The velocity vectors are shown in Fig. 5.5, and the volume fraction of carbon particles for different simulation time intervals from 0.2 second to 4.0 second are shown in Figs. 5.6 and 5.7. Since no reactions are simulated in this case, the temperature inside the domain is uniform and is not shown.

The aerodynamic drag force of air pushes the particles in upward direction and the gravitational force of particles (i.e. weight of carbon particles) pushes the particles in downward direction. When the upward aerodynamic drag force of air and downward gravitational force of particles are equal, the air velocity is known as the minimum fluidization velocity. This minimum fluidization velocity is an important milestone during simulation iteration because below this velocity the particles will not change their position (move to an upward direction in this case) and above this velocity the particles will be entrained by air to move around. If the air velocity is much larger than this velocity, some portion of the particles could be entrained passing through the exit which is not an ideal condition for operating a fluidized bed gasifier. There are many correlations published in the open literature as discussed in appendix "A". It is interesting to compare the CFD result of the minimum fluidization velocity with those obtained from the empirical correlations as shown in Table 5.1. The minimum fluidization velocity is determined by starting the velocity at a very low speed, 0.2 m/s and a relatively high speed at 5 m/s, which is closed to the value (4 m/s) calculated by Kumar and Gupta correlation (1980). Then the bisecting method is used to zig-zag the inlet air velocity values between a high value which shows the particles are moved and a low value which will not move the particles until the critical value (within once decimal value) is achieved. The result of CFD is 2.65 m/s, which is very close to the value calculated by Ergun rule (Eq. 2.16). In this study, the air inlet velocity at 4 m/s (above the CFD determined minimum fluidization velocity) is selected to provide a sustained fluidization.

Table 5.1 Minimum fluidization velocity values calculated from different correlations and obtained from the CFD result for 5 mm diameter and 0.5 volume fraction of carbon solid

Correlation	**Minimum fluidization velocity (m/s)**
Todes and Citovich (1981, Appendix A)	1.56
Saxena and Vogel (1977, Appendix A)	2.06
Ergun rule (1952, Eq. 2.16 or Appendix A)	2.32
Kumar and Gupta (1980, Appendix A)	4
Miller and Logwinuk (1980, Appendix A)	16.32
CFD result	2.65

Figure 5.5 shows the particle velocity field versus air velocity field. It can be clearly seen that all air streams move upward whereas particles circulate within the fluidized bed in the bottom part of the domain. At 4 m/s inlet air velocity, no particles are seen in the upper part of the domain. A sequence of snapshots up to 4 seconds of char volume fraction distributions is shown in Figs. 5.6 and 5.7.

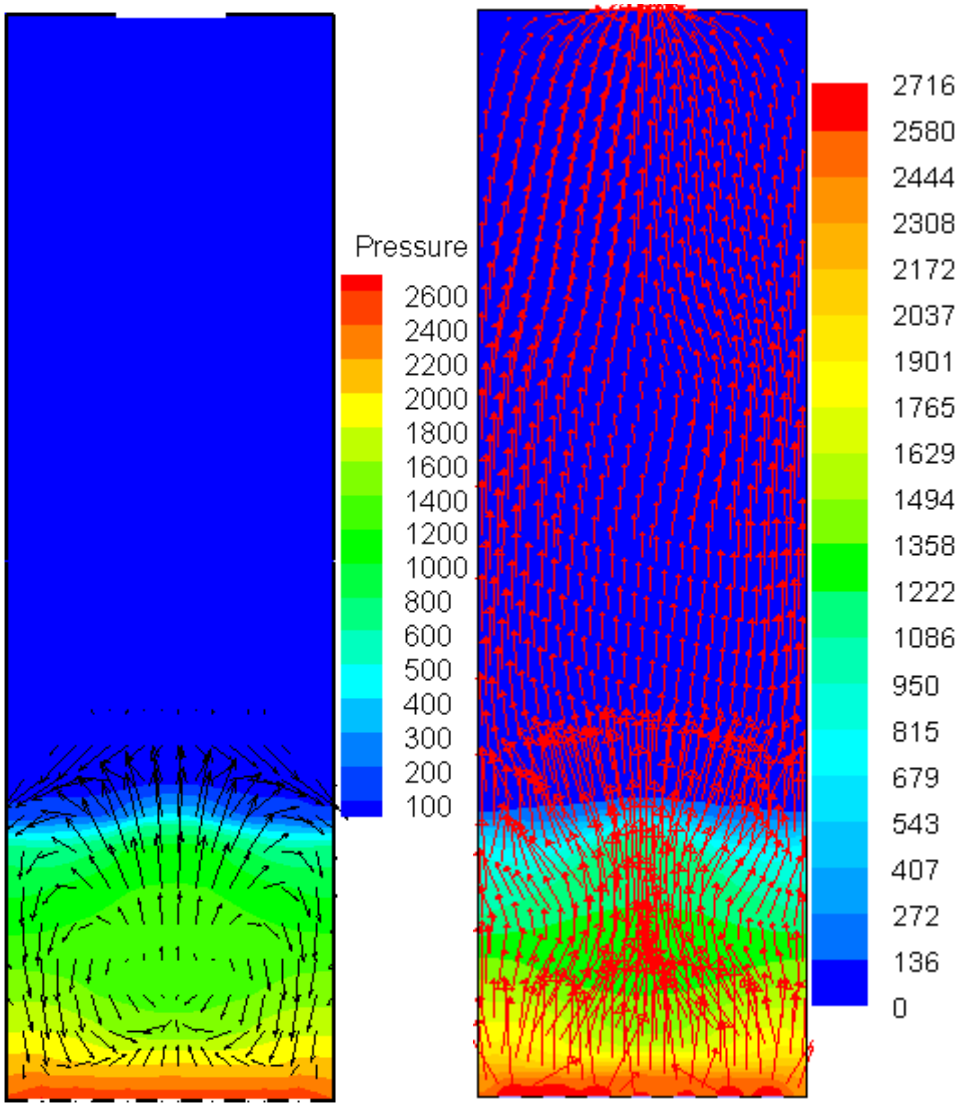

(a) (b)

Figure 5.5 Velocity vector plots for (a) particle and (b) air in the simplified 2D preliminary geometry colored by static pressure (Pascal) for Case 3

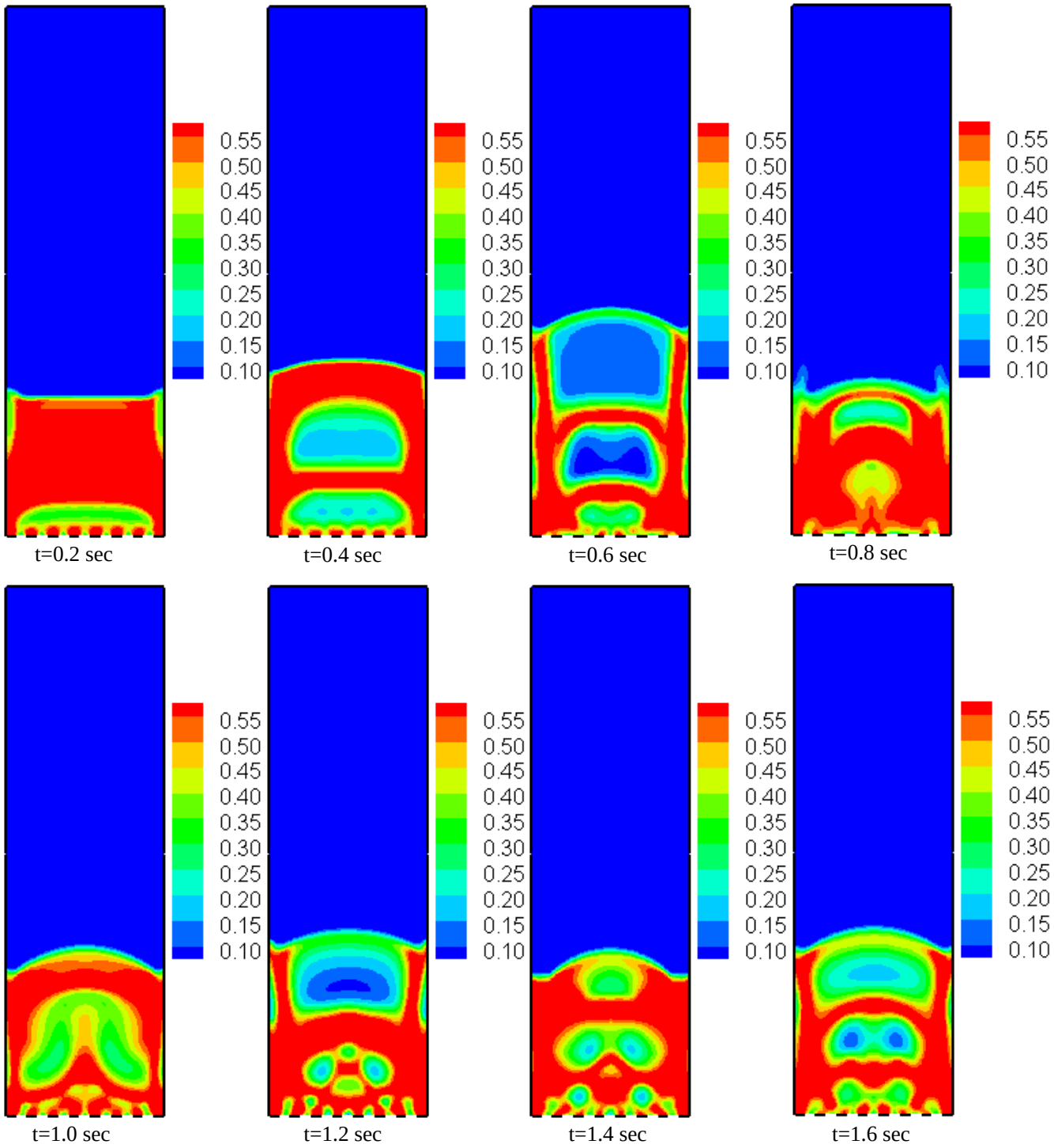

Figure 5.6 Distribution of volume fraction of carbon particles with 4 m/s air inlet from time interval between 0.2 and 1.6 seconds in the simplified 2D preliminary geometry without reactions (Case 3)

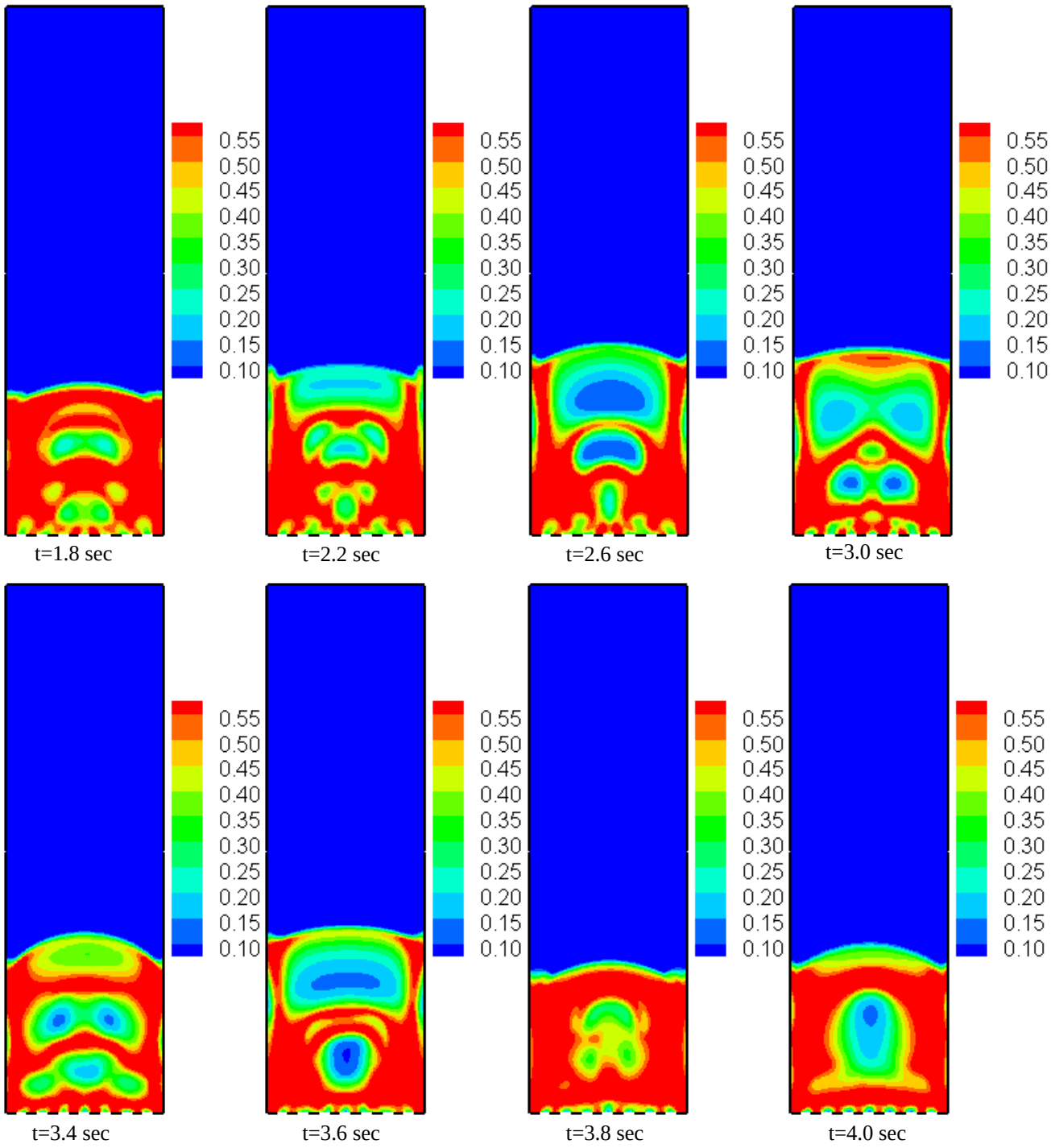

Figure 5.7 Distribution of volume fraction of carbon particles with 4 m/s air inlet from time intervals between 1.8 and 4.0 seconds in the simplified 2D preliminary geometry without reactions (Case 3)

5.2 Studies on Fluidized Bed Mild Gasifier (Cases 4, 5, 6 and 7):

The 2D fluidized bed mild gasifier used in the simulation domain is shown in Fig. 5.8. This conceptual design contains the following main components: three inlets, four outlets, a draft tube, perforated plates, and a particle deflector. The height and width of the bench-top mild gasifier is 34.25 inch (87 cm) and 18 inch (45.75 cm), respectively. In the three inlets, two for fluidized gas inlet and the third one, known as draft tube inlet, are for coal with transport gas for the multi-phase cases or only gas for the single-phase cases. The width of left and right horizontal gas inlet is 3 inch (7.65 cm), and the vertical coal inlet for the multi-phase case is 2 inch (5 cm). There are four outlets, two for char in the mid-height and two for produced syngas at top of the domain. The width of the syngas outlets is 5 inch (12.7 cm), and the char's outlet is 1.5 inch (3.8 cm) inclined 45 degrees. To create fluidization inside the gasifier, a total of 28 perforated interior surfaces with 0.15 inch (0.38 cm) width holes are generated side by side with equal distance apart. A draft tube is designated inside the domain with 4 inch (10.15 cm) width to isolate fluidized bed from contacting oxygen in the air and to transfer heat to the fluidized bed through the draft tube wall. Above the draft tube, a deflector with 8 inch (20.35 cm) width is installed to block the particles for the multi-phase case from being entrained out of the fluidized bed with the gases. Coal and air enter the draft tube for the multi-phase case through the draft-tube's bottom inlet and react to produce heat that drives out the volatiles during the journey moving upward through the draft tube.

5.2.1 Case 4: Thermal-flow behavior (no solids and no reactions) in gasifier

The fluidization air enters form the bottom horizontal inlets at 0.42 m/s and 300 K. The velocity 0.42 m/s at the horizontal fluidized gas inlet will convert to 0.6 m/s at perforated openings, which is due to the area difference between the fluidized gas inlet and the perforated bed. The air entering the draft tube from the central bottom inlet is at 0.6 m/s and 1000 K. In Case 4, no particles and reactions are considered, so the result in Fig. 5.8 shows thermal-flow mixing of these two air streams of different temperatures. The flow pattern inside the gasifier is complicated showing the flow field without the presence of particles. The difficulty in achieving computational convergence due to flow passing through small perforated holes and large circulations at the top of the gasifier flow have been resolved. The success of this case provides foundation to move forward to simulate more complicated cases by using the flow and

temperature results as the initial conditions for later cases. The inlet conditions are summarized in Table 5.2.

Table 5.2 Different velocity values at different inlets for Case 4

Parameters	***Cases 4***	
Inlet position	Fluidized bed inlet	Draft tube inlet
Air inlet velocity at horizontal , m/s	0.42	
Air inlet velocity at perforated openings , m/s	0.60	
Air inlet velocity at draft tube , m/s		0.6
Inlet temperature , K	300	1000

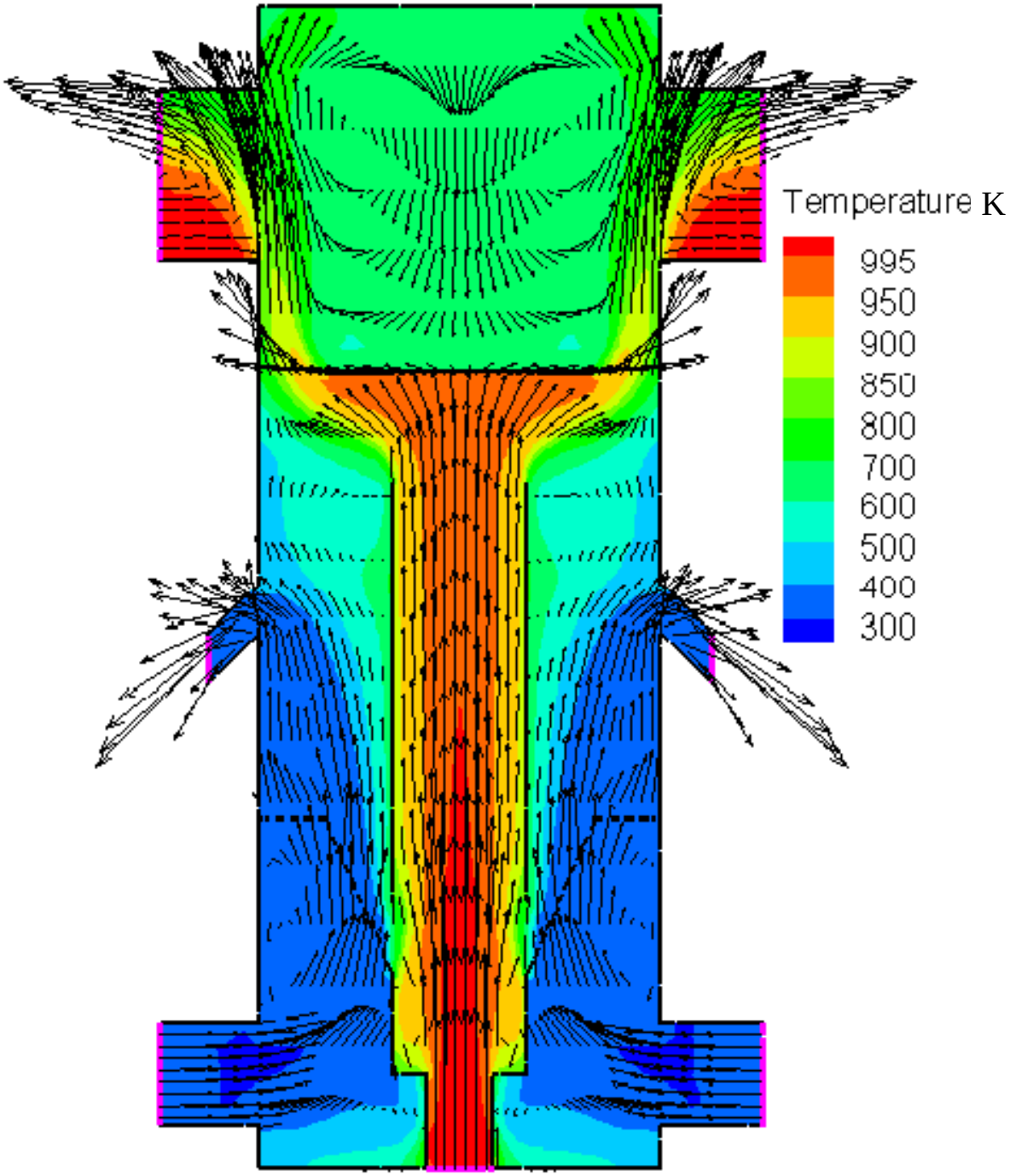

Figure 5.8 Air velocity vector plots in the mild gasifier colored by temperature (K) distribution without particles and reactions (Case 4)

5.2.2 Case 5: Homogeneous reactions (no solids) in gasifier with volatiles

This case investigates the adiabatic flame temperature and distribution of gas mass fraction by introducing the five global gasification reactions Eqs.R1.1 to R1.5 with nitrogen (N_2) as inert gas together with volatiles reactions Eqs.R1.6 and R1.7 in the fluidized bed mild gasifier, like in Case 2. The difference between Case 2 and Case 5 is the geometry, nitrogen (N_2) and volatiles. The results are shown in Fig. 5.9 and Fig. 5.10 of species mass fraction distribution and in Fig. 5.11 of velocity vectors colored by temperature. In Fig. 5.9, gasification occurs and completes very fast in the draft tube because in the draft tube, all the reactants (C, O_2, steam, C_6H_6, and volatiles) are quickly consumed to near zero, and all the products (Fig. 5.10) quickly reach the maximum amount (CO, CO_2, and H_2). The velocity and temperature profiles in Fig. 5.11 are different than in Case 4 (Fig. 5. 8). The inlet conditions are summarized in Table 5.3.
The additional two-step volatiles reactions are modeled as:

$$CH_{2.121}O_{0.585} \rightarrow 0.585CO+0.853H_2+0.069C_6H_6 \qquad \Delta H°_R = 416.84 \text{ MJ/kmol} \qquad \text{(R1.6)}$$

(Volatile cracking)

$$C_6H_6+3O_2 \rightarrow 6CO+3H_2 \qquad \text{(R1.7)}$$

The volatiles' enthalpy of formation is calculated as -233,299 kJ/kg as documented in Appendix "C". Due to the uncertainty of the coal compositions, this back-calculated enthalpy value possesses an uncertainty within 20%.

The equilibrium result of the five global reactions (R1.1 to R1.5) with nitrogen (N_2) and the two volatiles reactions (R1.6 and 1.7) can be obtained by combining them into one reacting equation. The benzene (C_6H_6) is an intermediate product, so it is not seen in the equilibrium equation, i.e. R1.7 is multiplied by 0.069 so the right hand side of C_6H_6 can be cancelled by the left hand site of C_6H_6 in Eq. R1.7.

$$3C(s) + 2H_2O\ (g) +1.207(O_2+3.76N_2) + CH_{2.121}O_{0.585} \rightarrow 3CO+ CO_2+ 3.06H_2+4.538N_2$$

The inlet mass fraction from the draft tube inlet consists of: C(s) =0.157, O_2=0.170, H_2O=0.015, $CH_{2.121}O_{0.585}$=0.103 (volatiles), N_2=0.555 and the fluidized bed inlet consists of: C(s) =0.188, O_2=0.182, N_2=0.630.

Based on the equilibrium result of the above reaction equation, the product gas mass fraction can be calculated as: CO=0.321, CO_2=0.168, H_2=0.023 and N_2=0.488.

This equilibrium result will be compared with the CFD results. If the gasifier is large enough and the residual time is sufficiently long, the CFD results should be identical with the equilibrium results.

The mass weighted averages of CO, CO_2, H_2 and N_2 compositions at outlet of the domain are 0.322, 0.168, 0.023 and 0.487 respectively, which are almost equal to the hand calculated equilibrium result of 0.321, 0.168, 0.023and 0.488 respectively. The mass weighted average of static temperature is 952.35 K at outlet of the domain of the mild gasifier.

Table 5.3 Parameters, boundary and operating conditions for Case 5

Parameters	***Cases 5***	
Inlet position	Fluidized bed inlet	Draft tube inlet
Fuel	carbon gas, air	carbon gas, water vapour, air, volatiles
Gas inlet velocity at horizontal, m/s	0.42	
Gas inlet velocity at preforated opening, m/s	0.60	
Gas inlet velocity at draft tube, m/s		2.00
Inlet temperature, K	300	300
Mass fraction at inlet		
C	0.188	0.157
H_2O	0	0.015
O_2	0.182	0.170
N_2	0.630	0.555
$CH_{2.121}O_{0.585}$	0	0.103
Operating pressure (Pascal)	101325	101325
Wall temperature, K	Adiabatic	Adiabatic

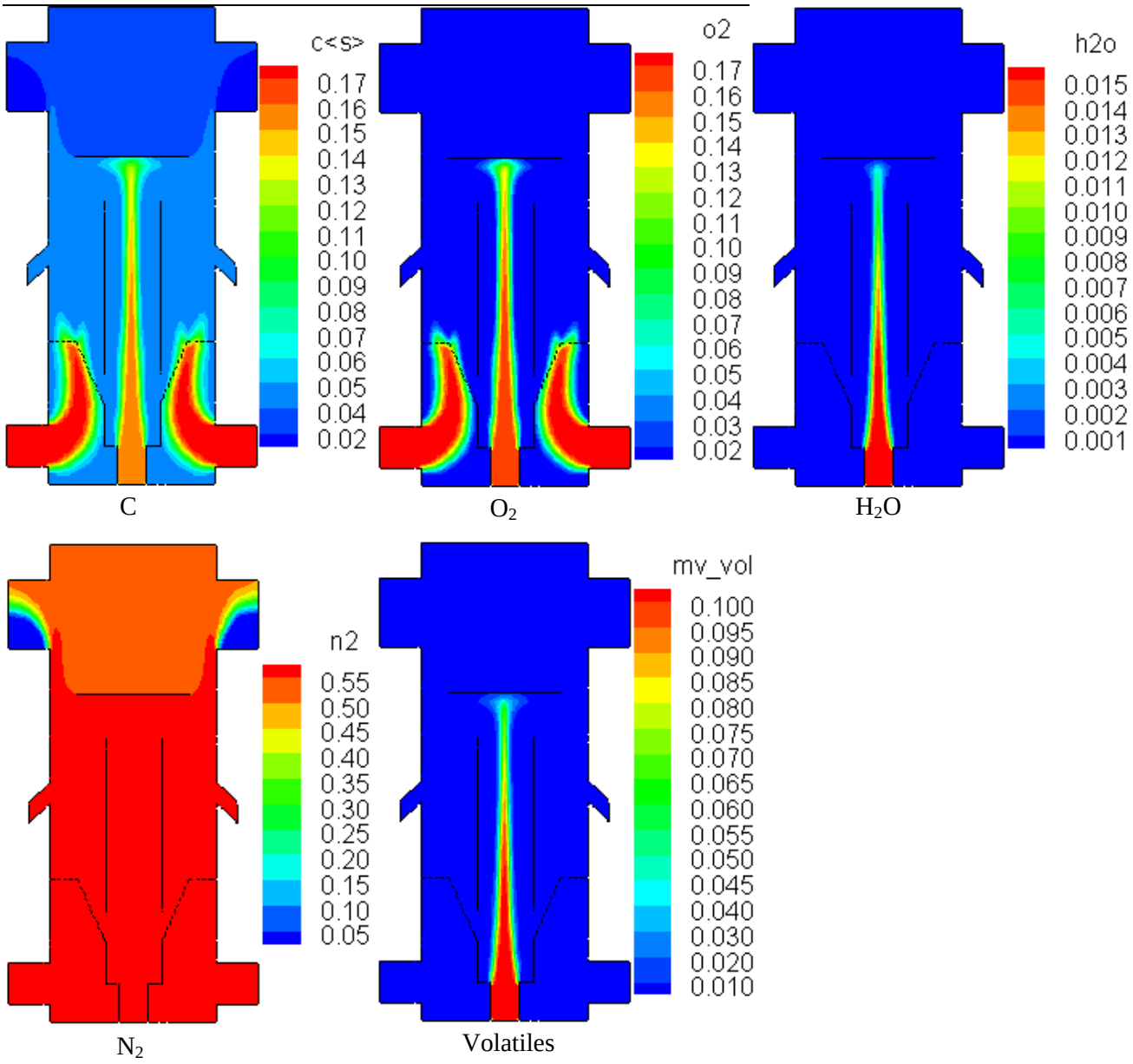

Figure 5.9 Distribution of reactant gas mass fractions in the mild gasifier with the instantaneous (homogeneous) gasification model including volatiles but without particles (Case 5)

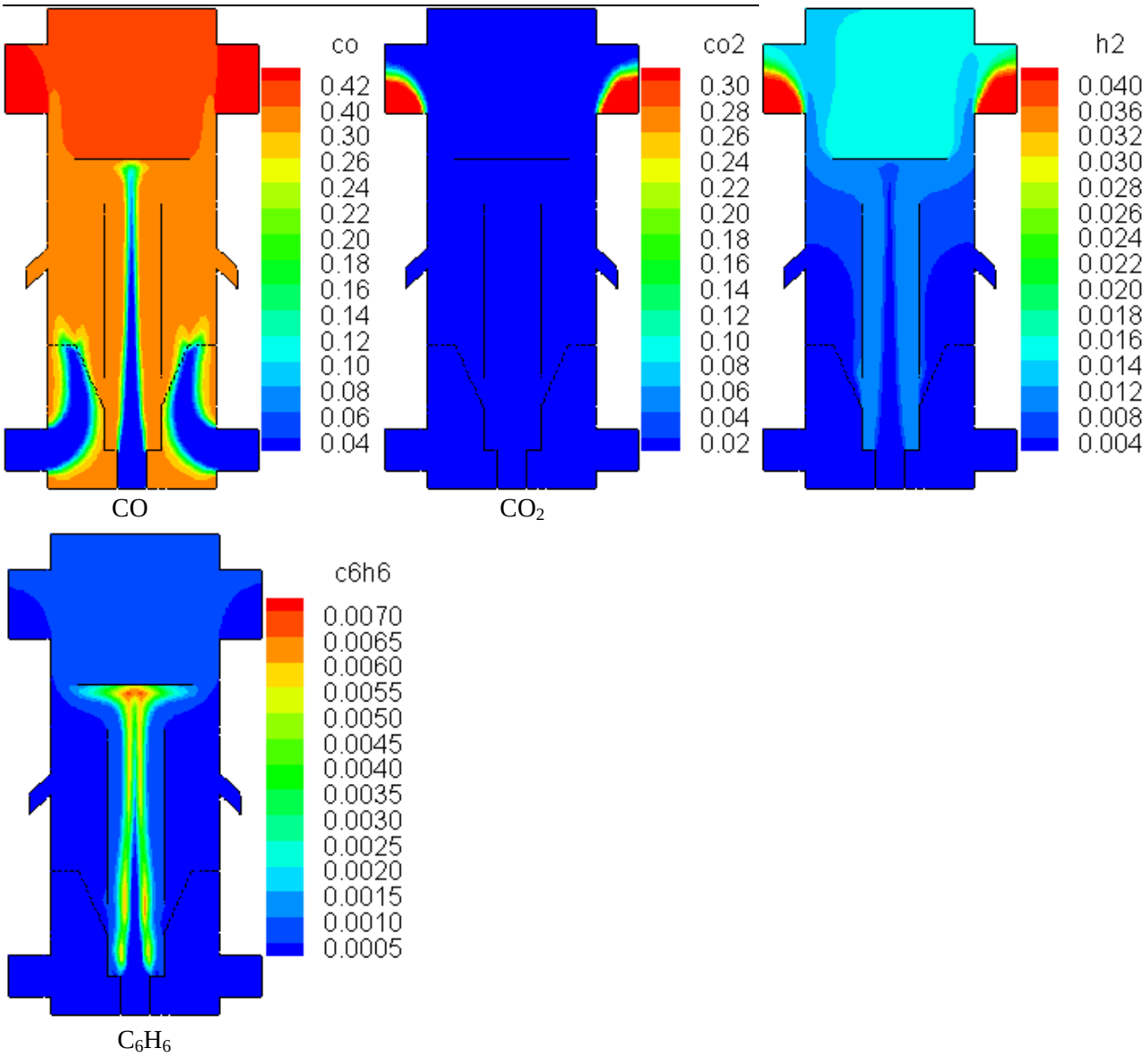

Figure 5.10 Distribution of product gas mass fractions in the mild gasifier with instantaneous (homogeneous) gasification model including volatiles but without particles (Case 5)

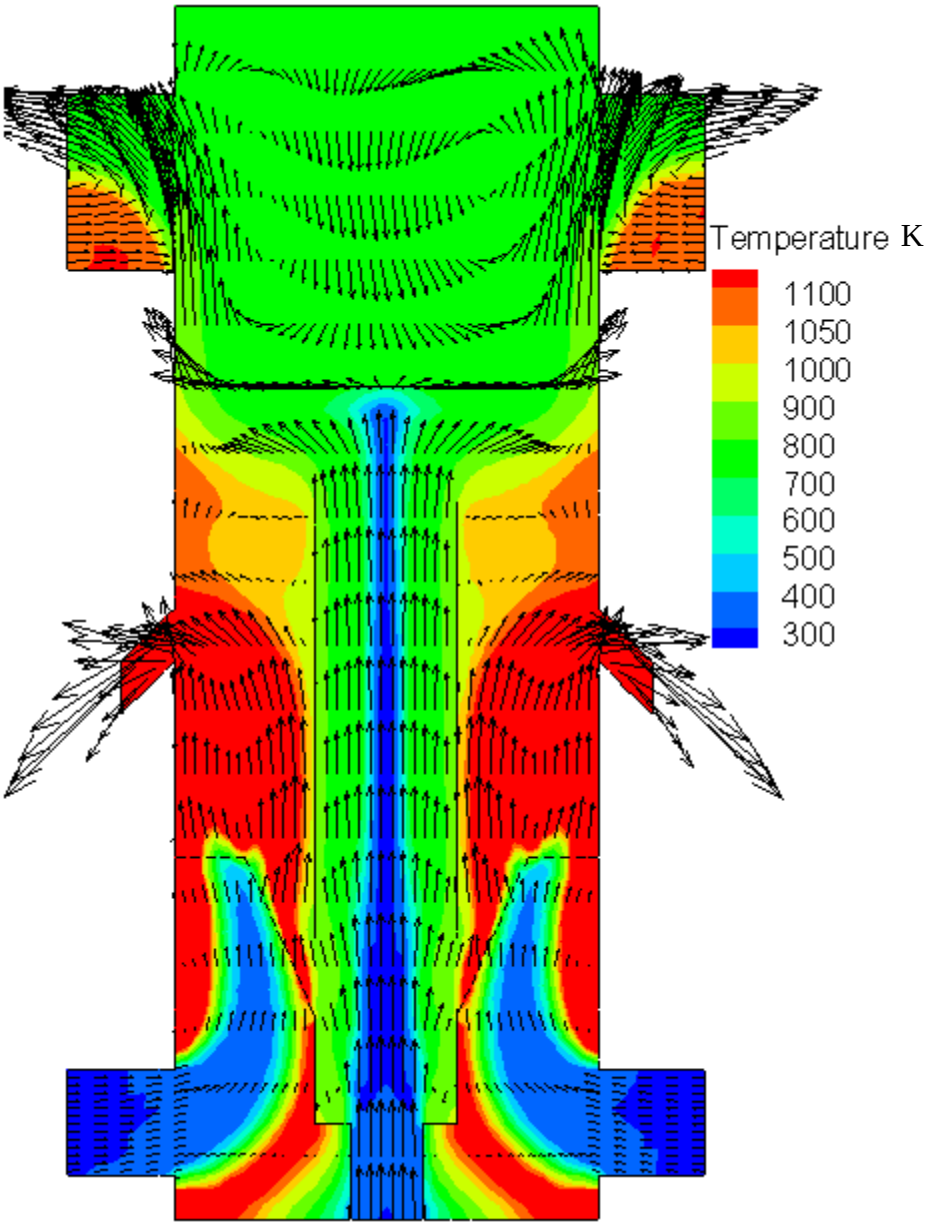

Figure 5.11 Gas velocity vector plots in the mild gasifier colored by temperature (K) distribution with instantaneous (homogeneous) gasification model including volatiles but without particles (Case 5)

5.2.3 Case 6: Thermal-flow behavior with solids (no reactions)

5.2.3.1 Case 6a: 4 m/s solid inlet at draft tube

This case investigates the thermal-flow as well as the multiphase fluidization phenomenon inside the fluidized bed mild gasifier as like Case 3. The difference between Case 3 and Case 6 is the geometry and the placement of perforated bed. To create fluidization inside the gasifier, a total of 28 perforated interior surfaces (0.15 inch each of them), 8 horizontally and 20 in the slanted line are created side by side spaced equally apart.

Initially, the 5 mm diameter carbon particles at room temperature (300 K) are placed side by side in the fluidized bed, like a bed of granular (solid) material. The air passes up through the perforated interior (holes) coming from the two horizontal fluidized gas inlets with 2.8 m/s velocity at 300 K. The carbon, transported by air, enters the draft tube through the vertical draft-tube's bottom inlet with the same velocity of 4 m/s but at 1000 K temperature.

Above the draft tube, a deflector is installed to block the particles from being entrained out of the domain. The particles deflected by the deflector falling down to the fluidized bed and heat the initially placed carbon particles.

Although the particle diameter (5 mm) is larger than the perforated opening (3.8 mm), few of the particles are seen to pass through the perforated opening and go down to the bottom wall of the domain and stay there for the remaining simulation. This unrealistic phenomenon has not been resolved in this study. The simulated results are shown in Figs 5.12 to 5.15. The velocity vectors colored by temperature with 2.8 m/s gas inlet at horizontal and 4 m/s solid inlet at the draft tube (Case 6a) are shown in Fig. 5.12. The species volume fractions for different simulation time intervals from 0.2 second to 4.0 second are shown in Fig. 5.13, Fig. 5.14, and Fig. 5.15 The inlet conditions are summarized in Table 5.4.

Table 5.4 Different velocity values at different inlet for Case 6a

Parameters	***Cases 6a***	
Inlet position	Fluidized bed inlet	Draft tube inlet
Air inlet velocity at horizontal, m/s	2.8	
Air inlet velocity at perforated openings, m/s	4.0	
Air inlet velocity at draft tube, m/s		4.0
Carbon solid inlet velocity at draft tube, m/s		4.0
Inlet temperature , K	300	1000

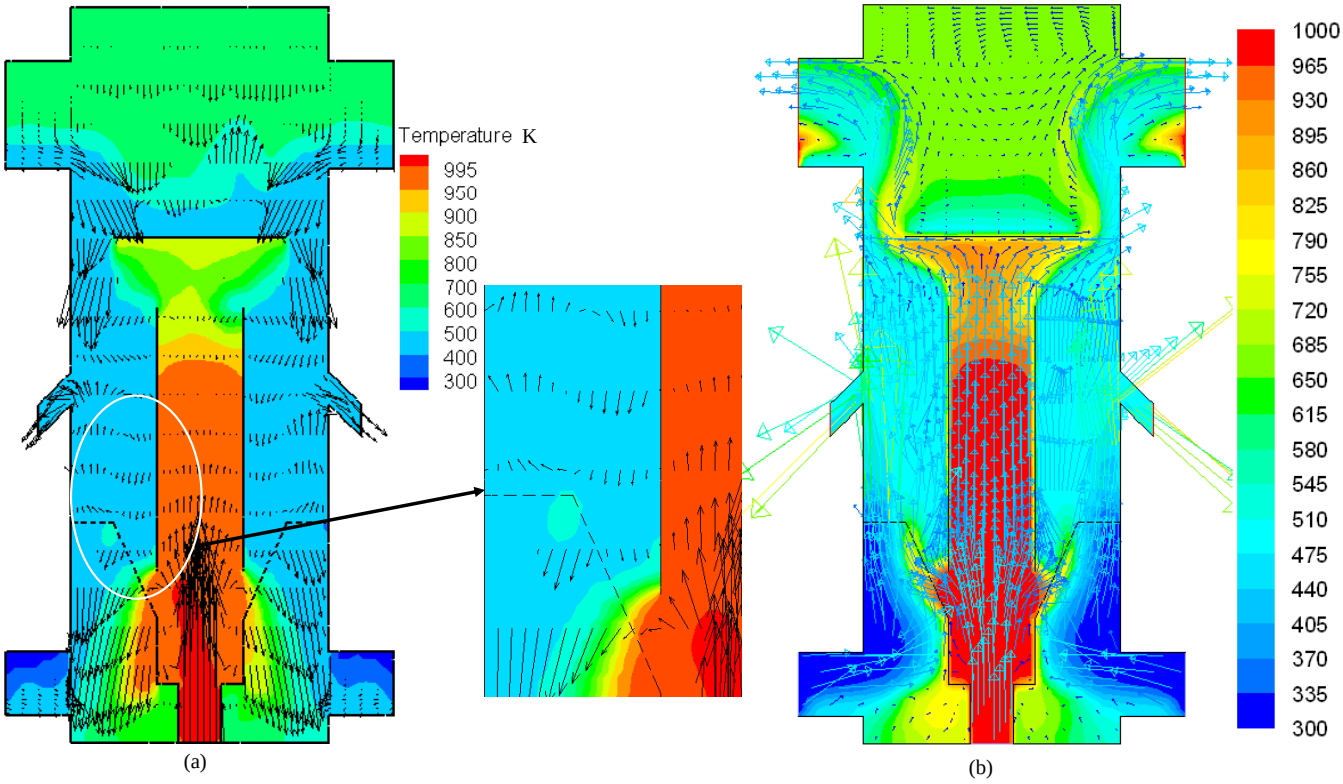

Figure 5.12 Velocity vector plots for (a) particles and (b) air colored by temperature in Kelvin with 2.8 m/s gas inlet at horizontal and 4 m/s solid inlet at draft tube in the fluidized bed mild gasifier (Case 6a)

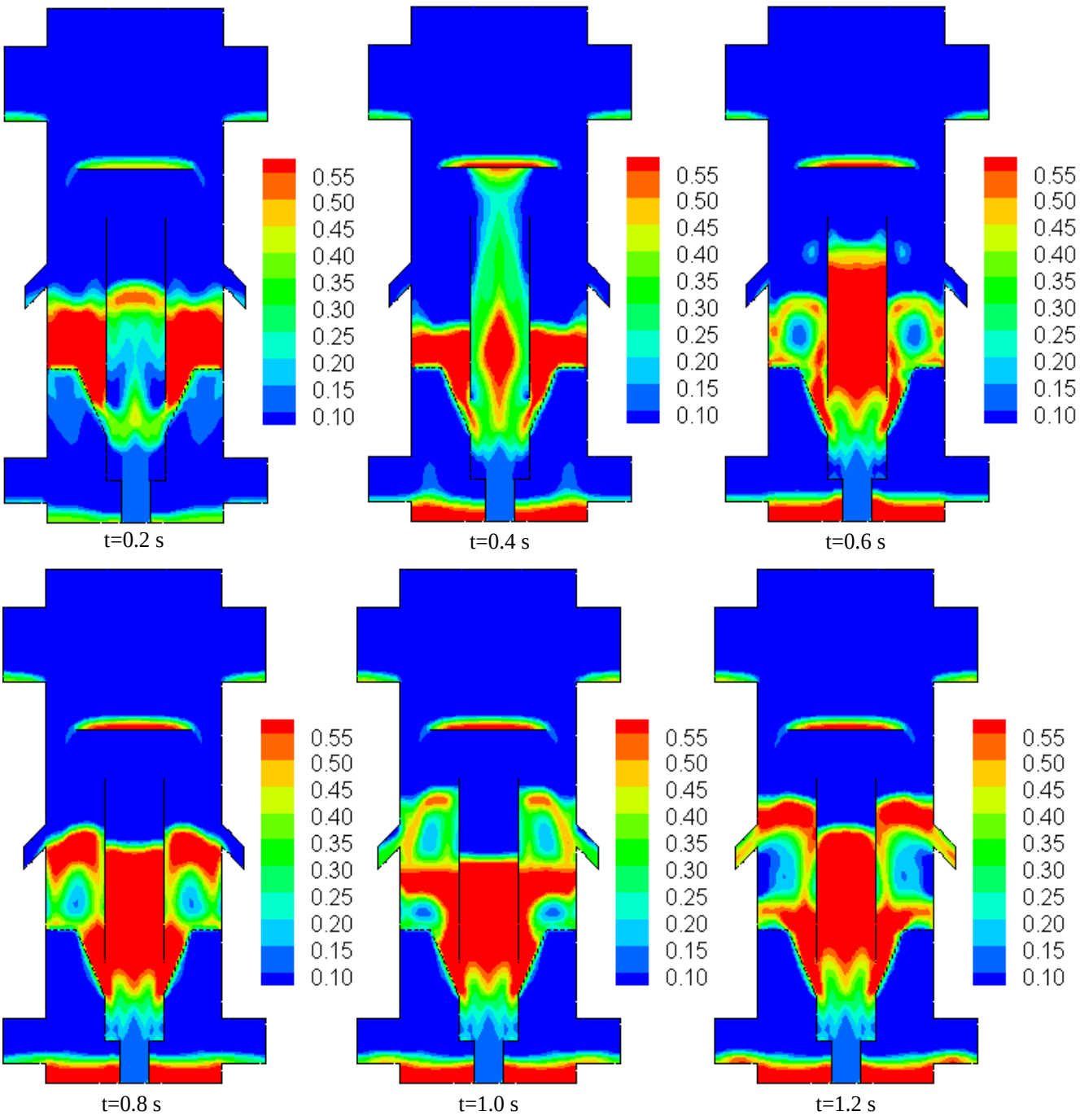

Figure 5.13 Distribution of volume fraction of carbon solid particles with 2.8 m/s at horizontal fluidization inlet and 4 m/s solid inlet at draft tube from time intervals 0.2 to 1.2 second in the fluidized bed mild gasifier (Case 6a)

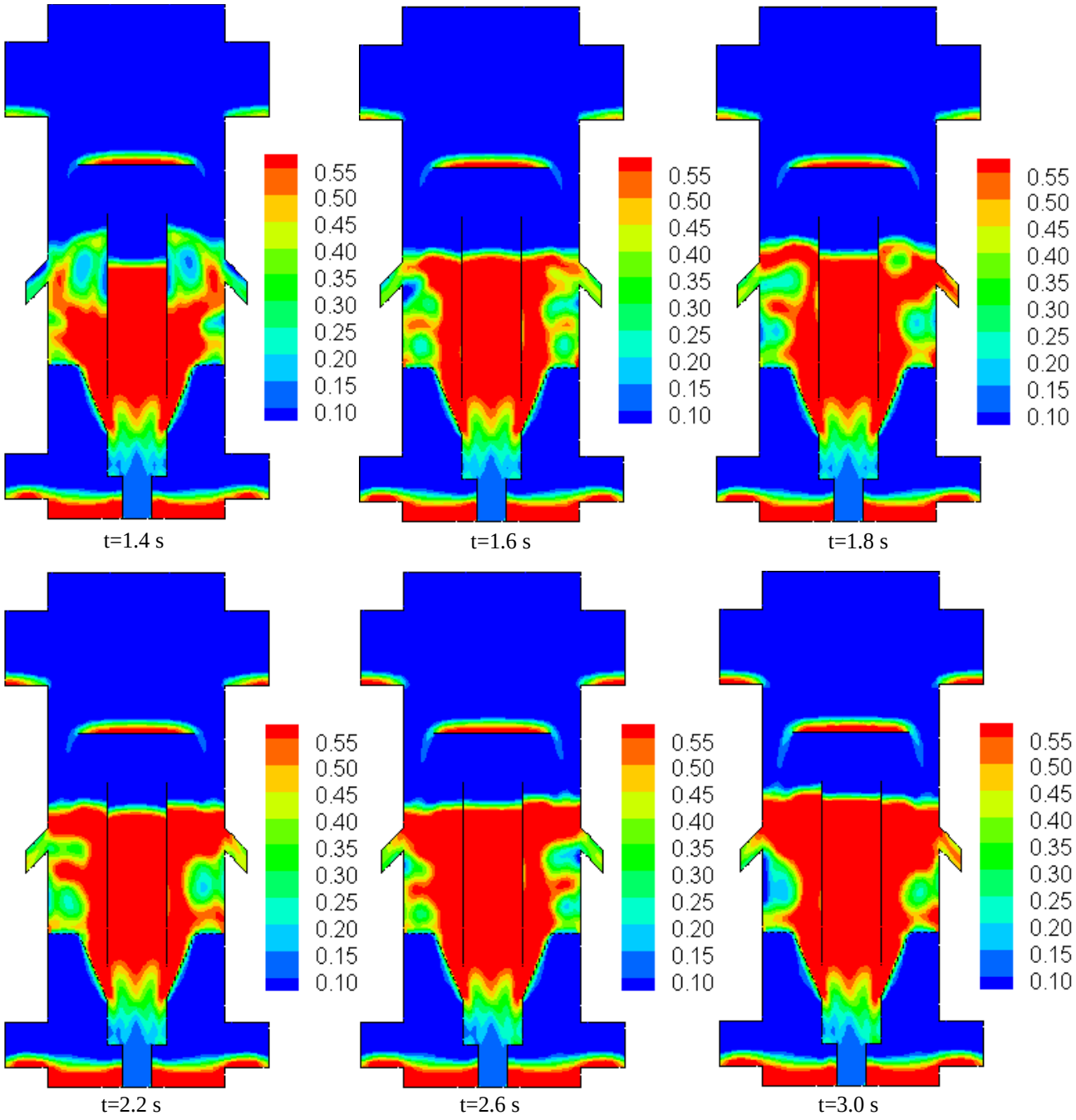

Figure 5.14 Distribution of volume fraction of carbon solid particles with 2.8 m/s fluidization air at the horizontal inlet and 4 m/s solid inlet at draft tube from time intervals 1.4 to 3.0 second in the fluidized bed mild gasifier (Case 6a)

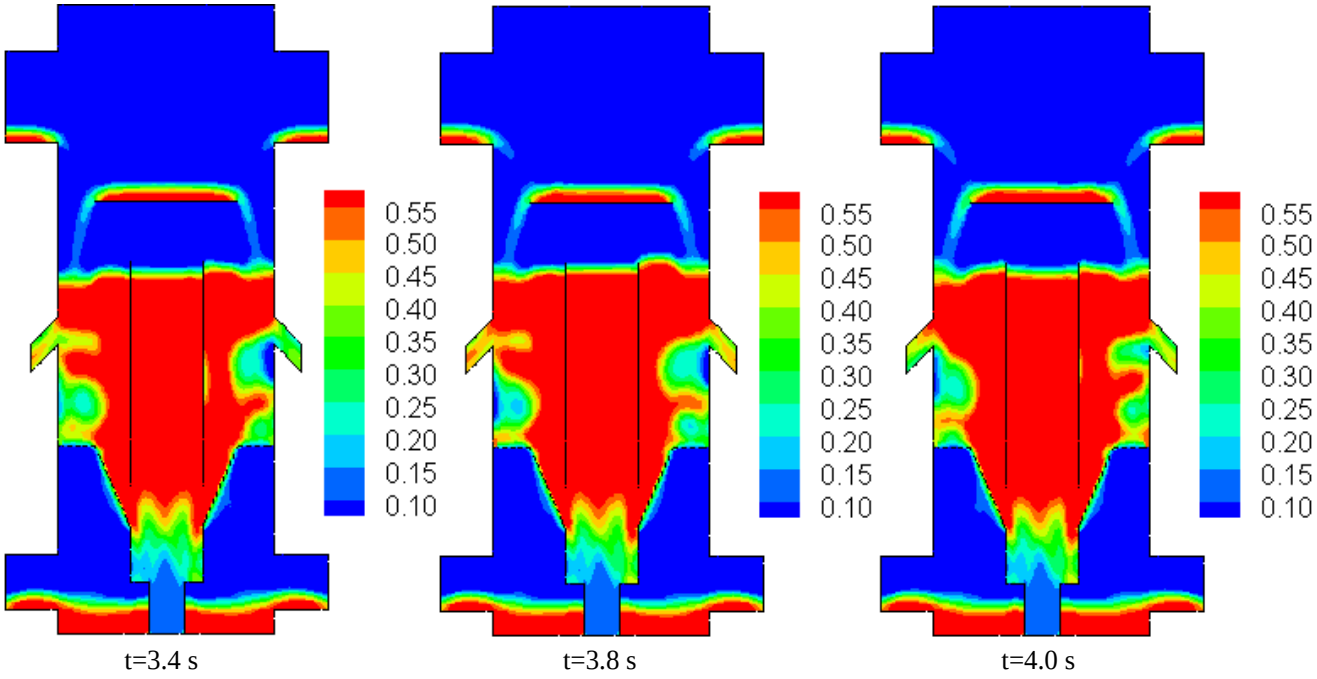

Figure 5.15 Distribution of volume fraction of carbon solid particles with 2.8 m/s gas fluidization air at the horizontal inlet and 4 m/s solid inlet at draft tube from time intervals 3.4 to 4.0 second in the fluidized bed mild gasifier (Case 6a)

5.2.3.2 Case 6b: 5 m/s solid inlet at draft tube

The velocity vectors colored by temperature distribution with 2.8 m/s fluidized gas inlet but 5 m/s solid inlet at draft tube (Case 6b) are shown in Figs. 5.16 to 5.19. The purpose of this case is to exam the effect of increasing the carbon transport air speed in the draft tube on the particle entrainment rate from the char bed into the draft tube near the bottom of the gaisifer and the potential of coal particles escaping from the outlet. It can be seen from the figure of carbon solid volume fraction for Case 6b, the carbon inlet with 5 m/s through draft tube goes upward and deflect by the deflector after 0.4 second and goes downward to the fluidized bed area after 0.6 second. This particle deflection does not happen in Case 6a; the particles stay near the outlet of draft tube during the entire simulation.

From the particle velocity vector plots (Fig. 5.16a versus Fig. 5.12a), Case 6b clearly shows more particles are entrained from the char bed into the draft tube than Case 6a near the bottom of draft tube. However, less particle volume fraction is seen (Fig. 5.19 versus Fig. 5.15) at the syngas outlet in Case 6b than Case 6a. The inlet conditions are summarized in Table 5.5.

Table 5.5 Different velocity values at different inlet for Case 6b

Parameters	***Cases 6b***	
Inlet position	Fluidized bed inlet	Draft tube inlet
Air inlet velocity at horizontal , m/s	2.8	
Air inlet velocity at perforated openings , m/s	4.0	
Air inlet velocity at draft tube , m/s		5.0
Carbon solid inlet velocity at draft tube , m/s		5.0
Inlet temperature , K	300	1000

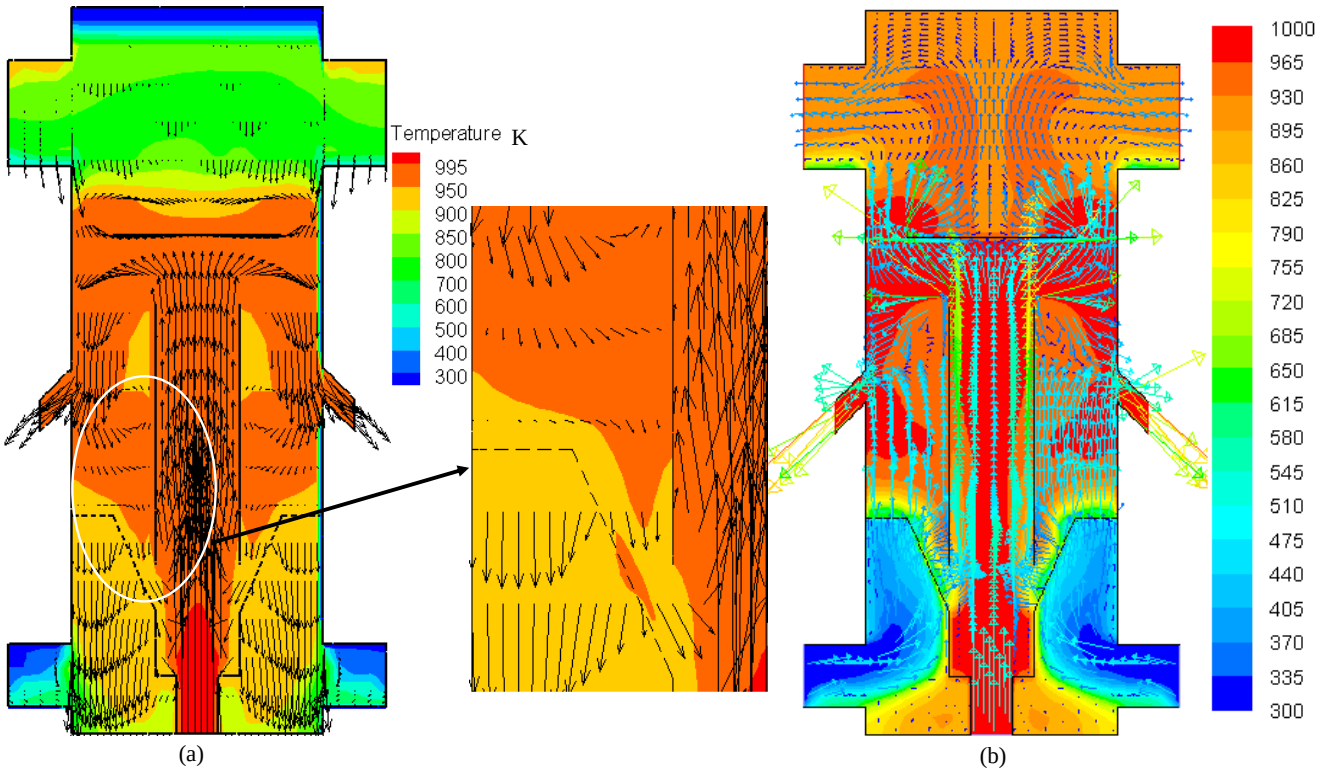

Figure 5.16 Velocity vectors plot for (a) particles and (b) air colored by temperature (K) distribution with 2.8 m/s fluidization air at the horizontal inlet and 5 m/s solid inlet at draft tube in the fluidized bed mild gasifier (Case 6b)

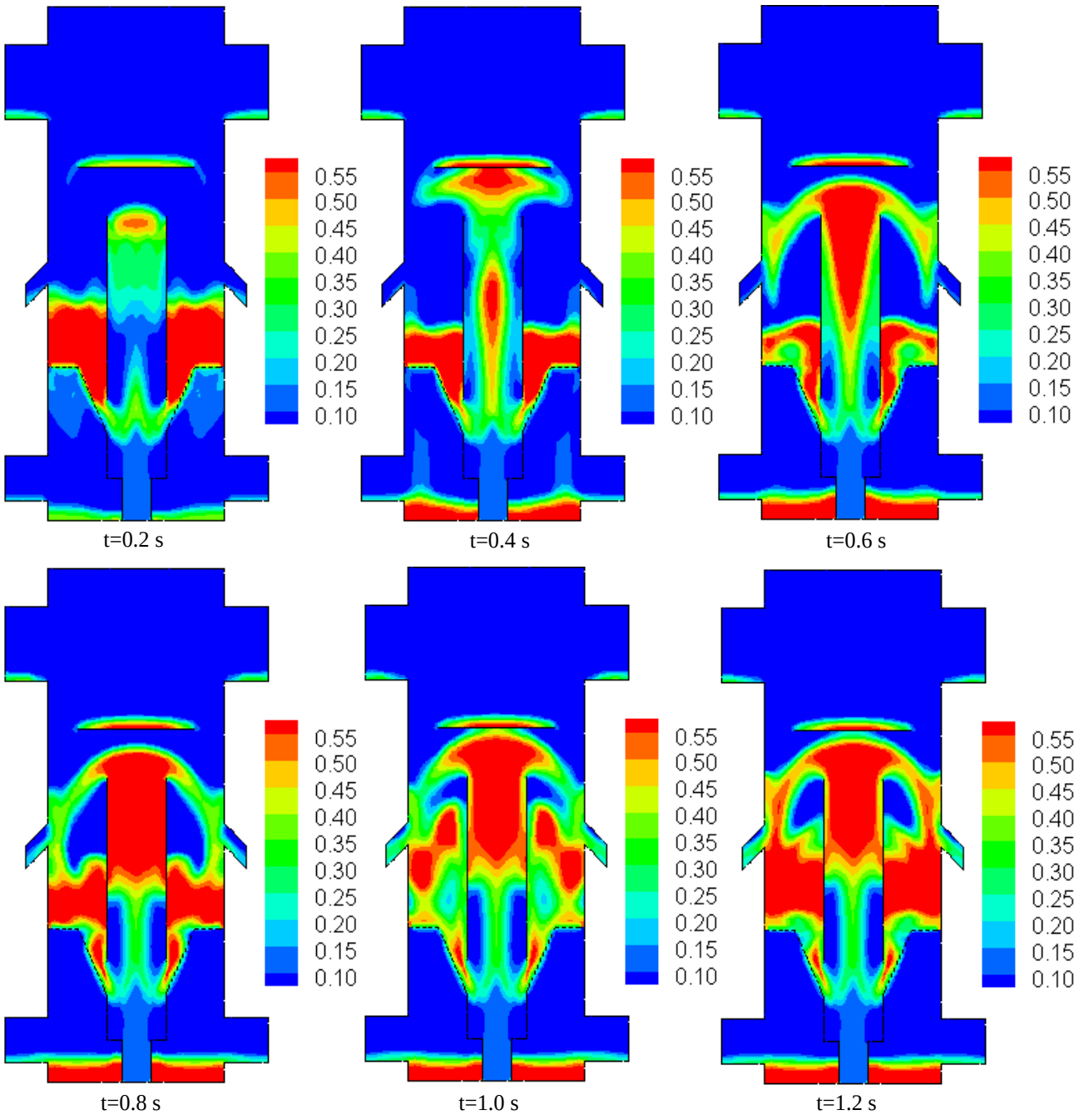

Figure 5.17 Distribution of volume fraction of carbon solid particles with 2.8 m/s fluidization air at the horizontal inlet a and 5 m/s solid inlet at draft tube from time intervals 0.2 to 1.2 second in the fluidized bed mild gasifier (Case 6b)

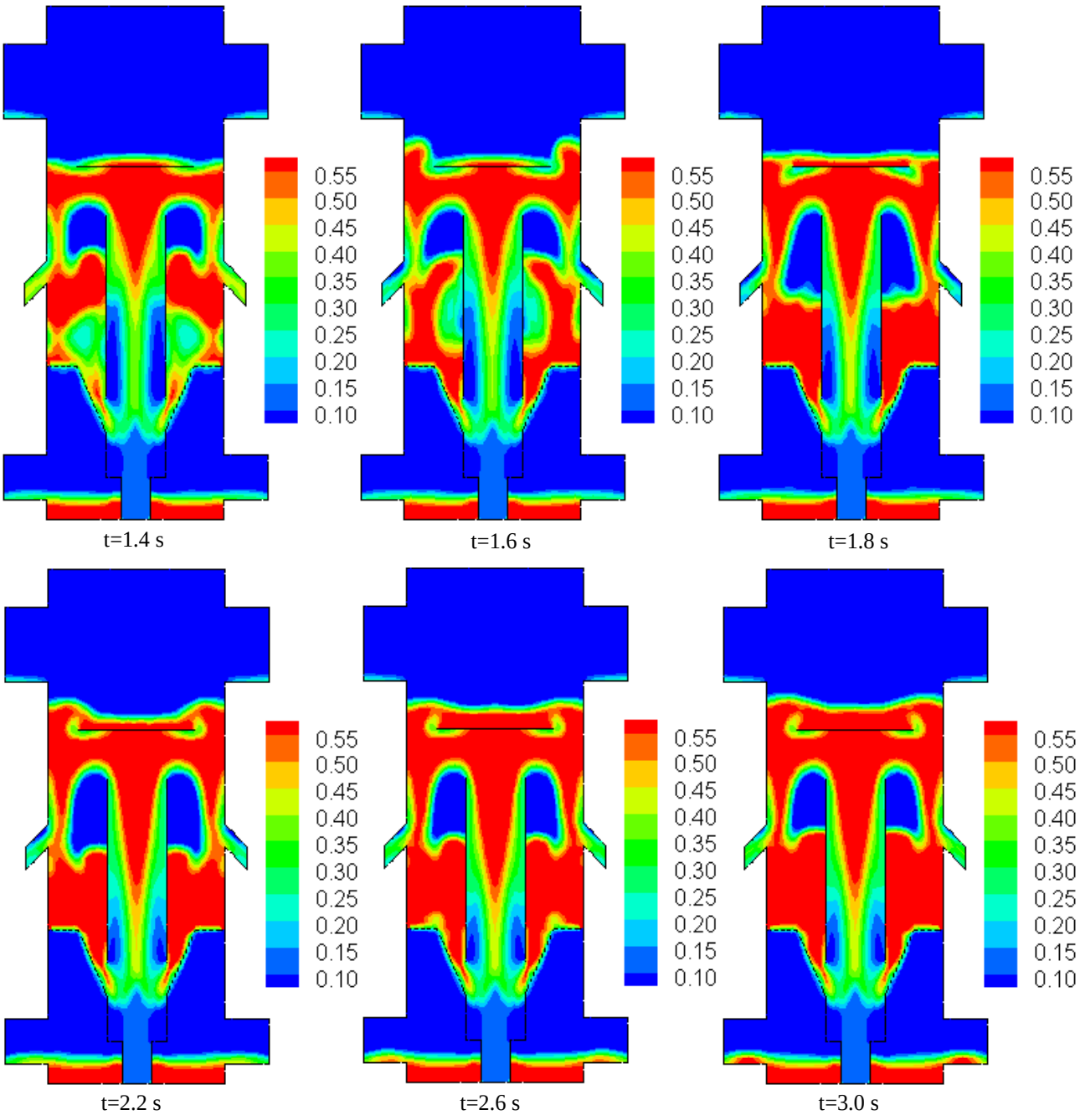

Figure 5.18 Distribution of volume fraction of carbon solid particles with 2.8 m/s fluidization air at the horizontal inlet and 5 m/s draft tube solid inlet from time intervals 1.4 to 3.0 second in the fluidized bed mild gasifier (Case 6b)

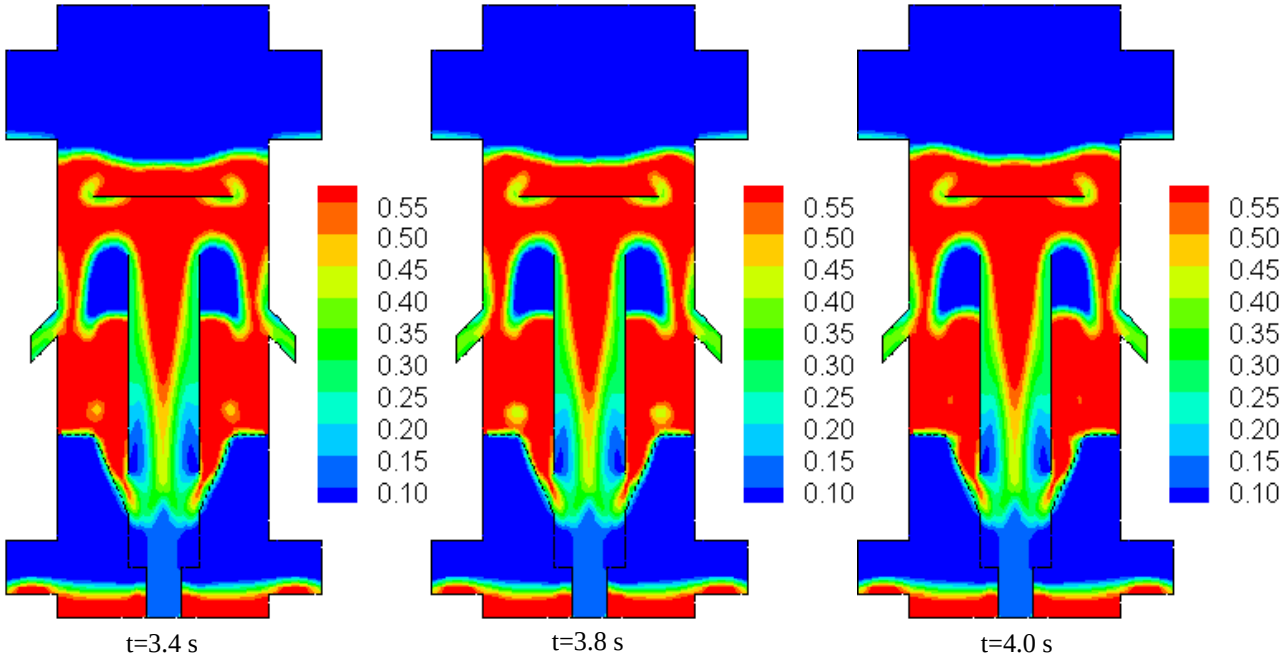

Figure 5.19 Distribution of volume fraction of carbon solid particles with 2.8 m/s at horizontal fluidization air inlet and 5 m/s solid inlet draft tube from time intervals 3.4 to 4.0 second in the fluidized bed mild gasifier (Case 6b)

5.2.4 Case 7: Heterogeneous (gas-solid) reaction with volatiles

Coal gasification is a multiphase problem between gases and coal particles, and is also a reactive flow that involves homogeneous reactions among gases and heterogeneous reactions between coal particles and gases. In this study, both gas phase (primary phase) and solid phase (secondary phase) are solved by using Eulerian multiphase model. Both homogeneous (gas-gas) reaction and heterogeneous (gas-solid) reactions are simulated in this case.

Initially, 5 mm diameter carbon solid particles are placed side by side in the fluidized bed like a bed of granular (solid) material. The air (O_2+3.76N_2) consisting of 21% O2 and 79% volume fraction of air enters the two horizontal gas inlets with 2.8 m/s velocity at 300 K and passes up through the perforated openings into the fluidized bed.

The carbon transported by air and water vapor enters the draft tube through the vertical draft-tube's bottom inlet with a velocity of 4 m/s at 300 K. The draft tube is designed to isolate fluidized bed from contacting oxygen in the air and to transfer heat to the fluidized bed through the draft tube wall. Above the draft tube, a deflector is installed to block the particles from being entrained out of the gasifier. There are four outlets, two for char at middle portion and two for

the produced syngas at the top portion of the gasifier. The inlet conditions are summarized in Table 5.6.

This case investigates the exit temperature and distribution of gas mass fraction by introducing the five global gasification reactions Eqs.R1.1 to R1.5 together with two volatiles reactions Eqs.R1.6 and R1.7 in the fluidized bed mild gasifier. The inlet conditions are summarized in Table 5.6. The Global Gasification Reaction used in this case is R1.1 to R1.5 with nitrogen (N_2) as inert gas.

As shown in Fig. 5.20, some carbon solid particles are carried away by the syngas at the syngas exits on top of the gasifier. These particles will be collected through a cyclone unit outside the gasifier. In this case, the finite rate/eddy-dissipation model is used for the three heterogeneous reactions R1.1 to R1.3, based on the work of A. P. Mann and J. H. Kent (1994) given in Chapter three. A user defined function (UDF) must be written and used in this case for getting the reaction rates effects incorporated into the simulation. Eddy-dissipation model is still used for the two homogeneous reactions R1.4 and R1.5 and two volatiles reactions Eqs.R1.6 and R1.7. The residence time as well as reaction rate is not sufficient for all the five global gasification reactions to be completed when the flow exits the gasifier. The distribution of various species mass fraction in the fluidized bed mild gasifier is shown in Fig. 5.20. The temperature distribution of carbon solid and air, and volume fraction of carbon solid are shown in Fig. 5.22. and Fig. 5.23 shows the particle and air velocity vectors colored by temperature distribution. Due to limited air supply in the draft tube, exothermic reaction is low in the draft tube. The oxygen in the fluidization air activates exothermic reactions to cook the char particles to above 1000 K (Fig. 5.22a) while the gas mixture temperature is about 1150K in the fluidization bed. Volatile matter is seen to be thermally cracked in the fluidized bed and freeboard (Fig. 5.20) with some trace of benzene.

The mass weighted averages of CO, CO_2, H_2, C_6H_6 (Benzene) and N_2 (as inert gas) at outlet of the domain are 0.2706, 0.1781, 0.0228, 0.0524 and 0.3687 respectively. The mass weighted average temperatures for the gas phase and solid phase are 907.04 K and 856.45 K respectively at the outlet.

Figure 5.23 shows side by side the particle velocity vectors versus the gas velocity vectors. The particle velocity field clearly shows the circulation in the fluidized bed and a minor entrainment of char from the bed to the draft tube.

Table 5.6 Parameters, boundary and operating conditions for Case 7

Parameters	***Cases 7***	
Inlet position	Fluidized bed inlet	Draft tube inlet
Fuel	air	carbon solid, air, volatiles
Air inlet velocity at horizontal, m/s	2.8	
Air inlet velocity at perforated openings, m/s	4.0	
Air inlet velocity at draft tube, m/s		4.0
Carbon solid inlet velocity at draft tube, m/s		4.0
Inlet temperature, K	300	300
Mass fraction at inlet		
O_2	0.2331	0.12
N_2	0.7669	0.3946
$CH_{2.121}O_{0.585}$	0	0.4854
Operating pressure (pascal)	101325	101325
Operating temperature (K)	288.16	288.16
Operating density (kg/m^3)	1.225	1.225
Gravitational acceleration (m/s^2)	9.81	9.81
Wall temperature, K	Adiabatic	Adiabatic

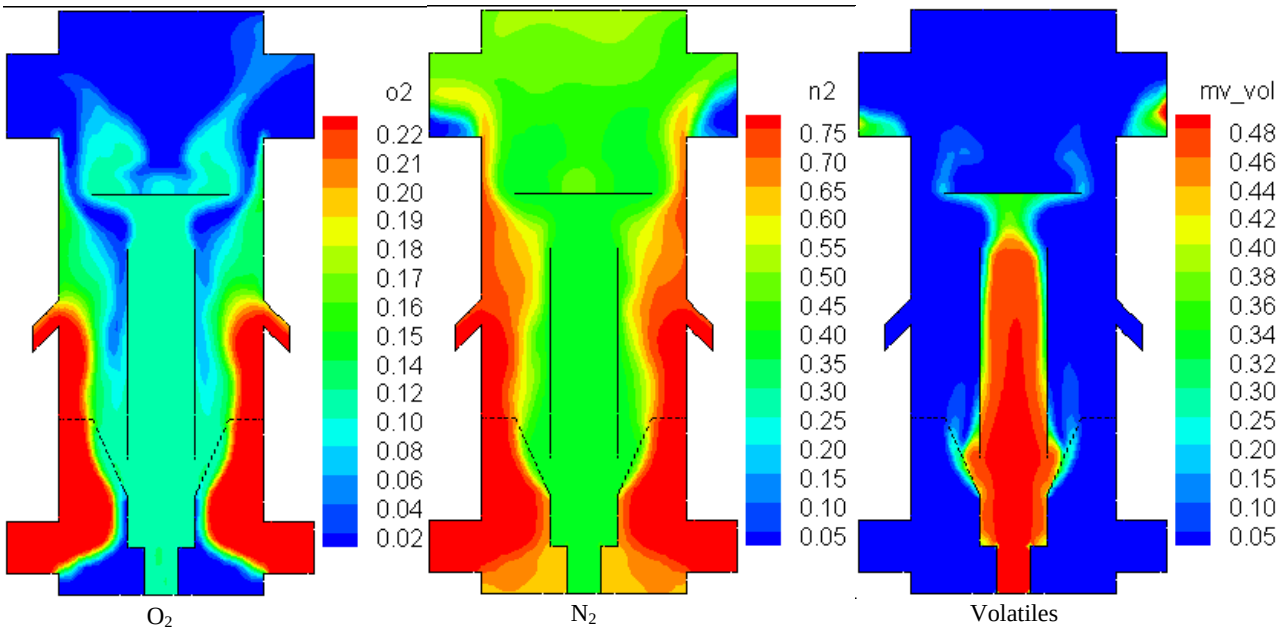

Figure 5.20 Distribution of reactant gas mass fraction in the fluidized bed mild gasifier including volatiles with particles (Case 7)

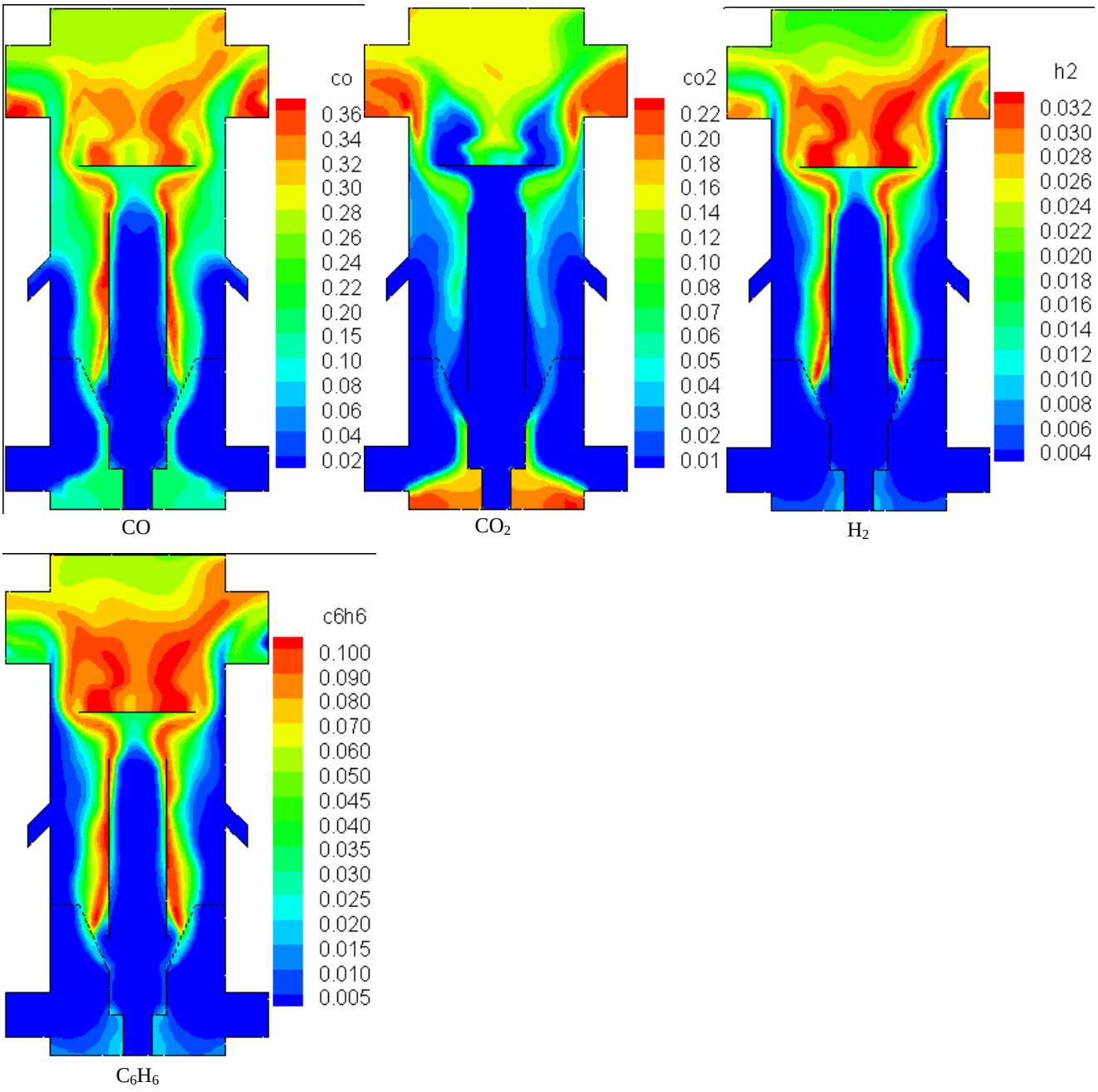

Figure 5.21 Distribution of product gas mass fraction in the fluidized bed mild gasifier including volatiles with particles (Case 7)

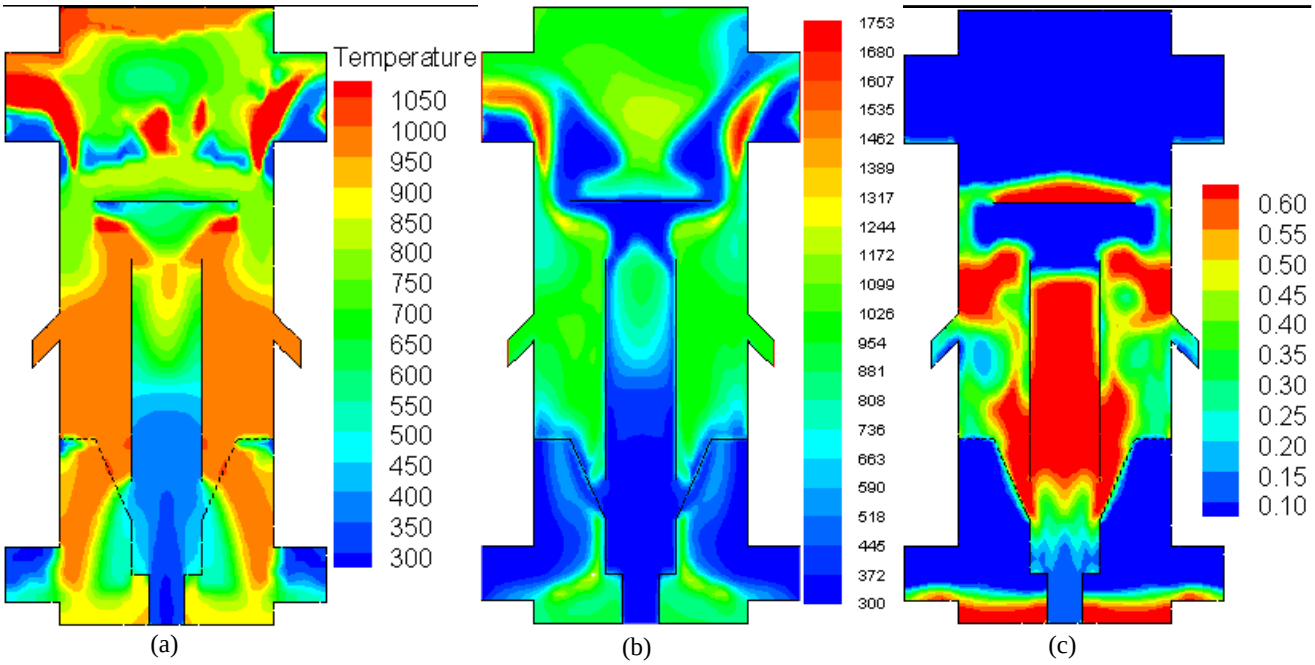

Figure 5.22 Temperature distribution of (a) carbon solid (b) gas mixture in Kelvin and (c) volume fraction of carbon solid in the fluidized bed mild gasifier (Case 7)

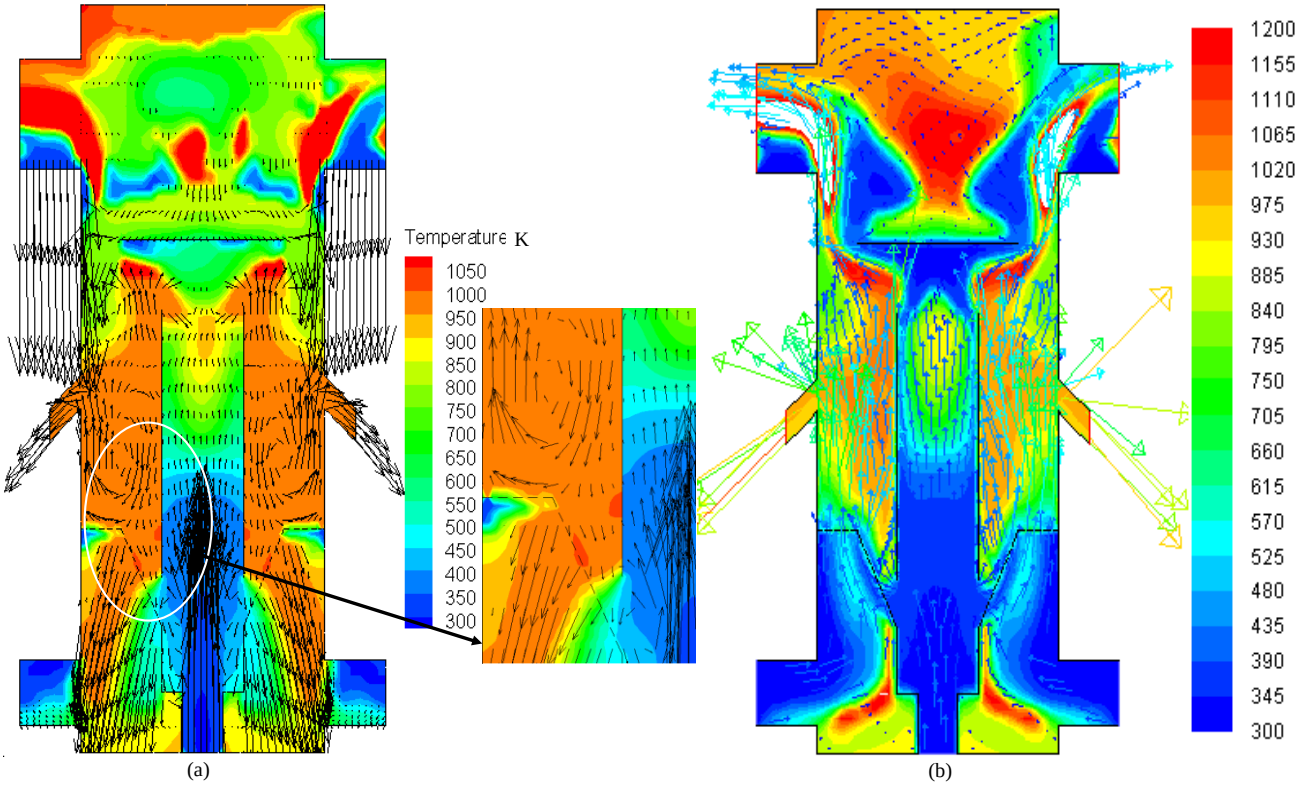

Figure 5.23 Velocity vector plots for (a) particles and (b) air colored by temperature (K) distribution in the fluidized bed mild gasifier (Case 7)

5.2.5 Compare the Velocity Fields of different Cases (Case 4 and 7)

Since the efforts of solving non-reactive flow field is much less than solving multiphase reactive flow, including both heterogeneous and homogeneous flow, one of the common questions for designs is whether the non-reactive flow field can be quickly used to obtain an adequate idea for screening various preliminary design concepts. To help answer this question, a comparison of three difference cases (Fig. 5. 24) is analyzed in this section. The flow field of Case 4 (without particles and non-reactive flow) is shown in Fig. 5.24a. The air enters with 1000 K in the draft tube inlet as well as in the fluidization inlet at 300K. The air from the draft tube hits the deflector, merges with the fluidization air, and passes through the narrow passage around the deflector. Part of the fluidization air exits from the char outlets in the middle of the gasifier in this case without including particles. The air flow exiting the char outlets should be significantly reduced when char particles are included. After the flow accelerates through the passage, part of the air exits through the upper section of the outlets and part of the air circulate in the top section of the gasifier. When the air accelerates through the passage, it generates a low pressure region near each of the gas outlets and creates a backflow in the outlet. The appearance of the backflow indicates inefficient fluid mechanics design of the current geometry and improvement is needed.

When particles are included with heterogeneous reactions in Case 7, the flow field shown in Fig. 5.24b is similar to Case 4. Although the appearance of the vector plot in Fig. 5.24b looks different from Fig. 5.24a, they are essentially similar because Fig. 5.24b has more cells to show the velocity vectors in a less structured approach. Note that the inlet gas temperature at the draft tube for Cases 4 is given as 1000K, whereas in Case 7, 300K is assigned.

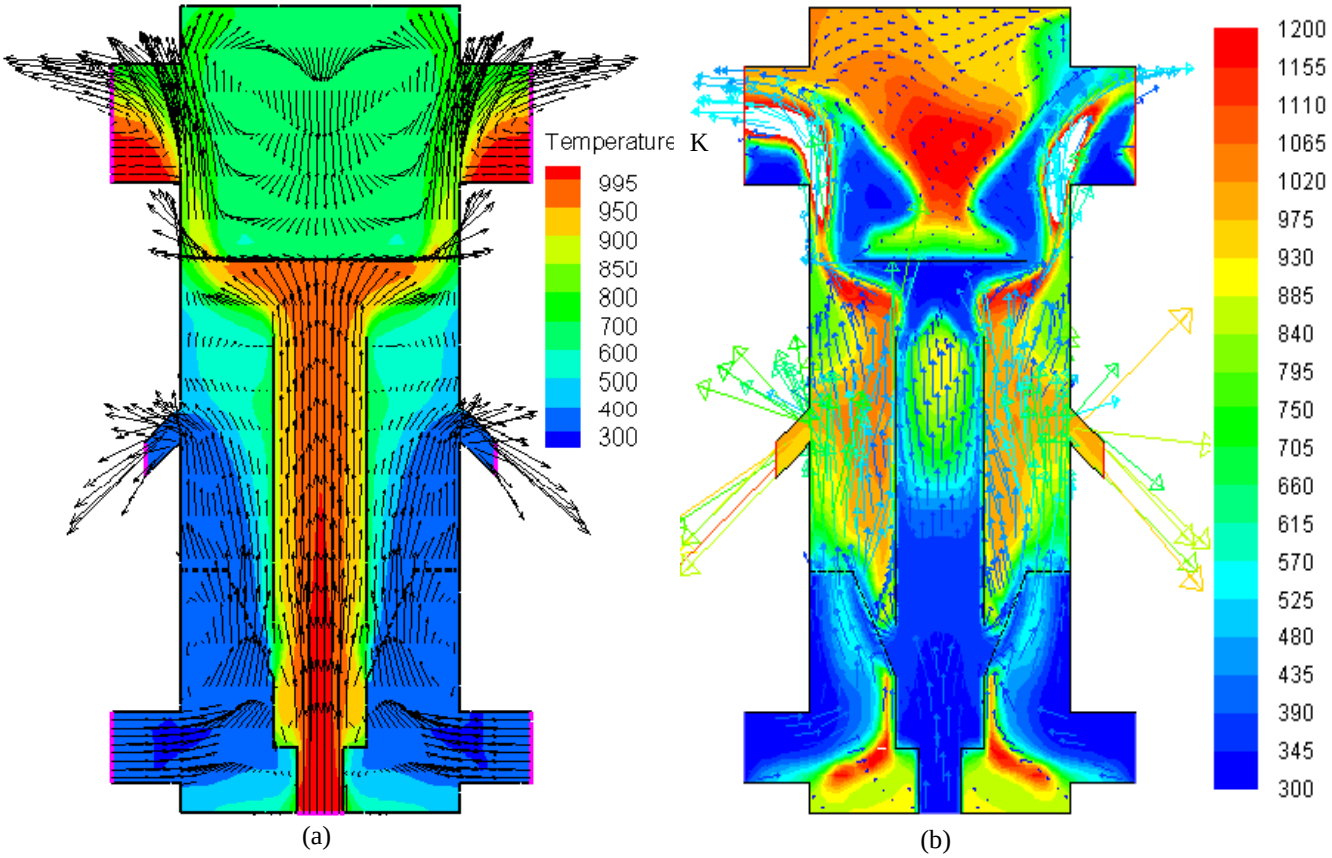

Figure 5.24 Air velocity vector plots (a) without particles and reactions (Case 4) and (b) with both particles and reactions (Case 7) in the fluidized bed mild gasifier colored by temperature (K) distribution. Note that the vectors are not in the same scale in each case.

Figure 5.25 shows that the particles velocity vectors for Case 6a without reactions is similar to Case 7 with reactions. Analysis and interpretation of these figures must be carefully done because the velocity vectors do not present the information of particle volume ratio. Some large downward particle velocity present below the perforated fluidization grid only represents very limited particle volume ratio as shown in Fig. 5.22c. Minimal particles are seen above the deflector indicating the current design and the flow velocity employed are adequate for containing particles inside the gasifier.

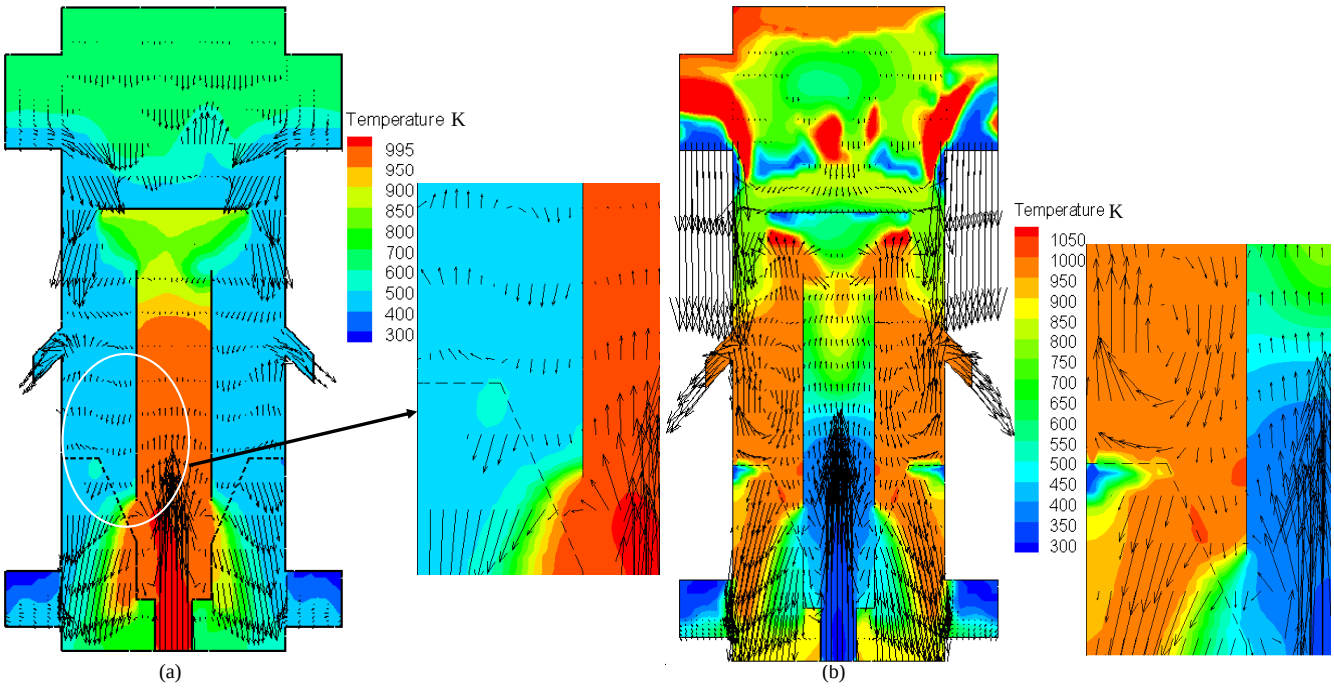

Figure 5.25 Particles velocity vector plots for (a) hot gas inlet in the draft tube without reactions (Case 6a) and (b) cold gas inlet in the draft tube with reactions (Case 7) colored by temperature in Kelvin with 2.8 m/s gas inlet at horizontal and 4 m/s solid inlet at draft tube in the fluidized bed mild gasifier (Case 6a)

5.2.6 Grid Sensitivity Study for Case 7

A grid sensitivity study has been conducted using three different grids: coarse grid (6,960 cells), medium grid (30,876 cells), and fine grid (65,355 cells). Parameters and operating conditions for Case 7 given in Table 5.7 are used in this grid sensitivity study. Table 5.7 shows, after 2.4 seconds, the mass-weighted average temperature and species mass fractions of the exit gas for all grids. In table 5.7, the exit temperature and product gas compositions are different for different grid sizes. Therefore, the simulation is very sensitive to grid size. It can be seen the solutions although all achieve convergence, they have not reached grid-independence. Since the goal of this project for establishing the simulation model has been achieved, further refinement of the solution will be left for future study when more computational resources are available.

Table 5.7 Grid sensitivity study of Case 7

Parameters	***Coarse Grid (6,960 cells)***	***Medium Grid (30,876 cells)***	***Fine Grid (65,355 cells)***
Exit gas temperature (K)	1311.61	938.69	840.64
Exit carbon solid temperature (K)	1289.58	869.24	809.32
Exit mass fraction of CO	0.1552	0.1915	0.1771
Exit mass fraction of CO_2	0.1823	0.1786	0.1696
Exit mass fraction of H_2	0.0023	0.0063	0.0033

CHAPTER SIX
CONCLUSIONS

In this study, a comprehensive modeling and numerical investigation of Fluidized Bed Mild Gasifier has been conducted to provide an innovative clean coal technology by using the commercial CFD solver ANSYS/FLUENT. The simulations were conducted with different boundary conditions and heterogeneous reaction rates compiled from the published experimental results. The results provide comprehensive information concerning the thermal-flow behavior and gasification process inside the specially designed fluidized-bed mild gasifier.

Eulerain-Eulerian method is employed to calculate both the primary phase (air) and the secondary phase (coal particles). The Navier-Stokes equations and seven species transport equations are solved with three heterogeneous (gas-solid) and two homogeneous (gas-gas) global gasification reactions with two volatiles reactions. For each homogeneous reaction both finite rate and eddy-breakup, reaction models are solved, and the smaller of the two rates is used.

The study begins with the simulation of single-phase turbulent flow and heat transfer inside a simplified 2D preliminary geometry. To understand the thermal-flow behavior, this simulation is followed by 2D fluidized bed mild gasifier.. This study also simulates the five global gasification reactions and two volatiles reactions that start with homogeneous (gas-gas) reactions and progressively adding one equation at a time in both simplified preliminary geometry and fluidized bed mild gasifier. Finally, the particles are introduced with heterogeneous reactions in fluidized bed mild gasifier. When no experimental data are available for verification, this progressive building process from simple to complex models allows step-by-step examinations of the effect from each addition of new parameters to ensure the simulated results are physically reasonable and fundamentally sound.

The results are summarized below:

- ✓ In the simplified preliminary geometry the adiabatic flame temperature (1070 K) predicted by homogeneous reaction model (Fig. 5.4 of Case 2) was validated with the equilibrium calculation and found to be a good match between these values. The mass fraction of product gas is also validated with the equilibrium calculation (Fig. 5.3 of Case 2).
- ✓ In the fluidized bed mild gasifier, the five global gasification reactions with two volatiles reactions are simulated. The mass fraction of product gas is also validated with the equilibrium calculation (Fig. 5.10 of Case 5).
- ✓ The minimum fluidization velocity is found to be 2.65 m/s seconds, which is close to the 2.06 m/s calculated from Ergun equation.
- ✓ Both instantaneous (homogeneous reaction) and finite-rate (heterogeneous reaction) gasification models are used in the simulation. The results show that the heterogeneous model predicts the temperature and species concentration reasonably well. The instantaneous gasification model over-predicts reaction rates. Gas temperature and species distributions indicate that reactions in the instantaneous gasification model occur very fast and finish very quickly with a indicating 100% carbon conversion rate (Fig. 5.3 of Case 2 and Fig. 5.9 of Case 5). Meanwhile, the reaction in the finite-rate model, which involves gas-solid reactions, occurs slower with unburned chars at the exit. The deflector is found successful in deflecting the majority of particles, but still some char particles escaped and are carried out by the syngas stream.
- ✓ One abnormal result is not resolved in this study and is left for future studies. The coal particles are injected with a larger diameter than the perforated plate openings; but during a non-reacted simulation, some particles are seen falling through the openings in Case 6. This could happen in a reacted flow simulation, but it should not occur in a non-reacted flow condition.

Recommended Future Studies

Based on the present studies, the following studies are recommended to improve the simulation model and the ongoing design of the ECCC's Fluidized Bed Mild Gasifier:

a. Implement different finite reaction rates for the reactions to obtain more accurate results.
b. Incorporate devolatilization and gasification models to simulate the volatiles releasing rate, reaction rate, and gasification phenomena inside the gasifier.
c. Compare the effect of different turbulence models on the results.
d. Conduct experiments to verify the CFD results.
e. Conduct simulation using various correlations of minimum fluidization velocity and different particle size.
f. Investigate and resolve modeling issues related to coal particles falling through perforated openings with a dimension less than the coal particle's diameter.

REFERENCES

Arastoopour, H., Lin, D., and Gidaspow, D., 1980, "Hydrodynamic Analysis of Pneumatic Transport of a Mixture of Two Particle Sizes," Multiphase Transport, Hemisphere Publishing Corp., Washington, 1980, pp 1853-1871.

Arastoopour, Hamid, Wang, Ching Huei, and Weil, Sanford A., 1982, "Particle-Particle Interaction Force in a Dilute Gas-Solid System," Journal of Chemical Engineering Science, Vol. 37, No. 9, 1982, pp 1379-1386.

Arastoopour, Hamid and Cutchin III, Joseph H., 1985, "Measurement and Analysis of Particle-Particle Interaction in a Cocurrent Flow of Particles in a Dilute Gas-Solid System," Journal of Chemical Engineering Science, Vol. 40, No. 7, 1985, pp 1135-1143.

Ahmadi, G. and Shahinpoor, M., 1983, "A Note on Collision Operators in Rapid Granular Flows of Rough Inelastic Particles," Journal of Powder Technology, Vol. 35, 1983, pp 119-122.

Benyahia, Sofiane., Syamlal, Madhava and O'Brien, Thomas J., 2004, "The Effect of Model Parameters on the Predictions of Core-Annular flow behavior in a fast Fluidized Gas/Solids Bed," Annual Meeting Conference Proceedings, 2004, pp 3283-3297.

Boerner, A., Renz, H. Qi, U., Vasquez, S., and Boysan, F., 1995, "Eulerian Computation of Fluidized Bed Hydrodynamics-A Comparison of Physical Models," Fluidized Bed Combustion, Vol. 2, ASME 1995, pp 775-787.

Comelissen, Jack T., Taghipour, Fariborz., Escudie, Renaud., Ellis, Naoko., Grace, John R., 2007, "CFD Modeling of a Liquid-Solid Fluidized Bed," Chemical Engineering Science, Vol. 62, 2007, pp 6334-6348.

Chapman, S. and Cowling, T. G., 1990, "The Mathematical Theory of Non-Uniform Gases," Cambridge University Press, Cambridge, England, 3rd edition.

Chejne, F. and Hernandez, J.P., 2002, "Modeling and Simulation of Coal Gasification process in Fluidized Bed," Fuel, Vol. 81, 2002, pp 1687-1702.

Dalla Valle, J. M., 1948, Micromeritics, Pitman, London.

Ding, Jianmin and Gidaspow, Dimitri, 1990, "A Bubbling Fluidization Model Using Kinetic Theory of Granular Flow," AlChE Journal, Vol. 36, No. 4, 1990, pp 523-538.
Elgobashi, S. E., and Abou-Arab, T. W., 1983, "A Two-Equation Turbulence Model for Two-Phase Flows," Phys. Fluids, Vol. 26, No. 4, pp 931–938.

Ergun, Sabri, 1952, "Fluid Flow through Packed Columns," Journal of Chemical Engineering Progress, Vol. 48, No. 2, 1952, pp 89-94.

Enwald, H. and Almstedt, A.E., 1999, "Fluid Dynamics of a Pressurized Fluidized Bed: Comparison between Numerical Solutions from Two-Fluid Models and Experimental Results," Journal of Chemical Engineering Science, Vol. 54, 1999, pp 329-342.

Enwald, H., Peirano, E., Almstedt, A.E., and Leckner, B., 1999, "Simulation of the Fluid Dynamics of a Bubbling Fluidized Bed. Experimental Validation of the Two-Fluid Model and Evaluation of a Parallel Multiblock Solver," Chemical Engineering Science, Vol. 54, 1999, pp 311-328.

Faeth, G.M., 1987, "Mixing, Transport and Combustion in Sprays," Progress in Energy Combustion Science, Vol. 13, pp 293-345.

Fedors, R.F. and Landel, R.F, 1979, "An Empirical Method of Estimating the Void Fraction in Mixtures of Uniform Particles of Different Size," Journal of Powder Technology, Vol. 23, 1979, pp 225-231.

FLUENT 6.3 User's Guide, February 2003.

Gidaspow, Dimitri and Ettehadleh, Bozorg, 1983, "Fluidization in Two-Dimensional Beds with a Jet. 2. Hydrodynamic Modeling," Journal of Industry Engineering Chemical Fundamentals, Vol. 22, No. 2, 1983, pp 193-201.

Gidaspow, Dimitri., Lin, Chungllang and Seo, Yong C., 1983, "Fluidization in Two-Dimensional Beds with a Jet. 1. Porosity Distributions," Journal of Industry Engineering Chemical Fundamentals, Vol. 22, No. 2, 1983, pp 187-193.

Gidaspow, D., Bezburuah, R. and Ding, J., 1992, "Hydrodynamics of Circulating Fluidized Beds, Kinetic Theory Approach," Fluidization VII, Proceedings of the 7th Engineering Foundation Conference on Fluidization, pp 75–82.

Gunn, D.J., 1978, "Transfer of Heat or Mass to Particles in Fixed and Fluidized Beds," Journal of Heat Mass Transfer, Vol. 21, 1978, pp 467-476.

Grewal, W.S., Saxena, S.C., 1980, "Comparison of commonly used relations for minimum fluidization velocity of small solid particles," Powder Technology, Vol. 26, No. 2, pp 229–238.

Hinze, J. O., 1975, Turbulence, McGraw-Hill Publishing Co., New York.
Huilin, Lu., Gidaspow, Dimitri., Bouillard, Jacques and Wentie, Liu, 2003, "Hydrodynamic Simulation of Gas-Solid flow in a riser using Kinetic Theory of Granular flow," Journal of Chemical Engineering, Vol. 95, 2003, pp 1-13.

Hong, R. Y., Guo, Q. J., Luo, G. H., Zhang, J. Y., and Ding, J., 2003, "On the Jet Penetration Height in Fluidized Beds with Two Vertical Jets," Powder Technology, Vol. 133, 2003, pp 216-227.

Jiradilok, Veeraya., Gidaspow, Dimitri., Damronglerd, Somsal., Koves, William J., and Mostofi, Reza, 2006, "Kinetic Theory based CFD Simulation of Turbulent Fluidization of FCC Particles in a riser," Chemical Engineering Science, Vol. 61, 2006, pp 5544-5559.

Kuipers, J.A.M., Prins, W. and Van Swaaij, W.P.M., 1992, "Numerical Calculation of Wall-to-Bed Heat-Transfer Coefficients in Gas-Fluidized Beds," AlChE Journal, Vol. 38, No. 7, July 1992, pp 1079-1091.

Keairns, D. L., Archer, D. H., Hamm, J. R., Lancaster, B. W., O'Neill, E. P., Newby, R. A., Peterson, C. H., Sun, C. C., Sverdrup, E. F., Vidt, E. J., and Yang, W. C., "Systems Implications of Desulfurization by Limestone in Pressurized Fluidized Bed Combustion," Westinghouse Research Laboratories, pp 493-523.

Lebowitz, J.L., 1964, "Exact Solution of Generalized Percus-Yevick Equation for a Mixture of Hard Spheres," Journal of Experimental and Theoretical Physical Review, Vol. 133, No. 4A, 1964, pp A895-A899.

Lun, C.K.K., Savage, S.B., Jeffrey, D.J., and Chepurniy, N., 1984, "Kinetic Theories for Granular Flow: inelastic particles in Couette flow and slightly inelastic particles in a general flowfield," Journal of Fluid Mechanics, Vol. 140, 1984, pp 223-256.

Mathiesen, Vidar., Solberg, Tron., and Hjertager, Bjqrn, H., 2000, "Predictions of Gas/Particle Flow with an Eulerian Model including a Realistic Particle Size Distribution," Powder Technology, Vol. 112, 2000, pp 34-45.

Nakamura, K. and Capes, C.E, 1976, "Vertical Pneumatic Conveying of Binary Particle Mixtures," Fluidization Technology, editors Keairns, D.L., Hemisphere Publishing Corp., Washington, 1976, pp 159-184.

Nakamura, M., Hamada, Yoichi., Toyama, Shigeki., Fouda, A.K. and Capes, C.E., 1983, "An Experimental Investigation of Minimum Fluidization Velocity at Elevated Temperature and Pressures," Proceedings: 33rd Canadian Chemical Engineering Conference, Vol. 2, 1983, pp 515-520.

O'Brien, T.J. and Syamlal, M., 1990, "NIMPF: A Non-isothermal Multi particle Fluidized Bed Hydrodynamic Model," Journal of ASME, Vol. 91, 1982, pp 65-72.
Ocampo, A., Areanas, E., Chejne, F., Espinel, J., Londono, C., Aguirre, J., and Perez, J.D., 2003, "An Experimental Study on Gasification of Colombian Coal in Fluidized Bed," Journal of Fuel, Vol. 82, 2003, pp 161-164.

Panneerselvam, R., Savithri, S., and Surneder, G. D., 2007, "CFD Based Investigation on Hydrodynamics and Energy Dissipation due to Solid motion in Liquid Fluidized Bed," Journal of Chemical Engineering, Vol. 132, 2007, pp 159-171.

Pain, C. C., Mansoorzadeh, S., and Oliveira, C. R. E. de, 2001, "A Study of Bubbling and Slugging Fluidized Beds using the Two-Fluid Granular Temperature Model," International Journal of Multiphase Flow, Vol. 27, 2001, pp 527-551.

Patanker, S.V., Numerical Heat Transfer and Fluid Flow, McGraw Hill, 1980.
Ranz, W. E., and Marshall, W. R., March 1952, Jr. Evaporation from Drops, Part I. Chemical Engineering Progress, Vol. 48, No. 3, pp 141–146.

Ranz, W. E., and Marshall, W. R., April 1952, Jr. Evaporation from Drops, Part II. Chemical Engineering Progress, Vol. 48, No. 4, pp 173–180.

Reuge, N., Cadoret, L., Saudejaud, Coufort C., Pannala, S., Syamlal, M., and Caussat, B., 2008, "Multifluid Eulerian Modeling of Dense Gas-Solid Fluidized bed Hydrodynamics: Influence of the Dissipation Parameters," Journal of Chemical Engineering Science, Vol. 63, 2008, pp 5540-5551.

Savage, S.B. and Jeffrey, D.J., 1981, "The Stress in a Granular Flow at High Shear Rates," Journal of Fluid Mechanics, Vol. 110, 1981, pp 255-272.

Saxena, S.C., Vogel, G.S., 1977, "The measurements of incipient fluidization velocities in a bed of coarse dolomite at temperature and pressure," Trans. Inst. Chem. Eng., Vol. 3, pp 184–195.

Schmidt, A., Renz, U., 1999, "Eulerian Computation of Heat Transfer in Fluidized Beds," Chemical Engineering Science, Vol. 54, 1999, pp 5515-5522.

Schiller, L. and Naumann, Z., 1935, Z. Ver. Deutsch. Ing., Vol. 77, pp 318.

Simonin, C. and Viollet, P. L., 1990, "Predictions of an Oxygen Droplet Pulverization in a Compressible Subsonic Co-flowing Hydrogen Flow," Numerical Methods for Multiphase Flows, FED, Vol. 91, pp 65–82.

Syamlal, M. and Gidaspow, Dimitri, 1985, "Hydrodynamic of Fluidization: Prediction of Wall to Bed Heat Transfer Coefficients," AIChE Journal , Vol. 31, No. 1, 1985, pp 127-135.

Syamlal, M. and O'Brien, T.J., 1989, "Computer Simulation of Bubbles in a Fluidized Bed," AlChE Symposium series, Vol. 85, No. 270, pp 22-31.

Syamlal, M., Rogers, W., and O'Brien T. J., 1993, MFIX Documentation: Volume 1, Theory Guide. National Technical Information Service, Springfield, VA, DOE/METC-9411004, NTIS/DE9400087.

Syamlal, M., 1987, "The Particle-Particle Drag Term in a Multi-particle Model of Fluidization," Topical Report, Work Performed under Contract No.: DE-AC21-85MC21353, May 1987.

Silaen, A. and Wang, Ting, 2004, "Simulation of Coal Gasification inside a Two stage Gasifier," Energy Conversion & Conservation Center Report, November 2004.

Silaen, A. and Wang, Ting, 2004, "Simulation of Coal Gasification inside a Two stage Gasifier," Energy Conversion & Conservation Center Report, November 2004.

Subramanian, Shankar R., "Flow Through Packed Beds and Fluidized Beds."

Todes, O.M., Citovich, O.B., 1981, "Reactors with Coarse Particle Fluidized Beds (in Russian)," Leningrad, Khimiya.

Turns, Stephen R., 2000, An Introduction to Combustion, Concepts and Application, 2nd Edition, McGraw-Hill, 2000.

Vuthaluru, Rupa, Tade, Moses, Vuthaluru, Hari, Tsvetnenko, Yuri, Evans, Louis, Milne, Jason, 2009, "Application of CFD Modeling to Investigate Fluidized Limestone Reactors for the Remediation of Acidic Drainage Waters," Journal of Chemical Engineering, Vol. 149, 2009, pp 162-172.

Wang, Shuyan., Lu, Huilin., Li, Xiang., Yu, Long., Ding, Jianmin., Zhao, Yunhua., 2008, "CFD Simulation of Bubbling Beds of Rough Spheres," Chemical Engineering Science, Vol. 63, 2008, pp 5653-5662.

Wang, Xiaofang, Jin, Baosheng, Zhong, Wenqi, 2009, "Three-Dimensional Simulation of Fluidized Bed Coal Gasification," Chemical Engineering and Processing: Process Intensification, Vol. 48, 2009, pp 695-705.

Wachem, B. G. M. van, Schouten, J. C., Bleek, C. M. van den, Krishna, R., and Sinclair, J. L., 2001, "Comparative Analysis of CFD Models of Dense Gas-Solid Systems," AIChE Journal, Vol. 47, No. 5, 2001, pp 1035-1051.

Yang, W.C. and Keairns, D.L., 1978a, "Design of Re-circulating Fluidized Beds for Commercial Applications," Fluidization, Cambridge University Press, Vol. 74(176), 1978, pp 218-228.

Yang, W.C. and Keairns, D.L., 1978b, "Design and Operating Parameters for a Fluidized Bed Agglomerating Combustor/Gasifier," Fluidization, Cambridge University Press, 1978, pp 208-214.

Yang, Wen Ching and Keairns, D.L., 1982, "Rate of Particle Separation in a Gas Fluidized Bed," Journal of Industrial Engineering Chemical Fundamentals, Vol. 21, 1982, pp 228-235.

Yang, Wen Ching, 2003, Handbook of Fluidization and Fluid-Particle Systems, Siemens Westinghouse Power Corporation, Pittsburgh, Pennsylvania, USA, Taylor & Francis Group LLC.

Yang, Wen Ching, 1998, "Comparison of Jetting Phenomena in 30-cm and 3-m diameter Semicircular Fluidized Beds," Powder Technology, Vol. 100, 1998, pp 147-160.

Yang, Wen Ching and Keairns, Dale L., "Momentum Dissipation of and Gas Entrainment into a Gas-Solid Two-Phase Jet in Fluidized Bed," Research and Development Center Report, Westinghouse Electric Corporation, Pittsburg, Pennsylvania 15235.

Yang, Wen Ching and Keairns, Dale L., 2000, "Operational Analysis of Ash-Agglomerating Fluidized Bed Gasifiers," Powder Technology, Vol. 111, 2000, pp 168-174.

Yang, Wen Ching and Keairns, D.L., 1975, "Tow-Dimensional Recirculating Bed Data with Simulated Heat Transfer Surface in the Downcomers," Industrial Engineering Chemical, Process Des. Dev., Vol. 14, No. 3, 1975, pp 259-264.

Yang, Wen Ching and Keairns, Dale L., 1979, "Estimating the Jet Penetration Depth of Multiple Vertical Grid Jets," Industrial Engineering Chemical Fundamentals, Vol. 18, No. 4, 1979, pp 317-320.

Yang, Wen Ching and Keairns, Dale L., 1983, "Studies on the Solid Circulation Rate and Gas Bypassing in Spouted Fluid-Bed with a Draft Tube," The Canadian Journal of Chemical Engineering, Vol. 61, 1983, pp 349-355.

Yan, H.M., Heidenreich, C. and Zhang, D.K., 1999, "Modeling of Bubbling Fluidized Bed Coal Gasifiers," Fuel, Vol. 78, 1999, pp 1027-1047.

Yu, Liang., Lu, Jing., Zhang, Xiangping., Zhang, Suojiang., 2007, "Numerical Simulation of the Bubbling Fluidized Bed Coal Gasification by the Kinetic Theory of Granular Flow (KTGF)," Fuel, Vol. 86, 2007, pp 722-734.

Zhong, Wenqi., Zhang, Mingyao., Jin, Baosheng., Yuan, Zhulin., 2007, "Flow Behaviors of a Large Spout-Fluid Bed at High Pressure and Temperature by 3D Simulation with Kinetic Theory of Granular Flow," Power Technology, Vol. 175, 2007, pp 90-103.

APPENDIX A

Minimum Fluidization Velocity of Carbon Solid

Correlations based on Ergun Rule

Consider a bed loaded with spherical granular material of carbon solid with diameter 0.005 m. To fluidize these particles by ambient air, the minimum fluidization velocity needs to be calculated as a reference for design or simulation purpose. One approach is to follow the Ergun Rule as shown below.

Table A1: Properties of the two phases are

Properties	Gas (air)	Particles (carbon solid)
Density, ρ (kg/m^3)	1.225	2000
Heat capacity, c_p (kJ/kg K)	1006.43	
Thermal conductivity, k (W/m K)	0.0242	
Viscosity, μ (kg/m s)	1.7894 x 10^{-5}	1.72 x 10^{-5}

According to Geldart's (1972) classification, these particles are of type B. The void fraction at the minimum fluidization is found to be ε_{mf} = 0.50. Assuming the sphericity of carbon solid Φ_s=1.0, first find out Archimedes number from the following equation:

$$\mathrm{Ar} = \frac{g\rho_g\left(\rho_s - \rho_g\right)d_p^3}{\mu_g^2}$$

$$\Rightarrow \mathrm{Ar} = \frac{(9.81)(1.225)(2000-1.225)(0.005)^3}{\left(1.7894\times10^{-5}\right)^2}$$

$$\Rightarrow \mathrm{Ar} = 9.377\times10^6$$

Then the Reynolds number at the minimum fluidization is found by solving the following equation:

$$\mathrm{Ar} = \frac{1.75(\mathrm{Re_{mf}})^2}{\phi_s(\varepsilon_{mf})^3} + \frac{150(1-\varepsilon_{mf})(\mathrm{Re_{mf}})}{(\phi_s)^2(\varepsilon_{mf})^3}$$

$$\Rightarrow 9.377\times10^6 = \frac{1.75(\mathrm{Re_{mf}})^2}{(1.0)(0.5)^3} + \frac{150(1-0.5)(\mathrm{Re_{mf}})}{(1.0)^2(0.5)^3}$$

$$\Rightarrow 1.75(\mathrm{Re_{mf}})^2 + 75(\mathrm{Re_{mf}}) - 1.17\times10^6 = 0$$

$$\Rightarrow (\mathrm{Re_{mf}})^2 + 42.85(\mathrm{Re_{mf}}) - 6.69\times10^5 = 0$$

$$\Rightarrow \mathrm{Re_{mf}} = \frac{-42.85 \pm \sqrt{42.85^2 - 4\times1\times\left(-6.69\times10^5\right)}}{2}$$

$$\Rightarrow \mathrm{Re_{mf}} = \frac{-42.85 \pm 1636.4}{2}$$

$$\Rightarrow \mathrm{Re_{mf}} = 796.77$$

From the above Reynolds number, the minimum fluidization velocity can be obtained as,

$$\mathrm{Re_{mf}} = \frac{\rho_g d_p U_{mf}}{\mu_g}$$

$$\Rightarrow 796.77 = \frac{(1.225)(0.005)U_{mf}}{1.7894\times10^{-5}}$$

$$\Rightarrow U_{mf} = 2.32\,\mathrm{m/s}$$

Todes and Citovich Correlation (1981)

$$U_{mf} = \frac{\mu_g}{d_p\rho_g}\left(\frac{\mathrm{Ar}}{1400+5.25\sqrt{\mathrm{Ar}}}\right)$$

$$\Rightarrow U_{mf} = \frac{\left(1.7894\times10^{-5}\right)}{0.005\times1.225}\left(\frac{9.377\times10^6}{1400+5.25\sqrt{9.377\times10^6}}\right)$$

$$\Rightarrow U_{mf} = 1.56\,\mathrm{m/s}$$

Saxena and Vogel Correlation (1977)

$$U_{mf} = \frac{\mu_g}{d_p\rho_g}\left[\left\{(25.28)^2 + 0.0571\times\mathrm{Ar}\right\}^{0.5} - 25.28\right]$$

$$\Rightarrow U_{mf} = \frac{\left(1.7894\times10^{-5}\right)}{0.005\times1.225}\left[\left\{(25.28)^2 + 0.0571\times\left(9.377\times10^6\right)\right\}^{0.5} - 25.28\right]$$

$$\Rightarrow U_{mf} = 2.06\,\mathrm{m/s}$$

Kumer and Gupta Correlation (1980)

$$U_{mf} = 0.005\frac{\mu_g}{d_p\rho_g}\,\mathrm{Ar}^{0.78}$$

$$\Rightarrow U_{mf} = 0.005\times\frac{\left(1.7894\times10^{-5}\right)}{0.005\times1.225}\left(9.377\times10^6\right)^{0.78}$$

$$\Rightarrow U_{mf} = 4\,\mathrm{m/s}$$

The results of these four correlations vary from 1.56 m/s to 4 m/s. Although the highest value is about 2.56 times of the lowest value, they provide a very useful estimate of the order of magnitude of the minimum fluidization velocity.

References

Geldart, D., 1972, "The effect of particle size and size distribution on the behavior of gas-fluidized beds," Powder Technology, vol. 6, pp 201–205.

Grewal, W.S. and Saxena, S.C., 1980, "Comparison of commonly used relations for minimum fluidization velocity of small solid particles," Powder Technology, Vol. 26, No. 2, pp 229–238.

Saxena, S.C. and Vogel, G.S., 1977, "The measurements of incipient fluidization velocities in a bed of coarse dolomite at temperature and pressure," Trans. Inst. Chem. Eng., Vol. 3, pp 184–195.

Todes, O.M. and Citovich, O.B., 1981, "Reactors with Coarse Particle Fluidized Beds (in Russian)," Leningrad, Khimiya.

APPENDIX B

Calculation Procedure for Adiabatic Flame Temperature

Adiabatic Flame Temperature of Partially Burnt Carbon with Only Oxygen

Case 1a:

$$C(s) + 0.5O_2 \Rightarrow CO$$

Species	$N_{react,i}$	$N_{prod,i}$	Enthalpy of formation at 298K $h^o_{f,i}$ (kJ/kmol)	Enthalpy of formation at 3400K $h_{f,i}$ (kJ/kmol)	Enthalpy of formation at 3500K $h_{f,i}$ (kJ/kmol)
C(s)	1	0	0	———	———
CO	0	1	– 110,541	– 2,051	1,694
O_2	0.5	0	0	———	———

First Law of Thermodynamics,

$$H_{react} = \sum_{react} N_i \bar{h}_i = H_{prod} = \sum_{prod} N_i \bar{h}_i$$

$$H_{react} = N_C \bar{h}_C + N_{O_2} \bar{h}_{O_2}$$

$$= 1 \times 0 + 0.5 \times 0 = 0 \text{ kJ/kmol}$$

$$\left(H_{prod}\right)_{3400K} = N_{CO} \bar{h}_{CO}$$

$$= 1 \times (-2{,}051) = -2{,}051 \text{ kJ/kmol}$$

$$\left(H_{prod}\right)_{3500K} = N_{CO} \bar{h}_{CO}$$

$$= 1 \times (1{,}694) = 1{,}694 \text{ kJ/kmol}$$

Interpolating between -2,051 kJ/kmol (for 3400K) and 1,694 kJ/kmol (for 3500K) for 0 kJ/kmol, The adiabatic flame temperature is obtained as ,

T_{ad} = 3454.76K = 5759.16°F

Adiabatic Flame Temperature of Partially Burnt Carbon with Nitrogen

Case 1b:

$$C(s) + 0.5O_2 + 1.88N_2 \Rightarrow CO + 1.88N_2$$

Species	$N_{react,i}$	$N_{prod,i}$	Enthalpy of formation at 298K $h^o_{f,i}$ (kJ/kmol)	Enthalpy of formation at 1400K $h_{f,i}$ (kJ/kmol)	Enthalpy of formation at 1500K $h_{f,i}$ (kJ/kmol)
C	1	0	0	———	———
CO	0	1	– 110,541	– 75,196	– 71,694
N_2	1.88	1.88	0	34,939	38,404
O_2	0.5	0	0	———	———

First Law of Thermodynamics,

$$H_{react} = \sum_{react} N_i \bar{h}_i = H_{prod} = \sum_{prod} N_i \bar{h}_i$$

$$H_{react} = N_C \bar{h}_C + N_{O_2} \bar{h}_{O_2} + N_{N_2} \bar{h}_{N_2}$$

$$= 1 \times 0 + 0.5 \times 0 + 1.88 \times 0 = 0 \text{ kJ/kmol}$$

$$\left(H_{prod}\right)_{1400K} = N_{CO} \bar{h}_{CO} + N_{N_2} \bar{h}_{N_2}$$

$$= 1 \times (-75{,}196) + 1.88 \times 34{,}939 = -9{,}510.68 \text{ kJ/kmol}$$

$$\left(H_{prod}\right)_{1500K} = N_{CO} \bar{h}_{CO} + N_{N_2} \bar{h}_{N_2}$$

$$= 1 \times (-71{,}694) + 1.88 \times 38{,}404 = 505.52 \text{ kJ/kmol}$$

Interpolating between -9,510.68 kJ/kmol (for 1400K) and 505.52 kJ/kmol (for 1500K) for 0 kJ/kmol, the adiabatic flame temperature is obtained as

T_{ad} = 1494.95K = 2231.51°F

Adiabatic Flame Temperature of Partially Burnt Carbon Monoxide with Only Oxygen

Case 2a:

$$CO + 0.5O_2 \Rightarrow CO_2$$

Species	$N_{react,i}$	$N_{prod,i}$	Enthalpy of formation at 298K $h^o_{f,i}$ (kJ/kmol)	Enthalpy of formation at 4600K $h_{f,i}$ (kJ/kmol)	Enthalpy of formation at 4700K $h_{f,i}$ (kJ/kmol)
CO	1	0	– 110,541	———	———
CO_2	0	1	– 393,546	– 139,794	– 133,408
O_2	0.5	0	0	———	———

First Law of Thermodynamics,

$$H_{react} = \sum_{react} N_i \bar{h}_i = H_{prod} = \sum_{prod} N_i \bar{h}_i$$

$$H_{react} = N_{CO} \bar{h}_{CO} + N_{O_2} \bar{h}_{O_2}$$

$$= 1 \times (-110{,}541) + 0.5 \times 0 = -110{,}541 \text{ kJ/kmol}$$

$$(H_{prod})_{4600K} = N_{CO_2} \bar{h}_{CO_2}$$

$$= 1 \times (-139{,}794) = -139{,}794 \text{ kJ/kmol}$$

$$(H_{prod})_{4700K} = N_{CO_2} \bar{h}_{CO_2}$$

$$= 1 \times (-133{,}408) = -133{,}408 \text{ kJ/kmol}$$

Extrapolating from -139,794 kJ/kmol (for 4600K) and -133,408 kJ/kmol (for 4700K) for -110,541 kJ/kmol, the adiabatic flame temperature is obtained as

T_{ad} = 5058.08K = 8645.14°F

Adiabatic Flame Temperature of Partially Burnt Carbon Monoxide with Nitrogen

Case 2b:

$$CO + 0.5O_2 + 1.88N_2 \Rightarrow CO_2 + 1.88N_2$$

Species	$N_{react,i}$	$N_{prod,i}$	Enthalpy of formation at 298K $h^o_{f,i}$ (kJ/kmol)	Enthalpy of formation at 2600K $h_{f,i}$ (kJ/kmol)	Enthalpy of formation at 2700K $h_{f,i}$ (kJ/kmol)
CO	1	0	– 110,541	———	———
CO_2	0	1	– 393,546	– 265,439	– 259,262
N_2	1.88	1.88	0	77,974	81,652
O_2	0.5	0	0	———	———

First Law of Thermodynamics,

$$H_{react} = \sum_{react} N_i \bar{h}_i = H_{prod} = \sum_{prod} N_i \bar{h}_i$$

$$H_{react} = N_{CO}\bar{h}_{CO} + N_{O_2}\bar{h}_{O_2} + N_{N_2}\bar{h}_{N_2}$$

$$= 1\times(-110{,}541) + 0.5\times 0 + 1.88\times 0 = -110{,}541 \text{ kJ/kmol}$$

$$(H_{prod})_{2600K} = N_{CO_2}\bar{h}_{CO_2} + N_{N_2}\bar{h}_{N_2}$$

$$= 1\times(-265{,}439) + 1.88\times 77{,}974 = -118{,}847.88 \text{ kJ/kmol}$$

$$(H_{prod})_{2700K} = N_{CO_2}\bar{h}_{CO_2} + N_{N_2}\bar{h}_{N_2}$$

$$= 1\times(-259{,}262) + 1.88\times 81{,}652 = -105{,}756.24 \text{ kJ/kmol}$$

Interpolating between -118,847.88 kJ/kmol (for 2600K) and -105,756.24 kJ/kmol (for 2700K) for – 110,541 kJ/kmol, the adiabatic flame temperature is obtained as

T_{ad} = 2663.45K = 4334.81°F

Adiabatic Flame Temperature of Completely Burnt Carbon with Only Oxygen

Case 3a:

$$C(s) + 0.5O_2 \Rightarrow CO$$
$$CO + 0.5O_2 \Rightarrow CO_2$$
$$\overline{C(s) + O_2 \Rightarrow CO_2}$$

Species	$N_{react,i}$	$N_{prod,i}$	Enthalpy of formation at 298K $h^o_{f,i}$ (kJ/kmol)	Enthalpy of formation at 4900K $h_{f,i}$ (kJ/kmol)	Enthalpy of formation at 5000K $h_{f,i}$ (kJ/kmol)
C	1	0	0	———	———
CO_2	0	1	– 393,546	– 120,626	– 114,233
O_2	1	0	0	———	———

First Law of Thermodynamics,

$$H_{react} = \sum_{react} N_i \bar{h}_i = H_{prod} = \sum_{prod} N_i \bar{h}_i$$
$$H_{react} = N_C \bar{h}_C + N_{O_2} \bar{h}_{O_2} + N_{N_2} \bar{h}_{N_2}$$
$$= 1\times 0 + 1\times 0 + 3.76\times 0 = 0 \text{ kJ/kmol}$$
$$\left(H_{prod}\right)_{4900K} = N_{CO_2} \bar{h}_{CO_2}$$
$$= 1\times(-120{,}626) = -120{,}626 \text{ kJ/kmol}$$
$$\left(H_{prod}\right)_{5000K} = N_{CO_2} \bar{h}_{CO_2}$$
$$= 1\times(-114{,}233) = -114{,}233 \text{ kJ/kmol}$$

Interpolating between -120,644 kJ/kmol (for 4900K) and -114,233 kJ/kmol (for 5000K) for 0 kJ/kmole, the adiabatic flame temperature is obtained as

T_{ad} = 6786.84 K = 11756.91 °F

Adiabatic Flame Temperature of Completely Burnt Carbon with Nitrogen

Case 3b:

$$C(s) + 0.5O_2 + 1.88N_2 \Rightarrow CO + 1.88N_2$$
$$CO + 0.5O_2 \Rightarrow CO_2$$
$$\overline{C(s) + O_2 + 1.88N_2 \Rightarrow CO_2 + 1.88N_2}$$

Species	$N_{react,i}$	$N_{prod,i}$	Enthalpy of formation at 298K $h^o_{f,i}$ (kJ/kmol)	Enthalpy of formation at 3400K $h_{f,i}$ (kJ/kmol)	Enthalpy of formation at 3500K $h_{f,i}$ (kJ/kmol)
C	1	0	0	———	———
CO_2	0	1	– 393,546	– 215,693	– 209,426
N_2	1.88	1.88	0	107,587	111,315
O_2	1	0	0	———	———

First Law of Thermodynamics,

$$H_{react} = \sum_{react} N_i \bar{h}_i = H_{prod} = \sum_{prod} N_i \bar{h}_i$$
$$H_{react} = N_C \bar{h}_C + N_{O_2} \bar{h}_{O_2} + N_{N_2} \bar{h}_{N_2}$$
$$= 1\times 0 + 1\times 0 + 1.88\times 0 = 0 \text{ kJ/kmol}$$
$$\left(H_{prod}\right)_{3400K} = N_{CO_2} \bar{h}_{CO_2} + N_{N_2} \bar{h}_{N_2}$$
$$= 1\times(-215{,}693) + 1.88\times 107{,}587 = -13{,}429.44 \text{ kJ/kmol}$$
$$\left(H_{prod}\right)_{3500K} = N_{CO_2} \bar{h}_{CO_2} + N_{N_2} \bar{h}_{N_2}$$
$$= 1\times(-209{,}426) + 1.88\times 111{,}315 = -153.8 \text{ kJ/kmol}$$

Interpolating between -13,429.44 kJ/kmol (for 3400K) and -153.8 kJ/kmol (for 3500K) for 0 kJ/kmol, the adiabatic flame temperature is obtained as

T_{ad} = 3501.15 K = 5842.67 °F

Adiabatic Flame Temperature of Completely Burnt Carbon with only Oxygen

Case 4a:

$$C(s) + 0.5O_2 \Rightarrow CO$$
$$C(s) + CO_2 \Rightarrow 2CO$$
$$C(s) + H_2O(g) \Rightarrow CO + H_2$$
$$CO + 0.5O_2 \Rightarrow CO_2$$
$$CO + H_2O(g) \Rightarrow CO_2 + H_2$$
$$3C(s) + O_2 + 2H_2O(g) \Rightarrow 2CO + 2H_2 + CO_2$$

Species	$N_{react,i}$	$N_{prod,i}$	Enthalpy of formation at 298K $h^o_{f,i}$ (kJ/kmol)	Enthalpy of formation at 1000K $h_{f,i}$ (kJ/kmol)	Enthalpy of formation at 1100K $h_{f,i}$ (kJ/kmol)
C	3	0	0	———	———
CO	0	2	– 110,541	-88,844	-85,495
O_2	1	0	0	———	———
H_2O	2	0	-241,845	———	———
H_2	0	2	0	20,664	23,704
CO_2	0	1	-393,546	-360,121	-354,635

First Law of Thermodynamics, $H_{react} = \sum_{react} N_i \bar{h}_i = H_{prod} = \sum_{prod} N_i \bar{h}_i$

$$H_{react} = N_C \bar{h}_C + N_{O_2} \bar{h}_{O_2} + N_{H_2O} \bar{h}_{H_2O}$$
$$= 3 \times 0 + 1 \times 0 + 2 \times (-241{,}845) = -483{,}690 \text{ kJ/kmol}$$
$$(H_{prod})_{1000K} = N_{CO} \bar{h}_{CO} + N_{H_2} \bar{h}_{H_2} + N_{CO_2} \bar{h}_{CO2}$$
$$= 2 \times (-88{,}844) + 2 \times (20{,}664) + 1 \times (-360{,}121) = -496{,}481 \text{ kJ/kmol}$$
$$(H_{prod})_{1100K} = N_{CO} \bar{h}_{CO} + N_{H_2} \bar{h}_{H_2} + N_{CO_2} \bar{h}_{CO_2}$$
$$= 2 \times (-85{,}495) + 2 \times (23{,}704) + 1 \times (-354{,}635) = -478{,}217 \text{ kJ/kmol}$$

Interpolating between -496,481 kJ/kmol (for 1000K) and -478,217 kJ/kmol (for 1100K) for -483,690 kJ/kmol, the adiabatic flame temperature is obtained as

T_{ad} = 1070.03 K = 1466.65 °F

Adiabatic Flame Temperature of Completely Burnt Carbon with Nitrogen

Case 4b:

$$C(s) + 0.5O_2 + 1.88N_2 \Rightarrow CO + 1.88N_2$$
$$C(s) + CO_2 \Rightarrow 2CO$$
$$C(s) + H_2O(g) \Rightarrow CO + H_2$$
$$CO + 0.5O_2 + 1.88N_2 \Rightarrow CO_2 + 1.88N_2$$
$$CO + H_2O(g) \Rightarrow CO_2 + H_2$$
$$3C(s) + 2H_2O(g) + O_2 + 3.76N_2 \Rightarrow 2CO + 2H_2 + CO_2 + 3.76N_2$$

Species	$N_{react,i}$	$N_{prod,i}$	Enthalpy of formation at 298K $h^o_{f,i}$ (kJ/kmol)	Enthalpy of formation at 800K $h_{f,i}$ (kJ/kmol)	Enthalpy of formation at 900K $h_{f,i}$ (kJ/kmol)
C	3	0	0	———	———
CO	0	2	– 110,541	-95,365	-92,140
N_2	3.76	3.76	0	15,046	18,222
O_2	1	0	0	———	———
H_2O	2	0	-241,845	———	———
H_2	0	2	0	14,701	17,668
CO_2	0	1	-393,546	-370,736	-365,499

First Law of Thermodynamics, $H_{react} = \sum_{react} N_i \bar{h}_i = H_{prod} = \sum_{prod} N_i \bar{h}_i$

$$H_{react} = N_C \bar{h}_C + N_{O_2} \bar{h}_{O_2} + N_{H_2O} \bar{h}_{H_2O} + N_{N_2} \bar{h}_{N_2}$$
$$= 3 \times 0 + 1 \times 0 + 2 \times (-241{,}845) + 3.76 \times 0 = -483{,}690 \text{ kJ/kmol}$$

$$(H_{prod})_{800K} = N_{CO} \bar{h}_{CO} + N_{H_2} \bar{h}_{H_2} + N_{CO_2} \bar{h}_{CO_2} + N_{N_2} \bar{h}_{N_2}$$
$$= 2 \times (-95{,}365) + 2 \times (14{,}701) + 1 \times (-370{,}736) + 3.76 \times 15{,}046 = -475{,}491.04 \text{ kJ/kmol}$$

$$(H_{prod})_{900K} = N_{CO} \bar{h}_{CO} + N_{H_2} \bar{h}_{H_2} + N_{CO_2} \bar{h}_{CO2} + N_{N_2} \bar{h}_{N_2}$$
$$= 2 \times (-92{,}140) + 2 \times (17{,}668) + 1 \times (-365{,}499) + 3.76 \times 18{,}222 = -445{,}928.28 \text{ kJ/kmol}$$

Interpolating between -503,777.52 kJ/kmol (for 800K) and -480,185.64 kJ/kmol (for 900K) for -483,690 kJ/kmol, the adiabatic flame temperature is obtained as

T_{ad} = 772.25 K = 930.65 °F

Table B1: Summary of theoretical and CFD simulated adiabatic flame temperatures for various cases

No.	Cases	Adiabatic Flame Temperature (K) Theoretical	Adiabatic Flame Temperature (K) ANSYS/FLUENT	Adiabatic Flame Temperature (^{o}F) Theoretical	Adiabatic Flame Temperature (^{o}F) ANSYS/FLUENT
1	Case 1a	3454.76	3463.05	5759.16	5774.09
2	Case 1b	1494.95	1495.90	2231.51	2233.22
5	Case 2a	5058.08	5101.84	8645.14	8723.91
6	Case 2b	2663.45	2665.76	4334.81	4339.59
9	Case 3a	6786.84		11756.91	
10	Case 3b	3501.15	3500.38	5842.67	5841.28
21	Case 4a	1070.03	1070.03	1466.65	1466.65
22	Case 4b	885.15	888.68	1133.87	1140.22

The comparisons between the theoretical and CFD simulated adiabatic temperature values for various cases are very close. This verifies the CFD model is adequate.

Reference

Turns, Stephen R., 2000, An Introduction to Combustion, Concepts and Application, 2nd Edition, Appendix A, McGraw-Hill, 2000.

APPENDIX C

Calculations of Molecular Compositions and Enthalpy of Formation of Volatiles

Table 1 Moisture-free (MF) composition of Indonesian coal

Proximate Analysis (MF), wt%		***Ultimate Analysis (MF), wt%***	
Volatile	51.29	C	73.32
Fixed Carbon (FC)	47.54	H	4.56
Ash	1.17	O	20.12
	100.00	N	0.72
		S	0.11
		Ash	1.17
			100.00

The reaction model employed in this study is different than the model employed in the previous studies, where instantaneous gasification model was used. In this study, Eulerian multi-phase model is used to model the coal particles, and finite-rate reaction is used to model their reaction rates.

Devolatilization Model

After all the moisture contained in the coal particle has evaporated, the particle undergoes devolatilization. The Chemical Percolation Devolatilization (CPD) model is used. The CPD model considers the chemical transformation of the coal structure during devolatilization. It models the coal structure transformation as a transformation of chemical bridge network, which results in release of light gas, char, and tar [Fletcher and Kerstein (1992), Fletcher et. Al (1990), and Grant et. Al (1989)]. In this study, the volatile contained is calculated to be $CH_{2.121}O_{0.5855}$. The detailed calculation process will be shown later. The initial fraction of the bridges in the coal lattice is 1, and the initial fraction of char is 0. The lattice coordination number is 5. The cluster molecular weight is 400, and the side chain molecular weight is 50.

The devolatilization model used in this study adopts a two-step process:

(i) Release of a volatile gas modeled using the CPD.

(ii) Thermally cracking the volatile gas into lighter gases CO, H_2 via an intermediate gas, C_6H_6.

Volatile's Chemical Composition

To model part (i), the chemical formula of volatile matters has to be known. However, coal composition given in Table 1 does not provide the volatiles' chemical composition. Thus, the chemical composition needs to be found out indirectly. Based on the proximate and ultimate analyses listed in Table 1, the elemental composition of the volatiles is determined below.

$$\text{wt\%}_{\text{C, volatiles}} = \frac{\text{wt\%}_{\text{C}}}{\text{wt\%}_{\text{volatiles}}} = \frac{\text{wt\%}_{\text{C, ultimate}} - \text{wt\%}_{\text{FC, proximate}}}{\text{wt\%}_{\text{volatiles}}} = \frac{73.32\% - 47.54\%}{51.29\%} = 50.26\%$$

$$\text{wt\%}_{\text{H, volatiles}} = \frac{\text{wt\%}_{\text{H}}}{\text{wt\%}_{\text{volatiles}}} = \frac{4.56\%}{51.29\%} = 8.89\%$$

$$\text{wt\%}_{\text{O, volatiles}} = \frac{\text{wt\%}_{\text{O}}}{\text{wt\%}_{\text{volatiles}}} = \frac{20.12\%}{51.29\%} = 39.23\%$$

$$\text{wt\%}_{\text{N, volatiles}} = \frac{\text{wt\%}_{\text{N}}}{\text{wt\%}_{\text{volatiles}}} = \frac{0.72\%}{51.29\%} = 1.40\%$$

$$wt\%_{S,\ volatiles} = \frac{wt\%_{S}}{wt\%_{volatiles}} = \frac{0.11\%}{51.29\%} = 0.22\%$$

The chemical formula of the volatiles is assumed to be in the form of $C_xH_yO_z$. The other elements, N and S, will be injected as gas, together with the oxidant through the inlet injections.

Weight percentages of C, H, and O in the volatiles after N and S have been removed are,

$$wt\%_{C\ in\ C_xH_yO_z} = \frac{wt\%_{C,\ volatiles}}{wt\%_{volatiles} - wt\%_{N,\ volatiles} - wt\%_{S,volatiles}} = \frac{50.26\%}{100\% - 1.40\% - 0.22\%} = 51.09\%$$

$$wt\%_{H\ in\ C_xH_yO_z} = \frac{wt\%_{H,\ volatiles}}{wt\%_{volatiles} - wt\%_{N,\ volatiles} - wt\%_{S,volatiles}} = \frac{8.89\%}{100\% - 1.40\% - 0.22\%} = 9.03\%$$

$$wt\%_{O\ in\ C_xH_yO_z} = \frac{wt\%_{O,\ volatiles}}{wt\%_{volatiles} - wt\%_{N,\ volatiles} - wt\%_{S,volatiles}} = \frac{39.23\%}{100\% - 1.40\% - 0.22\%} = 39.88\%$$

For part (ii), the volatile matters, $C_xH_yO_z$, are assumed to be thermally cracked into CO, H_2 and C_6H_6 according to the equation below,

$$C_xH_yO_z \rightarrow a\ CO + b\ H_2 + c\ C_6H_6$$

The coefficients a, b, and c are calculated by performing mass balance of each element in the equation above.

Mass of each element in terms of the reaction coefficients are,

C: $m_C = (a + 6c) \times 12 = 12a + 72c$

H: $m_H = (2b + 6c) \times 1 = 2b + 6c$

O: $m_O = a \times 16 = 16a$

Assuming 1 kg of volatiles, the actual mass of each element is calculated and is substituted into the equations above to determine the reaction coefficients.

$m_O = wt\%_{O\ in\ CxHyOz} \times 1\ kg = 0.3988\ kg$

$\Rightarrow 16a = 0.3988 \Rightarrow a = 0.02493$

$m_C = wt\%_{C\ in\ CxHyOz} \times 1\ kg = 0.5109\ kg$

$$\Rightarrow 12a + 72c = 0.5109 \Rightarrow c = \frac{0.5109 - 12(0.02493)}{72} = 0.002941$$

m_H = $wt\%_{H \text{ in } CxHyOz}$ x 1 kg = 0.0903 kg

$$\Rightarrow 2b + 6c = 0.0903 \Rightarrow b = \frac{0.0903 - 6(0.002941)}{2} = 0.03633$$

With the coefficients a, b, and c being known, the thermal-cracking equation is rewritten as,

$$C_xH_yO_z \rightarrow 0.02493CO + 0.03633H_2 + 0.002941C_6H_6$$

Mass balance of each element is done to determine the values of x, y, and z.

$\Rightarrow$ x = 0.02493 + 6(0.002941) = 0.04258

$\Rightarrow$ y = 2(0.03633) + 6(0.002941) = 0.09031

$\Rightarrow$ z = 0.02493

So, the volatiles' thermal-cracking equation becomes,

$$C_{0.04258}H_{0.09031}O_{0.02493} \rightarrow 0.02493\ CO + 0.03633\ H_2 + 0.002941\ C_6H_6$$

Normalize the coefficients to have the volatile in CH_mO_n form yields,

$$CH_{2.121}O_{0.5855} \rightarrow 0.5855\ CO + 0.8532\ H_2 + 0.06907\ C_6H_6$$

Enthalpy of Volatiles

The enthalpy of the volatiles is not known and thus needs to be calculated. A correct enthalpy value of the volatiles will ensure that energy is properly balanced in the volatiles thermal-cracking reaction.

The steps taken to find the enthalpy of the volatile, $CH_{2.121}O_{0.5855}$, are as follows.

(a) Calculate the volatiles' heating value

The volatiles' heating value is found by subtracting carbon's heating value from the coal's heating value as

$$HV_{CH2.121O0.5855} = HV_{coal} - HV_C$$

where,

HV_{coal} = 5,690 kcal/kg of coal ≈ 23.8 MJ/kg of coal

$$HV_C = 393{,}546 \frac{\text{kJ}}{\text{kmole of C}} \times \frac{1\text{ MJ}}{1000\text{ kJ}} \times 0.0396 \frac{\text{kmole of C}}{\text{kg of coal}} = 15.584\ \frac{\text{MJ}}{\text{kg of coal}}$$

Thus, the heating value of the volatiles is,

$HV_{CH2.121O0.5855}$ = (23.8 – 15.584) MJ/kg of coal = 8.216 MJ/kg of coal

Converting the volatiles' heating value in terms of mole number is,

$$HV_{CH2.121O0.5855} = 8.216\frac{\text{MJ}}{\text{kg coal}} \times \frac{1 \text{ kg coal}}{0.01971 \text{ kmole volatiles}} = 416.844\frac{\text{MJ}}{\text{kmole}}$$

(b) Calculate volatiles' enthalpy based on the volatile combustion reaction.

The chemical equation for the volatiles combustion is

$$CH_{2.121}O_{0.5855} + 1.2378O_2 \rightarrow CO_2 + 1.061H_2O\ (g)$$

The equation of the volatiles' heating value (at 25°C) is expressed as,

$$HV_{CH_{2.121}O_{0.585}} = \left[\left(1 \times h_{f,CH_{2.121}O_{0.585}}\right) + \left(1.2378 \times h_{f,O_2}\right)\right] - \left[\left(1 \times h_{f,CO_2}\right) + \left(1.061 \times h_{f,H_2O(g)}\right)\right]$$

Where,

$h_{f,CO2}$ = -393,546 kJ/kmole

$h_{f,H2O(g)}$ = -241,845 kJ/kmole

$h_{f,O2}$ = 0.

The equation is rearranged to give,

$$h_{f,CH_{2.121}O_{0.585}} = HV_{CH_{2.121}O_{0.585}} - \left(1.2378 \times h_{f,O_2}\right) + \left[\left(1 \times h_{f,CO_2}\right) + \left(1.061 \times h_{f,H_2O(g)}\right)\right]$$

Substituting the enthalpy values into the equation above gives,

$h_{f,CH2.121O0.585}$ = 416.844x10^3 – (1.2378 x 0) + [1 x (-393,546) + 1.061 x (-241,845)]

$h_{f,CH2.121O0.585}$ = 416,844 - 393,546 -256,597.54

$h_{f,CH2.121O0.585}$ = -233,299.54 kJ/kg

The value of -233,299.54 kJ/kg is used as the enthalpy of the volatile ($CH_{2.121}O_{0.5855}$) at 25°C.

The molecular weight of the volatile ($CH_{2.121}O_{0.5855}$) = 12+1 x 2.121+16 x 0.5855

= 12+2.121+9.368

= 23.489

APPENDIX D

Calculation of Inlet Gas Mass Fraction at the Draft Tube Inlet

In the draft tube inlet, the air-carbon mixture is fed with a velocity of 4 m/s with the carbon volume fraction of 0.1 as the secondary phase. The density of carbon solid is 2000. The mass flow rate of carbon = 0.1 x 2000 x 0.0508 x 4 = 40.64 kg/s-m. This is the same mass flow rate of carbon stated in Ch. 3, Case 6a and Case 7 in Ch. 5 used the same mass flow rate of carbon (40.64 kg/s-m); only Case 6b is different. The total mass flow rate at the draft tube inlet is calculated as below:

$C+ (O_2+3.76N2) = CO_2+3.76N_2$
L.H.S= [12+32+105.28] ==R.H.S= [44+105.28]
Air=32+105.28 =137.28

Mass fraction of oxygen (O_2) in air = 32/137.28=0.2331
Mass fraction of nitrogen (N_2) in air = 105.28/137.28=0.7669

The theoretical amounts of air needed for the complete combustion of carbon solid particles are following. For this reaction, the product contains only carbon dioxide and nitrogen (as inert gas).

$C+ (O_2+3.76N_2) = CO_2+3.76N_2$

Ratio of air and carbon (mass basis) = [air / carbon (C)] = [(32+3.76 x 28)/12] = [137.28/12] = 11.44 kg of air/kg of carbon (based on theoretical amount of air).

Only 10% of the theoretical amount of air is needed for mild gasification.

10% of the theoretical air = 10% of 137.28 = 13.728

Ratio of 10% of the theoretical air and carbon (mass basis) = [10% of air / carbon (C)] = [(137.28 x 0.1)/12] =1.144 kg of air/kg of carbon (based on 10% of the theoretical amount of air).

Ratio of mass flow rate [air/ carbon (C)] = [air /40.64] ==1.144 kg of air/kg of carbon (based on 10% of the theoretical amount of air).

Mass flow rate of air= 46.4921 kg/s-m

For Indonesian coal (according to Appendix "C"),
Ratio of fixed carbon and volatiles = [Fixed carbon/volatiles] = [47.54/51.29]
Ratio of mass flow rate [carbon (C)/volatiles] = [40.64/volatiles] == [47.54/51.29]

Mass flow rate of volatiles = 43.8457 kg/s-m

Total gas mass flow rate of (volatiles +air) = (43.8457+46.4921) =90.3378 kg/s-m.

Gas mass fraction of volatiles = 43.8457/90.3378 =**0.4854**
Gas mass fraction of oxygen (O_2) = (46.4921 /90.3378) x 0.2332 =**0.1200**
Gas mass fraction of nitrogen (N_2) = (46.4921 /90.3378) x 0.7668 =**0.3946**

Total gas mass fraction =0.4854+0.1200+0.3946 =1.0000

VITA

A. K. M. Monayem Hossain Mazumder was born in Comilla, Bangladesh, in 1982. He received his Bachelor's of Science in Mechanical Engineering from Bangladesh University of Engineering and Technology (BUET), Dhaka, Bangladesh in 2006. He then continued to pursue Master's of Science in Mechanical Engineering degree from the University of New Orleans. During his post-graduate program, he worked as a Research Assistant at the Energy Conversion and Conservation Center (ECCC) at University of New Orleans under the supervision of Dr. Ting Wang. He received his Master's of Science in Mechanical Engineering from University of New Orleans in 2010.